Structure and Energetics of Trivalent Metal Halides

Francis Hutchinson

Linacre College, Oxford

A thesis submitted in partial fulfilment of the requirements for the degree of Doctor of Philosophy of the University of Oxford

Michaelmas Term 1999

Structure and Energetics of Trivalent Metal Halides

Francis Hutchinson
Linacre College, University of Oxford

A thesis submitted in partial fulfilment of the requirements
for the degree of Doctor of Philosophy, Michaelmas Term 1999

Abstract

Metal trihalide (MX_3) systems represent a stern challenge in terms of constructing transferable potential models. Starting from a previously published set of potentials, 'extended' ionic models are developed which, at the outset, include only anion polarization. Deficiencies in these models, particularly for smaller (highly polarizing) cations, are shown to be significant. For example, crystal structures different to those observed experimentally are adopted. The potentials are improved upon by reference to *ab initio* information available for alkali halides with the 'constraint' that the parameters transfer systematically in a physically transparent manner, for example, in terms of ion radii. The possible influence of anion compression ('breathing') and the relative abundance of anion-anion interactions are considered. Simulation techniques are developed to allow for the effective simulation of any system symmetry and for the study of transitions between different crystals (constant stress). The developed models are fully tested for a large range of metal trichloride (MCl_3) systems. Particular attention is paid to the comparison with recent neutron and X-ray diffraction data on the liquid state. Polarization effects are shown to be vital in reproducing strong experimental features. The excellent agreement between simulation and experiment allows for differences in experimental procedures to be highlighted.

The transferability is further tested by modelling mixtures of the lanthanides with alkali halides with potentials unchanged from the pure systems. The complex evolution of the melt structure is highlighted as the concentration of MCl_3 increases. The effectiveness of the models is tested by reference to dynamical properties. Particular attention is paid to the comparison with Raman scattering data available for a wide range of systems and mixture concentrations. The simulated spectra are generated both by a simple molecular picture of the underlying vibrations and by a more complex (fluctuating polarizability) model in which the spectra are broken down into contributions from different mechanisms. This comparison allows for the validity of treating network-like systems as a series of 'isolated' molecules to be assessed. The transferability of the potentials is pushed to the limits by modelling metal tribromides, in which the parameters are obtained from the trichlorides by the same simple scaling arguments.

To my parents.

Acknowledgments

Above all I would like to thank my supervisor Prof. Paul Madden for all his help and encouragement over the last three years.

In addition, I am indebted to Mark Wilson for many useful discussions and for his contributions to the preparation of this thesis.

Thanks go also to the many other members of the Madden group, past and present. I would especially like to thank Malcolm, Michael, Richard, Angus and Leonardo for proof reading this thesis. Also to the many other people who have been involved with the group during the course of my DPhil.: Ben, Adrian, Patrick, John and Graham to name but a few.

I have also been fortunate enough to be involved in a number of stimulating collaborations. I would like to thank a number of experimentalists for the free-flow of ideas and information. I thank Dr. Phil Salmon and Dr. Jonathan Wasse both formerly of UEA for what has been a most productive project. I have also greatly benefitted from two very enjoyable trips to Greece and would like to thank George Papatheodorou, Litsa Pavlatou and Georgia Zissi for this. Thanks also go to Ashok Adya and Haruaki Matsuura of Abertay University, Dundee and sadly to the late Ryuzo Takagi of Tokyo Institute of Technology.

Finally I would like to thank the many good friends I have made in Oxford for all the good times over the last seven years.

Contents

Chapter 1

Introduction

1.1 Aims and Overview

In recent years considerable progress has been made in constructing "extended" ionic models to simulate a range of solid, liquid and glassy properties [1–4]. By "extended" ionic model we mean that the ion's response to the environment is included explicitly. For example, an ion may be polarized by electric fields and gradients. A major remit for such models is that they should be *transferable*, that is, the potential parameters should be transmutable between systems, for example in terms of a change in anion or cation radius.

Metal trihalide (MX_3) systems present a considerable challenge from this perspective as variation in cation size leads to massive changes in structural and dynamical properties. For example, $AlCl_3$, a system with a relatively small cation radius, forms a molecular structure consisting of Al_2Cl_6 dimers not normally associated with 'ionicity'. Larger cations such as La^{3+} and Tb^{3+}, form classical 'ionic' structures which may be understood basically in terms of packing of charged spheres. The challenge, therefore, is to be able to reproduce such a wide range of physical properties with essentially the same model in which parameters transmute systematically in terms of cation radii. The study of these systems is of more than academic interest. The preponderance of such systems for, in particular, the actinides, raises the possibility of their use in the reprocessing of highly dangerous, nuclear waste containing nuclear isotopes such as ^{238}U [5,6]. In such methods the spent fuel (typically an oxide) is reacted to form a soluble metal trihalide which can then be used in the process of electrorefining. However, the construction of such materials requires a wide knowledge of the structural and dynamical properties of both the pure trihalides and their mixtures with ions added to affect the various properties.

As a result, significant effort has recently been directed at determining the structures of the pure melts using both neutron and X-ray diffraction techniques [7–17]. The systematic changes observed in these experiments suggest the use of transferable models to describe their properties.

In this thesis we take up the challenge of systematically modelling a range of metal trihalides for which much experimental information has become available. The starting point will be earlier simulation pair potentials obtained from experimental Raman frequency data [18]. These potentials will be augmented with polarization effects already shown to be vital in representations of the experimental structural and dynamical properties of MX_2 systems [19–21]. To validate these models we shall refer to both the liquid and crystalline phases. MX_3 systems show a rich variety of crystal structures in which the anion environment changes markedly. In the liquid phase experimental neutron scattering and X-ray diffraction techniques give a wide range of structural information. The final potential models should therefore be able to reproduce these wide variations in both liquid and crystalline structure.

In addition to this, the large number of anions in these systems leads us to anticipate a significant role for the anion-anion short range terms. In alkali halides, for example, these anion-anion terms are dominated by the M-X short range interactions and so are relatively unimportant as anions may be reasonably considered to be completely surrounded by cations. In the MX_3 stoichiometry such an approximation is less valid as there will be many anion-anion 'contacts'. Again, in order to uncover these terms, contact will be made with *ab initio* data which focusses on the alkali halides [22].

In the process of investigating these systems we shall also consider the level of model complexity required to achieve our goal of transferability. For example, the effective modelling of oxides has been shown to require the inclusion of the spherical relaxation ("breathing") of the anion [2]. The large number of anions in the MX_3 stoichiometry may lead us to believe that such effects may be significant here. To assess these effects contact will be made with the structurally simpler alkali halides for which *ab initio* data is available.

In addition, the study of properties such as the relatively complex crystal structures will require the development of the modelling techniques. For example, many of the structures have a non-cubic symmetry and so require the simulation cell to adopt the required symmetry. Furthermore, the transitions (pressure or temperature driven) between these structures represents an additional useful point of contact with experiment. The study of these transitions requires the development of constant stress (Parrinello-Rahman [23]) techniques in which the cell volume and geometry evolves with time. Such techniques are non-trivial when many body forces are involved.

The validation of the models focusses on structural properties in two phases. To further test the effectiveness of the potentials we shall also consider dynamical properties such as the conductivity and Raman spectra. The latter, in particular, is very useful as it allows us to observe the systematic evolution of short-range structure as the concentration of metal trihalide changes.

Finally transferability with a change in anion radius - to model a number of bromides will be investigated.

1.2 Ions in the Condensed Phase

In order to understand the interactions in the condensed phase it is not sufficient to think of the ions as a collection of well-defined, gas-phase species. Ions in an ionic material are profoundly influenced by their environment [24]. For example, the oxide ion, O^{2-}, is unstable with respect to electron loss in the gas phase but is a common counter ion to many metal cations. The addition of the second electron to O^- is stabilised by the condensed phase Madelung potential. This phenomenon shows that the interaction of one ion with another is environment dependent and so the interaction potentials used must have an explicit many body character.

These many body effects can be understood by considering an anion surrounded by a lattice of point charges (figure 1.1). The Madelung potential ($V(\mathbf{r})$) experienced by an electron in the central ion due to electrostatic interactions with the charges of the other ions in the crystal can be written as

$$V(\mathbf{r}) = -\sum_j \frac{Q_j}{|\mathbf{r} - \mathbf{r}_j|}, \tag{1.1}$$

where Q_j and $\mathbf{r}_j$ are the ionic charge and position vector of ion j respectively. This *Madelung* potential contains a spherical part, $V_0(\mathbf{r})$ plus an angularly dependent contribution, which varies rapidly with the orientation of the electronic position, $\mathbf{r}$. Written as a spherical harmonic expansion the Madelung potential becomes

$$V(\mathbf{r}) = V_0(r) + V_4(r)\sum_m Y_{4,m}(\mathbf{r}) + V_6(r)\sum_m Y_{6,m}(\mathbf{r}) + \ldots. \tag{1.2}$$

Since the ground electronic state of a closed shell ion (such as the Cl^- ion) is an S state, the angular potential will only be significant to the extent that it can mix in excited states of G symmetry. For many ions (especially s-p valence

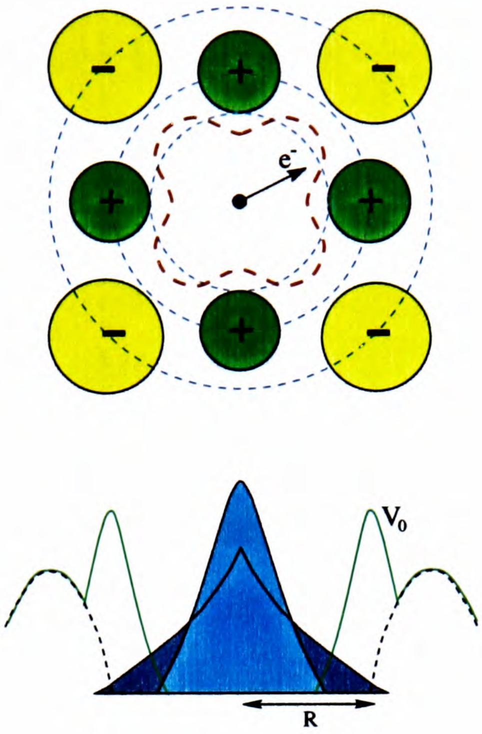

Figure 1.1: *Top panel: The origin of the spherically confining potential, V(0), in a cubic crystal. Bottom panel: A cross section through the spherical potential ,* V_0*. The Madelung contribution is represented by the green line and the dashed line is the potential due to exclusion from the region occupied by the other ions. The compression of the free ion electron density (cyan) is also shown.*

ions) such states are likely to be very far in energy from the ground state, so that only the spherical potential plays any role - and the electron density of the ion remains spherical.

The spherical potential, V_0, tends to compress the ion's electron density, relative to that of the free ion (figure 1.1). There is another contribution to the potential shown in figure 1.1. This is due to the electron's exclusion from the region occupied by the electron density of neighbouring ions.

An argument similar to that used for the anion's compression but with the opposite result can be applied to a cation surrounded by a lattice of anions. The cation's electrons tend to be more tightly bound and so are less sensitive than those of an anion to the crystal environment. Now the Madelung potential acts to destabilize the cation relative to the free state due to the repulsive interaction between the cation's electrons and the negatively charged anion.

So far the ions have been treated as point charges. Now, instead of point charges they are considered to have a finite electron density. This leads to a further compression of the anion's electron density. Mahan [25] showed that treating ions as finite resulted in one-electron pseudo-potentials with a form similar to that in equation 1.2. Again the potential can be considered to be spherical - but now with a radius appropriate to the anion radius at which the cation's electron density becomes non-zero (figure 1.2). Pyper [26] has shown that by considering the ions to be finite two new effects arise. These are

- an attractive interaction between the anion's electron density and the cation nuclei and
- a (much larger) repulsive interaction. This is due to the increase in the kinetic energy of the electrons in the repulsive overlap between cation and anion charge densities due to the Pauli Exclusion principle as shown in figure 1.2. The overall result of this is that the two effects – overlap and crystal field - act to compress the anion's electron density. This leads to a marked reduction of the polarizability of the ion in the crystal [27, 28] (for Cl^- it is reduced from 35au to 20au) and is responsible for the stability of the aforementioned oxide ion in condensed matter.

The naïve view of the origin of the repulsive forces which prevent the collapse of an ionic crystal under the influence of the Madelung potential is illustrated in the second panel of figure 1.2. As the lattice parameter is reduced, the degree of overlap between anion and cation charge densities increases, with a consequential increase in the electronic energy. If we take the electron densities to decay exponentially and the total overlap energy to be the sum of the overlap energies associated with each cation-anion pair, then referring to figure 1.2, the energy would depend on the total green coloured areas associated with the overlapping charge clouds. We would, therefore, have an energy of the form

$$U_{ov} = \sum_i \sum_{j>i} A exp[-(r_{ij} - \sigma_i - \sigma_j)/(\rho_i + \rho_j)], \tag{1.3}$$

ie. a pair potential of Born-Mayer form, to describe the interionic repulsion. Here r_{ij} is the separation between i and j, σ_i is a characteristic radius for the charge density of ion i and ρ_i describes how it falls off with increasing distance from the nucleus.

In fact what happens is what is illustrated in the bottom panel. As the lattice parameter is reduced, the anion's electron density is further compressed. This increases the intrinsic energy of that anion, which might be called a "rearrangement" or "self" energy, and, furthermore, because of the contraction of its electron cloud, the degree of overlap with the neighbouring cations is reduced (green shaded area). If this rearrangement is not large, it might be possible to ignore the distinction between the two effects and model the repulsion with the pair potential as above. If, on the other hand, the rearrangement and overlap energies have different dependencies on, say, the coordination number, it will be necessary to separate them and recognise explicitly the many-body nature of the repulsions.

An examination of this effect for halide systems is included in Chapter 5 - the "Compressible Ion Model". Note that if such compressibility effects are large, it is to be expected that to model the repulsive interactions in a general environment of lower symmetry than a cubic crystal the anion will need to be allowed a flexible *shape* which responds to the environmental potential.

1.2.1 Modelling Polarization

The origin of many body effects due to polarization is described as follows. In the case of an isolated ion pair, ij, the dipole induced on ion i by a permanent point charge located at the centre of ion j is given by

$$\mu^i = \alpha \mathbf{E}^{ij} \qquad (1.4)$$

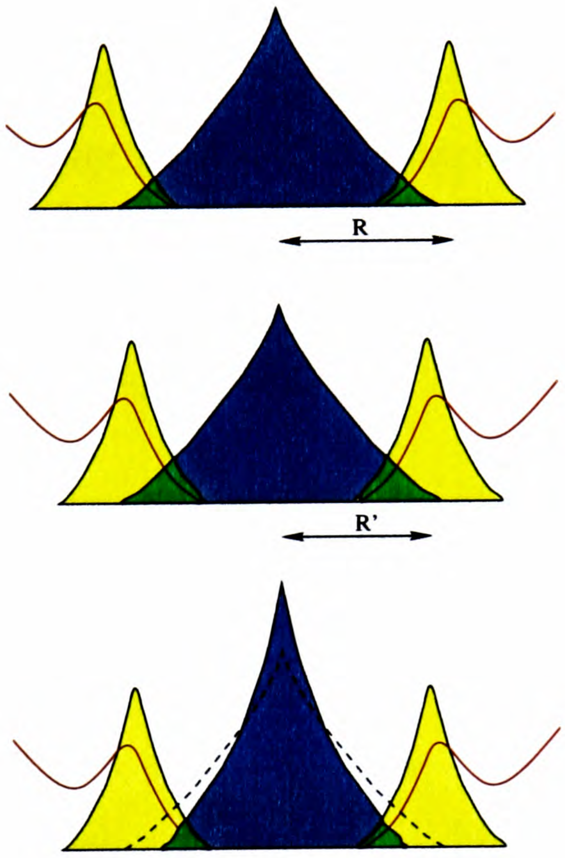

Figure 1.2: *Top: anion charge density (blue) in the crystal at lattice spacing* R*, as confined by* V_0*. The cation electron density is coloured yellow and the cation-anion overlap is coloured green.*

Middle: Compression of crystal to lattice spacing R'

Bottom: Compression of anion charge density by modified potential.

where α is the polarizability of i and $\mathbf{E}^{ij}$ is the electric field on i due to j. If this ion pair, ij, is now placed in a condensed environment with, among others, ion k, then the dipole induced on i by the charge on j will affect the dipole on k, which, in turn will alter the dipole on i. The self consistent dipoles are given by the equation [29]

$$\mu^i_{coul} = \alpha_i \sum_{j \neq i} \frac{Q_j \mathbf{r}_{ij}}{r^3_{ij}} - \sum_{j \neq i} \left[\frac{\mu^j}{r^3_{ij}} - \frac{3\mathbf{r}_{ij}(\mathbf{r}_{ij}.\mu^j)}{r^5_{ij}} \right]. \tag{1.5}$$

and compared to the pair potential alone (RIM) the inclusion of these effects will be very computationally expensive. Equation 1.5 has omitted any short-range contribution to the dipoles. As will be seen in later Chapters the effect of polarization on the structure and energetics of highly symmetric crystals is negligible. This is due to the cancellation of the electric fields in the sum $\sum_{j \neq i} \frac{Q_j \mathbf{r}_{ij}}{r^3_{ij}}$.

Polarization effects can be characterized by examining directly, using electronic structure methods, the induced multipoles on ions in distorted crystals. If an ion in a crystal at a relatively large distance from a specific ion is displaced off its lattice site, its effect on the potential felt by the electrons in the ion of interest is simply that of the electric field and field gradient at that site (these are the lower angular momentum terms we omitted in equation 1.2). The resulting induced dipoles are given by the multipole expansion.

$$\mu^{i,as}_{\alpha} = \alpha_{\alpha\beta} E_{\beta}(\mathbf{r}_i) + \frac{1}{3} B_{\alpha\beta,\gamma\delta} E_{\beta}(\mathbf{r}_i) E_{\gamma\delta}(\mathbf{r}_i) + \ldots \tag{1.6}$$

The superscript *as* means the sources of the field are *asymptotically* far away from ion i. $\boldsymbol{\alpha}$ is the dipole polarizability and $\mathbf{B}$ is the dipole-dipole-quadrupole hyperpolarizability. For a spherical ion the components of $\boldsymbol{\alpha}$ and $\mathbf{B}$ are specified by a single number [30]. If a near-neighbouring ion is displaced, there is an additional effect. Figure 1.3 shows what happens to the confining potential around an anion, when one of the first shell of cations is displaced outwards. Besides the field and field gradient (related to the gradient and curvature of the

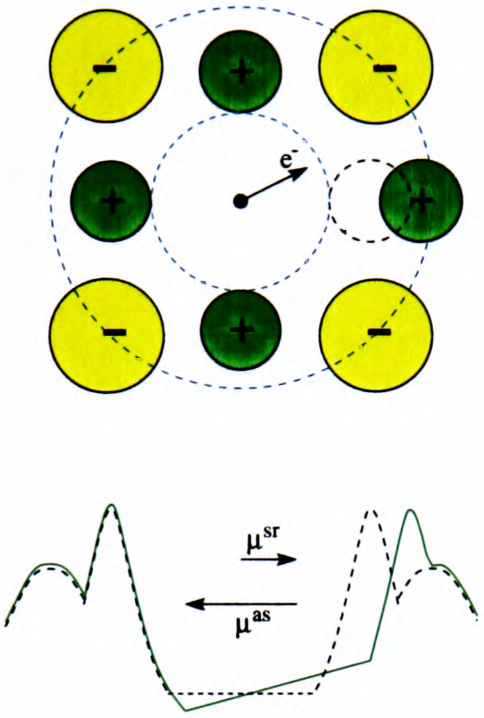

Figure 1.3: *Top panel: Origin of the 'asymptotic' and 'short-range' contributions to the dipole induced in an anion in a crystal which has been distorted. Bottom panel: A cross section for the undistorted crystal (dashed line) and after the distortion (green line)*

potential at the origin) a dent appears in the confining potential. Whilst the field and field gradient tend to push the electrons in one direction (away from the displaced cation), this 'dent-in-the-wall' allows them more freedom to move into the space vacated by the cation. Hence, there are two contributions to the resulting dipole – the coulombic dipole *ie.* the asymptotic dipole in equation 1.6 and a short range contribution which opposes the 'asymptotic' dipole. The electronic structure calculations [31] show that the short-range contributions are quite substantial. In alkali chlorides, the dipole induced when a first shell cation is displaced of its site is only ~40% of the value of the pure asymptotic dipole. It is clear that such effects must be included in any realistic model for polarization effects in the condensed phase.

The result is different for polarizable cations. If an anion is now displaced off its lattice site, the coulombic dipole now points towards the displaced anion. However, the short-range dipole will still point in the same direction as in the

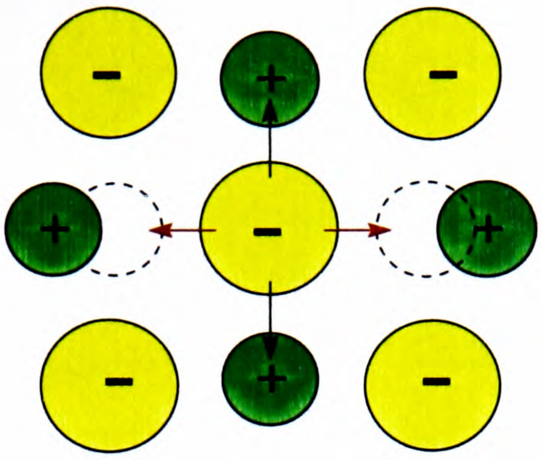

Figure 1.4: *Quadrupolar distortion about an anion*

above case *ie.* towards the displaced ion. Thus in the case of polarizable cations the short-range dipole *enhances* the asymptotic dipole. The role of cation polarization is thus much greater than is suggested by simply considering the relative magnitudes of anion and cation polarization.

An analogous observation is made for quadrupolar deformation around an ion (figure 1.4). The electric field gradient due to moving an opposing pair of cations forms a coulombic quadrupole with the electron density distorting towards the undistorted ions (black arrows). The electron density now also has the freedom to deform towards the displaced ions (red arrows).

1.3 The Rigid Ion Model (RIM)

In the simplest ionic model, the Rigid Ion Model, these many-body effects arising from the changes induced in an ion's properties by its environment are ignored. The ions are treated as spherical units whose interactions with other ions depends only on the separation between pairs of particles. In the most common form, the interactions are represented by a pair potential of the Born-Mayer [32] type (equation 1.7), which consists of a coulombic interaction between two ions, a short range (overlap) repulsion term, with the exponential form suggested above (equation 1.3), and attractive dispersion terms

$$u_{ij}(r_{ij}) = \frac{Q_iQ_j}{r_{ij}} + B_{ij}e^{-a_{ij}r_{ij}} - \frac{C^6_{ij}}{r^6_{ij}} - \frac{C^8_{ij}}{r^8_{ij}}. \tag{1.7}$$

Ionic systems have been studied for many years with such potentials. It is found that they account quite successfully for the properties of many systems, particularly the alkali halides [33].

The short-range potential terms are usually parameterized by fitting to experimental data such as lattice parameters, elastic constants and bulk moduli. It is found that the parameters for different systems can be linked to properties of the individual ions. For example, Fumi and Tosi [34] produced a class of potentials based upon the relationship $B_{ij} = Ae^{a_{ij}(\sigma_i+\sigma_j)}$ where A is a constant for a given class of materials, σ_i the ionic radius and $a_{ij} = 1/\rho$ (see equation 1.3) describes how the ion's electron density falls off with increasing r. This relationship can be recast in the Busing form [35] which expresses both the amplitude and range of the short-range potentials in terms of properties of the individual ions

$$B_{ij} = A_{ij}(\rho_i + \rho_j)e^{a_{ij}(\sigma_i+\sigma_j)} \tag{1.8}$$

where

$$a_{ij} = \frac{1}{(\rho_i + \rho_j)}. \tag{1.9}$$

These "scaling" relationships therefore enable the relationship between the interactions (and hence observables) of different materials to be traced back to these properties of the individual ions.

Generally, the dispersion terms are in the form of a summation

$$U_{disp} = -\sum_{n=6,8...} \frac{C^n_{ij}}{r^n}(1 + f^n_{ij}), \tag{1.10}$$

where $n = 6$ and $n = 8$ are the dipole-dipole and dipole-quadrupole terms respectively. Higher order terms are neglected. The f^n_{ij} term is a damping function which acts to reduce the dispersive interactions from the asymptotic limit at close separations where the electron densities of two atoms strongly overlap. The C^6 and C^8 values can be approximately related to the ionic polarizabilities (and hence experimental refractive indices) via the well understood formulae of Slater-Kirkwood [36]

$$C_{xy}^6 = \frac{\frac{3}{2}\alpha_x\alpha_y}{\left(\frac{\alpha_x}{p_x}\right)^{1/2} + \left(\frac{\alpha_y}{p_y}\right)^{1/2}}, \tag{1.11}$$

and Starkschall-Gordon [37],

$$C_{xy}^8 = \frac{\frac{3}{2}C_{xy}^6 < r_y^4 >}{< r_y^2 >}. \tag{1.12}$$

The first formula relates the dipole-dipole term to the polarizability α, and effective electron number p. For a particular ion the effective electron number is that value which gives the exact C^6 coefficient of the noble gas with which it is isoelectronic. The second formula relates the dipole-quadrupole term to the dipole-dipole and two expectation values for the electron density.

The dispersion term is calculated by consideration of two non-overlapping electron densities. However as the nucleii get closer together the electrons begin to overlap, this damps the interaction, reducing the dispersion energy as the overlap between ions increases. In many of the simulations which follow, this damping is omitted as it has little effect on the structure. However these effects have been shown to be important for crystal energy calculations. The $(1 + f^n)$ function in the dispersion energy term is a damping function in the form of Tang and Toennies [38] (equation 1.13),

$$f(r_{ij}) = -e^{-br_{ij}} \sum_{k=0}^{4} \frac{(br_{ij})^k}{k!}. \tag{1.13}$$

This function tends to zero for large ion separations when the dispersion energy tends to it's asymptotic value. The rate at which the function decays to this value is determined solely by the parameter b in equation 1.13

1.3.1 The necessity of including many-body effects

The RIM works well for ions in symmetrical environments such as alkali halides in which the idea of undistorted spherical ions seems to hold. In less symmetric environments, which become normal even in the crystal structures of more complex stoichiometries like M_2X_3 and MX_2 problems arise. For example the RIM does not predict the layered crystal structures encountered in divalent metal halides (eg. $MgCl_2$) [19]. Polarization effects provide a ready explanation for the prevalence of these structures. Indeed, the RIM even fails for alkali halide crystals when the ions move away from the highly symmetrical environment. For example, the model often predicts phonon modes to be far too stiff. A second failure of the RIM is due to the short range repulsion between ions being treated as being a simple two-body interaction. As has already been shown, the ion's size and hence the short-range interactions with neighbouring ions depends on the environment an ion finds itself in. This means that RIM potentials fail to account for phase transformations between crystal structures in which the co-ordination number differs. Since the focus of the present work is the structures of melts, where there is no symmetry or definite coordination structure at the typical, instantaneous ionic site it might be expected that these shortcomings of the RIM will always be serious. A third failure is seen in the parameterization of the potentials. As shall be examined in chapters 4 and 5 CsCl is one of the very few alkali halides to adopt the 8 coordinate B2 structure rather than the 6 coordinate B1. The RIM is unable to account for this observation unless a pair potential is constructed which has unphysically large dispersion terms. In effect, as will be shown, these large dispersion terms are compensating for the failure to allow for the ion compressibility. Whilst the RIM potential may replicate many experimental observations for the state at which the potential was parameterized (*ie.* the CsCl structure) on moving away from this state or to other alkali halides, the unrealistically large dispersion introduced will adversely affect the modelling of these systems. That is, the potential will not be transferable, and the desirable feature of the ionic model - that potentials may be scaled between different systems - will be lost.

Techniques to carry out simulations including the many-body compressibility and polarization effects have now been developed. In the simple Polarizable Ion Model (PIM) moments induced on the ions are modelled in such a way as to allow for their inclusion in a tractable computation scheme. The short-range terms are handled via the simple pair potentials such as those given by equations 1.7 and 1.8. In the Compressible Ion Model (CIM) the ion's radius is allowed to dynamically change in size ("breathe") which introduces a further many body character. These methods will be reviewed in chapters 3 and 5 respectively.

1.4 PIM Simulation of trivalent metal chlorides

Ionic materials of stoichiometry MX_3 pose an interesting challenge for the development of interaction models [39–43]. A very wide range of such materials are available for study, since the lanthanide elements as well as a number of transition metal (Y, Sc, Fe) and main group elements (Al etc.) form trivalent cations which systematically span a wide range of relative ionic radii. As the cation radius is reduced (from La to Al), the "ionic" character of the melt decreases. $LaCl_3$ melts at a high temperature with a volume change ($\sim$19%) typical of ionic compounds, whereas $AlCl_3$ melts at low temperature from an ionic crystal with an enormous ($\sim$88%) volume increase to form an insulating liquid, believed to be composed of Al_2Cl_6 dimers. Intermediate-sized cation systems, like YCl_3, are isomorphous to $AlCl_3$ in the crystal but melt to form network-liquids, with a tiny volume increase on melting (<1%) in the case of YCl_3. (see table 1.1 for a complete set of experimental data)

The basic aim of the work presented in this thesis is to assess how well a generalized ionic interaction model, including, if appropriate, the many-body ef-

Compound	$LaCl_3$	$CeCl_3$	$TbCl_3$	$DyCl_3$	YCl_3	$ScCl_3$	$FeCl_3$	$AlCl_3$
Crystal Structure	UCl_3	UCl_3	$PuBr_3$	YCl_3 †	YCl_3	BiI_3	BiI_3	YCl_3
Lattice Energy ($kJ.mol^{-1}$)	4343	4297	—	4481	4447	4874	5364	5376
T_m (K)	1131	1080	855	924	994	1240	577	466
ΔS_m ($JK^{-1}mol^{-1}$)	48.1	49.3	40.5	27.6	31.8	52.3	75.90	74.5
$(V_m - V_s)/V_s(\%)$	19.1	21.9	—	0.3	0.5	47	39	88
σ ($S.cm^{-1}$)	1.31	1.10	—	0.44	0.39	0.56	0.04	5.0×10^{-7}

Table 1.1: *Experimental data for trivalent metal chlorides.* † *High-temperature crystal structure; low temperature structure is* $PuBr_3$.

fects discussed above is able to account for this increasingly "covalent" behaviour with decreasing cation size. Polarization effects are likely to be particularly important in these systems because of the strength of the polarizing field of the trivalent cations and the high polarizability of halide anions. In addition the stoichiometry dictates that there must be low coordination about anions, which will result in the formation of electric fields and induced dipoles. As the cation radius reduces, the size of the polarization effects will increase, and this could be sufficient to explain the progressive departure from "ionic" behaviour. It is less clear *a priori* whether the ion compressibility effects, which influence the size and shape of the ion, as perceived through the short-range repulsion, must also be invoked. The starting point of the study will therefore be to examine the predictions of an interaction model which incorporates the polarization terms, but in which the compressibility effects are not explicitly included and the repulsive interactions described by a pair potential. In the spirit of the ionic model, it will be assumed that parameters in the short-range potential can be calculated from properties of the individual ions, such as radii and polarizabilities. The aim is to use the Polarizable ion model to enable us to rationalize the evolution of the observed structural data with ion size and to clarify the role of changing coordination number and network connectivity.

A major reason for wishing to pursue systems of this type is that their structures are experimentally accessible using both neutron scattering and X-ray diffraction techniques. The presence of the chloride ion, which has two stable isotopes with significantly different scattering lengths, allows for the extraction of partial structure factor information by isotopic substitution. Such information is significantly more useful as these functions arise directly from simulation models. Until recently, the only neutron diffraction data was on YCl_3 [7] together with some X-ray total structure factors for a few lanthanide halides [16] and for $AlCl_3$ [17]. Recently, this situation has improved markedly: Badyal and co-workers [8,9] have produced neutron diffraction data for $AlCl_3$ and $FeCl_3$, as well as X-ray diffraction results for $FeCl_3$, and Adya *et al* [10] have obtained *partial* structure factors for $DyCl_3$ by the method of isotope substitution in neutron diffraction. Very recently Salmon and Wasse [11–15] have measured the total structure factors for 16 MX_3 systems in the melt.

The work described in the remainder of this Introduction (and in the survey of crystal structures in the next chapter) should be regarded as a preliminary survey of how well a Polarizable Ion Model, constructed with literature values for the ionic properties, accounts for the structural changes in the melt which these studies have highlighted. It will set the scene for more detailed considerations in the remainder of the thesis. The details of the comparisons between simulated quantities and experimental information will be described in full in later chapters. For the present, the fact that structure factors *etc.* can be taken from simulation and experiment is taken for granted. In particular, we will compare with experimental [11–15] liquid state data for (La/Ce)Cl_3 ($\sigma_+ \sim 1.4$ Å), YCl_3 ($\sigma_+ \sim 1.2$ Å) and $ScCl_3$ ($\sigma_+ \sim 1.1$ Å).

1.4.1 MCl_3 Interaction Potentials.

The potentials used in the initial study consist of Born-Mayer-like pair potentials (equation 1.7) supplemented by an account of polarization effects *via* the polarizable ion model [2,44] (section 3.2). Throughout, formal charges (Q_i) of +3 for cations and -1 for anions are used.

The Cl^- radius (and other properties) are presumed to be the same in all the melts, so that the Born-Mayer potential between Cl^- ions is the same in all systems. In practice, the Coulombic repulsion between cations is so strong, that the short-range repulsion between cations is always negligible, as is the cation-cation dispersion, on account of the relatively small polarizability.

The pair potentials were based upon potentials devised by Tatlipinar *et al* [18] to fit Raman frequencies for a range of MCl_6^{3-} ions. In fitting the frequencies of a range of systems, only the cation properties were allowed to vary, the properties of the Cl^- ion were held fixed. The fitted potentials included an account of cation-anion polarization effects, but only the pair parts of the potentials were used in subsequent integral equation [39] and simulation [40] studies of melt properties. The dispersion terms were re-parameterized in order to tie them to the values of the ionic polarizabilities *via* the Slater-Kirkwood formula (equation 1.11) [2,26]. The dispersion terms (C^6 and C^8) are found to make little difference to calculated structures but do affect energetics.

For most of the systems studied, we simply supplemented the pair potentials with an account of *anion* dipole polarization. The anion polarization [44] is controlled by two parameters – the Cl^- polarizability, α, and the 'induction-damping' parameter b [1,44] (section 3.2.2) which is analogous to the dispersion damping in equation 1.13. The polarizability of Cl^- was maintained at 20 au, the value appropriate to crystalline NaCl [28], possibly an underestimate for the systems of interest here. In the full potential therefore, all terms are controlled simply by the cation radius, which exerts its direct effect through the cation-anion short-range repulsion and, since this determines the distance of closest approach of cations and anions, indirectly affects the magnitude of the polarization terms.

The sense in which the potential is a 'generic' and 'ionic' one should be clear. We aim to show how this simple, physically motivated potential is able to account, qualitatively, for the structure across a wide range of chemically distinct systems, with minimal parameter changes.

1.4.2 Polarization and the 'Ionic' to 'Molecular' Transition

For the larger cations adopting this MX_3 stoichiometry, such as La^{3+} and Ce^{3+}, up to 9 anions may be packed around each cation to form a short-range coordination polyhedron. This can be simply understood in terms of the anion-cation coulombic attraction (anions surround cations) and the relative size of the cation and anion (essentially radius-ratio rules). The high ratio of anions to cations means that each anion may be shared by more than one cation - the anions form M-Cl-M bridges between pairs of cations. If each polyhedra shares only one anion with a neighbour it is termed vertex-sharing (figure 1.5). Furthermore, the relatively high cation charge would lead us to believe that cation-cation repulsive coulombic forces may be significant. If such forces were truly dominant this would lead to linear M-Cl-M triplets. However, we may anticipate that polarization effects will affect the geometries of these bridges. Smaller cations, such as Y^{3+} and Dy^{3+}, form local octahedral coordination polyhedra as their smaller size allows less anions to pack around each cation than for La^{3+} and Ce^{3+}. The increased polarizing power of these smaller cations results in dipoles being induced on the bridging anions which have their negative end pointing between pairs of cations *ie.* there is a greater shielding by the anion electron density. This leads to the bending of the bonds to form a network of octahedra (figure

1.5). Considering figure 1.5 it is clear that, if the polarization effects are large enough, the bonds may bend to such an extent as to stabilize edge-sharing pairs of octahedra, that is, an octahedron shares two anions with a neighbouring unit. It will be seen in section 7.3.4 that for one case this argument can be further extended to face-sharing octahedra.

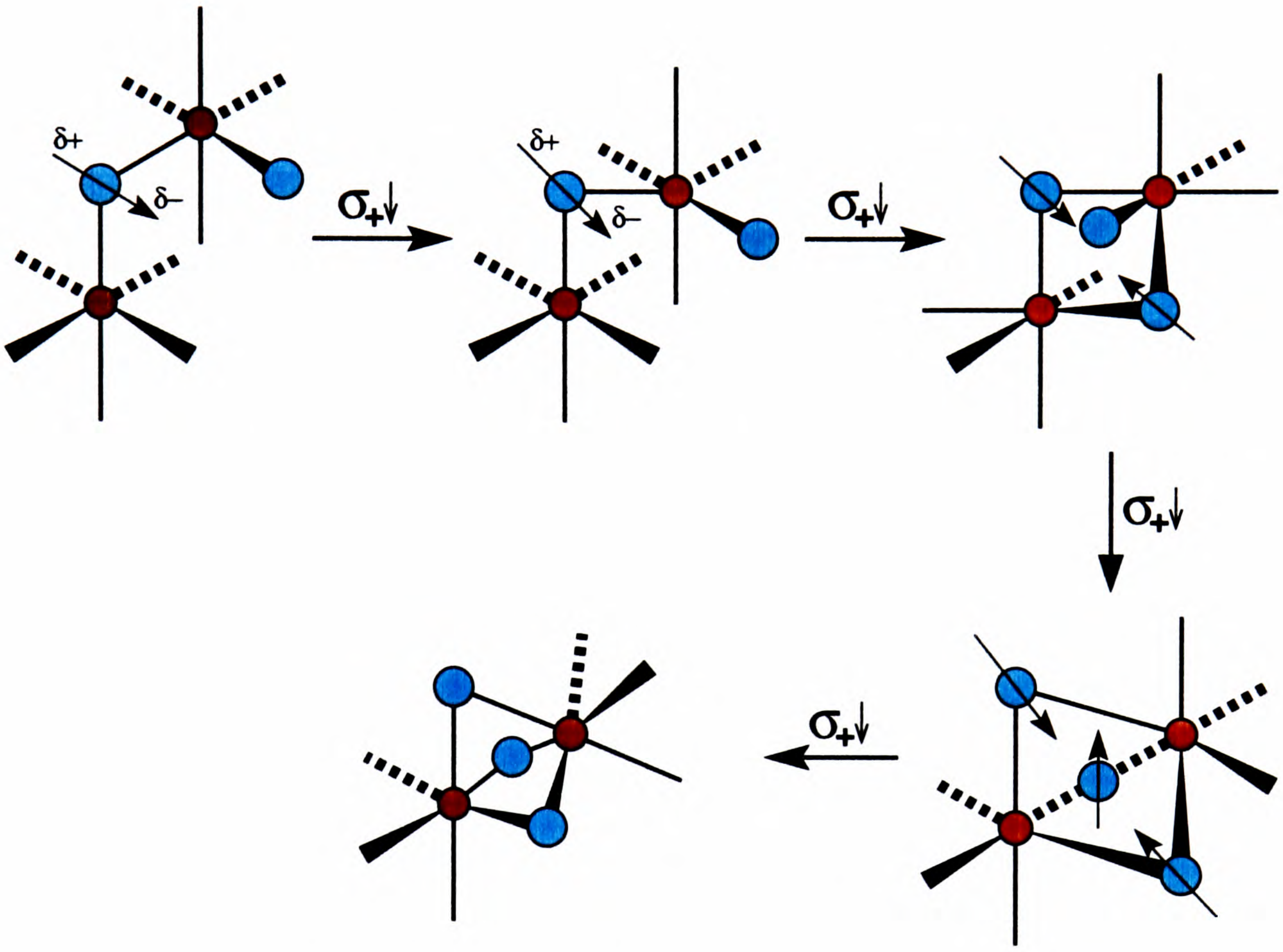

Figure 1.5: *Bending of M-Cl-M bonds due to increasing polarization. The decrease in cation radius shown results in an increased polarizing power of the cation and hence more shielding of the cation-cation coulombic repulsive forces by the anion's electron density.*

The smallest cations considered here, Al^{3+} and Fe^{3+}, form local tetrahedra which are believed to share edges and so form molecular Al_2Cl_6 units and Fe_2Cl_6 units (figure 1.6).

The presence of these molecular species in the melt is qualitatively consistent with the relatively low density of the melts and their low conductivity (table 1.1). $AlCl_3$ and $FeCl_3$ apparently change from ionic to molecular mate-

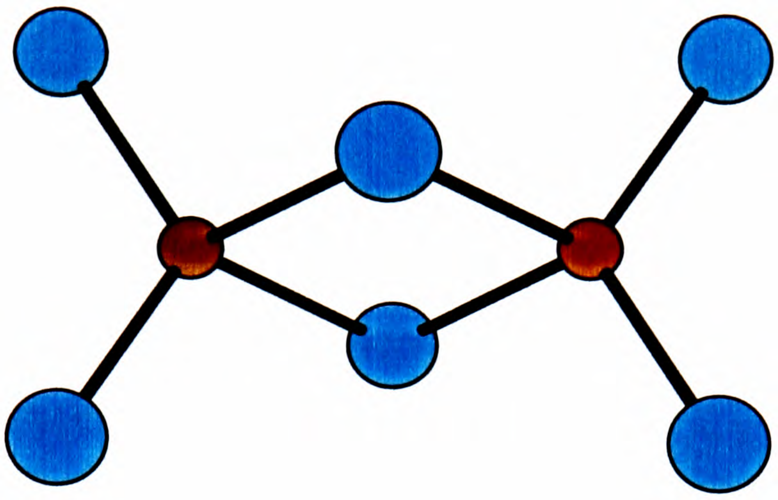

Figure 1.6: Al_2Cl_6 *dimer*

rials on melting. It is interesting to anticipate how the extended ionic model might allow for the type of structural change which apparently occurs when $AlCl_3$ and $FeCl_3$ melt. Two key ingredients are, firstly, the idea that, from simple radius ratio considerations, these compounds might be on the border of 4– and 6–fold coordination and that melting might tip the balance in favour of the lower coordination number. Secondly, the polarization of the Cl^- units by the small highly charged Al^{3+}/Fe^{3+} cations can be expected to be very strong. As previously shown, [1](figure 1.5), the polarization effects influence the linkage between local polyhedra and, in particular, can stabilise edge–sharing arrangements. Edge–sharing tetrahedra in $AlCl_3$ form neutral units with a similar geometry to that established for the Al_2Cl_6 molecule in the gas phase [45]. Such neutral units would simply be held together by van der Waals forces in the liquid phase. This is different to the situation for larger cations, such as in YCl_3, where the reduction of coordination number is prevented by ion size effects and edge–sharing octahedra form on melting [46,47]. Such a configuration cannot be subdivided into local, uncharged entities: hence, there must always be a long-range coulombic (Madelung) contribution to the energetics. The local structure must therefore extend to form a network. Recently, the occurrence of similar phenomena has been demonstrated in a comparison of $ZnCl_2$ [48,49] and $BeCl_2$

melts [50].

1.4.3 Comparison of Simulated and Experimental Data

In order to make comparison with experiment we need to transform the output of the computer simulation into a form which is readily measured by experiment. The structure of the simulated system is characterized by a pair distribution function, $g(r)$ which gives the probability of finding a pair of atoms a distance r apart, relative to the probability for a completely random distribution at the same density. Clearly for systems of stoichiometry MX_3 we will obtain three partial pair distribution functions, $g_{ClCl}(r)$,$g_{MCl}(r)$ and $g_{MM}(r)$. These partial pdfs are then Fourier transformed as in equation 1.14 to obtain partial structure factors.

$$S_{\alpha\beta}(k) = \delta_{\alpha\beta} + 4\pi n_0 \sqrt{c_\alpha c_\beta} \int_0^\infty dr(g_{\alpha\beta}(r) - 1)r\frac{\sin(kr)}{k}, \qquad (1.14)$$

where n_0 is the number density of the ions in the melt and c_α and c_β are the relative concentrations of species α and β respectively. The quantity directly measured by experiment is an appropriately weighted combination of the three partial structure factors (section 6.4.1).

In addition, the coordination number of ion β around α ($\bar{n}_\alpha^\beta$) can be determined from the pdfs by integrating over the pdfs up to the first minimum as in equation 1.15 .

$$\bar{n}_\alpha^\beta = 4\pi n_0 c_\beta \int r^2 g(r) dr \qquad (1.15)$$

1.4.4 $LaCl_3$

We first discuss the data for the largest cation considered (La^{3+}) and compare the experimental and simulated total neutron structure factors in figure 1.7.

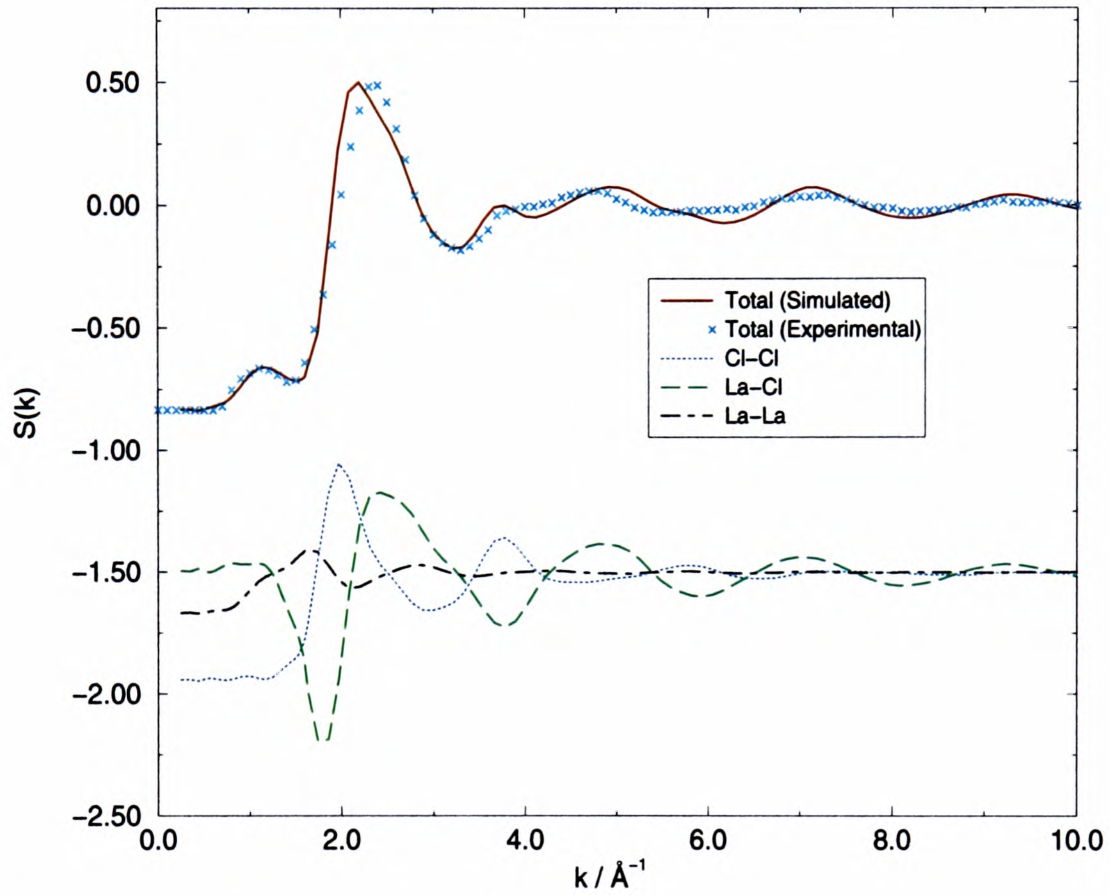

Figure 1.7: *Simulated total neutron weighted structure factor for $LaCl_3$ compared with the experimental total structure factor and, below, the neutron-weighted partials shifted by a constant of -1.5*

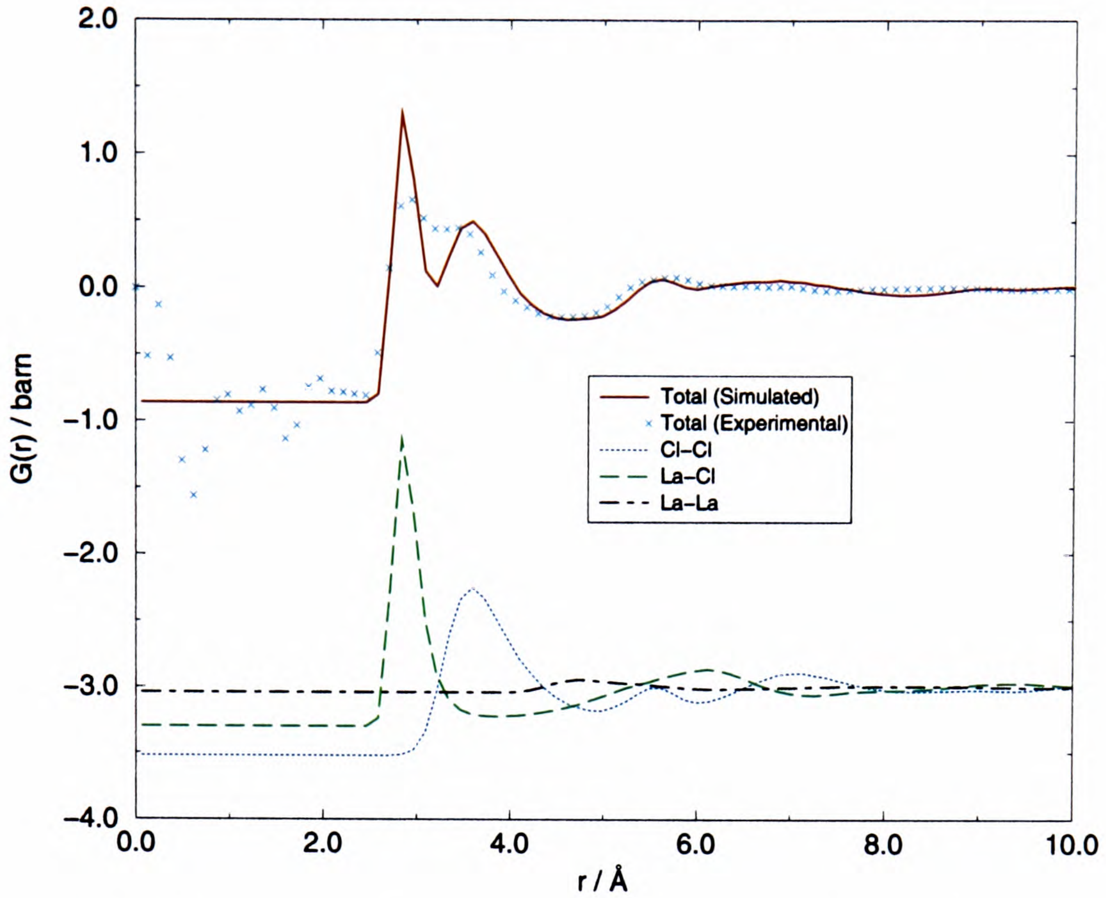

Figure 1.8: *Comparison of simulated and experimental neutron weighted total pdfs for $LaCl_3$. Also shown are the simulated partial pdfs shifted by a constant of -3*

The agreement of the two seems generally very good. In particular, the amplitude and position of the first-sharp-diffraction peak, or pre-peak, (at $\sim 1.2\text{Å}^{-1}$) is excellent – indicating that the simulation is reproducing the intermediate-range order of the liquid (section 6.5.2). The amplitude of the predicted principal peak agrees very well with experiment, but it is shifted slightly to low k. As can be seen by comparison of the total structure factor with the neutron-weighted partials shown in the lower part of figure 1.7, the shape of this peak is affected by a strong cancellation between $S_{MCl}(k)$ and $S_{ClCl}(k)$. The shift in this peak can therefore reflect a still smaller error in the absolute positions of the peaks in these partials.

In figure 1.8 we show the comparison of the total neutron weighted pair distribution function (pdf) obtained from the experimental total neutron weighted structure factor by Fourier transformation, $G_{tot}(r)$, with the total neutron-weighted pdf calculated in the simulation.

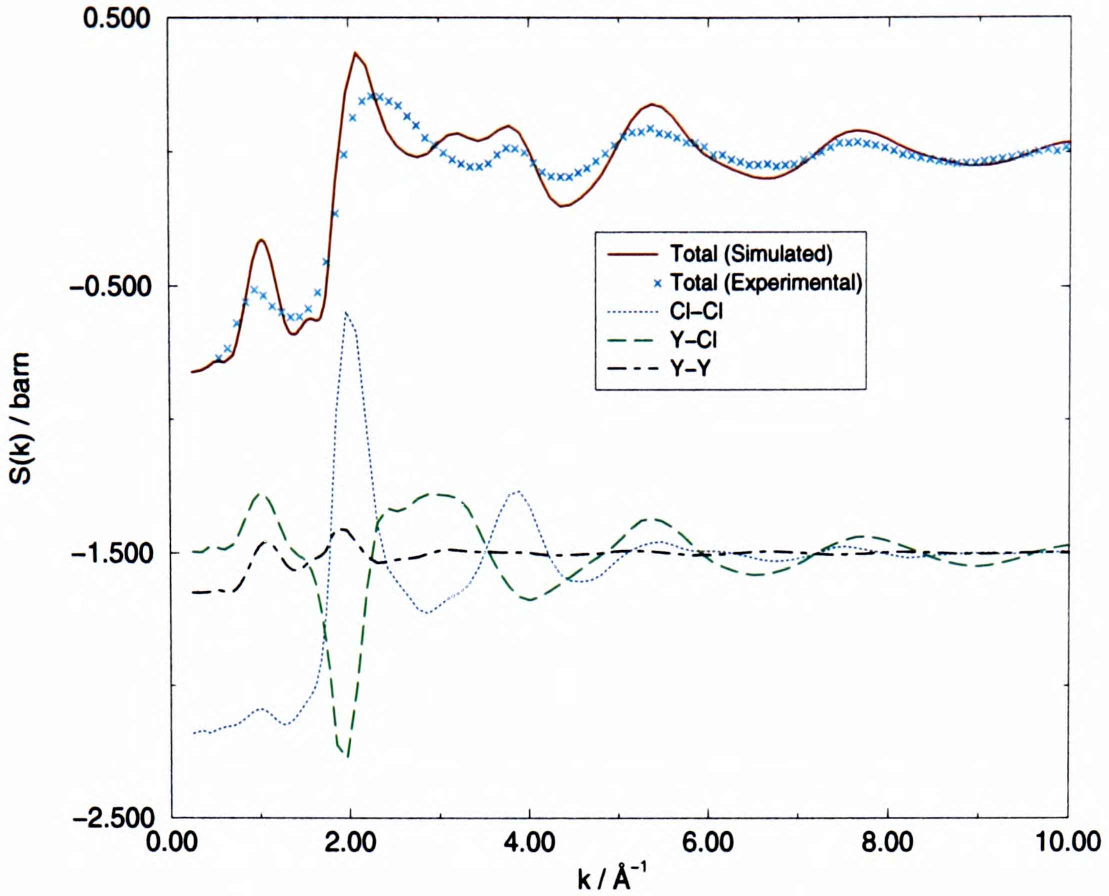

Figure 1.9: *Comparison of simulated and experimental total neutron weighted structure factors for YCl_3. The neutron weighted partials are shown shifted by a constant of -1.5*

Good agreement is seen in the positions and areas of the peaks in the two functions out to at least 7 Å. However, the peaks in the simulated pdf are significantly narrower than observed experimentally: the extent to which this is due to deficiencies in the simulation potentials versus the loss of real-space resolution on Fourier transforming the structure factor from a finite range of k will be discussed in section 6.6.3. Similarly good agreement is seen across the range of M^{3+} ion radii to YCl_3 (1.20Å). However, the generic potential begins to fail for the intermediate sized cations YCl_3 and $ScCl_3$.

1.4.5 YCl_3 and $ScCl_3$

Considering the good agreement between the simulation predictions and experiment obtained for the larger cations (La^{3+} and Ce^{3+}) the comparison between simulation and experimental structure factors for the intermediate sized cations, YCl_3 and $ScCl_3$ is generally disappointing (figures 1.9 and 1.11). Again we note

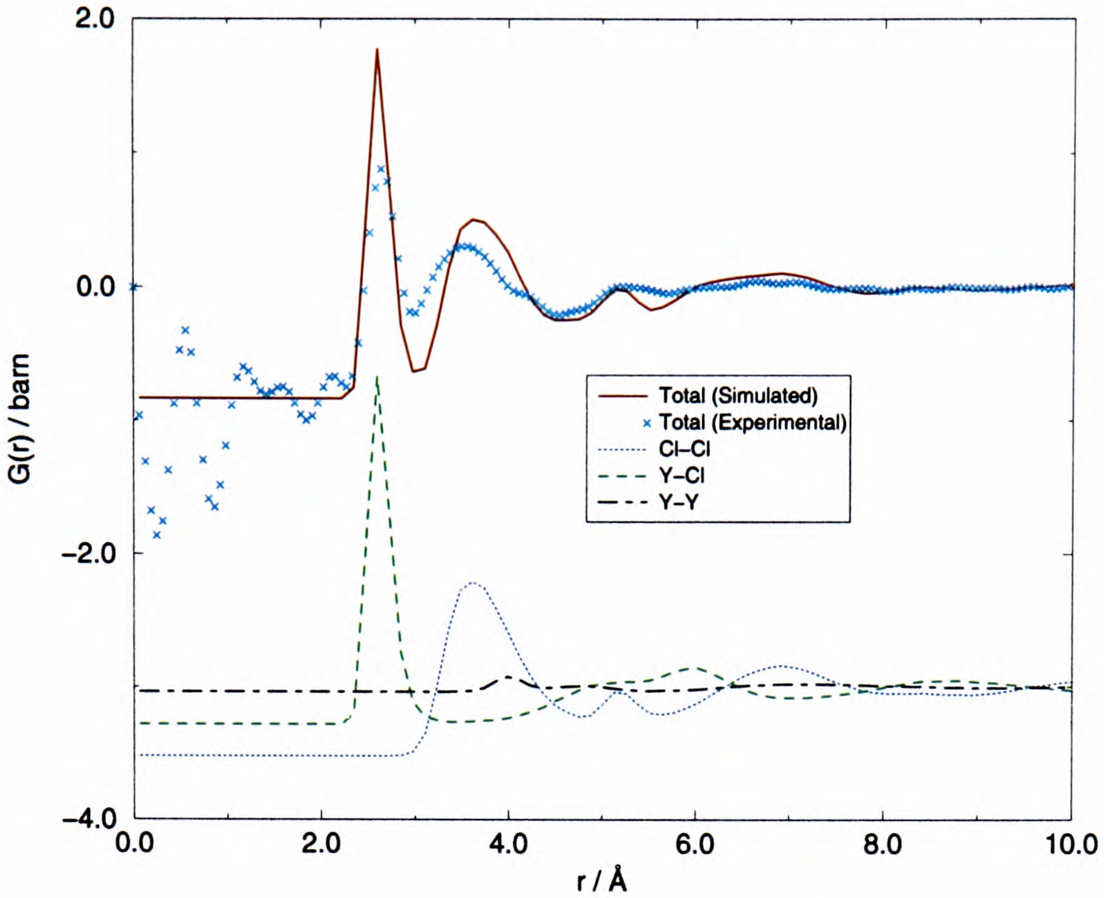

Figure 1.10: *Comparison of the experimental and simulated total neutron-weighted pdfs for YCl_3 with the partial neutron-weighted pdfs shifted by a constant of -3.*

that the region where the discrepancies are most pronounced – between 2.5 and 4.5 Å^{-1} – is one where the partial structure factors exhibit strong cancellation. It would seem that there is no reason to believe that the simulation predictions of the structure have broken down fundamentally. In Sc^{3+} however, we are now seeing a major discrepancy between the position of the pre-peak.

In real-space (figures 1.10 and 1.12) the comparison of the experimental and simulation data shows that the agreement of the position of the second peak in the total pdf – essentially the first peak of $g_{ClCl}(r)$ – is becoming significantly worse than in the larger cation cases. When translated back to reciprocal space, such a discrepancy could well be the cause of a large change in the degree of cancellation of $S_{MCl}(k)$ and $S_{ClCl}(k)$, and responsible for the problems noted above.

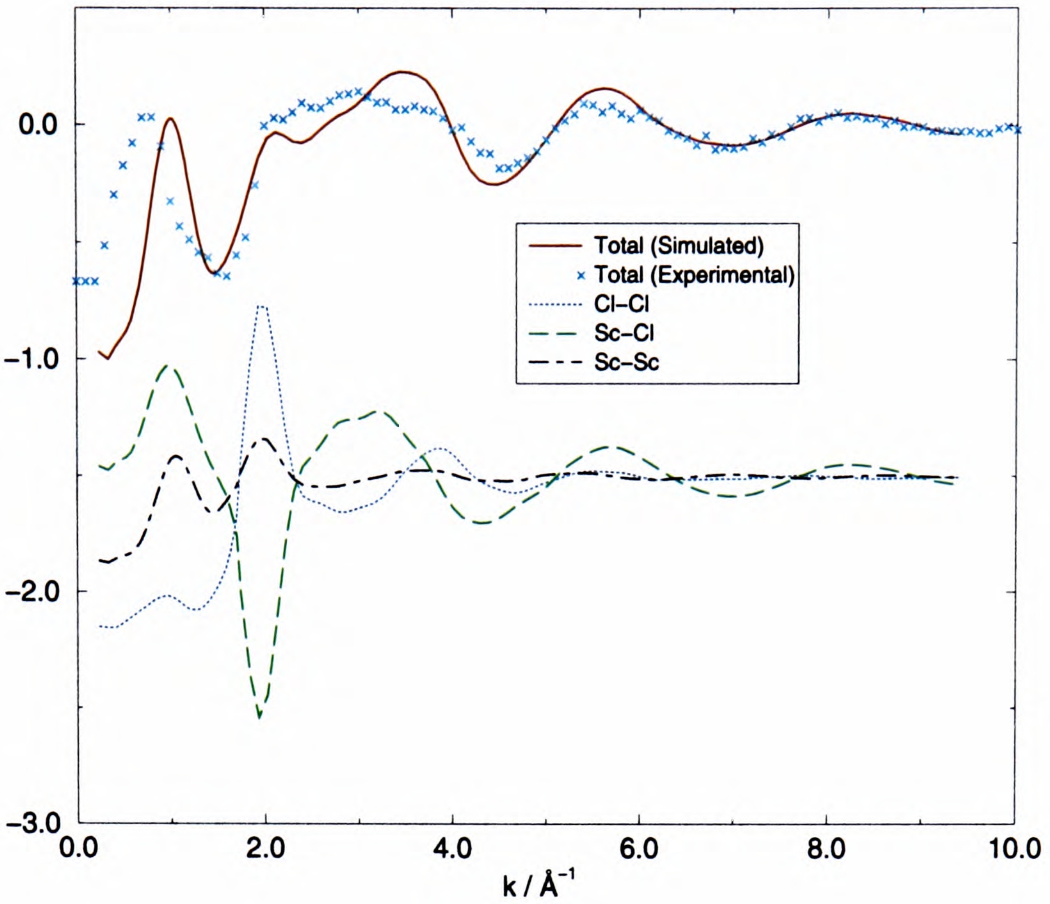

Figure 1.11: *Comparison of simulated and experimental $ScCl_3$ neutron weighted structure factors, with the partial structure factors shown shifted by a constant of -~~3.0~~ 1.5.*

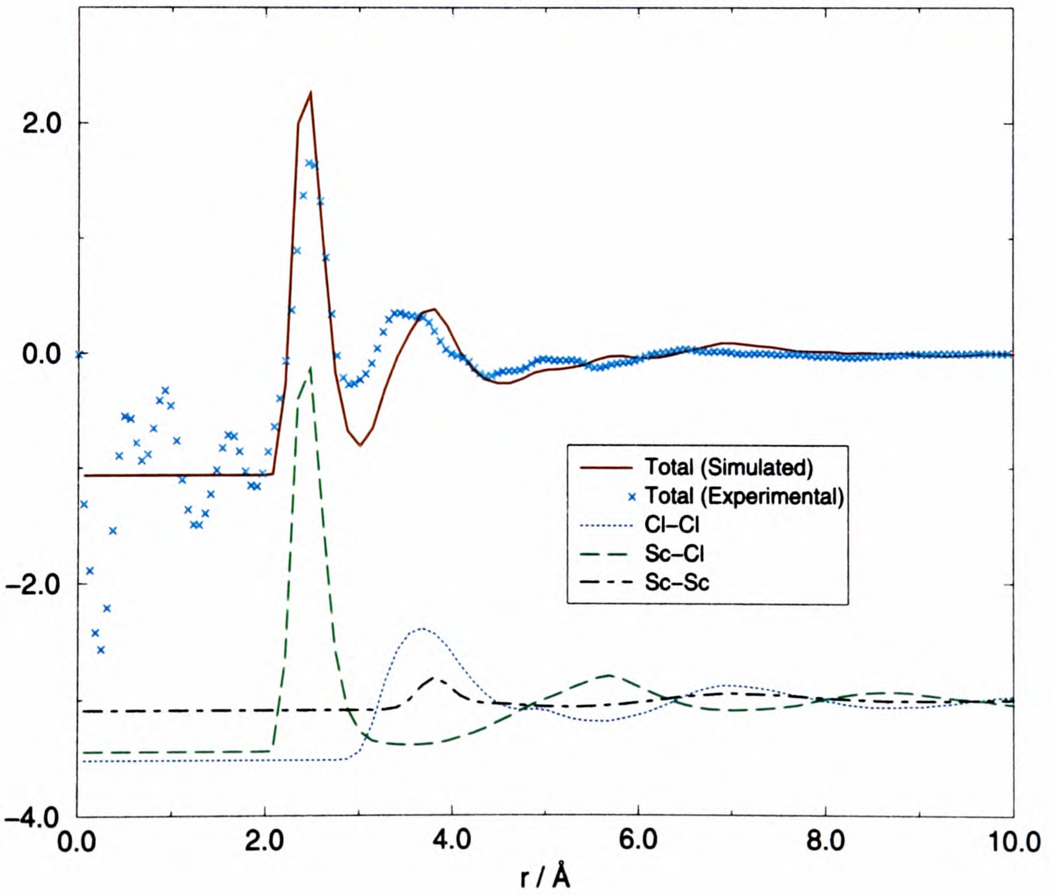

Figure 1.12: *Comparison of simulated and experimental neutron weighted total pdfs for $ScCl_3$ with the partials shown shifted by a constant of -3.0*

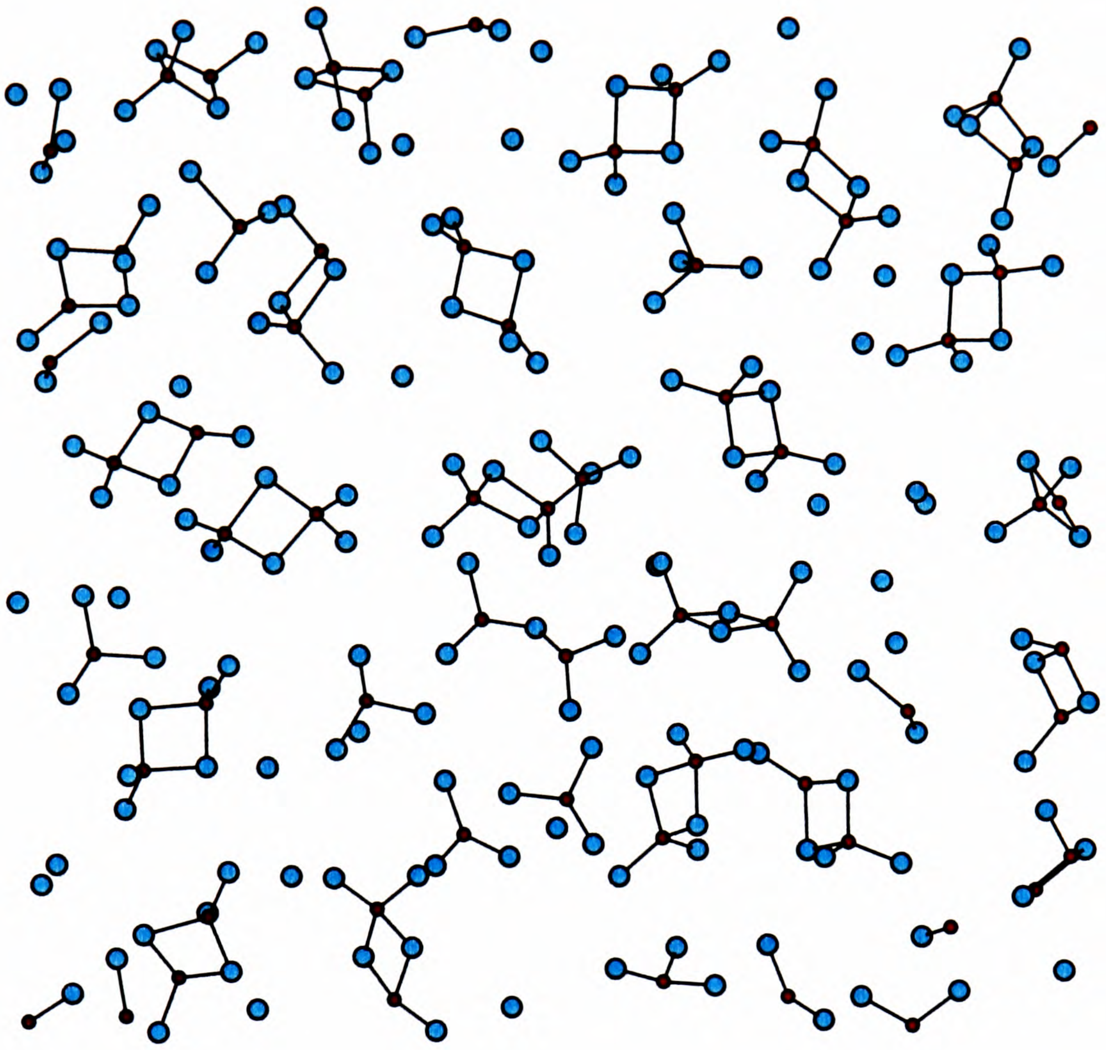

Figure 1.13: *Snapshot of ion positions in $AlCl_3$ simulated with the Tatlipinar potential. The Al_2Cl_6 dimers can clearly be seen.*

1.4.6 $AlCl_3$ and $FeCl_3$

The simulated total neutron structure factors and X-ray diffraction spectra for both $AlCl_3$ and $FeCl_3$ are in very good agreement with experiment [51]. A slice through the simulation cell for $AlCl_3$ (figure 1.13) shows that the model is accounting for the formation of M_2Cl_6 dimers in the melt. This suggests that our preliminary Tatlipinar potential is working adequately for these systems and so we will not consider them further in this chapter.

1.5 Conclusions

While the agreement with experiment is good across the range of M^{3+} ion size, it is far from perfect becoming much worse for the intermediate sized Y^{3+} and Sc^{3+} ions and consideration of the nature of these discrepancies suggests that we may need to review the representation of the short-range ion-ion interactions to improve this situation. Presently, these are described by simple Born-Mayer repulsions. This representation has worked well for the MX and MX_2 materials that have been considered previously but in MX_3 materials, where the stoichiometry dictates that there must be many anion-anion "contacts", its limitations appear to be exposed. The predicted total structure factors for MX_3 materials, where cancellations between different partials are paramount, are not as good – especially in the case of YCl_3 and $ScCl_3$. This indicates that there are small shifts in the relative positions of the peaks in the different partials, which are not being replicated in the simulations. The comparison between the positions of the first peaks in $g_{ClCl}(r)$ in figures 1.8, 1.10 and 1.12 is telling. In the simulations, this peak remains in the same position in all systems studied, whereas in the experimental total pdfs, the corresponding peak appears to shift to smaller r. Thus, it seems that the effective Cl^- ion size is decreasing in the smaller cation systems. Related effects may be the apparent over-structuring of the first coordination shell, as witnessed by the excessive sharpness of the predicted first peak in $g_{MCl}(r)$.

Chapter 2

Modelling the Crystal Phase: Trivalent metal halides

2.1 Introduction

The crystal structures adopted by the MCl_3 systems provide an interesting insight into the interplay between the effects of ion size and polarization and their influence on the local structure adopted in the lowest energy crystal. MX_3 systems exhibit the consequences of these effects rather dramatically, simply as a consequence of the stoichiometry. If we regard the ionic crystal structures as comprising a close-packed structure of anions, with cations occupying holes of a suitable size, we see the possibility of an increasingly widening range of structures as the ratio of the number of cations to anions decreases. If the cation size dictates octahedral hole occupancy, then in MX stoichiometry, there is only one possible crystal structure (for, say, cubic close-packing), whereas in MX_2 and MX_3 only a half and a third of the octahedral holes are occupied respectively and different spatial arrangements become possible. In general terms, the coulombic repulsion prefers to locate the highly charged cations as far apart as possible in systems; this usually leads to a very high site symmetry for the anion.

The polarization effects oppose this tendency; they favour an asymmetrical anion site, in which induced multipoles may form on the anion. The consequence of this is that cations are drawn together so as to occupy neighbouring holes in the anion lattice, which frequently leads to "covalent" layered crystal structures.

2.2 Trivalent Metal Halides

Seven structural motifs may be identified for systems of stoichiometry MX_3 [52,53].

Of these, the **ReO_3 structure**, which consists of a cubic lattice of vertex-sharing octahedral units (in which each cation is surrounded by six anions) is the most symmetric. It maximizes the separation of the highly charged cations ($r_{++} = 2r_{+-}$) and symmetrically interposes an anion between each cation pair; as such, it is the structure which minimizes the coulombic interactions and is predicted to be the most stable structure for the pair potential alone (for a given anion-cation separation), where all polarization effects are neglected. However, this structure is not adopted by any of the real chloride systems and we will not consider it further. For the larger lanthanide ions, the octahedral holes in a close-packed anion lattice are too small to accommodate the cations and so high coordination number structures are adopted, such as the UCl_3 (figure 2.1) and $PuBr_3$ (figure 2.2) structures.

The **UCl_3 structure** is adopted by the largest cations and has a coordination number of anions about cations of 9 with the local symmetry around a cation a tricapped trigonal prism. This is the only three dimensional (*i.e.* non-layered) lattice formed by the trivalent metal chlorides.

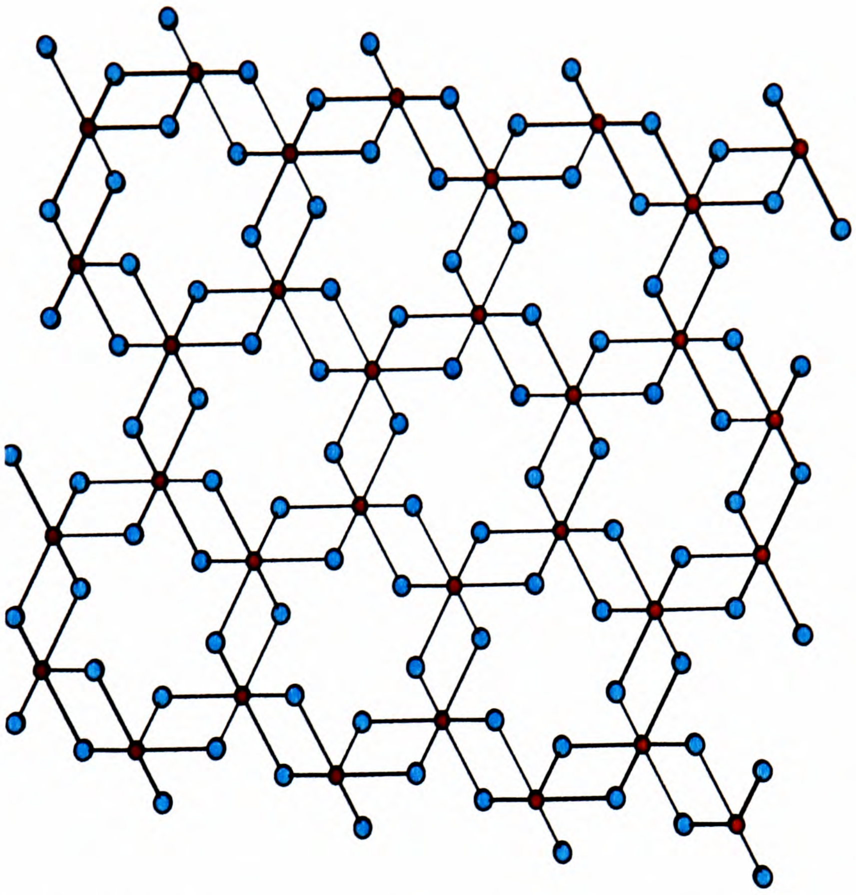

Figure 2.1: *UCl_3 Crystal Structure - View down the c axis of the unit cell i.e. down an axis perpendicular to the triangular faces of the trigonal prism. The anions are coloured cyan and the cations red. Each cation is surrounded by 9 equidistant anions, three of which are obscured.*

The **$PuBr_3$ structure** is adopted by cations of intermediate radii, as in $TbCl_3$ and the low temperature form of $DyCl_3$. The coordination in this structure is 8 + [1]. This is a layered structure with 8 neighbours in the same layer and the 9th neighbour lying in the adjacent layer at a slightly larger distance.

The UCl_3 and $PuBr_3$ crystal structures are very close in energy due to the similar local arrangements of the ions. The $PuBr_3$ structure formed by $TbCl_3$, for example can be described as consisting of triangular prisms with Tb^{3+} ions at the centres and the Cl^- ions at the vertices. These prisms share triangular faces to form parallel columns. The UCl_3 structure can be described in terms of similar triangular columns, but the two structures differ in the way the columns are packed together. In the UCl_3 type structure there are three neighbouring columns arranged so that each U^{3+} ion has three Cl^- neighbours adjacent to the

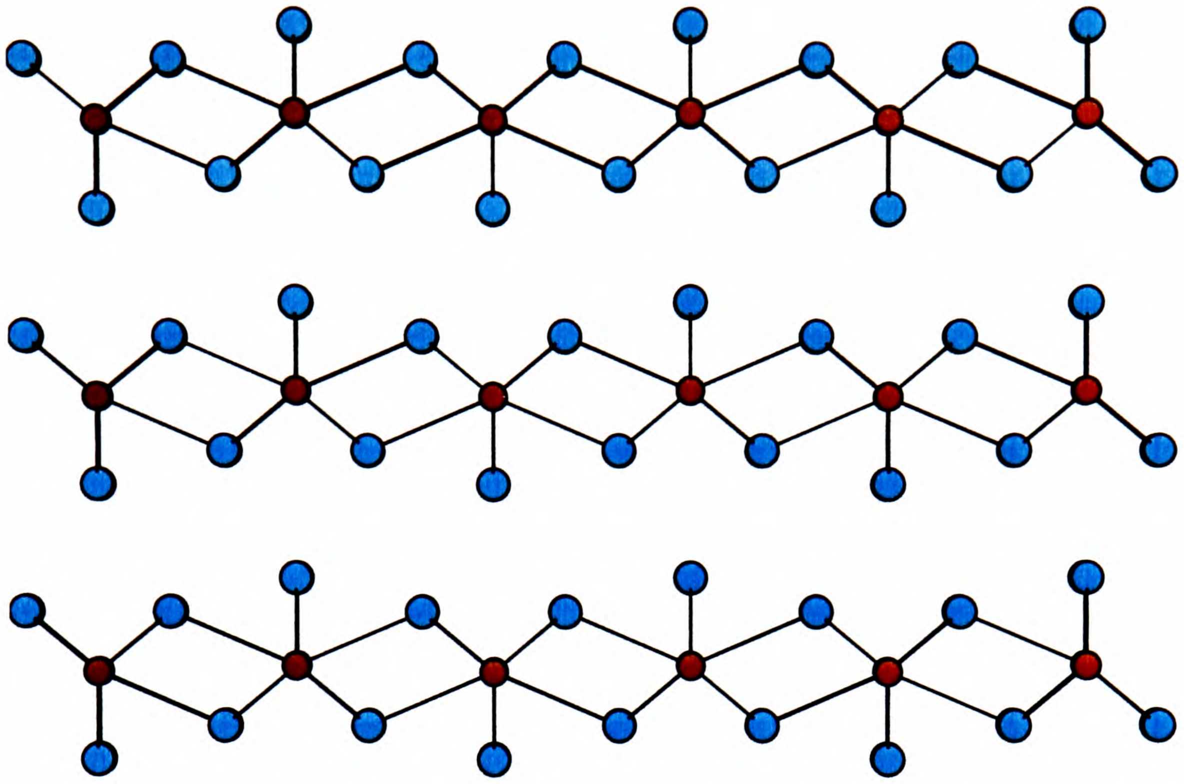

Figure 2.2: *$PuBr_3$ Crystal Structure – View down an axis perpendicular to a triangular face of the trigonal prism. The layered structure is clear and the local coordination of 8 anions (cyan) around a cation (red) can be seen. Again three of the anions around each cation are obscured.*

lateral faces of the prism (giving a tricapped prism). In $TbCl_3$ there are four neighbouring columns, but only two of them provide a close Cl^- neighbour to the Tb^{3+} ion. A ninth neighbour is in the direction of the third lateral face, but it is further away than the others.

Of the remaining structures, the **YCl_3 and BiI_3 structures** share a common local arrangement, which consists of planes of *edge*-sharing octahedra. Both structures may be viewed as derived from a close-packed lattice of Cl^- ions (with the cations in octahedral holes) and differ only in the stacking sequence of the close-packed layers, the YCl_3 being cubic and BiI_3 hexagonal. As such, their energies are very similar. These two structures are clearly illustrated in references [52] and [53]: it can be seen that the pattern of occupation of octahedral holes gives alternating planes of vacancies and two-thirds of the octahedral sites filled, thus creating a layered crystal structure in which the cations are crowded into a single layer and in which each plane of anions is sandwiched between a

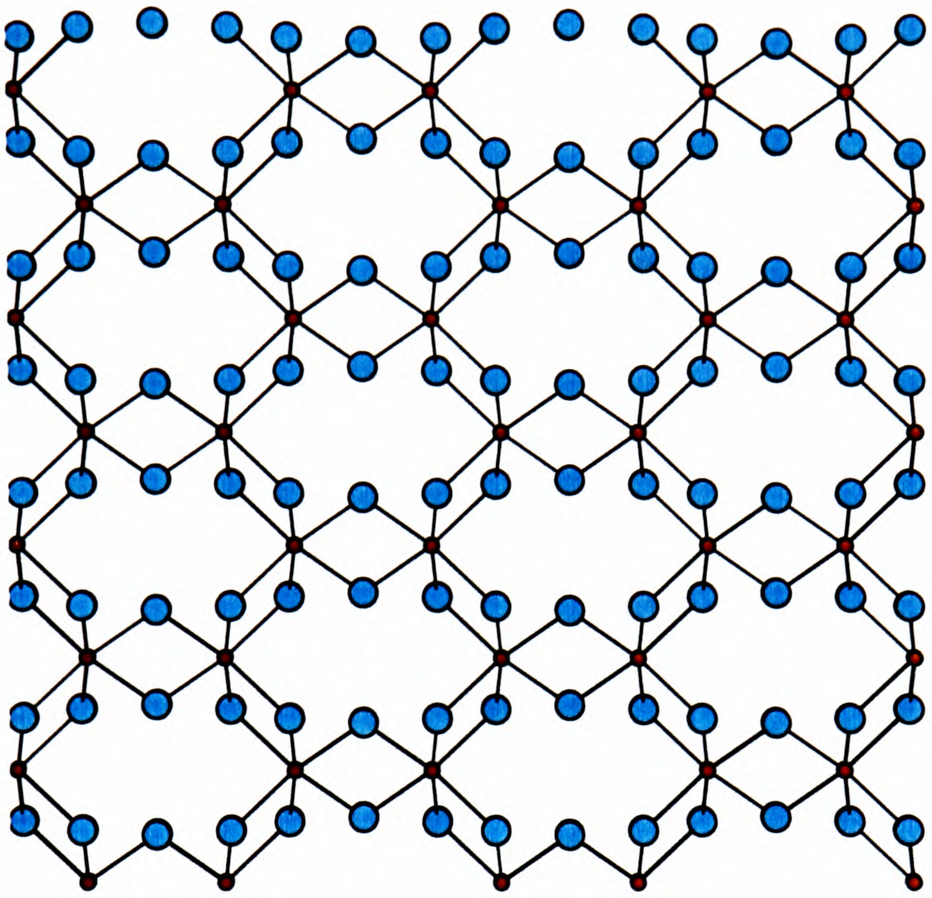

Figure 2.3: *YCl_3 Crystal Structure - View of the layer structure indicating the edge-sharing octahedral local structure.*

cation layer on one side and an anion layer on the other. The situation is clearly unfavourable for the interion coulombic interactions but, as discussed previously in work on MX_2 systems [19], the layered structure promotes a large negative polarization contribution to the lattice energy. Within a cation-filled layer, 2/3 of the available octahedral sites are occupied, which creates a pattern of edge-sharing octahedra, as illustrated in figures 2.3 and 2.4.

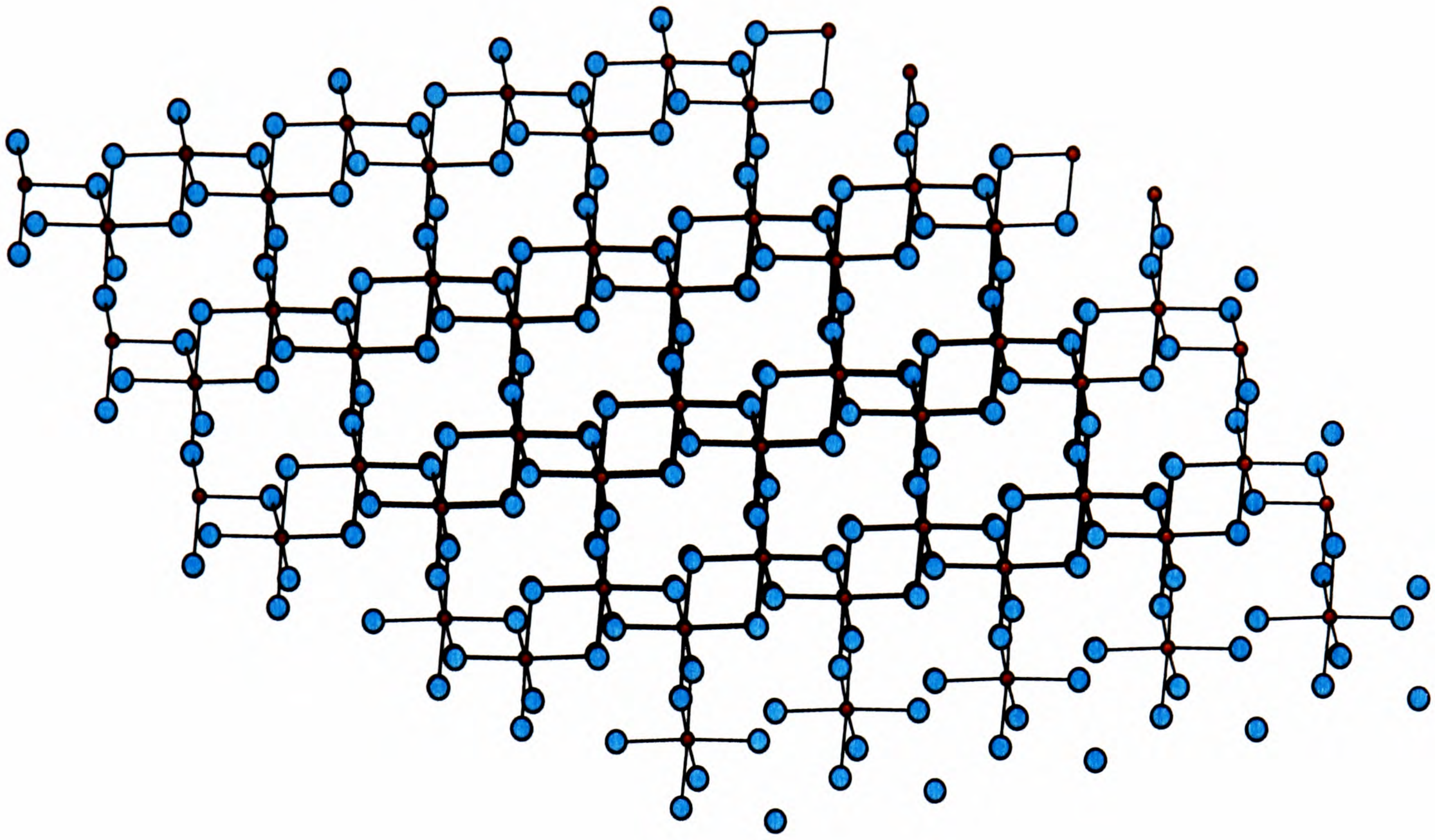

Figure 2.4: *BiI_3 Crystal Structure - View of the layer structure indicating the edge-sharing octahedral local structure.*

The **ZrI_3 structure** is also based on a pattern of octahedral hole filling in a hexagonally packed anion lattice. However, the pattern of hole filling is here such that chains of *face*-sharing octahedra, which run along the c axis of the crystal, are formed. In reality, the ZrI_3 structure is not formed in any of the chlorides of interest in this work and, in our calculations, it was at a substantially higher energy than the other structures. It is therefore omitted from consideration here.

The **$AlBr_3$ structure** may be viewed as a close-packed anion lattice but in which the cations occupy the *tetrahedral* holes. It would therefore be expected to become important for a large cation:anion radius ratio. This may be visualised, alternatively, as a molecular solid of Al_2Br_6 units [8], in which the highly asymmetric anion sites are clear (figure 2.5). Such Al_2Br_6 units are overall

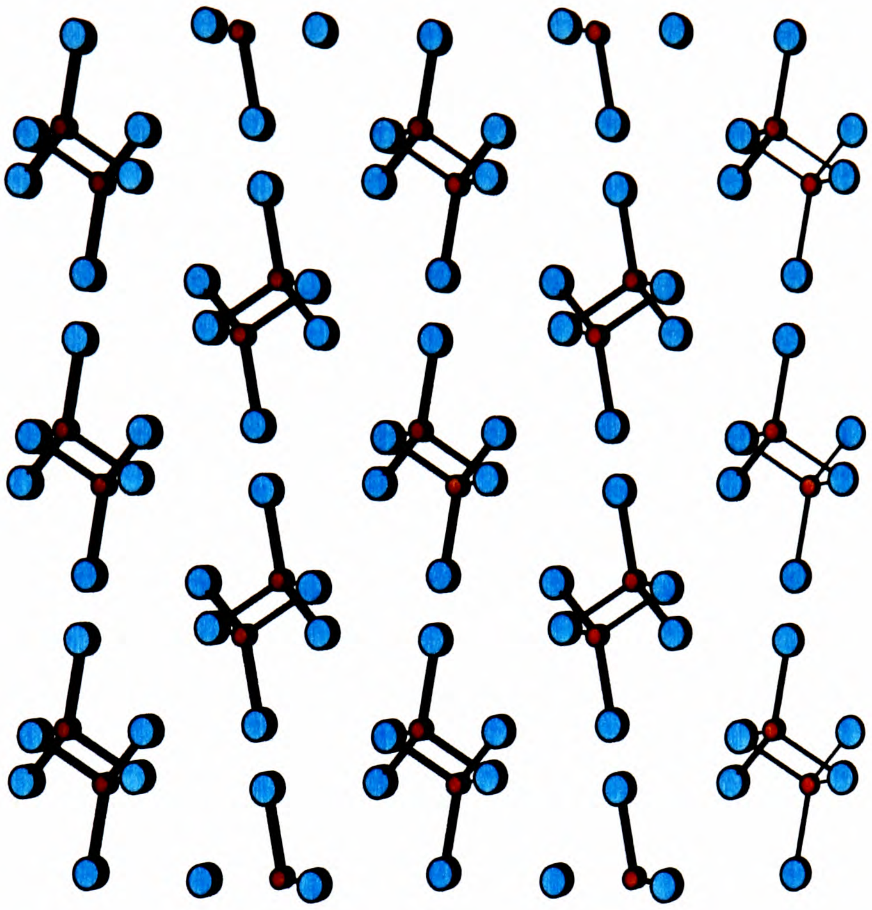

Figure 2.5: *$AlBr_3$ Crystal Structure - The Al_2Br_6 dimers formed by the cations occupying tetrahedral holes can clearly be seen.*

charge neutral and so are held together by dispersion forces alone. This may be expected to have significant implications for the physical properties of systems occupying this structure.

2.3 Simulation details

The structures are set up using idealized atomic positions in the unit cell (see [52, 53] and references therein), and then rescaled to a number of different total cell volumes without allowing any change in the shape of the unit cell. All the calculations were performed with the Tatlipinar potential that was used in the previous chapter for the liquids. Single point energy calculations are performed, after minimization of the polarization energy with respect to the dipoles on each ion, as described in section 3.2 [54]. Where necessary structural relaxation was allowed. This is analogous to minimizing the polarization energy in the annealing of the dipoles but quenching the ion velocities instead. This was only found to be neccessary for $AlCl_3$ and made very little difference to the position of the energy minima for the remaining MCl_3 systems.

However, *cell relaxation*, where the simulation cell can change shape is likely to be important for these systems where the crystal structures are very close in energy, but the framework in which to perform such calculations has not been available to date. The number of ions used in the crystal calculations were as follows, UCl_3 - 1120, $PuBr_3$ - 768, YCl_3 - 960 and $AlBr_3$ - 960.

2.4 $LaCl_3$

The crystal energy versus cell volume for $LaCl_3$ is shown in figure 2.6. Whilst the cell volume and lattice energy of the UCl_3 structure are similar to those observed experimentally (117.668 *vs* 105.590Å^3 [55] and 4060 vs 4343kJ.mol^{-1} [56]), the UCl_3 structure is not predicted to be the most stable. Instead, the 6-coordinate YCl_3 structure is predicted to be the lowest in energy. Allowing relaxation of the ion positions is not seen to affect the position of the energy minima.

2.5 $TbCl_3$

While there is no lattice energy information available for $TbCl_3$ it is illustrative to see how the change in radius affects the predicted energies and volumes. The energy-volume curves are shown in figure 2.7. The predicted cell volume of the $PuBr_3$ structure is very similar to the experimental value, however, once again the YCl_3 structure is predicted to be the most stable. The energy difference between the UCl_3 and YCl_3 structures has now increased. Allowing for relaxation of the ion positions had a negligible effect on the position of the energy minima.

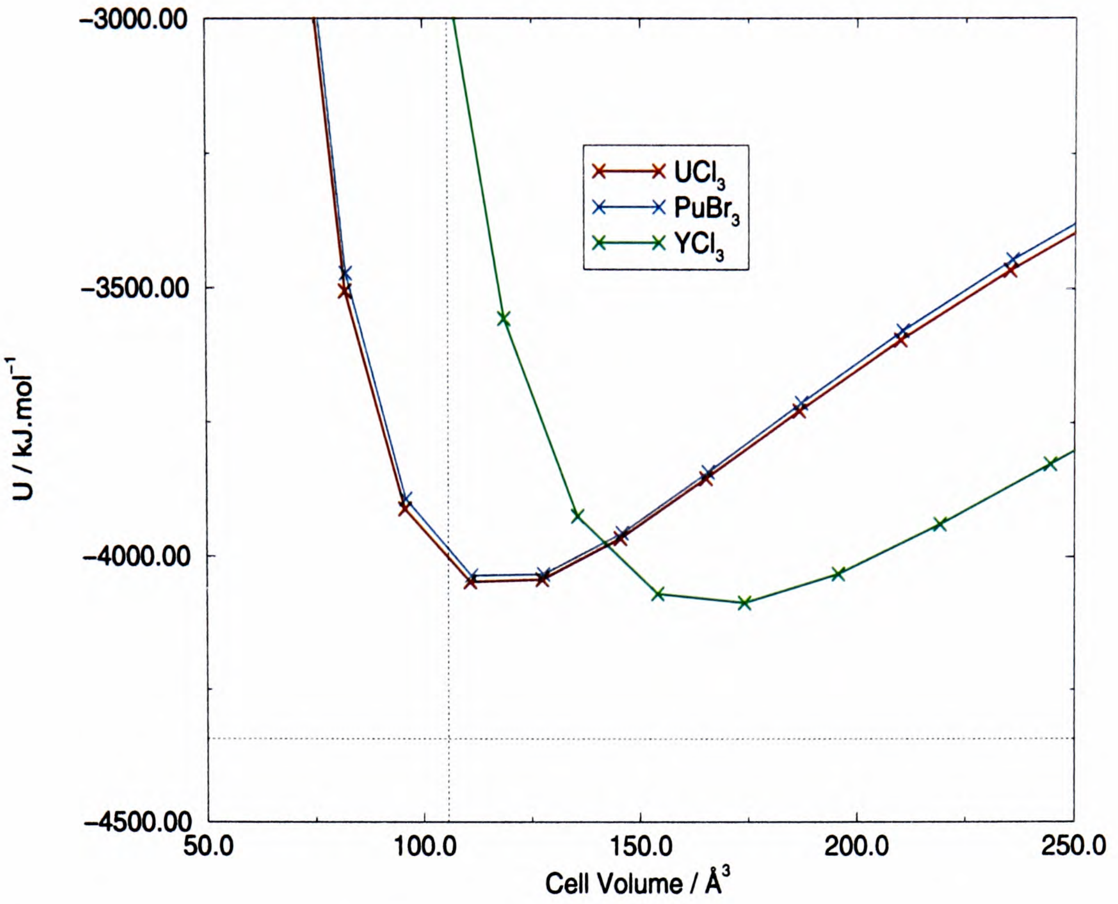

Figure 2.6: *Energy-Volume curves for* $LaCl_3$ *(calculated with the Tatlipinar potential) for three different crystal structures. The dotted lines show the experimental cell volume and lattice energy.*

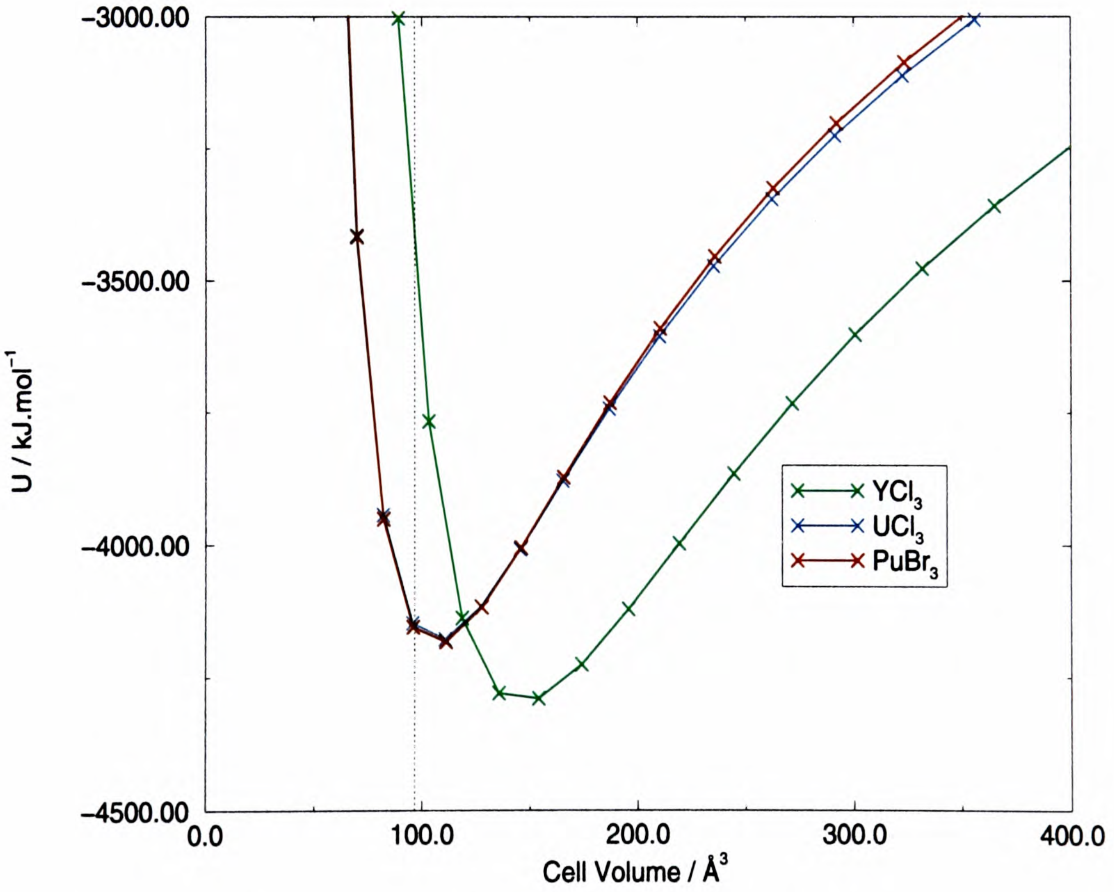

Figure 2.7: *Energy-Volume curves for* $TbCl_3$ *(with the Tatlipinar potential) for three different crystal structures.*

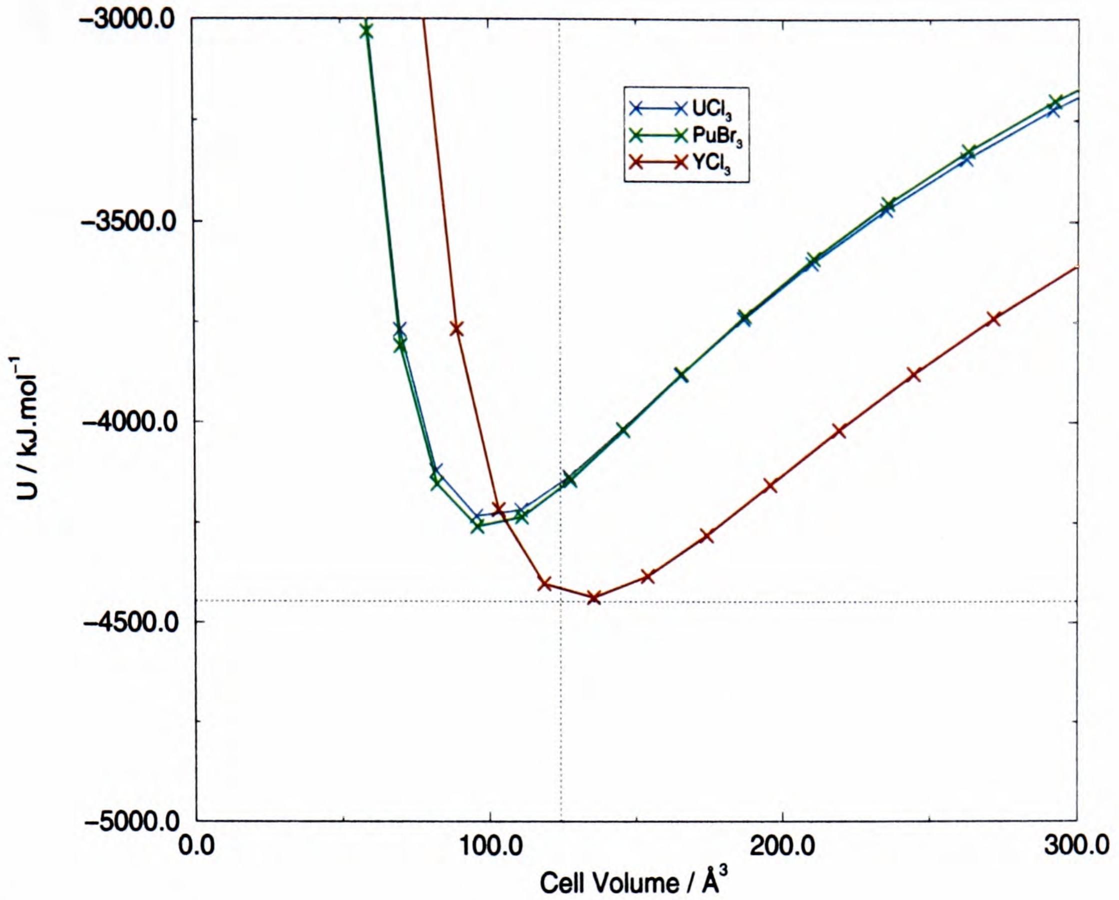

Figure 2.8: *Energy-Volume curves for YCl_3 (with the Tatlipinar potential) for three different crystal structures*

2.6 YCl_3

The energy-volume curves exhibited in figure 2.8 predict the YCl_3 crystal structure to be the most stable with a lattice energy of 4437kJ.mol^{-1} (compared to 4447kJ.mol^{-1} experimentally [56]) and cell volume of 131.832Å^3 (compared with 124.250Å^3 experimentally [57]). Both these values are in good agreement with experiment.

Clearly a trend is emerging here. As the cation radius is reduced the energy difference between the $PuBr_3$ (and the very similar structure UCl_3) and YCl_3 structures is increasing. In the $PuBr_3$ and UCl_3 structures the larger cations can accomodate more anions than the YCl_3 structure. The calculated energy minima remained at the same energy and volume after allowing for relaxation of the ion positions.

2.7 $AlCl_3$

For $AlCl_3$ we once again compare the energetics of the different crystal structures in two stages. In this case, however, ion relaxation is seen to have quite a dramatic effect. First, we consider the energy against volume curves for the unrelaxed crystal structures as has been done for the other systems. The pattern of the data for the crystal energy versus cell volume for $AlCl_3$ exhibited in figure 2.9 establishes that the (six-coordinate) YCl_3 and BiI_3 structures and the 4-coordinate $AlBr_3$ structures have similar energies. They are much more stable than any other crystal structure, the next lowest is the UCl_3 structure shown in figure 2.9. The close relationship between the BiI_3 and YCl_3 structures is evident from the similarity of the internal energy against volume curves [51], – the energetic difference between these structures is not really significant. The molecular volume at the minimum energy for the six-coordinate structure is similar to the experimental one (97 $Å^3$ *vs.* 89 $Å^3$ [57]). This suggests that the crystal is somewhat underbound, and this is confirmed by the fact that the lattice energy at the minima of the experimentally observed structure is significantly lower than the experimental value deduced from Born-Haber cycles:- 5000 kJ mol^{-1} *vs.* 5376 kJ mol^{-1} [56].

More significantly for our immediate concerns, figure 2.9 shows that the $AlBr_3$ structure emerges with a slightly lower energy than the experimentally observed 6-coordinate YCl_3 structure by about 100 kJ mol^{-1}. This energy is small compared to the total lattice energy: from one viewpoint this is reassuring as the local ionic arrangement in the $AlBr_3$ structure is close to that believed to occur in the liquid, and since the 6-coordinate solid melts to this liquid the underlying 4-coordinate solid must have a similar energy. However, they do suggest that the potential model is overstabilizing the 'molecular', 4-coordinate $AlBr_3$ structure relative to the 'ionic' 6-coordinate YCl_3.

Having established the pattern of energies against volume for the ideal crys-

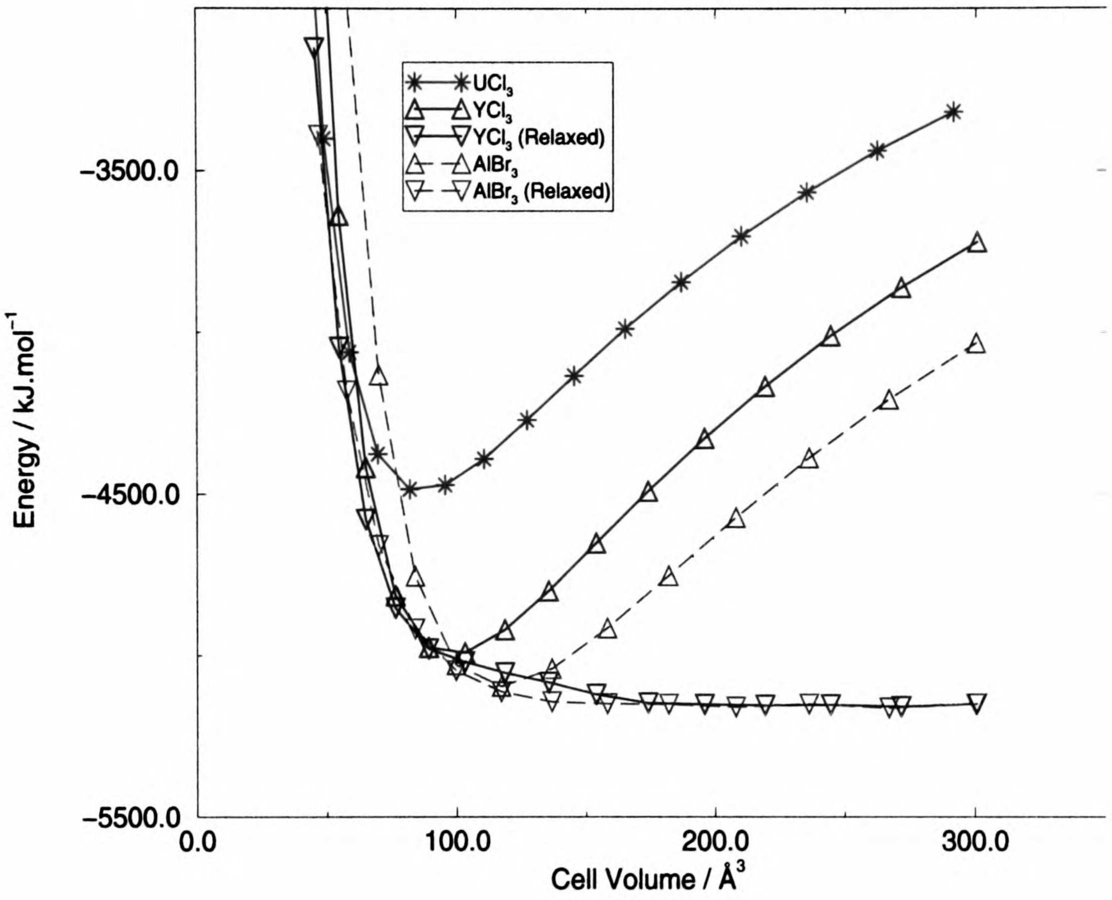

Figure 2.9: *The energies versus cell volumes for three possible crystal structures calculated with the polarizable ion potential appropriate for* $AlCl_3$. *Also shown are the energy-volume curves for the* YCl_3 *and* $AlBr_3$ *structures after allowing for relaxation of the ion positions.*

tal structures, we now allow for relaxation in the atomic positions. The results are illustrated in figure 2.9. Relaxation is allowed at fixed cell volume starting from both the YCl_3 and $AlBr_3$ structures. Examination of the ionic arrangements shows that, for molecular volumes less than $\simeq 100$ Å^3 both structures relax into the YCl_3 arrangement, whereas for larger volumes both relax into the $AlBr_3$ structure. The additional stabilization of the YCl_3 structure due to relaxation is very small, so that the lattice energy estimates discussed above for the 6-coordinate structures remain valid. In the $AlBr_3$ structure, the Al_2Cl_6 'molecules' are able to separate readily (being held together, in the limit, only by van der Waals interactions) and so the calculated potential energy curve exhibits a very broad, flat minimum reflecting simply the loss in dispersion energy between the molecules as the volume is increased.

Unfortunately, the absolute minimum of the crystal energies is associated with the $AlBr_3$ structure, though this is only ~ 100 kJ mol^{-1} lower than the lowest energy for the experimentally observed structures.

2.8 Conclusions

For each crystal system studied we have predicted the lower coordinated, more tightly bound structures to be more stable than is actually the case. The only exception is for YCl_3 which is predicted quite accurately. However, the general trends observed with a decrease in cation radius are encouraging.

This failure may well be a problem with the simplicity of the interaction model itself and we will focus on this possibility in chapter 5.

It is interesting to speculate on what might be missing from the potential model, which might help to stabilize the experimentally observed structures at smaller molecular volumes and lower energies. The model used includes only dipole polarization of the anion, and neglects the breathing and shape deformation effects which have been found necessary to account for the properties of oxides [3]. The latter effects have been found to be particularly important to achieve an accurate description of transitions between crystalline phases where a change of coordination number occurs, as they stabilize the more tightly-packed, high-coordination number structures relative to predictions with simple pair potentials. A possible origin for the underestimate of lattice energies is that the in-crystal Cl^- ion [54] relaxes as it is extracted from the crystal (the breathing effect [2]). This effect has been discussed in the case of the oxide ion by Harding and Pyper [58]; for the oxide ion it is a considerable effect. The halides have been less studied. We will see in chapter 5 that on the basis of Pyper's [22] estimate for CsCl, we would estimate an additional contribution to the calculated lattice energies in the region of 100kJ mol^{-1} from this source, but it is possible that this substantially underestimates the true effect.

We will return to the deficiencies in the MCl_3 interaction potential in chapter 5, and undertake a thorough re-evaluation.

A second failure is that the simulation models presented for determining the lowest energy crystal structure are not adequate. Relaxation of ion positions is seen to only have a very small effect (with the exception of $AlCl_3$). Rather for different crystal structures which are so close in energy we need to be able to let the simulation cell change shape as in the Parrinello-Rahman scheme [23]. The technical details of this are in the following chapter. It will then be validated on alkali halides and then in chapter 6 applied to trivalent metal halides.

Chapter 3

Development of the Simulation Method

3.1 Introduction

Reproducing experimental crystal structures and crystalline phase transitions is an important way of validating the interaction model outlined in chapter 1 as well as an important topic in its own right.

The majority of polarizable ion (PIM) simulations which have been performed to date have been carried out in an NVT ensemble with cubic periodic boundary conditions. This greatly limits the ability to simulate crystals as only crystals whose structure is commensurate with a cubic supercell may be generated.

In order to extend the range of possible calculations the NVT ensemble PIM has been generalized to allow a constant N,T and stress ensemble in which both the cell size and shape may vary. The presence of the many-body terms makes this more problematic than for a simple pair-potential.

In this chapter, the standard techniques used in NVT PIM simulations are first summarised. These techniques have been developed over a number of years and they have been described in full detail by previous workers [59, 60]. The generalization to the constant stress ensemble is then developed in detail. Some of the more lengthy derivations are given in Appendices.

3.2 The Standard Polarizable Ion Technique.

As outlined in the Introduction, in order to represent interionic interactions at a realistic level it is necessary to allow for many-body effects, such as polarization, in the interionic potential. In the PIM, developed by Wilson and Madden [54], this is accomplished by introducing additional degrees of freedom to describe the instantaneous value of quantities such as the dipole moment of each ion. The potential energy of a set of ions with dipole moments is given by

$$\begin{aligned}\mathcal{U} &= \sum_{i=1}^{N-1}\sum_{j=i+1}^{N}\{U_{sr}(r_{ij}) + T^{ij}Q_iQ_j + T^{ij}_{\alpha}(Q_j\mu^i_\alpha - Q_i\mu^j_\alpha) - T^{ij}_{\alpha\beta}\mu^i_\alpha\mu^j_\beta\}\\ &+ k^\mu\sum_{i=1}^{N}\mu^{i^2}, \qquad (3.1)\end{aligned}$$

where it has been assumed that a simple pair potential may be used for the repulsive and dispersion interactions (the ion compressibility will be described in chapter 5) and, for the moment, short-range contributions to the induced dipoles have been ignored. Here the interaction tensors T^{ij} are given by:

$$T^{ij}_{\alpha\beta\gamma\delta} = \nabla_\alpha\nabla_\beta\nabla_\gamma\nabla_\delta\ldots\frac{1}{r_{ij}}, \qquad (3.2)$$

Q_i is the charge on ion i and μ^i_α the α^{th} cartesian component of its dipole.

In equation 3.1 the final term $k^\mu\sum\mu^{i^2}$ is a "self-energy" which accounts for the increase in the energy of the electron density of i when a dipole is induced. If expression 3.1 is minimized with respect to each of the dipoles μ^i_α, *i.e.*

$$2k^\mu\mu^i_\alpha = E^i_\alpha, \qquad (3.3)$$

where E^i_α is the α^{th} component of the electric field at ion i

$$E^i_\alpha = \sum_{j \neq i}^{N} \{-T^{ij}_\alpha Q_j + T^{ij}_{\alpha\beta} \mu^j_\beta\} \tag{3.4}$$

it can be seen that, by choosing the parameter $k^\mu = (2\alpha)^{-1}$, where α is the ionic polarizability, the induced dipole takes the physical value

$$\mu^i_\alpha = \alpha E^i_\alpha. \tag{3.5}$$

Furthermore, by substituting this value for the dipole back into the expression for the potential energy (equation 3.1) it is seen that the contribution of the dipoles to the energy is

$$U^{ind} = -\frac{1}{2}\sum_i \alpha (E^i)^2 \tag{3.6}$$

which again is the physically consistent value. Hence, if the expression for the potential energy, which explicitly involves the dipoles is evaluated, with the dipoles taking these minimizing values it will yield a correct expression for the polarization energy (including the self-consistency of the dipoles). Although this polarization energy gives rise to a many-body potential, when viewed purely as a function of the interionic positions, it is evaluated from the purely pairwise additive expression (equation 3.1).

Car and Parrinello [61] showed how equations of motion for a dynamical system which contained additional variables obeying a variational condition (like these dipoles) could be derived. In the PIM context a dynamical system consisting of the coordinates *and dipoles* of all ions is imagined in the manner proposed by Sprik [62]. Its time evolution is governed by the Lagrangian

$$\mathcal{L} = \mathcal{T} - \mathcal{U}, \tag{3.7}$$

where $\mathcal{T}$ is the kinetic energy

$$\mathcal{T} = \frac{1}{2}\sum_{i=1}^{N} m_i \dot{\mathbf{r}}_i^2 + \frac{1}{2}\sum_{i=1}^{N} m^\mu_i (\dot{\boldsymbol{\mu}}^i)^2 \tag{3.8}$$

and $\mathcal{U}$ is the potential energy of equation 3.1. In equation 3.8, m_μ is the 'fake' mass of ion i, governing the inertia of the dipolar degrees of freedom, and m_i the regular ionic mass. The equations of motion for the ions are given by

$$\frac{d}{dt}\left(\frac{\partial \mathcal{L}}{\partial \dot{\mathbf{r}}_i}\right) - \frac{\partial \mathcal{L}}{\partial \mathbf{r}_i} = 0, \tag{3.9}$$

or,

$$m_i \ddot{\mathbf{r}}_i = \nabla_r U, \tag{3.10}$$

which is just Newton's Law. The dipoles obey

$$\frac{d}{dt}\left(\frac{\partial \mathcal{L}}{\partial \dot{\mu}^i_\alpha}\right) - \frac{\partial \mathcal{L}}{\partial \mu^i_\alpha} = 0, \tag{3.11}$$

which is,

$$m^\mu_i \ddot{\mu}^i_\alpha = \sum_{j \neq i}^{N} \{-T^{ij}_\alpha Q_j + T^{ij}_{\alpha\beta}\mu^j_\beta\} - 2k^\mu \mu^i_\alpha. \tag{3.12}$$

Note that the right hand side of this equation is the condition (equations 3.3 and 3.4) for obtaining the dipoles which minimize $\mathcal{U}$ (and give the correct polarization energy). Hence, if these coupled equations of motion can be integrated in such a way that the accelerations of the dipoles $\ddot{\mu}^i_\alpha$ are always small, the forces acting on the ionic positions will correctly include the contributions from the polarization interactions. This is known as *maintaining the adiabatic condition* on the dipoles. It is achieved by making a suitable choice for the 'fake mass', and also by controlling the temperature of the dipoles as described in the following section.

3.2.1 Thermostatting

Since most experimental data is obtained at constant temperature rather than constant energy, it makes sense to perform our simulations at constant temperature (NVT ensemble). Furthermore, the maintenace of the adiabatic condition on the dipoles in the PIM is equivalent to ensuring that they are maintained at a low temperature. We choose to use a method (thermostatting) proposed by Nosé [63] and Hoover [64] which treats the system as in contact with a thermal reservoir. This is achieved by including an extra degree of freedom which represents this reservoir, and carrying out a simulation on this 'extended' system.

The Nosé-Hoover equations of motion for the ionic coordinates replace the Newtonian equations obtained above. They may be written

$$\frac{d\mathbf{r}_i}{dt} = \frac{\mathbf{p}_i}{m_i}, \tag{3.13}$$

$$\frac{d\mathbf{p}_i}{dt} = \mathbf{f}_i - \frac{p_\xi}{Q}\mathbf{p}_i, \tag{3.14}$$

where $\mathbf{f}_i$ is the force acting on ion i and p_ξ is the 'momentum' of the thermostat, which itself obeys

$$\frac{dp_\xi}{dt} = \sum_{i=1}^{N} \frac{\mathbf{p_i}^2}{m_i} - N_f kT, \tag{3.15}$$

$$\frac{d\xi}{dt} = \frac{p_\xi}{Q}, \tag{3.16}$$

$$Q = N_f kT\tau^2. \tag{3.17}$$

Here N_f is the number of degrees of freedom ($3N - 6$), T is the thermostat temperature (*i.e.* the required temperature) and τ is the thermostat relaxation time *i.e.* a measure of the time taken for the thermostat to react to a move away from the desired temperature.

A useful check on the accuracy with which the Nosé-Hoover form of the equations have been treated in any numerical integration scheme may be provided by examining the extended system Hamiltonian,

$$H'(\mathbf{p}, \mathbf{r}, \xi, p_\xi) = V(\mathbf{r}) + \sum_{i=1}^{N} \frac{\mathbf{p}_i^2}{2m_i} + \frac{p_\xi^2}{2Q} + NkT\xi, \tag{3.18}$$

which should be conserved throughout the simulation.

A separate thermostat may be introduced to control the dipole temperature, so that the equations of motion for the ionic coordinates and dipoles become:

$$m_i \ddot{r}_i^{\alpha} = -\sum \{\nabla_{r_{\alpha}^i}(U^{sr}(r_{ij}) - Q^j E_{\alpha}^i - \mu_{\beta}^j E_{\alpha\beta}^i)\} - \xi_{ion} m_i \dot{r}_i^{\alpha}, \qquad (3.19)$$

and

$$m_{\mu}^i \ddot{\mu}_{\alpha}^i = \sum \{-T_{\alpha}^{ij} Q_j + T_{\alpha\beta}^{ij} \mu_{\beta}^j\} - 2k^{\mu} \mu_{\alpha}^i - \xi_{\mu} m_{\mu} \dot{\mu}_{\alpha}^i. \qquad (3.20)$$

These are integrated in parallel with the equations (3.15 and 3.16) for the two thermostat degrees of freedom (ξ_{ion} and ξ_{μ}).

In most systems the movements of the particles are sufficiently chaotic to ensure that the NH thermostat yields a canonical (NVT) distribution. However, for small or stiff systems, the NH thermostat may fail to generate a canonical distribution. To alleviate these ergodicity problems Martyna *et al.* [65] have proposed a scheme in which the NH thermostat is coupled to another thermostat, or, if necessary to a whole chain of thermostats.

The Nosé-Hoover equations of motion are applied by using the Velocity-Verlet finite-difference algorithm [66]. For the ionic coordinates, this gives (where $\mathbf{r}_i$, $\mathbf{v}_i$ and $\mathbf{a}_i$ are the ionic position, velocity and acceleration respectively),

$$\begin{aligned} \mathbf{r}_i(t+\delta t) &= \mathbf{r}_i(t) + \mathbf{v}_i(t)\delta t + \mathbf{a}_i(t)\frac{\delta t^2}{2} \\ &= \mathbf{r}_i(t) + \mathbf{v}_i(t) + \left[\frac{\mathbf{f}_i(t)}{m_i} - \mathbf{v}_i(t) v_{\xi}(t)\right]\frac{\delta t^2}{2}, \end{aligned} \qquad (3.21)$$

and

$$\begin{aligned} \mathbf{v}_i(t+\delta t) &= \mathbf{v}_i(t) + [\mathbf{a}_i(t) + \mathbf{a}_i(t+\delta t)]\delta t \\ &= \mathbf{v}_i(t) + \left[\left\{\frac{\mathbf{f}_i(t)}{m} - v_{\xi}(t)\mathbf{v}_i(t)\right\}\right. \\ &+ \left.\left\{\frac{\mathbf{f}_i(t+\delta t)}{m} - v_{\xi}(t+\delta t)\mathbf{v}_i(t+\delta t)\right\}\right]\delta t, \end{aligned} \qquad (3.22)$$

It is clear from equation 3.22 that $\mathbf{v}_i(t+\delta t)$ needs to be iterated to self consistency. For the thermostat itself

$$v_\xi(t+\delta t) = v_\xi(t) + \left[G_\xi(t) + G_\xi(t+\delta t)\right]\frac{\delta t}{2} \tag{3.23}$$

where

$$G_\xi(t) = \frac{1}{Q}\left[\sum_{i=1}^{N} m_i \mathbf{p}_i(t)^2 - N_f kT\right]. \tag{3.24}$$

3.2.2 Short-range contributions to the induced dipoles

As discussed in the Introduction, the coulombically-induced dipoles included in the above equations of motion, are appreciably affected by short-range effects in real materials. There is now a substantial body of accumulated evidence, both from electronic structure calculations [28,67] and, more empirically from a comparison of the results of PIM simulation with experiment, that such effects can be accounted for by a straightfoward extension of the above scheme. This is achieved by modifying the radial form of the charge-dipole interaction tensor (T_α^{ij}) in equation 3.1 by multiplying it with a suitable 'damping function'

$$T_\alpha^{ij} \rightarrow \left[1 - e^{-b_1 r^{ij}} \sum_{k=0}^{4} \frac{(b_1 r^{ij})^k}{k!}\right] T_\alpha^{ij}. \tag{3.25}$$

The function chosen (in square brackets), is a 'Tang-Toennies' damping function [38], which varies between the value one, when $r^{ij}b_1 >> 1$ and zero, when $r^{ij}b_1 < 1$. The rate at which this happens is determined by k, which was chosen to be four in all calculations. At long-range, the charge dipole interaction takes the normal coulombic form, but at small r its value is much reduced to reflect the opposition of the coulombic dipole by the short-range one as shown in the Introduction. The distance over which this happens is set by the parameter b_1, which is known as the 'induction damping parameter'. The value for b_1 has been examined in electronic structure calculations [67] and, for related classes of materials, has been found to scale with the sum of ionic radii

$$b_1 = \frac{c}{\sigma_i + \sigma_j}, \tag{3.26}$$

where c is a constant for a given class of compunds (7.42 for all the systems considered in this work).

3.2.3 Treatment of long-range interactions: the Ewald Sum

Coulombic interactions are of infinite range and cannot be truncated inside the simulation cell, which is the standard way of treating all short-range interactions in computer simulations [66]. The Ewald sum [68] is a technique for efficiently summing the interaction between the ions in the simulation cell and all it periodic images. The formulae for charge-charge interactions are given below, the treatment of the charge-dipole and dipole-dipole interactions which appear in equation 3.1 are given in Appendix A.

In the Ewald method, the expression for the charge-charge coulomb energy in the infinitely periodic system consisting of the simulation cell and all its images is written as a sum of three terms

$$\frac{1}{2}\sum_{i,j,\mathbf{l}}{}' \frac{1}{r_{ij}} Q_i Q_j = U_{real} + U_{recip} + U_{const} \tag{3.27}$$

where the sum over i, j is over all pairs of ions in the cell and the sum over **l** is over all image cells. The prime indicates the exclusion of terms where **l**=0 and i=j. In this equation

$$U_{real} = \sum_{i}\sum_{j\neq i} Q_i Q_j \frac{\operatorname{erfc}(\eta' r_{ij})}{r_{ij}} \tag{3.28}$$

is known as the 'real-space' term. It involves the complementary error function

$$\operatorname{erfc}(\eta' r) = \left((2/\pi^{1/2}) \int_{\eta' r}^{\infty} e^{-t^2} dt \right) \tag{3.29}$$

in which parameter η' appears, it has the role of ensuring that all the real space interactions die out within the simulation cell. Longer-range contributions to the coulombic interactions are dealt with in the 'reciprocal-space term'

$$\begin{aligned} U_{recip} &= Q_i Q_j \left[\frac{1 - \mathrm{erfc}(\eta' r_{ij})}{r_{ij}} \right] \\ &= \frac{1}{2\pi V} \sum_i \sum_{j<i} \sum_{\mathbf{k}\neq 0} Q_i Q_j \frac{1}{k^2} e^{-\pi^2 k^2/\eta'^2} \cos(\mathbf{k} \cdot \mathbf{r}_{ij}), \qquad (3.30) \end{aligned}$$

which involves the sum over all the vectors $\mathbf{k}_n$ in the reciprocal lattice of the periodically replicated simulation system. In practice, since the sum involves the function $e^{-\pi^2 k^2/\eta'^2}$, which dies away rapidly for large k, only a finite number of vectors around the origin need be included. The final term in equation 3.27 is the constant term arising from the interaction of the ion with all its images. This is given by

$$U_{const} = -\sum_i \frac{(Q_i)^2 \eta'}{\pi^{(1/2)}}. \qquad (3.31)$$

The first term in 3.27 is an expansion which converges rapidly at large η'. On the other hand, the second term converges fast near $\eta' = 0$. If we choose an appropriate value for η', then both expansions converge reasonably fast. The computational cost of evaluating the reciprocal space sum is halved by using the inversion symmetry of k-space. Additionally, the sum over i and j in k-space may be reduced to a sum over i by writing $\mathbf{r}_{ij}$ as $\mathbf{r}_i - \mathbf{r}_j$, the reciprocal space sum may be rewritten as

$$U_{recip} = \frac{1}{2\pi V} \sum_i \sum_{j<i} \sum_{k\neq 0} Q_i Q_j \frac{1}{k^2} e^{\frac{\pi^2 k^2}{\eta'^2}} \cos(\mathbf{k} \cdot \mathbf{r}_{ij}), \qquad (3.32)$$

$$\begin{aligned} U_{recip} &= \frac{1}{2\pi V} \sum_{k\neq 0} \frac{1}{k^2} e^{-\frac{\pi^2 k^2}{\eta'^2}} \left(\sum_i \sum_j Q_i Q_j \cos[\mathbf{k} \cdot (\mathbf{r}_i - \mathbf{r}_j)] \right) \\ &= \frac{1}{2\pi V} \sum_{k\neq 0} \frac{1}{k^2} e^{-\frac{\pi^2 k^2}{\eta'^2}} \left(\sum_i Q_i \cos(\mathbf{k} \cdot \mathbf{r}_i) \sum_j Q_j \cos(\mathbf{k} \cdot \mathbf{r}_j) \right. \\ &+ \left. \sum_i Q_i \sin(\mathbf{k} \cdot \mathbf{r}_i) \sum_j Q_j \sin(\mathbf{k} \cdot \mathbf{r}_j) \right). \qquad (3.33) \end{aligned}$$

Charge-dipole and dipole-dipole interactions in our model will give rise to additional coulombic terms. From Allen and Tildesley [66] long-range interactions are those which fall off no faster than r^{-d} where d is the systems dimensionality. These will be treated by an Ewald summation in order to avoid truncation errors.

The charge-charge Ewald sum can be described by the zeroth order T tensor, T^{ij}. Calculation of charge-dipole terms etc. requires terms such as T^{ij}_{α} and $T^{ij}_{\alpha\beta}$ which are obtained by differentiation of T^{ij}. These are determined in appendix A.

3.3 Implementing the constant-stress ensemble

In the remainder of the Chapter, the formal structure of the generalization of the PIM simulation, outlined above, to the constant temperature, constant stress algorithm is described.

3.3.1 Non-cubic simulation cells

To facilitate the implementation of molecular dynamics in a non-cubic cell, it is convenient to define two frames of reference for a general, noncubic simulation cell. This is similar to the scheme of Nosé and Klein. [69] The Cartesian frame is defined by the standard orthogonal Cartesian vectors, $\mathbf{s}_i$. The cell frame may have non-orthogonal axes (figure 3.1) which are defined by the crystallographic cell vectors, **a**, **b** and **c**.

This cell may be represented by **h**, the cell matrix, which is a 3× 3 matrix constructed from the vectors **a** , **b** and **c**.

$$\mathbf{h} = \begin{pmatrix} a_x & b_x & c_x \\ a_y & b_y & c_y \\ a_z & b_z & c_z \end{pmatrix} . \tag{3.34}$$

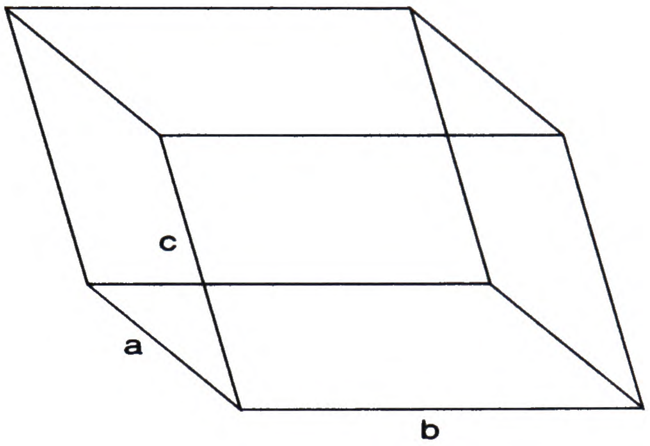

Figure 3.1: *MD cell spanned by the vectors* **a**, **b** *and* **c**

Additionally, we define the transformation matrix

$$\hat{\mathbf{h}} = \begin{pmatrix} \hat{a}_x & \hat{b}_x & \hat{c}_x \\ \hat{a}_y & \hat{b}_y & \hat{c}_y \\ \hat{a}_z & \hat{b}_z & \hat{c}_z \end{pmatrix}. \tag{3.35}$$

Hence,

$$\mathbf{h} = \hat{\mathbf{h}} \begin{pmatrix} l_1 \\ l_2 \\ l_3 \end{pmatrix}, \tag{3.36}$$

where $l_1 = |\mathbf{a}|$ etc., $\hat{a}_x$ is the unit component of **a** along the x-axis etc. The ion coordinates are stored in the cell frame and so transformations to the Cartesian frame are required in order to calculate energies and forces. For example, to transform the ion coordinates from the Cartesian frame (**s**) to the cell frame (**r**)

$$\mathbf{r}_i = \hat{\mathbf{h}}\mathbf{s}_i. \tag{3.37}$$

Similarly, to transform from the cell frame to the Cartesian frame,

$$\mathbf{s}_i = \hat{\mathbf{h}}^{-1}\mathbf{r}_i. \tag{3.38}$$

The introduction of the cell frame allows straightforward application of the minimum image convention in which the distance between two particles is calculated taking into account the periodic boundary conditions in the simulation [66]. Calculated interparticle separations may then be transformed into the Cartesian frame for evaluation of the real space interionic interactions. In order to calculate the properties of long range energy functions, calculations in reciprocal space are required. For the non-cubic cell it is necessary to consider the formal definition of the reciprocal lattice basis vectors.

$$\mathbf{k}_1 = \frac{1}{V}(\mathbf{b} \times \mathbf{c}), \tag{3.39}$$

$$\mathbf{k}_2 = \frac{1}{V}(\mathbf{c} \times \mathbf{a}), \tag{3.40}$$

$$\mathbf{k}_3 = \frac{1}{V}(\mathbf{a} \times \mathbf{b}), \tag{3.41}$$

where $V = \mathbf{a} \cdot (\mathbf{b} \times \mathbf{c}) = \det[\mathbf{h}]$, is the simulation cell volume. Therefore, a general k-vector may be expressed as

$$\begin{aligned}
\mathbf{k}_n &= \mathbf{k}_1 n_1 + \mathbf{k}_2 n_2 + \mathbf{k}_3 n_3 \\
&= \frac{1}{\mathbf{a} \cdot (\mathbf{b} \times \mathbf{c})}[(\mathbf{b} \times \mathbf{c})n_1 + (\mathbf{c} \times \mathbf{a})n_2 + (\mathbf{a} \times \mathbf{b})n_3] \\
&= \mathbf{h}^{-1^t} \begin{pmatrix} n_1 \\ n_2 \\ n_3 \end{pmatrix} \\
&= \mathbf{h}^{-1^t}\mathbf{n}.
\end{aligned} \tag{3.42}$$

where n_i are integers. As a result of these definitions etc. calculation of quantities such as $\mathbf{k}_n \cdot \mathbf{s}_i$, which we will require for the evaluation of the reciprocal space part of the Ewald sum (equation 3.33), are greatly simplified when we use the cell frame representation of the ionic coordinates,

$$\begin{aligned}
\mathbf{k}_n \cdot \mathbf{s}_i &= \mathbf{h}^{-1^t} \begin{pmatrix} n_1 \\ n_2 \\ n_3 \end{pmatrix} \cdot \begin{pmatrix} s^i_x \\ s^i_y \\ s^i_z \end{pmatrix} \\
&= \mathbf{h}^{-1^t} \begin{pmatrix} n_1 \\ n_2 \\ n_3 \end{pmatrix} \mathbf{h}^{-1} \begin{pmatrix} l_1^{-1} \\ l_2^{-1} \\ l_3^{-1} \end{pmatrix} \cdot \begin{pmatrix} r^i_x \\ r^i_y \\ r^i_z \end{pmatrix} \\
&= \left(\frac{n_1 r_x}{l_1} + \frac{n_2 r_y}{l_2} + \frac{n_3 r_z}{l_3} \right). \qquad (3.43)
\end{aligned}$$

3.3.2 Treatment of velocities

We must now also consider how we are going to treat the other variables in this two-frame scheme. For example, it is clear that calculation of kinetic energies will depend on which reference frame is used for the ion velocities. We can apply the Velocity-Verlet algorithm unchanged to the velocities in the cell frame as we did for the positions. However, because the cell frame axes are not now generally orthogonal the kinetic energy is no longer simply.

$$T_{ion} = \frac{1}{2} \sum_i m_i (\mathbf{v}_i^{cell})^2, \qquad (3.44)$$

but the velocities must now be transformed into the orthogonal Cartesian frame. And so

$$T_{ion} = \frac{1}{2} \sum_i m_i (\hat{\mathbf{h}}^{-1} \mathbf{v}_i^{cell})^2 \qquad (3.45)$$

Since only the Cartesian form of all the interaction terms involving the additional degrees of freedom are required, these are all formulated in the Cartesian frame and their treatment remains unchanged from the cubic case.

3.3.3 A Fully Flexible Cell

The constant pressure method of Andersen [70] has been extended by Parrinello and Rahman [23] to allow the simulation box to change shape as well as size. This method is much more useful than an isotropic change as it will permit the study of systems which do not crystallise with a cubic unit cell. In the most flexible model the cell can undergo full relaxation in that both the cell lengths and angles may vary. However, in order to test aspects of the algorithm the method is constructed such that the isotropic fluctuations can be separated from the change in shape of the cell. In doing this we can use the same scheme to investigate isotropically flexible cells, orthorhombic cells (in which the cell angles are maintained at 90° but the cell lengths can vary anisotropically) and also the fully flexible cells already described. The method of Martyna *et al* [71] makes it possible to separate out the isotropic fluctuations from changes of shape of the cell. By introducing different masses for the momenta corresponding to the isotropic and anisotropic changes, different timescales can be associated with the two different fluctuations. This method requires the introduction of the volume normalized matrix of cell parameters

$$\mathbf{h}_0 = \frac{\mathbf{h}}{V^{1/3}}. \tag{3.46}$$

The equations of motion are then :

$$\frac{d\mathbf{r}_i}{dt} = \frac{\mathbf{p}_i}{m_i} + \frac{\mathbf{p}_{g_0}}{W_{g_0}}\mathbf{r}_\mathrm{i} + \frac{p_\epsilon}{W}\mathbf{r}_\mathrm{i}, \tag{3.47}$$

where p_ϵ is the barostat momentum, $\mathbf{p}_{g_0}$ are the cell parameter momenta and W and W_{g_0} are the mass parameters of the barostat and cell parameters respectively, and

$$\frac{d\mathbf{p}_i}{dt} = \mathbf{f}_i - \frac{\mathbf{p}_{g_0}}{W_{g_0}}\mathbf{p}_i - \left(1 + \frac{d}{N_f}\right)\frac{p_\epsilon}{W}\mathbf{p}_i - \frac{p_\xi}{Q}\mathbf{p}_i, \tag{3.48}$$

d is the dimensionality of the cell. For all the systems considered in this work $d = 3$. The cell volume obeys the equations of motion

$$\frac{dV}{dt} = \frac{dVp_\epsilon}{W}, \tag{3.49}$$

$$\frac{dp_\epsilon}{dt} = dV(P_{int} - P_{ext}) + \frac{d}{N_f}\sum_{i=1}^{N}\frac{\mathbf{p}_i^2}{m_i} - \frac{p_\xi}{Q}p_\epsilon, \tag{3.50}$$

where P_{int} is the instantaneous pressure and is given by the trace of the stress tensor (see below) and is equal to $\mathrm{Tr}[\mathbf{P}_{int}]$. P_{ext} is the desired external pressure at which the simulation should proceed. The variables which control the shape of the cell are given by:

$$\frac{d\mathbf{h}_0}{dt} = \frac{\mathbf{p}_{g_0}\mathbf{h}_0}{W_{g_0}}, \tag{3.51}$$

$$\frac{d\mathbf{p}_{g_0}}{dt} = V(\mathbf{P}_{int} - \mathbf{I}P_{ext}) - \frac{V}{d}Tr[\mathbf{P}_{int} - \mathbf{I}P_{ext}]\mathbf{I} - \frac{p_\xi}{Q}\mathbf{p}_{g_0}, \tag{3.52}$$

where $\mathbf{P}_{int}$ is the pressure (or stress) tensor. The fluctuations in the cell dimensions affect the equations for the Nosé-Hoover thermostat, which become

$$\frac{d\xi}{dt} = \frac{p_\xi}{Q}, \tag{3.53}$$

$$\frac{dp_\xi}{dt} = \sum_{i=1}^{N}\frac{\mathbf{p}_i^2}{m_i} + \frac{p_\epsilon^2}{W} + \frac{1}{W_{g_0}}Tr[\mathbf{p}_{g_0}^t\mathbf{p}_{g_0}] - (N_f + d^2)kT. \tag{3.54}$$

In order to complete these equations, we need an expression for the stress tensor. This is non-standard, since the 'additional' variables (dipoles *etc.*) of the extended ionic model play a role, in addition to the pairwise additive forces which have been considered previously. It will be considered in a separate section below.

The equations are integrated using the Velocity-Verlet algorithm. The resulting expressions, directly implemented in the simulation code, are derived in Appendix B.

3.3.4 Elimination of cell rotations

Since the equations of motion were derived using the full cell matrix, $\hat{\mathbf{h}}$, then, as shown by Nosé [63] the simulation cell can rotate in space. Clearly this rotation is undesirable and can cause problems in the results produced. This rotation stems from the pressure tensor, and the fact that is it not constrained to be symmetrical. Thus at any point in time if the pressure tensor is unsymmetrical the cell will experience a torque causing it to rotate. To overcome these problems we have chosen to work with the symmetrized tensor $P_{\alpha\beta} = (P_{\alpha\beta} + P_{\beta\alpha})/2$. Now if the total angular momentum of the cell is initially zero, it will not rotate.

3.4 The Stress Tensor within the PIM

In order to complete the prescription of the variable cell method, we need an expression for the stress (or pressure) tensor. The stress tensor is useful in other contexts. The sum of its diagonal elements is the pressure of the system, and the time correlation functions of its components may be used to calculate the viscosity.

The stress tensor is given by [66, 72]

$$(P_{int})_{\alpha\beta} = \frac{1}{V}\left[\sum_{i=1}^{N} \frac{(p_i)_\alpha (p_i)_\beta}{m_i} + \Pi_{\alpha\beta} V\right], \tag{3.55}$$

where Π is the 'configurational' contribution, arising from the interionic interactions. The trace of the stress tensor gives (three times) the instantaneous value for the pressure of the system. The configurational contribution to the stress tensor may be evaluated from the change in potential energy of the system under a general strain, *i.e.* [69]

$$-\frac{\partial U}{\partial h_{\alpha\beta}} = \sum_{\gamma} \Pi_{\alpha\gamma} V h^{-1}_{\beta\gamma}, \tag{3.56}$$

where, in the PIM, U is the instantaneous potential energy of equation 3.1, with the modified charge-dipole interaction tensor to allow for induction damping. (equation 3.25).

Evaluation of the contribution to $\Pi_{\alpha\beta}$ of the parts of U described by the simple pair potential is straightforward [66, 72]:

$$\Pi_{\alpha\beta} = -V^{-1} \sum_i \sum_{j<i} r_{ij,\alpha} \frac{\partial U_{sr}(r_{ij})}{\partial r_{ij,\beta}}. \tag{3.57}$$

However, the evaluation of the contribution of the remaining terms, which involve the interactions of the charges and dipoles, presents a greater problem. Firstly, these interactions are of long-range and are treated with Ewald summation methods in the program. This leads to considerable algebraic complexity to establish the appropriate expressions, which is dealt with in Appendix C. Secondly, there is a point of principle arising from the way in which we consider the *additional degrees of freedom* to be affected by the strain on the simulation cell. That is, in evaluating equation 3.56 in the PIM, how is the derivative of the dipole moment with respect to the elements of the cell matrix to be handled? The answer is that such derivatives are to be ignored, the derivative only acts on the ionic positional variables. The reason is that because their values are determined by the variational principle (equations 3.3 and 3.4) they are wholly determined by the ionic positions and are not independent variables. This result is analogous to the Hellmann-Feynman Theorem of quantum mechanics where, in evaluating the force in a (variational) electronic structure calculation (which involves the derivative of the expectation value of the Hamiltonian with respect to the atomic position), one neglects the derivative of the wavefunction with respect to the ionic position and simply evaluates the expectation value of the derivative of the Hamiltonian.

The resulting contributions to the stress tensor are listed in Appendix C.

Chapter 4

Modelling the Crystal Phase: Alkali Halides

4.1 Introduction

In this chapter, the use of computer simulation methods to study crystallographic phase transitions will be exemplified. As will be seen, reproducing the thermodynamic conditions under which a phase transformation is observed is a very demanding requirement for an interaction potential, and will be of great utility in devising improved potentials for the simulation of MCl_3 systems. Furthermore, the study of the mechanism of solid-state phase transformation by computer simulation with realistic potentials is in its infancy and we hope to illustrate the potential of the methods which have been developed in this work. The standard problem is that the boundary conditions introduced in simulations to eliminate surface effects prevent the transformation from taking place. Here, the focus will be on alkali halide systems, where the structural changes are relatively simple to understand. The study of these simple systems was undertaken to test the Parrinello-Rahman constant-stress method, developed as described in the preceding chapter. Application of this method to the MCl_3 crystals will be described in chapter 6.

4.2 Alkali Halides: Background

4.2.1 Alkali halide crystal structures

Systems of stoichiometry MX may adopt a wide range of possible structures. In the cubic symmetry the three most common structures are the zinc blende (4 coordinate anions and cations), NaCl (6-coordinate) and CsCl (8-coordinate), termed B3, B1 and B2 respectively. These three structures are shown in figure 4.1.

In this chapter we shall consider in detail two pressure driven phase transitions between these structures. In the first case the B1→B2 (6→8 coordinate) transition will be investigated followed by the B3→B1 (4→6 coordinate) transition. We choose to follow two transitions as it is anticipated that the two mechanisms may be very different and, as a result, provide stern tests of the Parrinello-Rahman technique developed in chapter 3. To study these transitions two RIM pair-potentials, for CsCl and LiCl [33,34] respectively, will be considered which predict the B1 and B3 crystals respectively as ground states. Although both are at odds with the experimental structures (for reasons discussed in chapter 5) they have relatively easily accessible higher coordinate structures.

4.2.2 Pressure of Transition

A thermodynamic phase transition occurs when the free energy of two phases is the same at a given pressure (P). For example, for a B1→B2 transition

$$G^{B1}(P) = G^{B2}(P). \tag{4.1}$$

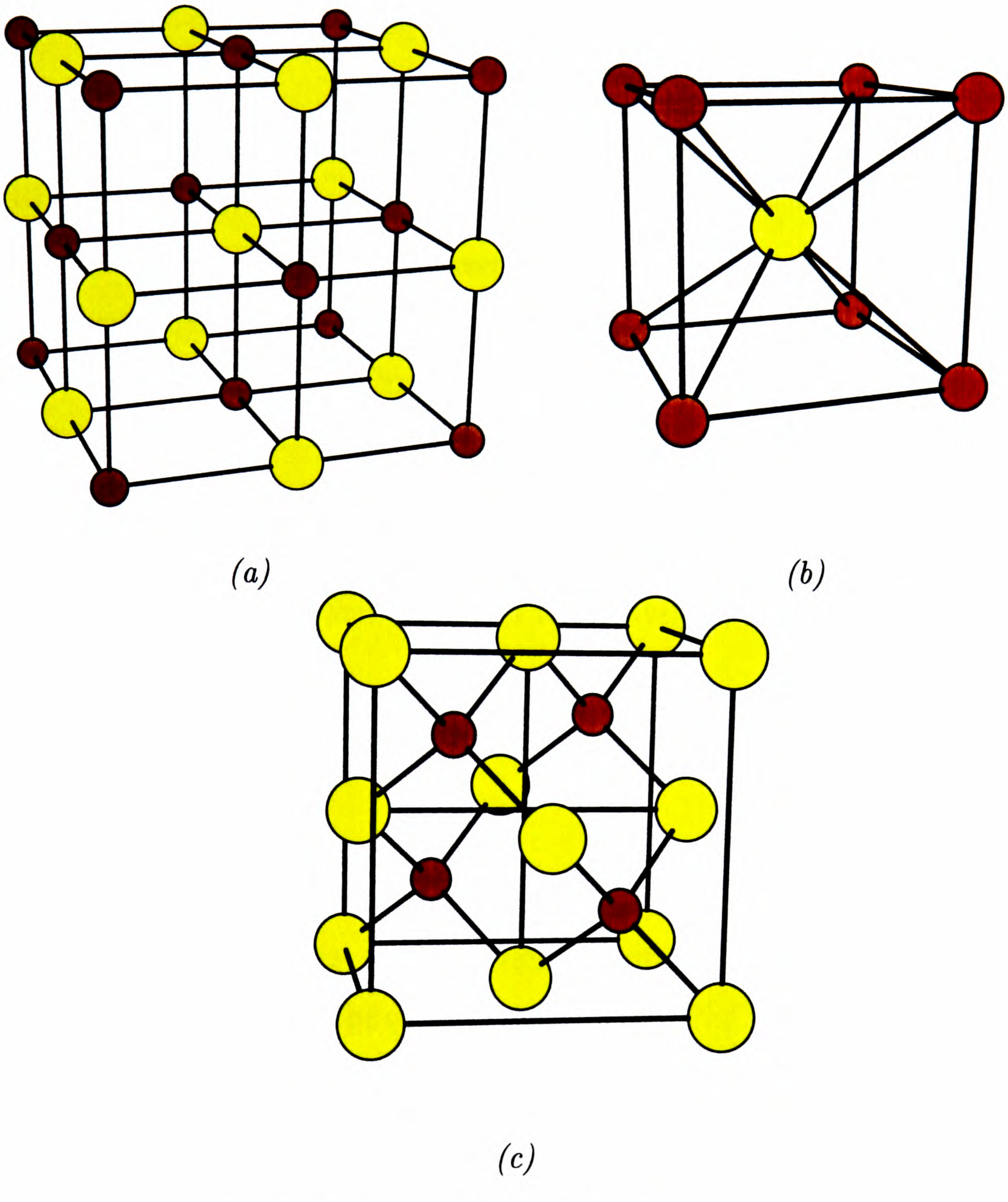

Figure 4.1: *(a) B1 (b) B2 and (c) B3 Crystal Structures*

At absolute zero the enthalpy, H, and Gibbs free energy, G, are equivalent.

$$G(P) = U^{crys}(V_m) + PV_m, \tag{4.2}$$

where P is the system pressure and V_m the volume which minimises the free energy at this pressure, *i.e.* at which

$$P = -\left(\frac{\partial U^{crys}}{\partial V}\right)_{V=V_m} \tag{4.3}$$

Thus from energy-volume curves we can obtain the free energy as a function of pressure for the two phases of interest. The point at which the lines representing each phase cross gives the transition pressure.

Results for the internal energy *vs.* volume for the B1, B2 and B3 phases of CsCl and LiCl obtained with the literature Sangster and Dixon and Fumi-Tosi [34] RIM potentials are discussed below. These results were obtained from single point energy calculations at a series of volumes on systems of 512, 432 and 512 ions for the B1, B2 and B3 phases respectively in cubic periodic boundary conditions.

4.3 CsCl

The crystal energies plotted against volume for both the B1 and B2 phases of CsCl are shown in figure 4.2. The experimental cell volume [73] and lattice energy [56] are shown by the dotted lines. The B1 (NaCl, 6-coordinate) phase is seen to have a lower energy at the minimum than the observed B2 (8-coordinate) phase. We therefore see that this RIM potential predicts the wrong ground state crystal structure, a deficiency which will be discussed further in chapter 5.

For our current requirements, however, we can use this RIM to investigate the nature of the B1→B2 phase transition in the variable cell. Since the minimum energy of the B2 phase of CsCl is at a lower volume and a higher energy than the B1 phase, then a pressure driven transition may occur. From the free energy-pressure curve (figure 4.3) the transition from the B1 to the B2 phase is predicted to occur at 0.14GPa.

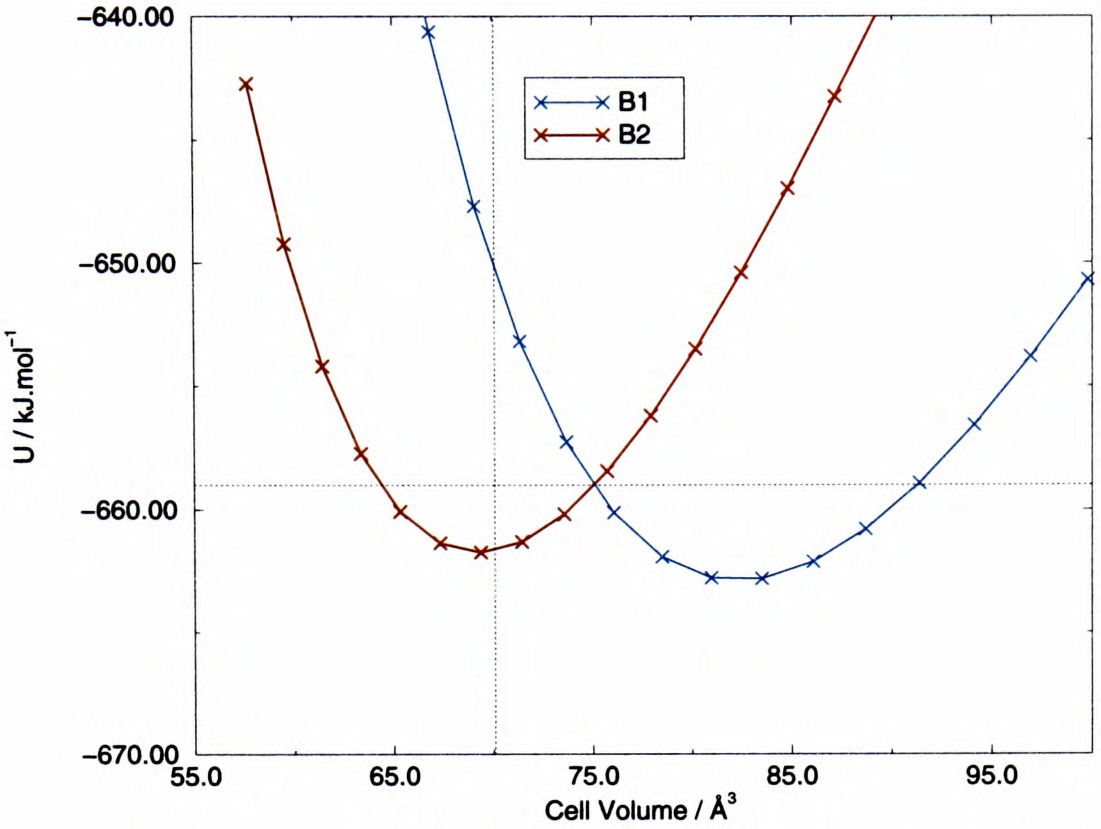

Figure 4.2: *Energy-Volume curves for the B1 and B2 phases of CsCl, calculated using the Fumi-Tosi RIM potential.*

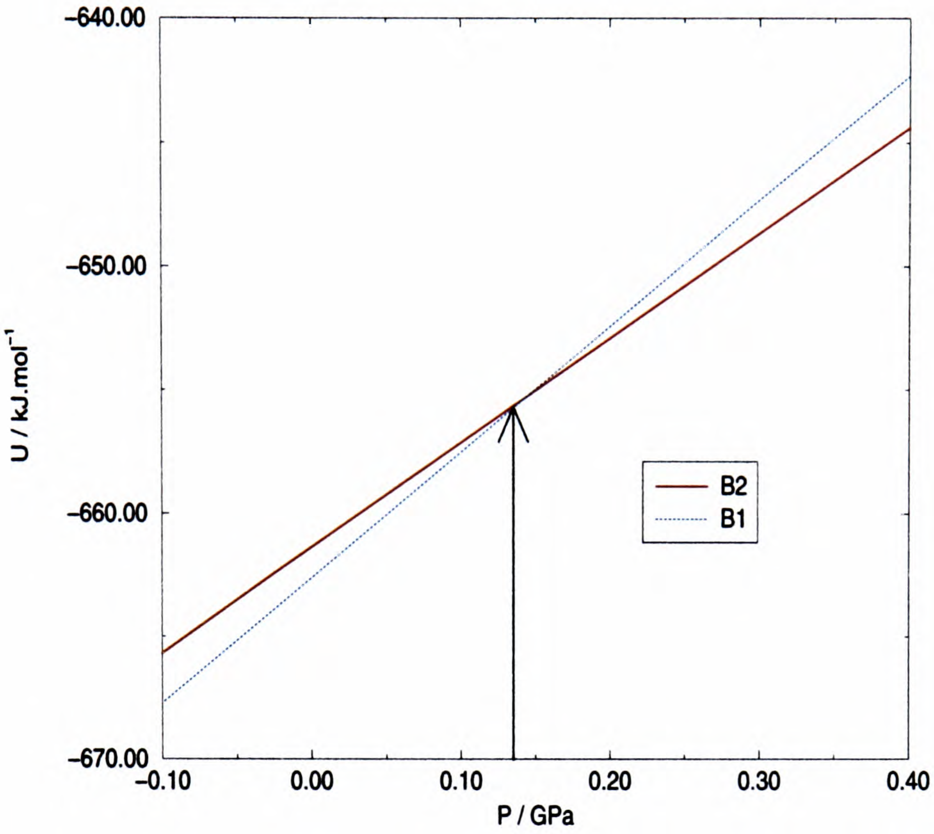

Figure 4.3: *Free energy vs. pressure for the B1 and B2 phases of CsCl calculated with the RIM*

4.3.1 B1→B2 Pressure Driven Transition

A possible theoretical transformation mechanism for the B1→B2 phase transition can be understood by considering figure 4.4. The B1 structure has space group $Fm3m$ whilst the B2 has the space group $Pm3m$ and so they share a subgroup of $Rm3m$ symmetry. The distorted B2 unit cell can be readily identified in figure 4.4 inherent in the unstrained B1 lattice. As a result, a uniform stretching transformation along the 111 direction (from corner to corner in the figure) will give a Martensitic transformation between the two phases [74]. In the simulation, a positive pressure of 3GPa is applied to the CsCl RIM in the B1 structure (with an initial volume of 83Å^3 per molecular unit) and the structure allowed to evolve. The ion velocities are initially selected from a Gaussian distribution.

The progression of the phase transition can best be monitored in terms of the evolution of the cell shape as indicated by the cell angles and boxlengths (initially 90° and 14.69Å for the 512 ion B1 starting condition). Figure 4.5 shows how these quantities vary over around 18ps (50000 steps) of molecular dynamics. In the first 4ps of the simulation the cell angles and box lengths are fixed to allow for suitable equilibration of the crystal at a temperature of 100K. At 4ps the cell is allowed to fluctuate isotropically, that is, the cell angles remain fixed at 90° whilst the boxlengths are free to change. The isotropic barostat mass (*i.e.* W in equations 3.47 *et seq.* is 10000au). During this time the fluctuations in boxlength are small with no hint of any underlying phase transition when the cell geometry is constrained in this fashion. At around 6.0ps the full cell relaxation is switched on (with W_{g0}=10000au) and the boxlengths become systematically reduced by ~4% during which the cell angles begin to fluctuate. At ~6.5ps a rapid transformation occurs in that the 3 cell angles and the boxlengths separate. After a further ~10 ps the cell angles settle to give a triclinic cell with two of these angles at 110° and one at 70° with boxlengths of 25.95Å and 27.52 Å. This corresponds to a volume of 64 $Å^3$ per molecular unit. Figure 4.6 shows molecular dynamics snapshots of the simulation cells at the beginning and end of this run. In 4.6(a) the viewpoint is looking directly at a face of the $Rm3m$ sublattice as highlighted in figure 4.4. In this projection these faces appear as diamonds with four cations at the corners (red circles) and an anion (yellow circles) at the diamond centre. The effect of the pressure on the B1 starting configuration is to cause a compression of such diamonds along the two directions bisecting the acute (60°) angle in figure 4.6(a). The resulting, near square, units can clearly be seen in figure 4.6(b). Analysis of the coordination numbers and pdfs shows this high pressure phase to be a slightly distorted B2. The bondlengths have increased by ~ 3%, consistent with the volume change predicted by figure 4.5. The final cell angles of ~ 70° and 110° are slightly different from the 60°, 120° which would be expected for an ideal B2 crystal from figure 4.4, reflecting the slight defect structure of the final B2 phase.

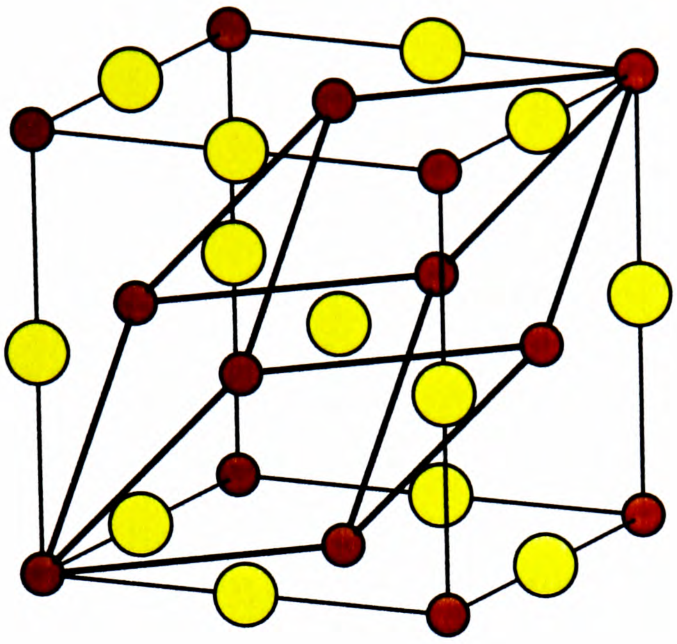

Figure 4.4: *NaCl (B1) Crystal Structure showing subcell of Rm3m symmetry. Note that the latter is like the B2 unit cell elongated along diagonally opposite corners.*

The initial system size of 512 ions (256Cs^+ and 256 Cl^- ions) is commensurate with an ideal B1 structure with four unit cells along each cube axis. However, the nearest sized B2 cell consists of six 2 ion unit cells per side giving 432 ions in total. As a result, the final structure in figure 4.6(b) contains some defects which account for the slight deviations from the ideal angles. However, the bulk of the formed structure is clearly B2.

4.4 LiCl

Having studied the largest experimentally accessible alkali halide, we now move on to consider the smallest – LiCl. Here, again the Fumi-Tosi RI potential (table 5.1) fails to predict the correct ground state structure, instead predicting the 4 coordinate blende structure (B3) (figure 4.1(c)) to be the most stable. The massive destabilization of the 8 coordinate B2 phase, compared with the relative stabilization of the 4 coordinate with respect to the 6 can be understood purely in terms of relative sizes of the Li^+ and Cl^- ions compared with respect to Cs^+

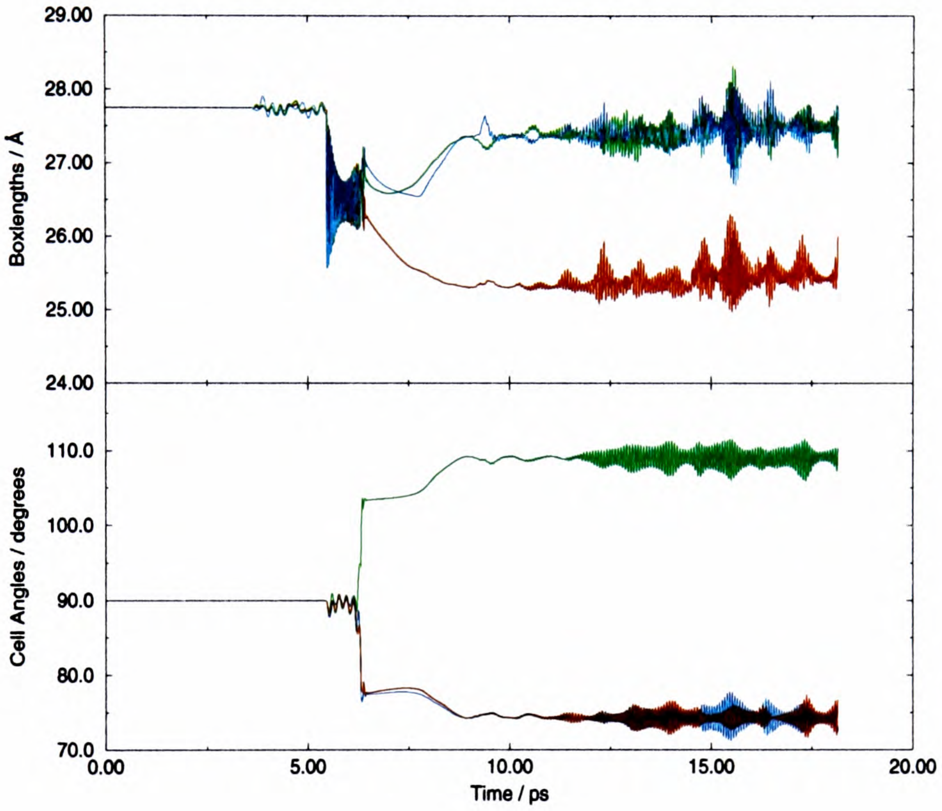

Figure 4.5: *Variation of boxlengths and cell angles for B1→B2 transition in CsCl calculated with the RIM*

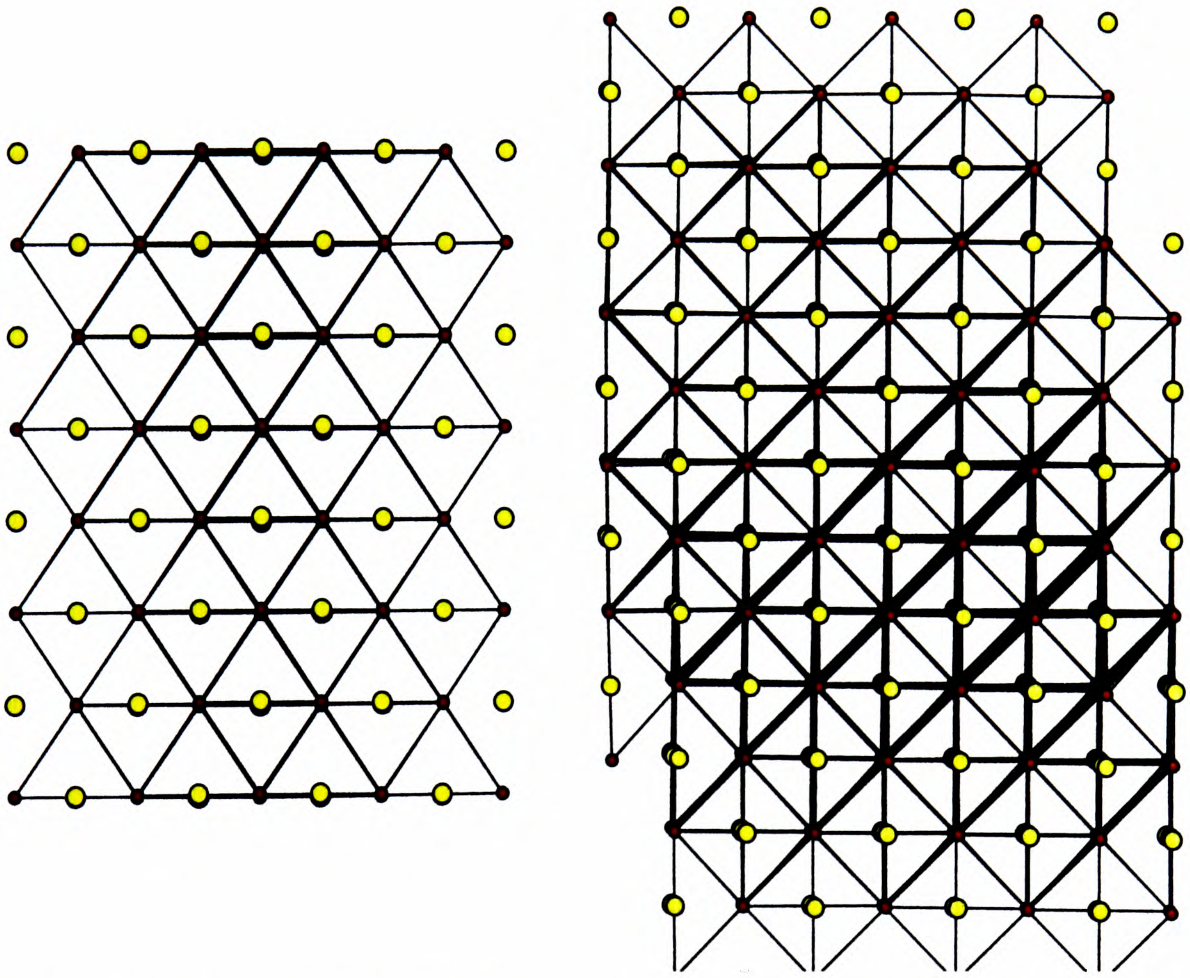

Figure 4.6: *Schematic of B1→B2 phase transition in CsCl calculated with the RIM. (a) Initial B1 structure (b) Structure after transition*

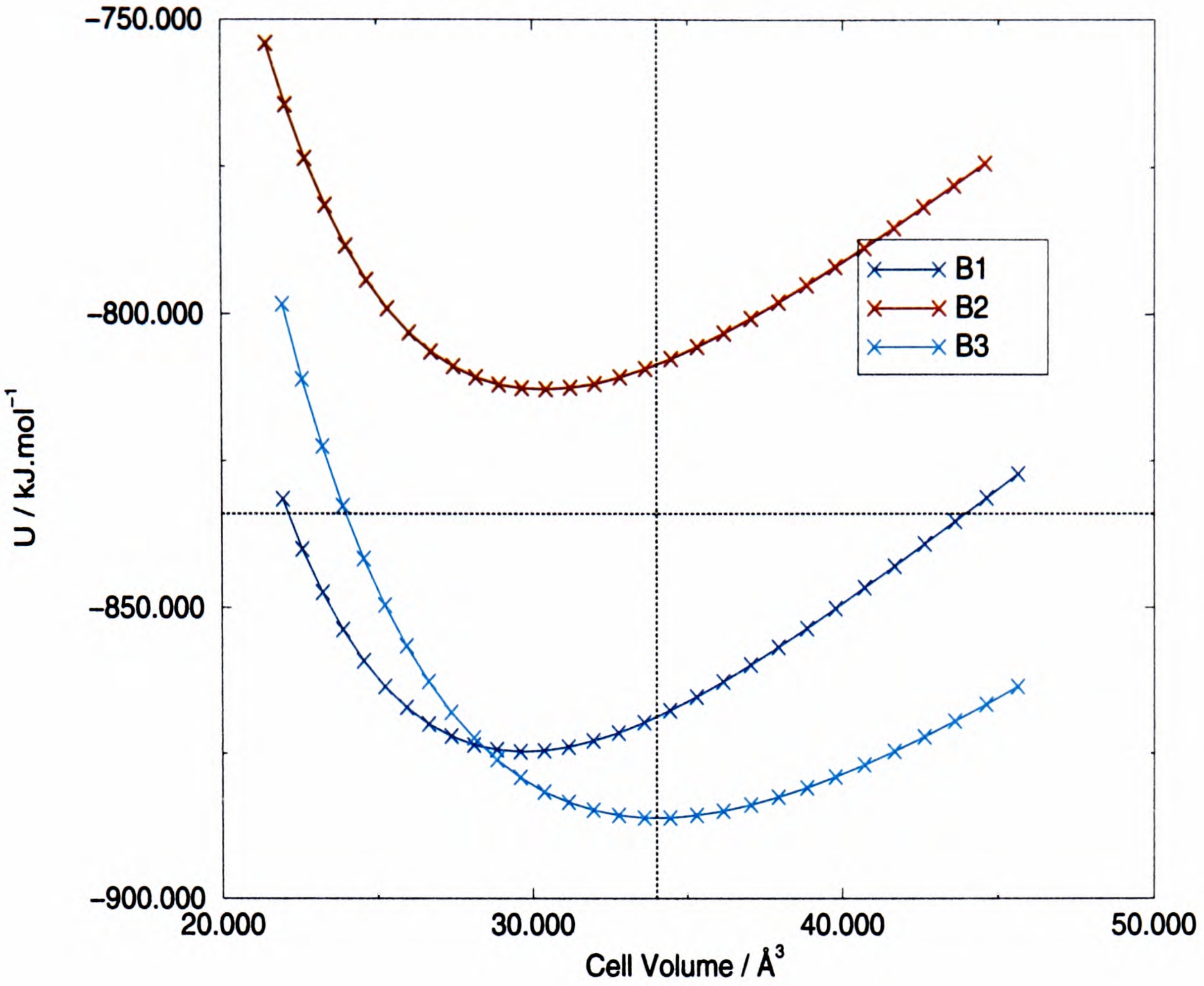

Figure 4.7: *Energy-Volume curves for the B1, B2 and B3 phases of LiCl using the RIM*

and Cl$^-$. In order to see the possible effect of the simulation model on the transformation mechanism the B3→B1 transition is studied using both a RIM and PIM.

4.4.1 B3→B1 pressure driven transition with the RIM

The crystal energies as a function of volume for the three crystal structures B1, B2 and B3 are shown in figure 4.7. As well as the RIM potential predicting the wrong ground state structure (B3 rather than B1) the predicted cell volume and lattice energy of the B1 phase are much lower than the experimental values (shown by the dotted lines in figure 4.7) [73] [56].

From the differential of the energy-volume curves the calculated pressure neccesary to drive the transition for B3 to B1 is found to be 5.3GPa. Using the Parrinello-Rahman ensemble (section 3.3.3) with a pressure of 17.7GPa resulted in the transition from the B3 to the B1 phase taking place. The initial B3 crystal consisted of 512 ions (256 Li^+ and 256 Cl^-) in a cubic simulation cell with boxlengths of 20.49Å. The volume of a single LiCl unit is thus 33.60Å^3. The barostat masses (W and W_{g0}) in this case were both 50000au. The simulation procedure was as for the B1→B2 transition. The resulting simulation cell had two angles of 90° and one of 84° and boxlengths of 21.4, 14.5 and 19.3 Å giving a volume of a single LiCl unit to be 23.49 Å^3. The almost cubic nature of the transformed cell is due to the number of ions involved (512) being commensurate with an ideal B1 and B3 simulation cell.

From a theoretical viewpoint, the mechanism of the B3→B1 transition is more complicated than the pure uniform strain by which the B1→B2 is accomplished. In the B3 structure, the cations occupy half of the tetrahedral holes in the close-packed cubic anion sublattice, whereas in the B1, they occupy the octahedral holes. In effect, the transition appears to require a translation of one sublattice with respect to the other [75]. Figure 4.8 show snapshots of the simulation cell during the B3→B1 transformation. On completion of the phase transition (figure 4.8(d) and 4.9) the fully transformed structure can be seen to have a grain boundary structure. We may trace the transition as follows: the anions and cations in the planes labelled **A** and **B** in figure 4.8(a) become coplanar by a movement indicated by the arrows. If we look along the directions of these coplanar displacements (fig 4.10) we see a second (simultaneous) distortion in which the square labelled **CDEF** distorts to become rectangular with **CD**>**DE**. Grain boundaries are formed as the whole cell is unable to undergo a fully concerted transition. As can be seen in figures 4.8 and 4.9 the B3→B1 transition occurs in the centre of the block shown with the resulting stress fields dissipated by the formation of grain boundary structures.

The region where the grains join in the resulting structure (figure 4.9) can be clearly picked out. The lattice of the two grains can be made to coincide by

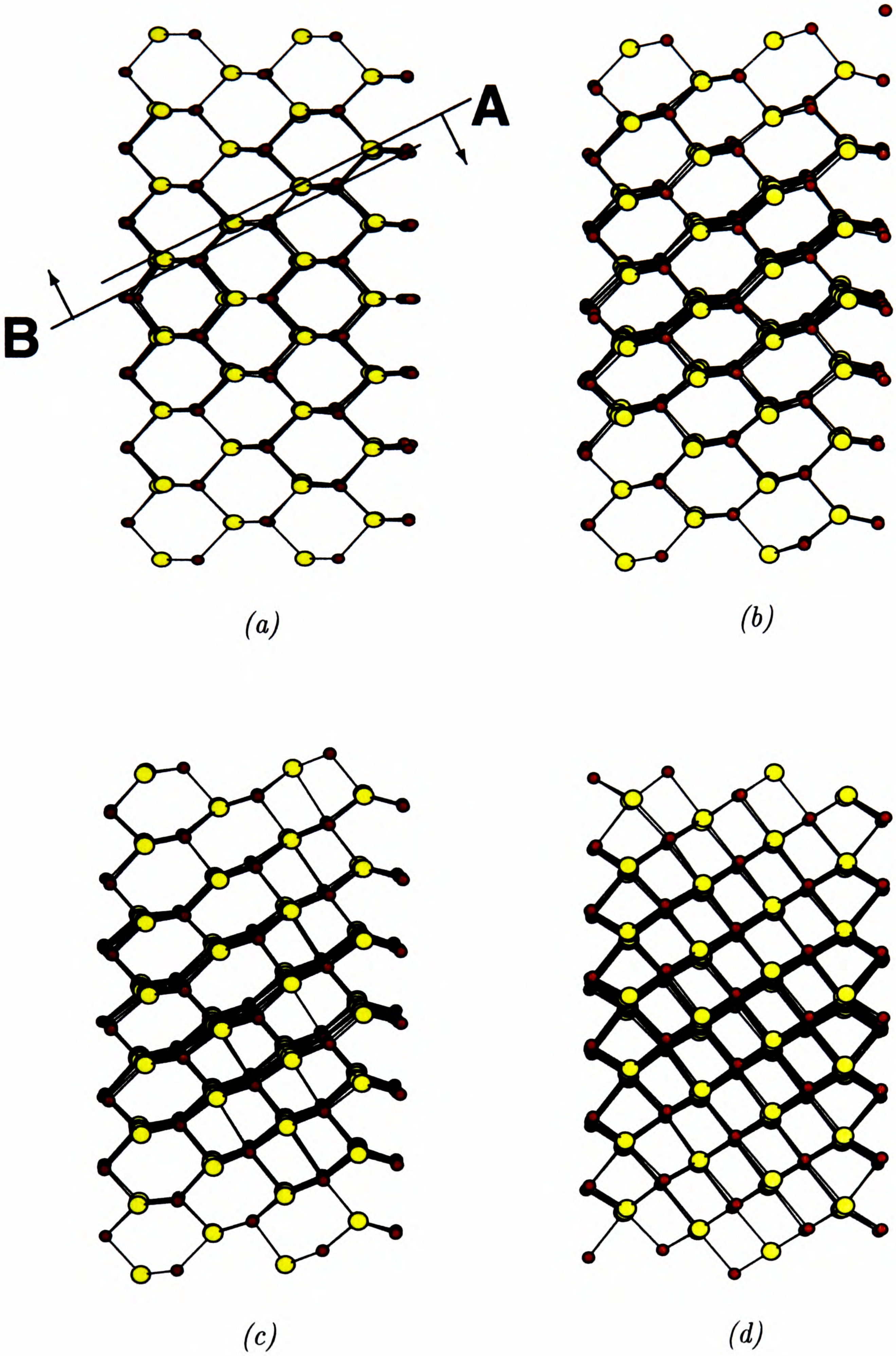

(a) (b)

(c) (d)

Figure 4.8: *B3→B1 transition in LiCl using the RIM*

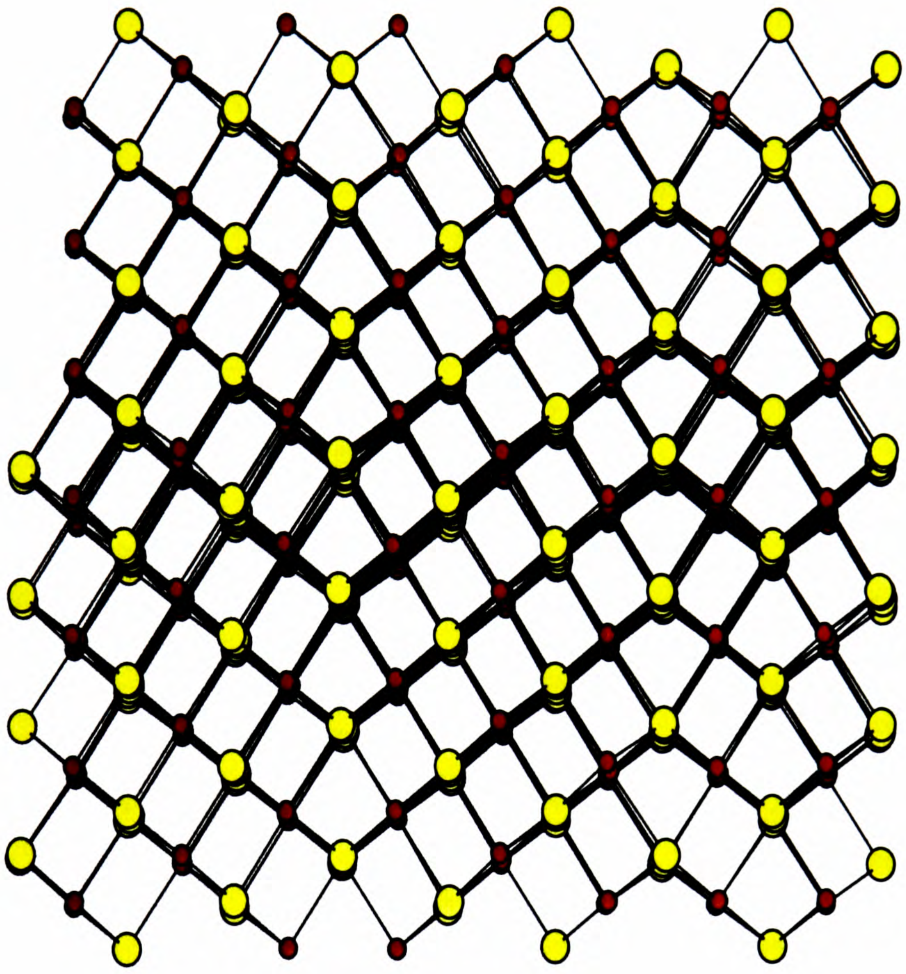

Figure 4.9: *Transformed phase after applying a pressure of 17.7 GPa to LiCl (B3) using the RIM*

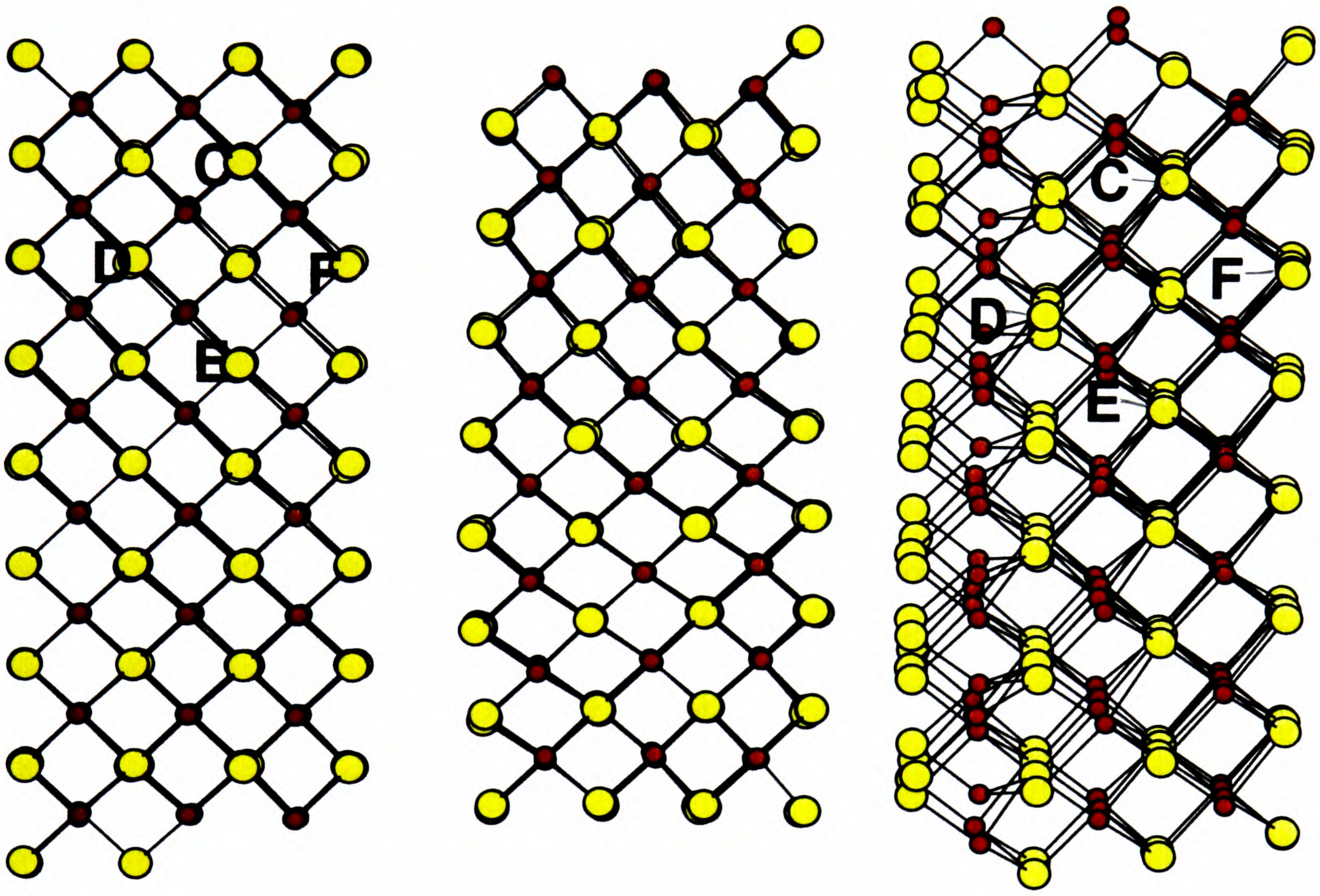

Figure 4.10: *B3→B1 transition in LiCl using the RIM. The angle of view is perpendicular to the planes* **A** *and* **B** *in figure 4.8*

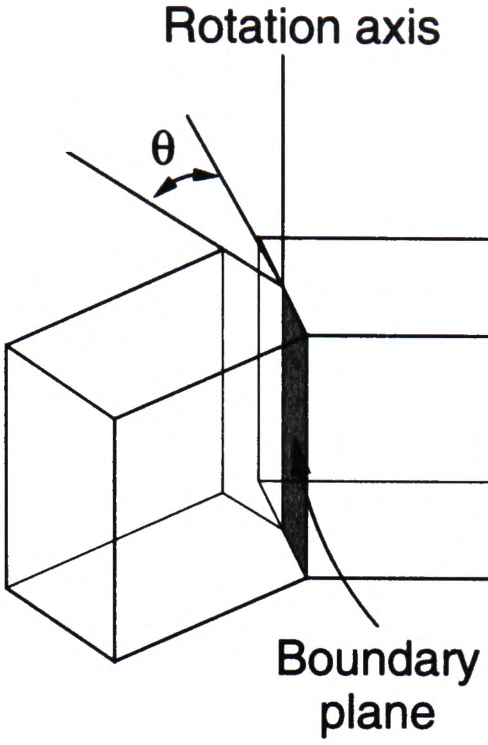

Figure 4.11: *Schematic showing the formation of a pure tilt grain boundary*

rotating one of them through a suitable angle about a *single* axis. Such a grain boundary is termed a pure tilt boundary and occurs when the axis of rotation is parallel to the plane of the boundary (figure 4.11). When θ >10-15° the boundary is termed a high-angle grain boundary. In such distortions there are often large areas of poor fit and the bonds between atoms are generally highly distorted. These are known as random high angle boundaries. The one observed for LiCl, however, has relatively little distortion of the interatomic bonds and will have a significantly lower energy than random boundaries. The boundary is between two twins and the boundary is parallel to the twinning plane. This is known as a *coherent twin boundary* [76]. As can be seen in figure 4.9 there are a total of three of these boundaries present. The twins arise because in the initial stages of the mechanism, there is an arbitrary choice amongst several orientations of cation-anion layers as to which will become planar.

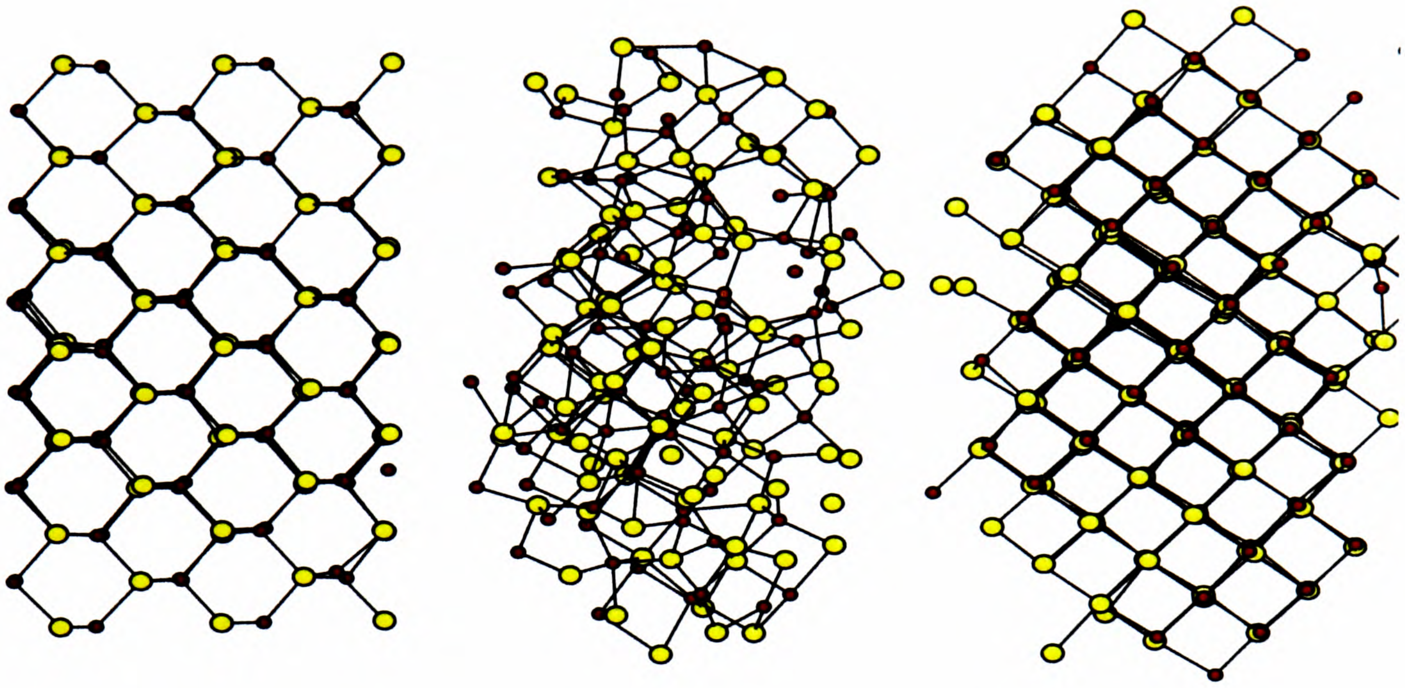

Figure 4.12: *Evolution of B3→B1 transition in LiCl using the PIM. The angle of view is the same as that in figure 4.8*

4.4.2 B3→B1 transition with the PIM

In order to illustrate the concept that changing the potential could affect the mechanism of the phase transition, a further simulation was attempted under identical conditions except that anion polarization effects were also included in the interaction model (PIM). The inclusion of polarization effects would be expected to lower the energy of asymmetric coordination structures around the anion, opening up the possibility that the transition occurs *via* a different intermediate state. This appears to be what is seen in the simulation. In the PIM simulation the crystal appears to melt (characteristic of a pressure driven amorphisation) from the B3 phase and then recrystallises to give the B1 phase (figure 4.12). Interestingly, the final B1 structure does not appear to exhibit any grain boundaries, indicating a far less concerted mechanism than for the RIM transition. The final cell angles in this case are 94, 95 and 98° with boxlengths of 16.9, 19.0 and 19.6 Å^3 giving a volume of 23.9Å^3 for each LiCl unit.

4.5 Conclusion

The study of both the B1→B2 and B3→B1 pressure driven phase transitions demonstrates the effectiveness of the Parrinello-Rahman method developed in chapter 3 in the study of the detailed underlying mechanisms. The two transitions studied appear to have very different underlying mechanisms. Furthermore, the mechanism for the B3→B1 transformation appears to change with the inclusion of polarization effects which act to stabilize more asymmetrical (intermediate) structures. Despite these differences the Parrinello-Rahman method manages to reproduce the transitions. Furthermore, the use of the Parrinello-Rahman techniques will allow us to confirm that a proposed low energy structure is stable against transformation to a different (not considered) phase.

Now that the constant stress ensemble has been successfully tested on the alkali halides we will, in chapter 6, attempt to model a crystal-crystal phase transition in a trivalent metal halide.

Chapter 5

Development of Potential Models

5.1 Introduction

In chapter 1 we saw that whilst the potential model qualitatively reproduced the evolution of liquid structure of the MCl_3 systems with changing cation size, it failed to accurately predict the structure factors, particularly for cations of intermediate size. While the large scattering angle predictions were generally good, the prediction in the region of the principal peak (and pre-peak for $ScCl_3$) were far from satisfactory. Additionally, in chapter 2 we saw that the model did not predict the correct ground state crystal structures to be the most stable (except for YCl_3). There was a clear tendency to overestimate the stability of lower coordinated structures than those observed.

In this chapter the focus will be on improving the potential used. Possible improvements include

(1) allowance for the compressibility of the anions, as outlined in the Introduction and

(2) a re-evaluation of the anion-anion potential used.

The model used so far neglects the breathing and shape deformation effects which have been found necessary to account for the properties of oxides [60].

These effects stabilise the more tightly bound, higher coordination number crystal structures relative to predictions with simple pair potentials, and this might well improve the crystal structure predictions. The degree of compression could itself depend on the cation size, so that effectively smaller anions would be found in the small cation systems. Evidence for a possible need to treat the chloride ions as compressible comes from a comparison between the positions of the second peaks (corresponding to the Cl-Cl separation) in $G_{TOT}(r)$ for $LaCl_3$, YCl_3 and $ScCl_3$ in figures 1.8, 1.10 and 1.12. In the simulation, this peak remains in the same position in all three systems, whereas in the experimental total pdfs, the corresponding peak appears to shift to smaller r. Thus, it seems that the effective Cl^- ion size is decreasing in the smaller cation systems.

The short-range anion-anion potential merits scrutiny for the same reason. In most halide systems which have been studied intensively (primarily of MX stoichiometry), the average anion-anion separations are sufficiently large that this interaction has little influence on the material properties. Consequently it has not been optimised in work done to date (the Fumi-Tosi parameters, for example, were obtained by empirical fits to the properties of alkali halides). Values of the potential parameters used in equation 5.1

$$u_{ij}(r_{ij}) = \frac{Q_i Q_j}{r_{ij}} + B_{ij} e^{-a_{ij} r_{ij}} - \frac{C_{ij}^6}{r_{ij}^6} - \frac{C_{ij}^8}{r_{ij}^8}. \tag{5.1}$$

for two such pair potentials (Sangster and Dixon, and Fumi-Tosi) are listed in table 5.1 - the large difference between the anion-anion terms for the two parameterizations of NaCl is noteworthy.

However, in MX_3 materials, where the stoichiometry dictates that there must be many anion-anion 'contacts', it is possible that this potential will begin to influence the structure. Although the calculated and experimental *partial* structure factors (where available) seem generally good [47, 77], the predicted total structure factors, where cancellations between different partials are paramount, are less good. This indicates that there are small shifts in the relative positions of the peaks in the different partials, which are not being replicated in the simulations. The good prediction of the position of the M-Cl peak and the relatively bad prediction of the position of the Cl-Cl peak in the total neutron weighted pdfs for $LaCl_3$, YCl_3 and $ScCl_3$ (figures 1.8, 1.10 and 1.12) suggests that these discrepancies are in the Cl-Cl interactions rather than the M-Cl interactions.

No information is available at an *ab-initio* level on the short-range interactions in condensed phase MX_3. The primary difficulty is that the low site symmetry in the crystals means that polarization effects strongly influence the energetics and the short-range interactions cannot be isolated. As a result we shall return to a consideration of interactions involving the chloride ion in the alkali halides where the relevant crystal structures are cubic in order to highlight the possible magnitudes of the two effects identified above. The starting point will be CsCl crystal calculations where *ab initio* information is available in two coordination environments.

5.2 Compression of ions

Experimentally, CsCl is known to adopt the 8-coordinate B2 structure (figure 4.1(b)). However, all the available CsCl pair potentials predict the incorrect bulk structure, putting the 6-coordinate rock-salt structure (B1) (figure 4.1(a)) lower in energy than the 8-coordinate CsCl (B2) [22]. May [78] found that the B2 phase could be stabilized with respect to the B1 structure only if the dispersion terms were taken to be much greater than those of Mayer [79], which are consistent with reasonable estimates from the ionic polarizabilities.

5.2.1 Relationship to *Ab-initio* data

Pyper [22] has recently performed *a priori* calculations of the inter-ionic interactions in both the 8 and 6-fold coordinated phases of CsCl. The crystal is

au	NaCl(SD)	CsCl(SD)	NaCl(FT)	LiCl(FT)
a_{--}	2.2265	1.8586	1.670	1.55
B_{--}	14887.169	973.774	128.502	61.660
C_{--}	165.762	165.762	165.762	115.987
a_{+-}	2.2265	1.8586	1.670	1.55
B_{+-}	532.655	853.050	46.263	8.678
C_{+-}	13.137	143.28	13.137	2.090
a_{++}	2.2265	1.8586	1.670	1.55
B_{++}	17.867	700.587	15.615	1.1456
C_{++}	1.583	125.918	1.583	0.0763

Table 5.1: *Sangster and Dixon and Fumi-Tosi potentials for alkali halides*

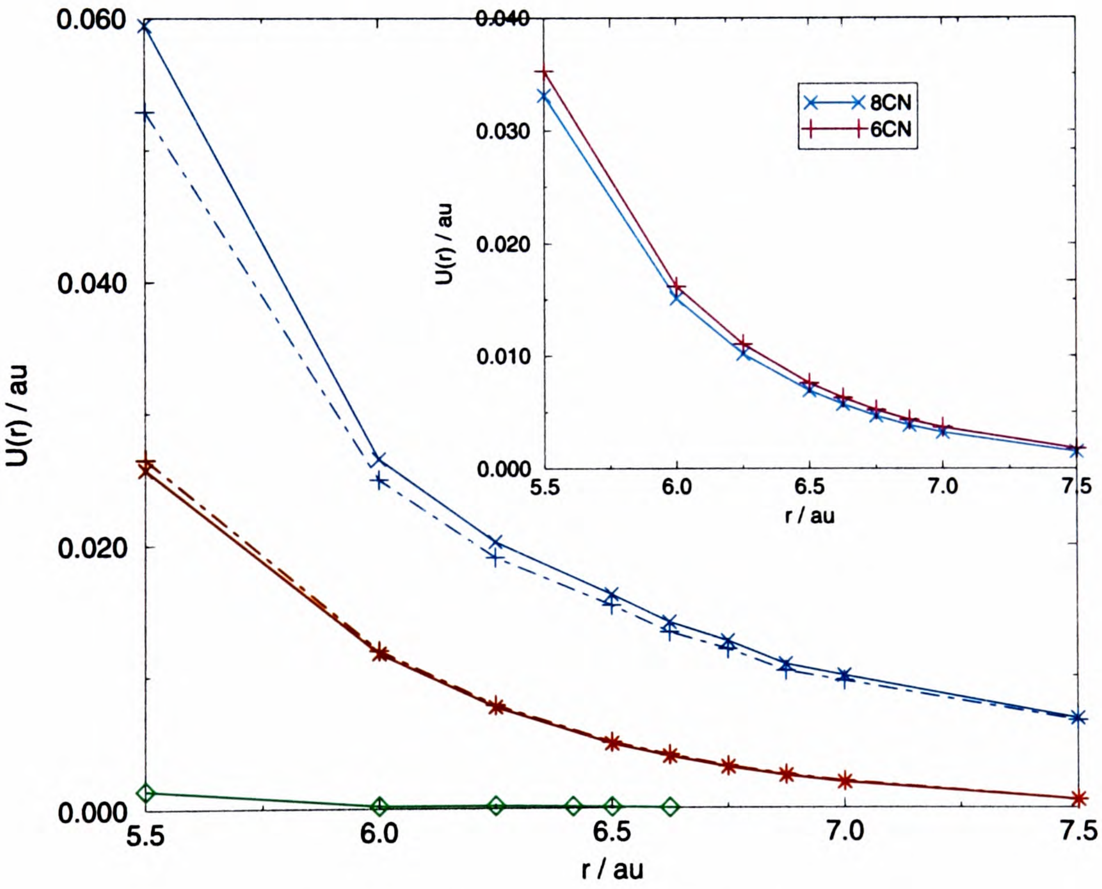

Figure 5.1: *Ab-initio data for the self energy of a chloride ion (red lines) and overlap energy (blue lines) as a function of the lattice parameter in 6 and 8 coordinate structures. Also shown is the frozen data for Cl-Cl (green lines). The inset shows the pair potentials calculated from this data for each structure.*

taken to be fully ionic *i.e.* its total electronic wavefunction is written as an anti-symmetrized product of the wavefunctions of the individual ions. There is abundant evidence that the properties of a cation with an outermost np^6 electronic configuration are unaffected by its environment in an ionic crystal.

Wavefunctions optimal for an anion in the crystal having a cation-anion spacing r were computed with a Dirac-Fock program, by adding the spherical confining potential discussed in the Introduction to the intra-anion electron-electron and electron nucleus interactions. The output of the calculation is thus the anion wavefunction appropriate to r and the corresponding energy – which is the energy, $E_{re}(r)$, required to create the ion in this crystalline environment – called the "rearrangement energy". As illustrated in the Introduction, E_{re} will be expected to vary with r and the coordination number. Using the optimised wavefunction appropriate to r, Pyper also calculates the energy associated with the overlap between the anion and cation charge densities; this is called the "overlap" energy, $E_{ov}(r)$. Both E_{ov} and E_{re} will increase with decreasing r and contribute to the repulsive energy that stabilizes the crystal. Results for both quantities for CsCl in the 8-coordinate B2 (CsCl) and 6-coordinate B1 (rocksalt) crystal structures are shown in figure 5.1. Note that the rearrangement energy makes a large contribution to the total repulsive energy, and *varies with coordination number.* This means that the effective repulsive interactions in the B2 and B1 structures are different.

It is instructive to use the *ab initio data* to produce an effective pair potential (EP) to describe the cation-anion interactions. For an ion-pair in the B2 phase

$$U_{EP}^{+-}(r) = \frac{8E_{ov}(r) + [E_{re}(r) - E_{re}(\infty)]}{8} = B_{EP}^{+-} e^{-a_{EP}^{+-} r}, \qquad (5.2)$$

where the factor of 8 is for the eight nearest neigbours in the B2 structure. Similarly the B1 structure *ab initio* data may be used to form a pair potential for the rocksalt structure. As illustrated in the inset to figure 5.1 the optimum pair potentials for the two crystal structures are seen to be different. It is to this

	a / au	B / au
Cl-Cl	2.409	5822.65
Cs-Cl	1.570	185.838
Cs-Cs	2.062	4978.31

Table 5.2: *EP potential parameters for the 8-coordinate CsCl from ab-initio data*

effect that Pyper attributes the failure of a *single* pair potential to reproduce the correct crystal structure for CsCl: in effect, such a potential fails to recapture the coordination number dependence of the rearrangement energy.

The *ab initio* data may be used to parameterize the Born-Mayer form of the short-range effective pair potential which may be combined with information on the dispersion interactions to predict the crystal energetics. Table 5.2 lists the parameters obtained in this way from U_{EP} from the B2 data for the Cs-Cl interactions.

Pyper also calculates an overlap energy between a pair of anion wavefunctions separated by distance r, this is a measure of the interion short-range term. The most consistent results are obtained by taking the anion wavefunction appropriate to the experimental lattice parameter r_e, irrespective of the interion separation, to give the so-called “frozen” Cl-Cl potential. Using the optimised wavefunction for r gives a potential for large r, which is attractive. This seems to be an artefact of the method, as the short-range interactions between a pair of Cl^- ions in the gas phase is repulsive at all separations [80]. The “frozen” data for the B2 structure has been fitted to a Born-Mayer form with the results shown in table 5.2.

The dispersion terms have also been parameterized by Pyper. The dipole-dipole and dipole-quadrupole dispersion interactions are damped as described in chapter 1. The dispersion terms parameterized from the *ab-initio* data are given in table 5.3.

	C^6 / au	b_6 / au	C^8 / au	b_8 / au
Cl-Cl	223.353	1.40	7568.0	1.35
Cs-Cl	164.976	1.55	5555.92	1.51
Cs-Cs	125.918	1.90	4077.99	1.80

Table 5.3: *Dispersion terms for CsCl parameterized from Pyper's ab-initio data*

The crystal energies plotted against volume for both the B1 and B2 phases of CsCl are shown in fig 4.2. The results are similar to those obtained with the literature Sangster-Dixon potential. The experimental cell volume [73] and lattice energy [56] are shown by the dotted lines. The B1 (NaCl) phase is seen to have a lower energy at the minimum than the B2 phase, incorrectly predicting the B1 phase to be the most stable. This shows that the anion-cation short range energy cannot simply be represented by a rigid ion Born-Mayer function to the accuracy required to predict the crystal structure of CsCl correctly. We need to investigate a more subtle representation which will allow for the coordination number dependence of the rearrangement energy.

5.3 Compressible Ion Model

To model this breathing of the ions we will implement the Compressible Ion Model (CIM). Initially we will consider both anion compression by cations and anion compression by anions. We anticipate that in light of the small anion-anion contribution to the total energy, that the effect of anion compression by anions will be very small.

To incorporate compressible ion effects into the molecular dynamics scheme, we must find a representation of them in terms of generalised ionic coordinates. In addition to the ionic positions, these coordinates must include suitable additional variables which specify the state of each ion in the environment in which it finds itself. The simplest representation is to express the internal state of each ion by a dynamical radius which adapts to the local structure. The instantaneous radius of each ion is expressed as

$$\sigma_i = \bar{\sigma_i} + \delta_i, \tag{5.3}$$

where δ_i gives the departure of the ion's radius from some fixed reference value $\bar{\sigma}_i$. The total short-range interaction energy of an ion i in a system of ions with coordinates $\{r_i\}_{i-1,N}$ and radii $\{\delta_i\}_{i-1,N}$ is expressed as

$$U^{sr} = \sum_{j<i} u_{ij}^{CI}(r_{ij} - (\sigma_i + \delta_i) - (\sigma_j + \delta_j)) + F(\delta_i), \tag{5.4}$$

where u_{ij} represents the pair overlap term and $F(\delta_i)$ the rearrangement energy - which is assumed to depend only on the ion radius. In a manner analogous to the dipoles in section 3.2 we must first determine the values of the ionic radii $\{\delta_i^{opt}\}_{i=1,N}$ that minimize U^{sr} before evaluating energies and forces.

5.3.1 Parameterization of a CI Potential

The *ab-initio* data are fitted using suitable functions for the chloride rearrangement energy and for the cation-anion overlap interaction. The functions used to fit the *ab-initio* data are

$$\begin{aligned} u_{CI}^{+-}(r_{ij}, \delta_i) &= (A^{+-}/r_{ij})exp[-a^{+-}(r_{ij} - \delta_i - \sigma_+)] \\ &+ (B^{+-}/r_{ij})exp[-2a^{+-}(r_{ij} - \delta_i - \sigma_+)] \\ &+ (C^{+-}/r_{ij})exp[-3a^{+-}(r_{ij} - \delta_i - \sigma_+)], \end{aligned} \tag{5.5}$$

for the pair overlap function between anion i and cation j and

$$F(\delta) = B\delta^2 + \gamma\delta^3 + \gamma_2\delta^4 + \gamma_3\delta^5, \tag{5.6}$$

for the rearrangement energy, $E_{re}(r)$. The cation radius is taken to be constant and is set to the Fumi-Tosi values listed in table 5.1. The $A^{+-}exp[-a^{+-}(r^{ij} - \delta^i - \sigma^+)]/r_{ij}$ type terms gave a better fit to the *ab-initio* data than the more common $A^{+-}exp[-a^{+-}(r^{ij} - \delta^i - \sigma^+)]$ [81] at larger r.

The variable parameters in equations 5.5 and 5.6 (A^{+-}, B^{+-}, C^{+-}, a^{+-}, β, γ, γ_2 and γ_3) are therefore adjusted to satisfy

$$E_{ov}(r) = 8u_{CI}^{+-}(r, \delta^{opt}), \tag{5.7}$$

and

$$E_{re}(r) = F(\delta^{opt}) \tag{5.8}$$

over the whole range of r values at which *ab-initio* calculations were performed. Here δ^{opt} is the value of the anion radius that minimises the short-range energy at each value of r and is determined from

$$\left(\frac{\partial U^{sr}}{\partial \delta}\right)_r = 8\left(\frac{\partial u_{CI}^{+-}}{\partial \delta}\right)_r + \left(\frac{\partial F}{\partial \delta}\right)_r = 0. \tag{5.9}$$

Such a CIM potential parameterized to correctly describe the compression of the chloride ion in one crystal phase, should transfer unchanged to another crystal phase of the same system.

Anion compression by anions

In the previous section we saw that the energy contribution due to anion compression by cations was given by U_{CI}^{+-}. For anion compression by anions we follow a similar approach for U_{CI}^{+-} but with just a single exponential,

$$U_{CI}^{--}(r_{ij}, \delta_i, \delta_j) = A^{--}exp[-a^{--}(r_{ij} - (\sigma_i + \delta_i) - (\sigma_j + \delta_j))]. \tag{5.10}$$

The new parameters are fitted to the *ab-initio* data by simply adding this new energy on to U_{sr} in calculating the optimised value of δ and requiring that U_{CI}^{--} reproduces the optimal anion-anion *ab initio* data.

5.3.2 CIM Potential Parameterization for CsCl

The *ab-initio* values are available over the range $5.50\text{au} < r < 7.50\text{au}$. The fit is applied to the *ab initio* data for the B2 phase. It proved difficult to fit the data accurately over the whole of this range with the above functions. Since we are primarily interested in the range of r values close to the equilibrium lattice parameters of the B1 and B2 phases ($r_e \sim 6.75\text{au}$), the fits were biased to strongly weight the region $6.50\text{au} < r < 7.0\text{au}$. The resulting parameter values are shown in tables 5.4 and 5.5. The quality of the fit to the B2 phase data is illustrated in figure 5.2. The fit to E_{re} and to E_{ov} for the Cs-Cl interaction is excellent in the chosen range. The fit to the Cl-Cl potential is considerably poorer; this is because the *ab initio* Cl-Cl potential becomes weakly (and spuriously) attractive at large separations and this is not allowed for by the simple exponential function used in the fit of this term. Note, however, that the Cl-Cl potential makes only a very small contribution compared to the Cs-Cl potential in the relevant range of interionic separations.

The CIM potential (fitted to the B2 data) may be used to *predict* E_{ov} and E_{re} for the B1 phase. The comparison of the *ab initio* B1 data and the CIM prediction is shown in figure 5.3. It can be seen that the prediction is not perfect, there is an error of order 0.001au (~ 2 kJ mol^{-1}) in each of these predictions in the significant r range, but note that the errors tend to cancel for the two terms.

The CIM potential (together with the dispersion potential described above) may be used to calculate the internal energy *versus* volume for the two crystal phases of CsCl. The results are compared in figure 5.4. These curves behave unphysically at large separations, where the limitations of the use of the fifth order polynomial representation of $F(\delta)$, rather than a globally concave function, become apparent. This r range is not significant for any of the practical calculations described below. Values of δ_{opt} are shown in the lower panel of the figure. They show how the anion is compressed at different rates in the two crystal structures. The abrupt jump in the value of δ_{opt} at large r is the origin of the unphysical behaviour of the internal energy referred to above.

Note that the use of the CIM representation of the *ab initio* data has brought the minimum for the B2 phase below that of the B1, in contrast to what happens when *the same data* is fitted with a simple pair potential. The figure also shows (dotted lines) the positions of the energy minima in the two phases given by Pyper [22]. The agreement between the cell volume and lattice energy from the molecular dynamics calculations and *ab initio* calculations is now excellent as is the agreement between predicted and experimental cell volumes and lattice energy, given table 5.6 [73].

The CIM potential would therefore appear to contain all the necessary effects to account for the subtleties of the transformations between the perfect crystal structures in CsCl. It is an excellent representation of the *ab initio* data for the two phases and recaptures the experimental data very well. It is therefore a useful basis for which to examine the importance of ion compression effects in other chloride systems. Note that the ion compression effects are not associated with large absolute energy changes; the effects in CsCl are much smaller than in the study of the equivalent transition in MgO. It is the close proximity of the B1 and B2 phases in CsCl which makes this case particularly sensitive amongst the halides. Unfortunately, the CsCl crystal structure is such that the Cl-Cl interactions are not sampled sufficiently strongly to come to firm conclusions about the Cl-Cl interactions; we may use the *ab initio* data as a guide, but its reliability is not well tested.

U_{sr} / au	
a^{+-}	1.10
A^{+-}	10
B^{+-}	9.94×10^4
C^{+-}	6.2×10^7
a^{--}	0.0
A^{--}	0.0

Table 5.4: *CsCl CIM overlap potential parameters*

Parameter / au	
β	0.30
γ_1	1.10
γ_2	1.40
γ_3	0.22

Table 5.5: *CsCl CIM Self energy potential parameters*

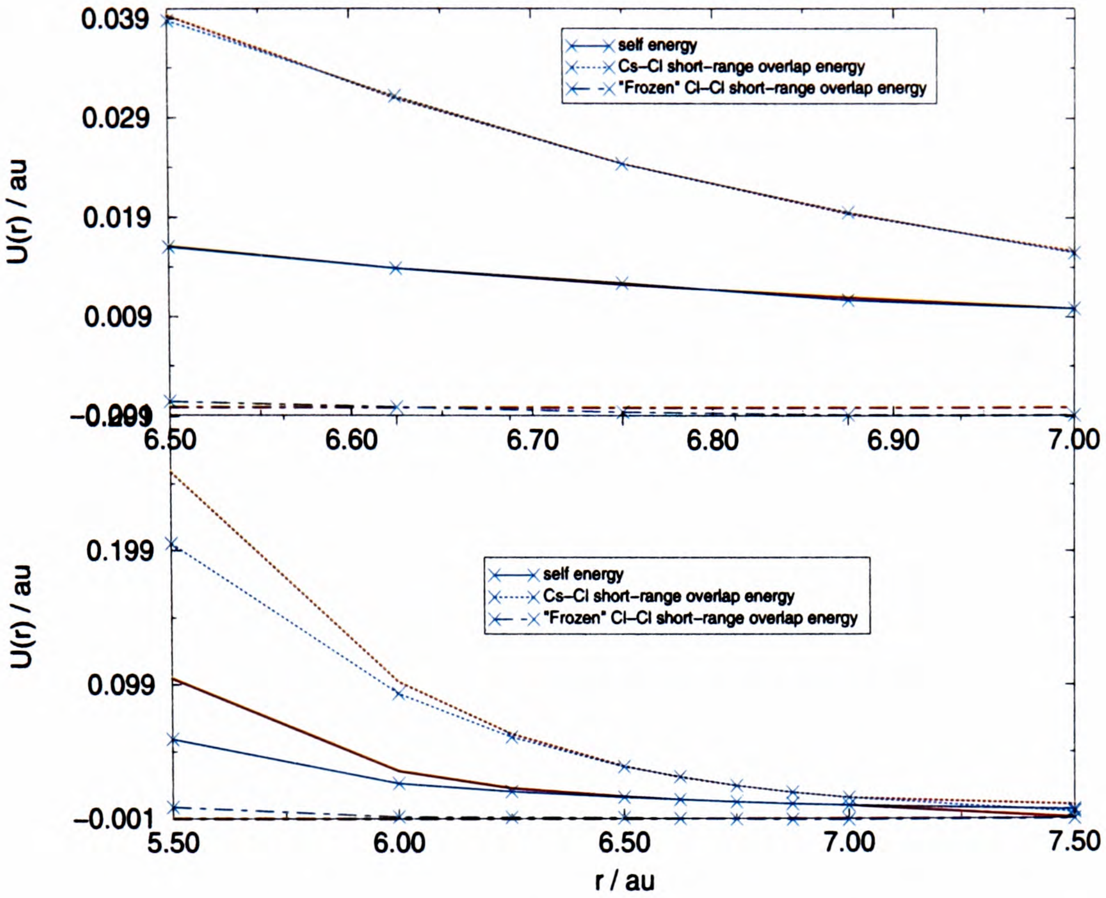

Figure 5.2: *Top panel: CIM potential fit to 8-coordinate B2 phase ab initio data in immediate vicinity of lattice parameter. Bottom panel: CIM fit over whole range of ab-initio data. The crosses are the ab initio values - the blue lines being a guide to the eye. The red lines show the CIM fit.*

5.4 LiCl

It should be possible to "transmute" the CsCl potential into a potential appropriate for other alkali halides by changing the cation radius in the u_{+-} term. This will enable the transferability of the potential to be examined, and also the importance of the compressibility effect to be assessed in a wider range of materials.

Property	RIM	CIM	Expt
LE / kJ.mol^{-1}	661.7	658.9	656.659
Lattice spacing / au	6.720	6.70	6.748

Table 5.6: *Crystal properties of CsCl calculated with the RIM and CIM*

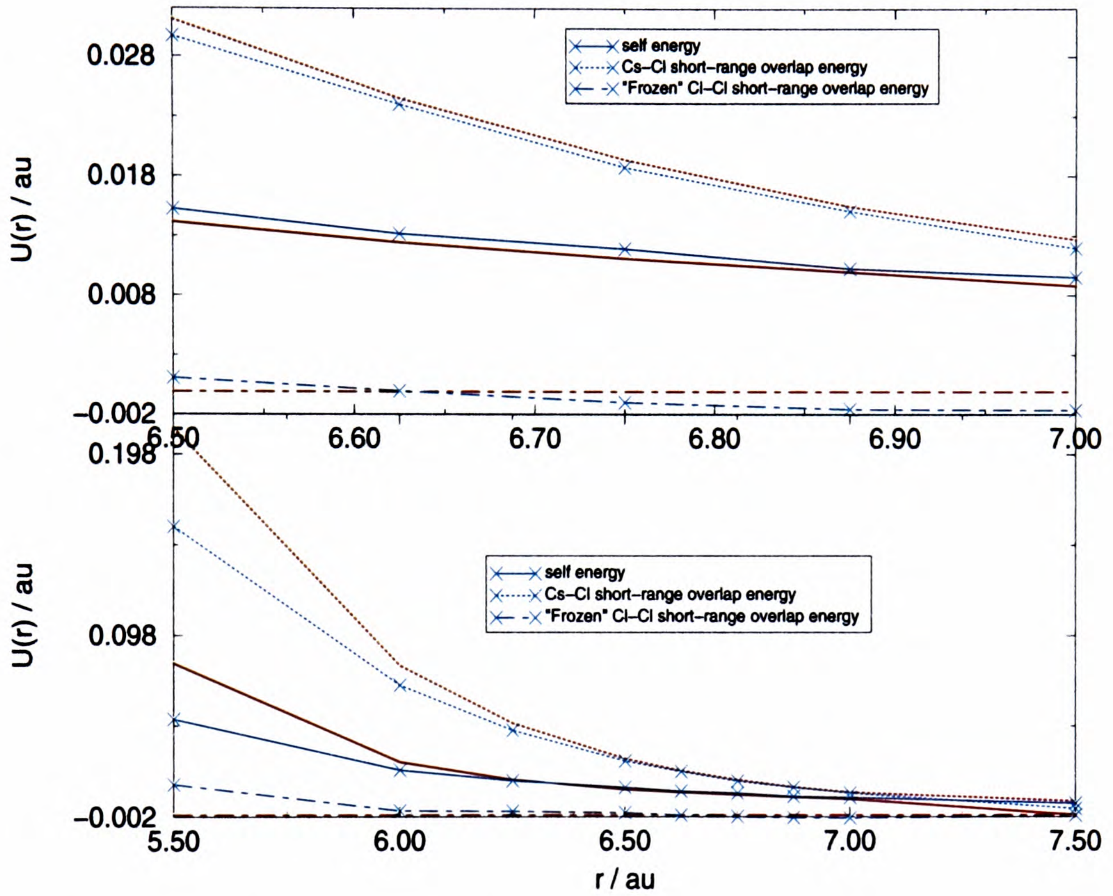

Figure 5.3: *Top panel: CIM potential from B2 phase applied to 6-coordinate B1 phase ab-initio data in immediate vicinity of lattice parameter Bottom panel: CIM fit over whole range of ab-initio data. The crosses are the ab initio values - the blue lines being a guide to the eye. The red lines show the CIM fit.*

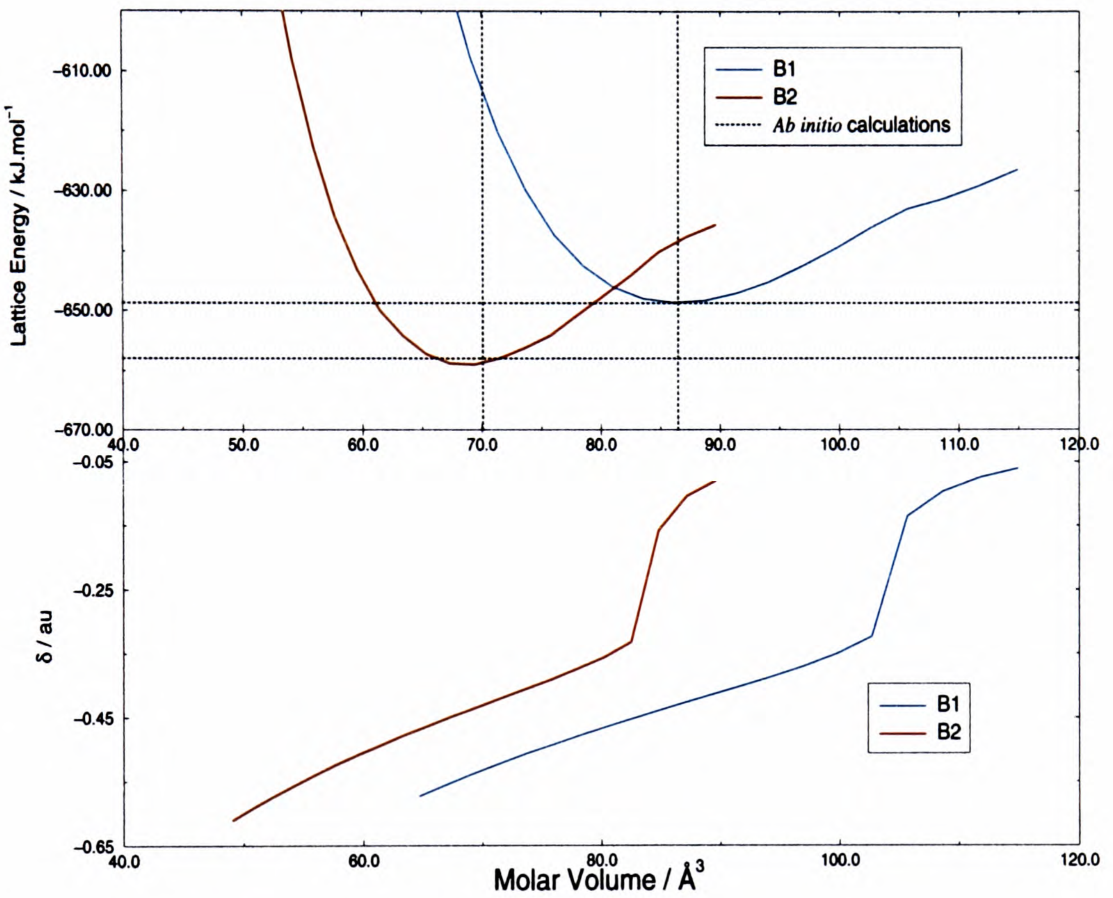

Figure 5.4: *Top panel: Energy-Volume curves for B1 and B2 phases of CsCl calculated with the CIM. The dotted lines show the calculated ab-initio values. Lower panel: The variation of δ with cell volume.*

An analogous case to CsCl, in alkali halide solid state structural chemistry, is that of LiCl. From X-ray diffraction experiments it is known that lithium chloride adopts the 6 co-ordinate Rocksalt (B1) structure. However, again the literature Fumi-Tosi pair potential (table 5.1) fails to predict the correct ground state structure, instead predicting the four co-ordinate blende structure (B3) to be the most stable, as illustrated in figure 4.7. As well as the RIM potential predicting the wrong ground state structure (B3 rather than B1) the predicted cell volume and lattice energy of the B1 phase are much lower than the experimental values (shown by the dotted lines in figure 4.7). [56, 73]

To date there have been no *ab-initio* calculations on LiCl but it should be possible to scale the anion-cation potential between alkali chlorides. We can obtain a compressible ion potential for LiCl by scaling the CsCl potential with the cation radii

$$A^{+-}_{LiCl} = A^{+-}_{CsCl} e^{a^{+-}(\sigma^{+}_{Li} - \sigma^{+}_{Cs})}, \tag{5.11}$$

and similarly for B^{+-} and C^{+-}

$$B^{+-}_{LiCl} = B^{+-}_{CsCl} e^{2a^{+-}(\sigma^{+}_{Li} - \sigma^{+}_{Cs})}, \tag{5.12}$$

$$C^{+-}_{LiCl} = C^{+-}_{CsCl} e^{3a^{+-}(\sigma^{+}_{Li} - \sigma^{+}_{Cs})}. \tag{5.13}$$

Using the values for the cation radius in the crystals ($\sigma^{+}_{Li} = 1.474$ au, $\sigma^{+}_{Cs} = 3.118$ au [82]) and $a = 1.1$ gives the CIM parameters listed in table 5.7. The dispersion parameters used to allow for the change of cation polarizability are calculated from equation 1.11. The energy-volume curves for the B1 and B3 phases of LiCl are plotted in figure 5.5. The B1 phase is now predicted to be the most stable phase with a cell volume and lattice energy in good agreement with experiment (table 5.8). Cl^- ion compression would again seem to have helped to stabilize the more highly coordinated structure. The result suggests that the potentials uncovered from the *ab initio* study of CsCl accurately capture the nature of

U_{sr}^{+-} / au	
a	1.1
A	1.639
B	2670.731
C	2.73×10^5

Table 5.7: *LiCl CIM overlap potential parameters scaled from CsCl*

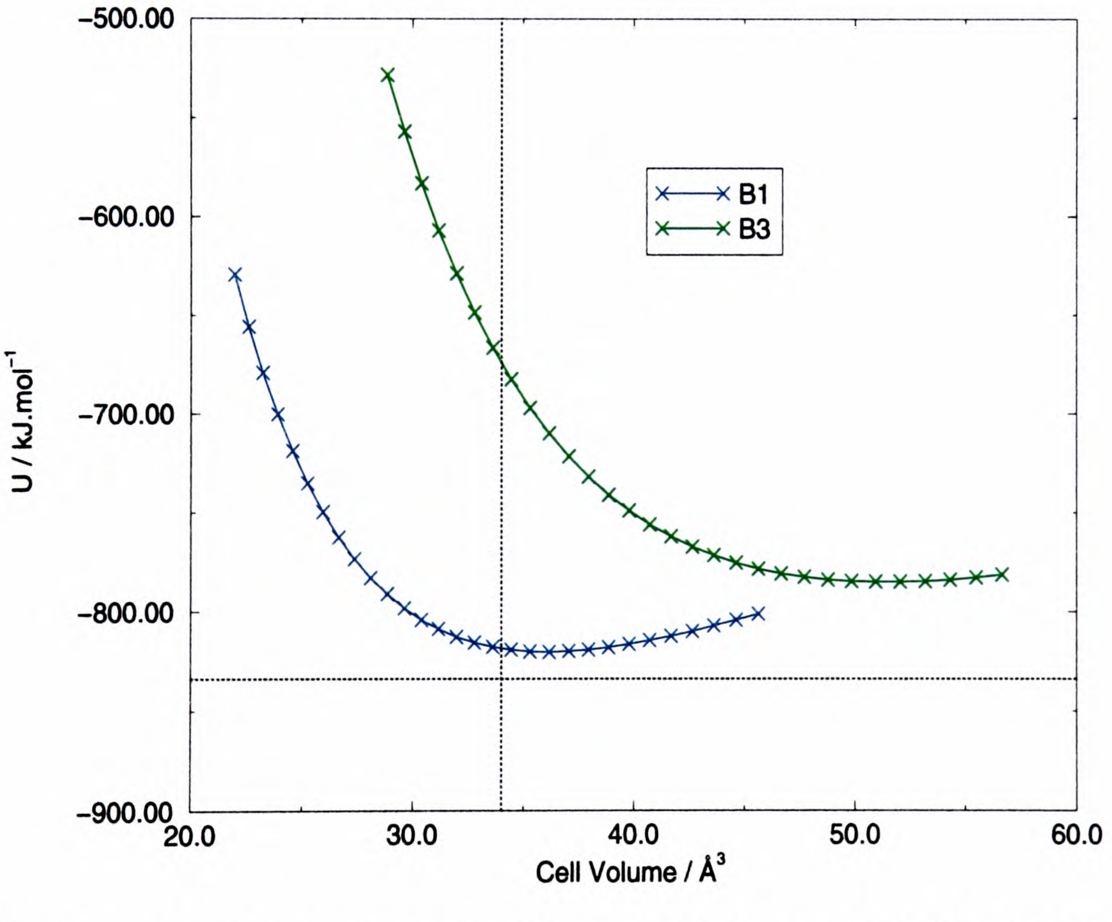

Figure 5.5: *Energy-Volume curves for B1 and B3 phases of LiCl calculated with the CIM*

Property	RIM	CIM	Expt
LE / kJ.mol^{-1}	874.5	820.5	834
Cell Volume / Å^3	29.70	36.04	34.009

Table 5.8: *LiCl simulated and experimental crystal properties*

interactions involving the chloride ion and may be transferred to other chloride systems by simply scaling the cation radius.

5.5 NaCl

NaCl has played a pivotal role in the development of ionic potentials; it is the system on which most empirical parameterization schemes have been developed and it is therefore not surprising to find that the Fumi-Tosi pair potential (table 5.1) for this case provides an excellent representation of the perfect crystal properties. In similar calculations to those described above with this potential, the B1 (rocksalt) phase is found to be most stable, and the predicted transition pressure to the B2 structure is 25Gpa, which compares favourably with the experimental value of 30 GPa [83]. The predicted cell volume (B1) is in good agreement with experiment [73] [84] (table 5.9) but the lattice energy is too large [56]. This is a feature common to the RIM predictions for CsCl and LiCl as well. We can also compare the bulk modulus from our simulation with that obtained experimentally from the single crystal elastic constants [56](equation 5.14).

$$B = \frac{1}{3}(c_{11} + 2c_{12}). \tag{5.14}$$

For NaCl these give an experimental bulk modulus of B=25.08GPa. The value of B from the simulation is 28.23GPa which comes from a Birch and Murnahan [85] fit to the calculated pressure *vs.* volume curve (equation 5.15).

Property	RIM	CIM1	Expt
U_{latt} / kJ.mol^{-1}	774.5	759.7	769
Cell Volume / Å^3	44.98	47.69	44.85
Bulk Modulus / GPa	28.23	-	25.08

Table 5.9: *Comparison of simulated and experimental crystal constants for NaCl*

U_{sr}^{+-} / au	
a	1.1
A	2.484
B	6134.644
C	9.506×10^5

Table 5.10: *NaCl CIM overlap parameters, scaled from CsCl*

$$P = \frac{3}{2}K_0\left\{\left(\frac{V_0}{V}\right)^{7/3} - \left(\frac{V_0}{V}\right)^{5/3}\right\}\left\{1 + \frac{3}{4}(K_0' - 4) \times \left[\left(\frac{V_0}{V}\right)^{2/3} - 1\right]\right\} \quad (5.15)$$

where K_0 and K_0' are the bulk modulus and its first pressure derivative respectively. On the basis of these excellent predictions, there would seem to be no need to invoke the compressible potential to account for the properties of NaCl. Nevertheless, it is of interest to invoke the same scaling procedure as applied above, and to test its reliability by comparison with the Fumi-Tosi potential. Again we scale the cation-anion potential parameters according to equations 5.11 *et seq* and using the tabulated (Fumi-Tosi) ionic radii for Cs^+ and Na^+ ($\sigma(Na^+) = 1.852$au, $\sigma(Cs^+) = 3.118$au). The resulting parameters are given in table 5.10 and the resulting energy-volume curves are shown in figure 5.6. For comparison we have also shown on this figure the energy-volume curves obtained with the Fumi-Tosi potential. The quality of the results for the B1 phase is seen to be reasonable considering that no direct information about NaCl has been

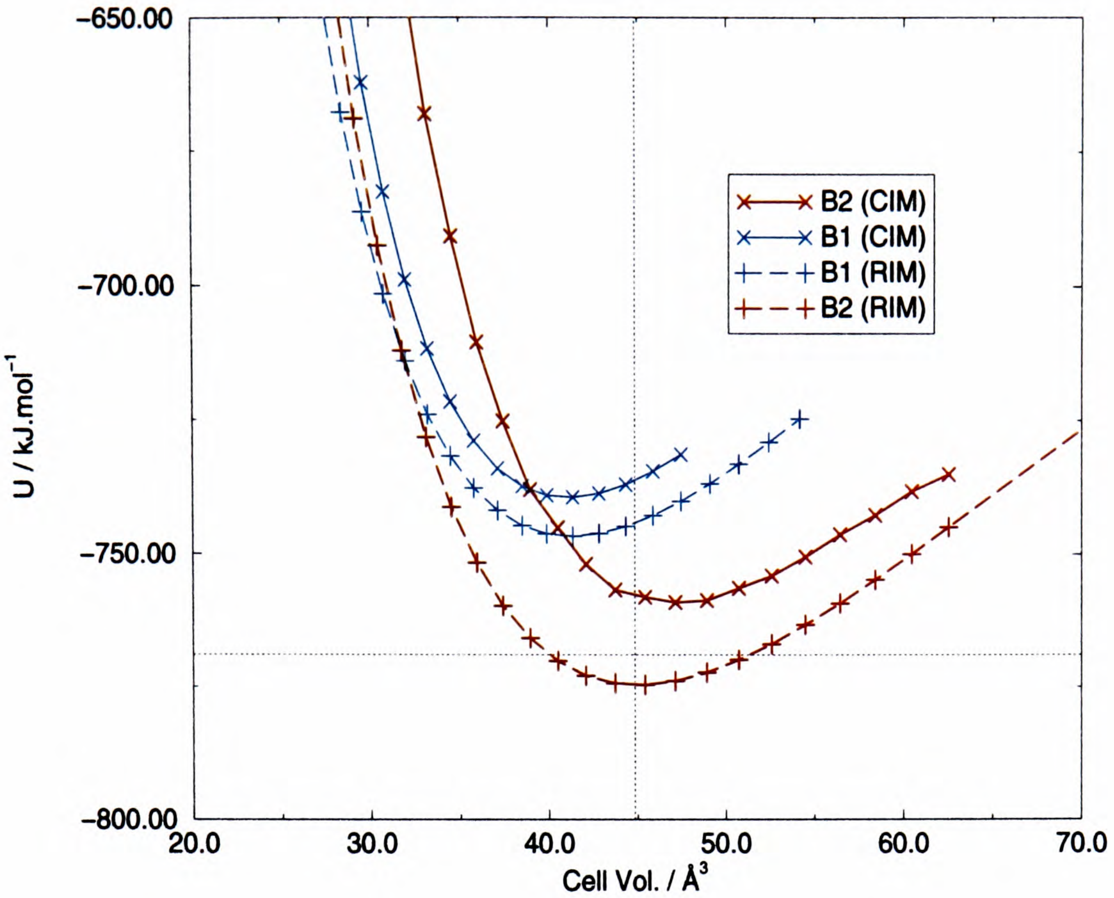

Figure 5.6: *Energy-Volume curves for B1 and B2 phases of NaCl calculated with the CIM and RIM*

included in the parameterization (unlike the Fumi-Tosi which is a direct fit). The overestimate of the cell volume (by an amount comparable to that found for LiCl) is, perhaps, the most notable deficiency (table 5.9).

This shows that the the CIM potential and the Fumi Tosi potential are very similar. We conclude that the *ab initio* data gives us no reason to suspect that the Fumi-Tosi potential is not a good representation of the pair interactions.

It is noteworthy that a much closer agreement between the scaled potential and the properties of NaCl could be obtained by using slightly different ionic radii for the Na^+ ion. If the Na^+ ion were taken to be slightly smaller, the molar volume for the B1 phase would be reduced. Furthermore, the calculated transition pressure to the B2 phase, which is only about 10 Gpa, would be increased. However, since the intention in making these comparisons was to clarify the consequences of a *standard* scaling procedure from the *ab initio* data, this has not been pursued.

Overall, it would seem that scaling the *ab initio* data to the other halides will produce reasonable potentials. Nevertheless, errors are introduced by scaling with standard cation radii, and the magnitude of the errors may be such as to overwhelm the effect of allowing for the ionic compressibility of the Cl^- ion.

5.5.1 NaCl Phonon Dispersion Curve

So far, the evaluation of the interaction potentials involving the Cl^- ion has been confined to perfect crystal properties. However, we need to consider how well the potential works for distorted geometries in order to be able to model the melt. To do this we have examined the phonon dispersion curves, which give quantitative information about the interionic interactions in distorted lower symmetry environments.

The phonon dispersion relation describes the frequencies of the lattice vibrations as a function of the reciprocal lattice vector **k**. The method we have chosen to calculate the phonons is to calculate the mass and charge current longitudinal and transverse correlation functions via molecular dynamics at finite temperature. These correlation functions are defined as

$$C^L_{XX}(\mathbf{k},t) = \left\langle \left(\sum_{j=1}^{N} -X^j(t) i\mathbf{k} \cdot \mathbf{v}^j(t) e^{-i\mathbf{k}\cdot\mathbf{r}^j(t)} \right) \left(\sum_{l=1}^{N} X^l(t) i\mathbf{k} \cdot \mathbf{v}^l(t) e^{-i\mathbf{k}\cdot\mathbf{r}^l(t)} \right) \right\rangle, \tag{5.16}$$

and

$$C^T_{XX}(\mathbf{k},t) = \left\langle \left(\sum_{j=1}^{N} -X^j(t) i\mathbf{k} \wedge \mathbf{v}^j(t) e^{-i\mathbf{k}\cdot\mathbf{r}^j(t)} \right) \cdot \left(\sum_{l=1}^{N} X^l(t) i\mathbf{k} \wedge \mathbf{v}^l(t) e^{-i\mathbf{k}\times\mathbf{r}^l(t)} \right) \right\rangle, \tag{5.17}$$

where $\mathbf{v}^j$ is the velocity of ion j and $X^j(t)$ represents the charge of species j for the optic modes and the ion mass for the acoustic frequencies. The Fourier transforms of these functions give peaks at the phonon frequencies for a range of **k**-vectors. The range of values is controlled by the condition that the **k**-vector be

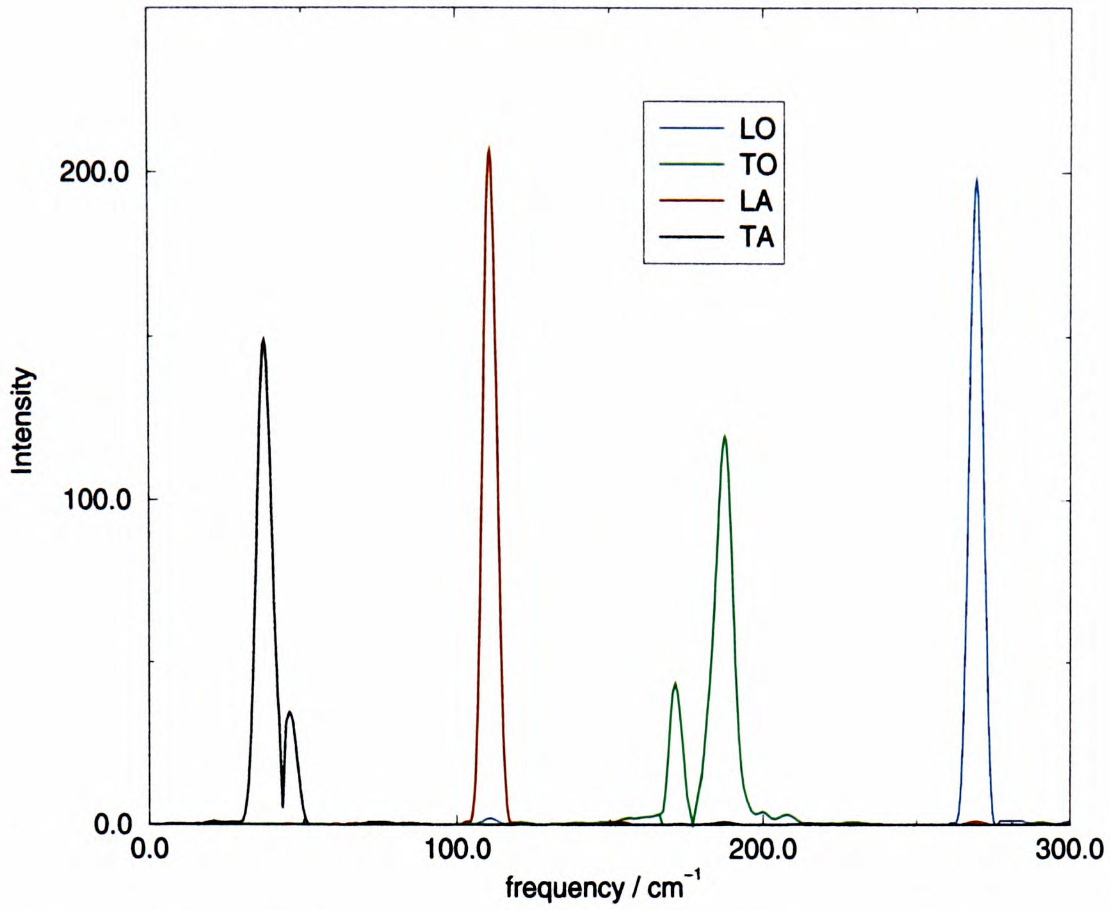

Figure 5.7: *Fourier-Transforms of phonon correlation functions*

commensurate with the size of the cell used in the MD simulation. For example, possible **k**-vectors along high symmetry directions of the crystal for a 216-ion cell for NaCl are $\mathbf{k} = \frac{2\pi}{3}\{n, m, l\}$ where n, m, l are integers since the system consists of $3 \times 3 \times 3$ unit cells. With different system sizes we are able to sample the phonon frequencies at different positions through the Brillouin zone.

The phonons were measured experimentally at 100K and so this is the temperature at which our simulations were performed. The lattice parameter used was 5.640Å [84]. The run was started from the perfect crystal with velocities selected randomly from a Maxwell-Boltzmann distribution. The simulation was equilibrated for 3.6ps and data accumulated for 7.2ps and the phonons calculated along the three high symmetry directions $\{\zeta, 0, 0\}$, $\{\zeta, \zeta, 0\}$ and $\{\zeta, \zeta, \zeta\}$

The $\{\zeta, \zeta, 0\}$ transverse phonons split into two modes. The phonon spectra at $\frac{1}{3}, \frac{1}{3}, 0$ obtained using the above method are shown in figure 5.7. The splitting of the transverse modes can clearly be seen.

RIM Phonons

The phonon dispersion curves calculated with the Fumi-Tosi potential for NaCl are shown in figure 5.8. We compare the experimental phonons from neutron scattering [86] (solid lines) with those predicted by the RIM (diamonds). There is fairly good agreement throughout, apart from the LO mode which is consistently too high. However, the shape of the LO mode is fairly well reproduced. The ion displacements for the LO(X) mode are shown in figure 5.9. The asymmetrical arrangement of the ions will result in the formation of ion dipoles. The movement of the ions away from their lattice sites causes the Madelung potential to distort resulting in an electric field on the anion as outlined in section 1.2.1. It becomes apparent that the phonons will be very sensitive to polarization effects even though, as we saw in section 5.5 these effects have no effect on the equilibrium crystal structure. The LO-TO splitting at the Γ point is predicted by the Lyddane-Sachs-Teller relation [87]

$$\omega_{LO}^2/\omega_{TO}^2 = \epsilon_0/\epsilon_\infty \tag{5.18}$$

For the RIM calculations ω_{LO} ~335cm^{-1} and ω_{TO} ~170cm^{-1} and so $\epsilon_0/\epsilon_\infty$=3.9 compared with an experimental value from ref. [87] of $\epsilon_0/\epsilon_\infty$=2.52. Allowing the ions to be polarizable will effectively increase ϵ_∞ (which is unity in the RIM), and therefore improve the LO-TO gap.

PIM Phonons

Next we consider including polarization effects in the model (section 3.2). We will only consider induced dipoles and ignore cation polarization ($\alpha(Na) = 1.002au$, $\alpha(Cl) = 20au$). The inclusion of polarization effects has the most pronounced effect on the longitudinal optic mode, reducing the LO-TO splitting at the Γ-point from ~165cm^{-1} to ~110cm^{-1} ($\epsilon_0/\epsilon_\infty$=3.1).

The phonons obtained by including polarization effects are shown in figure 5.10 The main effect of including polarization effects is to lower the frequency

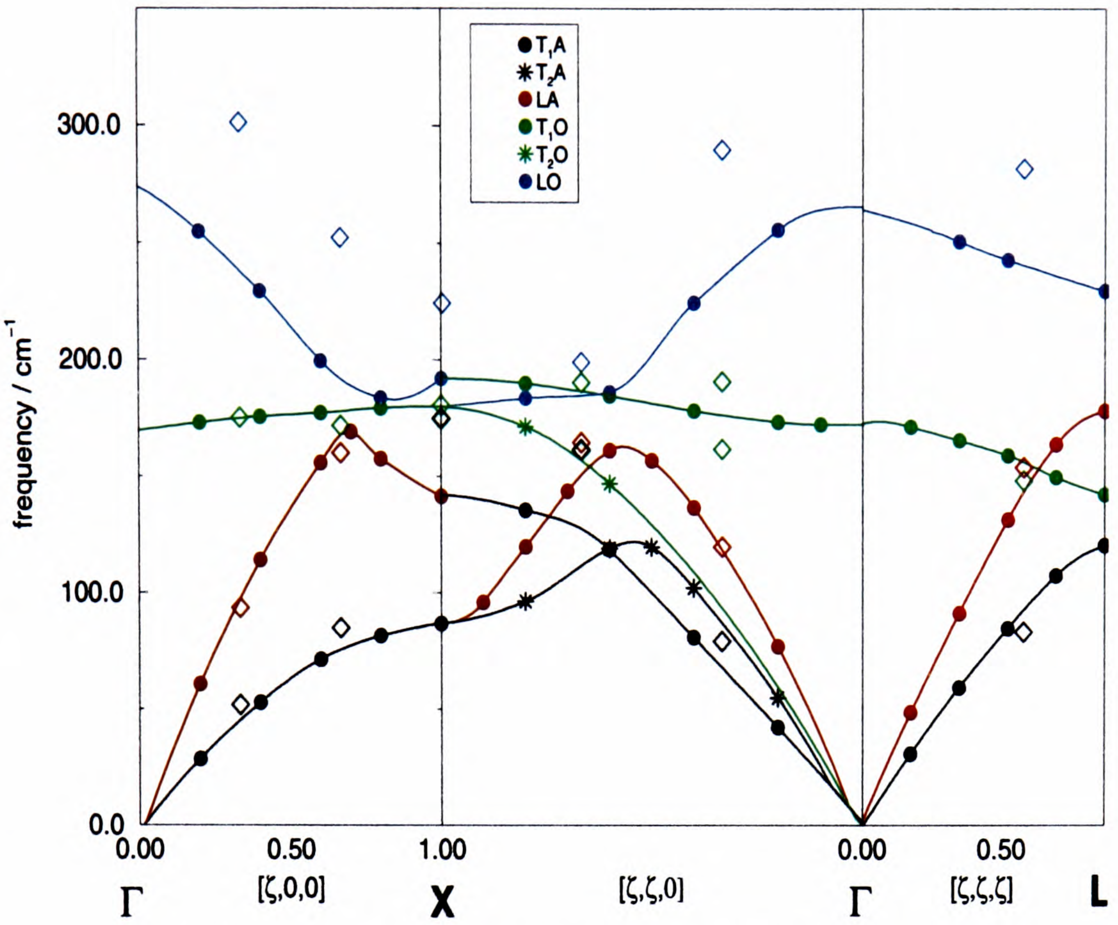

Figure 5.8: *NaCl Phonons calculated with the RIM*

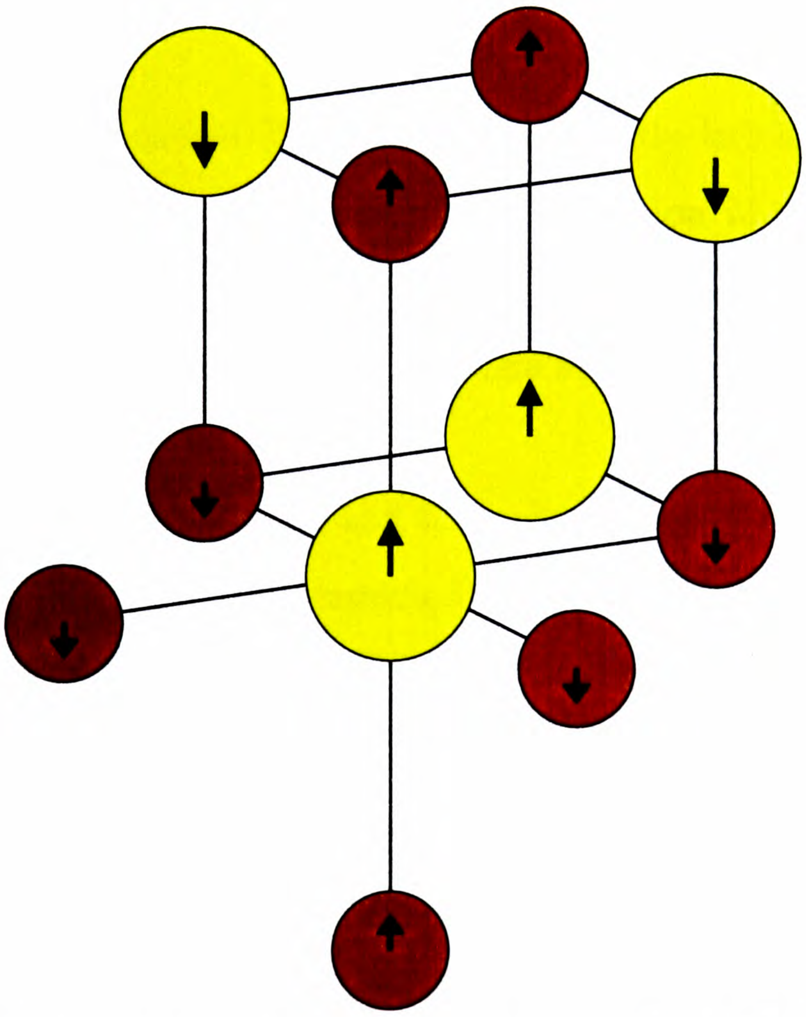

Figure 5.9: *Representation of the ionic motion in the LO(X) phonon mode.*

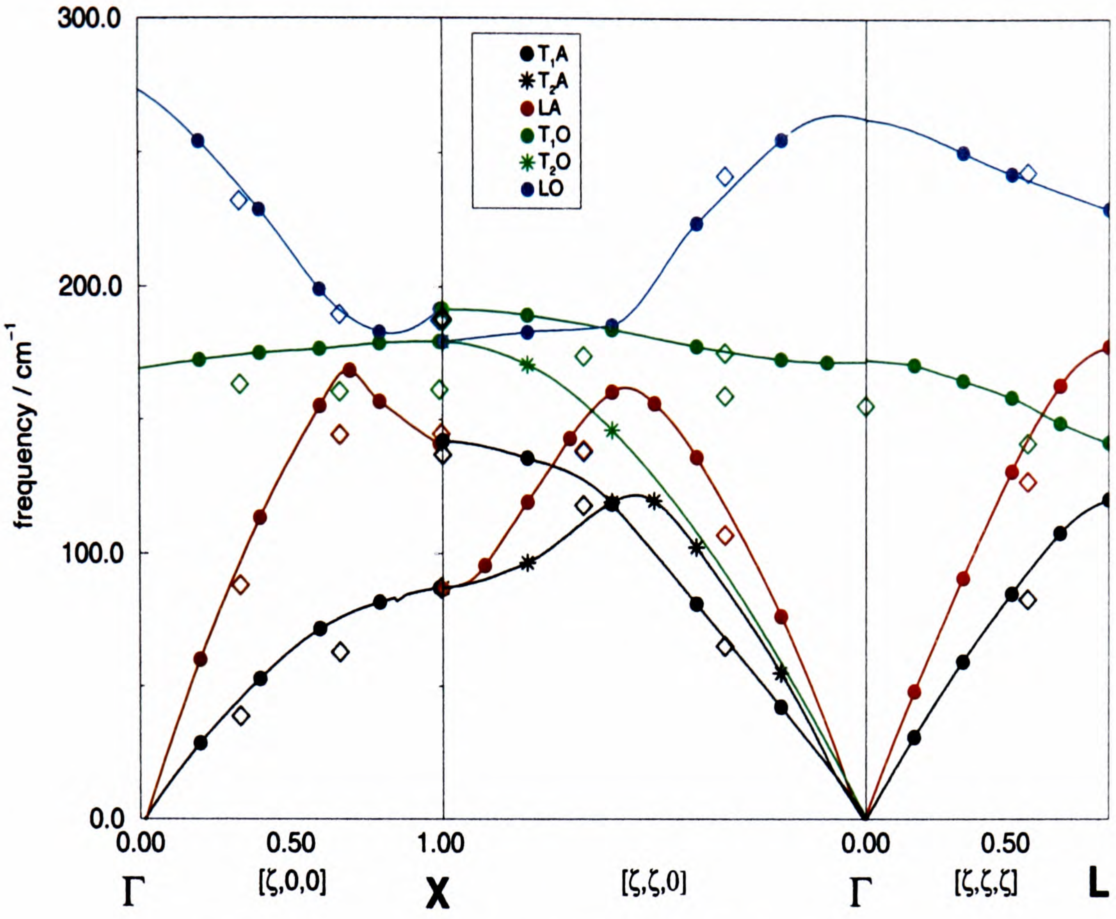

Figure 5.10: *NaCl phonons calculated with the PIM*

of the LO mode along all directions. Also seen is a slight lowering of the T_1O and T_1A modes.

Apart from the simulated TO mode lying slightly below the experimental, the phonon dispersion curves from the Polarizable Ion Model look very good. The ionic motion for the TO mode at the Γ point is shown in figure 5.11.

The pattern of ionic displacement is of one sublattice oscillating against the other.

Large electric fields are formed and the polarization of the anions lowers the phonon frequency. It should be expected that the TO mode also would move to a lower frequency. The LA and TA modes are only very slightly affected. At the Γ point the sublattices are in phase and so these modes have zero frequency. The motion of the sublattices becomes more out of phase on moving away from the Γ point, so the greatest polarization effects are seen in these modes at the X point.

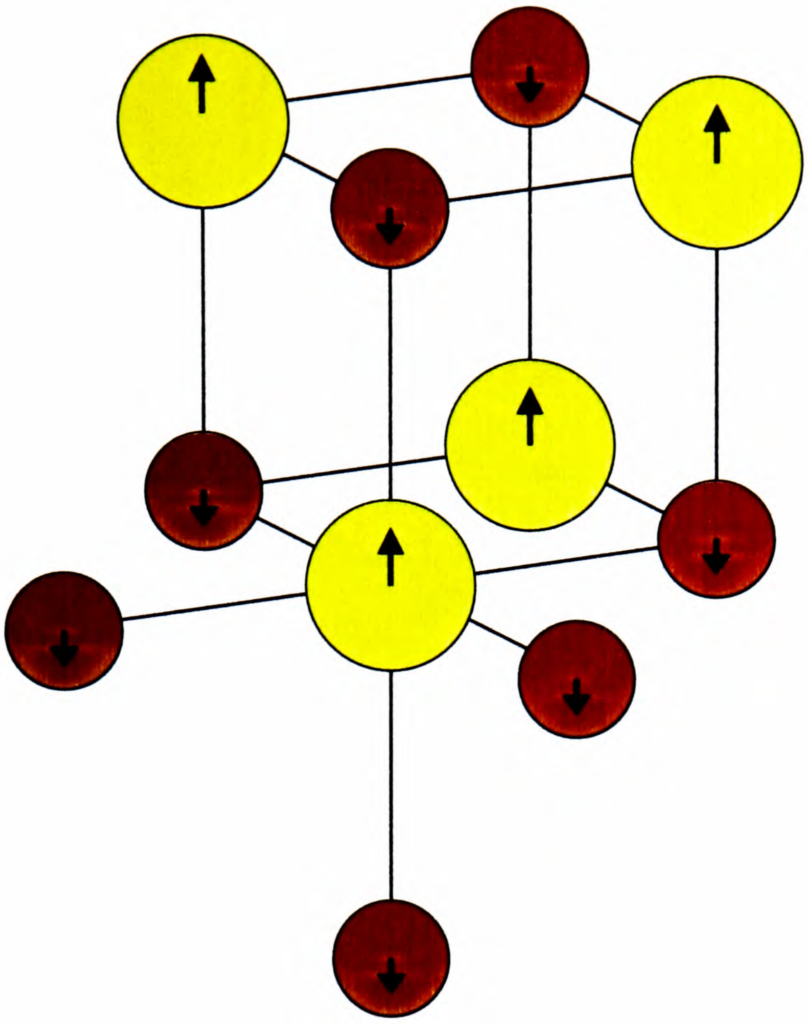

Figure 5.11: *Representation of the ionic motion in the TO(Γ) phonon mode.*

CIM Phonons

The agreement of the phonons calculated with the CIM with the experimental phonons is much worse than seen with the incompressible ion simulations. Both the optic modes are greatly overestimated, although the shapes are quite good. This model is much worse than the RIM/PIM. The reasons for this deficiency of the CIM potentials was explained in reference [2]: briefly, the compression of the ion, which softens the repulsive interactions, is not activated by the types of ionic displacement illustrated in the figures. Consequently, the CIM potential appears much stiffer than a pair potential which gives similar properties for the perfect crystal. In order to respond to such displacements, the ion must be able to compress *aspherically*. For oxides, where the compression effects are very important, a generalization of the CIM to allow for this aspherical compression [60] has been shown to give excellent predictions for the phonon

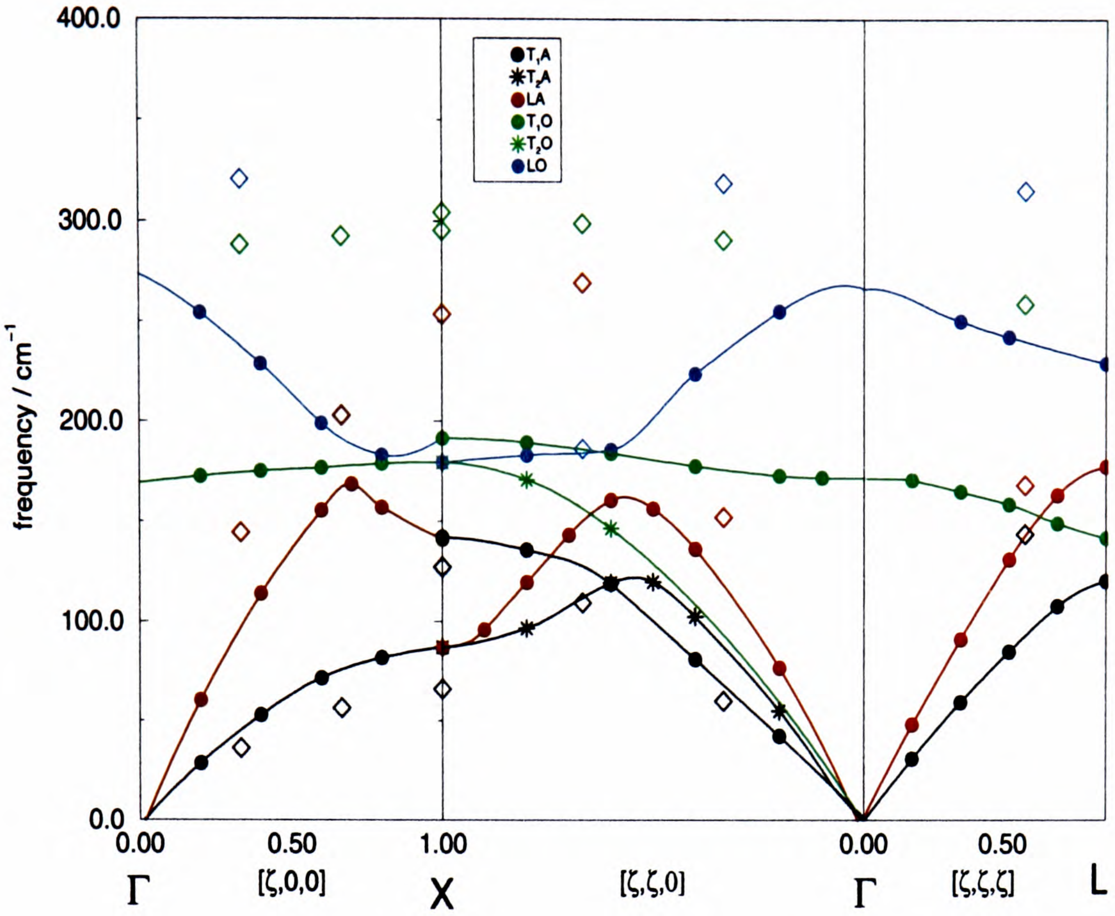

Figure 5.12: *NaCl phonons calculated with the CIM+PIM*

dispersion relationships.

The phonons from the CIM+PIM model are in figure 5.12. Again, the LO modes have been strongly shifted by the polarization effects, but the underlying problems caused by the deficiencies of the CIM for distorted geometries remain serious.

5.6 Conclusion

In this chapter we have explored what can be learnt about interionic interactions from the available *ab initio* data. This data gives excellent agreement with the experimentally observed properties of CsCl, and must include the correct "physics". A careful representation of the overlap and rearrangement energies, using the compressible ion model, is necessary to account for the correct crystal structure of CsCl. The ion compression helps to stabilize the more highly coordinated structure. However, the absolute energies involved with the compression of the Cl^- ion are much smaller than for O^{2-}. The *ab initio* potential may be scaled with the cation radius to produce respectable potentials for other chlorides. Errors are introduced into this procedure by the use of standard ionic radii, and the size of these errors is comparable to the energies associated with the ion compression effect. Furthermore, using a simple spherically-compressible CIM gives very poor potentials when the anion is not at a high symmetry site. In principle, such deficiencies can be corrected, but the considerable effort involved in doing this is probably not merited by the relatively small size of the compressibility effects in Cl^- systems. In view of these remarks, and in the light of the fact that a pair potential (supplemented with polarization effects) is shown to be working extremely well for NaCl (where subtle phase transitions are absent), it was concluded that the use of a compressible potential for the cation-anion interactions in MX_3 systems was probably not essential, and could lead to further problems because of the typically asymmetric anion environments in these systems.

Little can be firmly concluded about the Cl-Cl interactions from the available *ab initio* data, or indeed from empirical representations of this interaction derived on systems of MX stoichiometry. It would seem that the Cl-Cl separations in these materials are always so large as to make overlap interactions between Cl^- ions very small. It would seem that this potential will have to be regarded as something about which we learn from studies on the MCl_3 systems. Nevertheless, if we take the information from the *ab initio* calculations at face value, it is found that the anion-anion potential from Pyper's *ab-initio* data is substantially shorter range than that of Tatlipinar (which has been used in MCl_3 until now) and is very similar to that of the Fumi-Tosi potential for NaCl.

It would seem reasonable therefore to return to the simulation of MCl_3 systems with a pair potential representation of all short-range interactions, and with parameters similar to the Tatlipinar type for the M-Cl term, and to change the Cl-Cl term to a shorter range function similar to that of Fumi and Tosi. Ion compressibility effects may play a role in adjusting the effective size of the Cl^- ion in different coordination environments, but this will have to be accommodated indirectly and not explicitly included in the potentials used.

Chapter 6

Trivalent metal chlorides: Structure

6.1 Introduction

The work described in the preceding chapters has highlighted the inadequacy (at a quantitative level) of the PIM with the short-range, repulsive interactions that are represented by the pair potential with the parameters of Tatlipinar. Close examination of the available *ab initio* data for interactions involving the Cl^- ion indicated that neglect of the ion compressibility effect was not likely to be a major shortcoming, and that use of pair potentials for the repulsive interactions *per se* was not the origin of the problem. Therefore, attention is narrowed to the actual parameters appearing in the Tatlipinar potentials. Both the empirical observation that the predicted positions of the first peak in the Cl-Cl pdfs were too small (chapter 1) and the indications from the *ab initio* data suggest that the major problem may lie in the Cl-Cl repulsive potential, which is effectively making the ion too large. In figure 6.1 the differences between known Cl-Cl potentials are highlighted. The crosses and triangles indicate the Tatlipinar (Cl^1_{POT}) and Fumi-Tosi (Cl^2_{POT}) Cl-Cl potentials, respectively. The former can

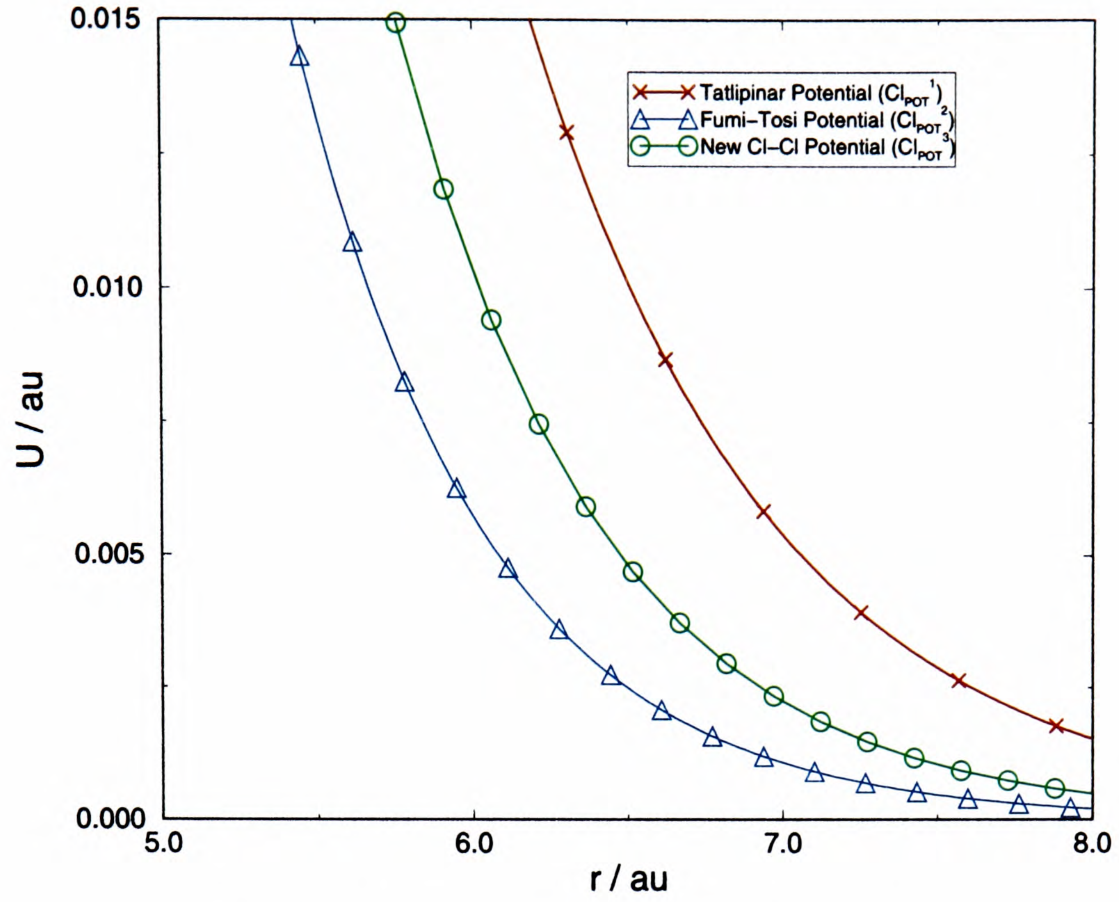

Figure 6.1: *Comparison of Cl-Cl potentials*

be seen to be of longer range. The range and amplitude of the FT potential are very similar to the Cl-Cl potential which provides the best fit to Pyper's *ab initio* data. Furthermore, the FT potential is very similar to that which has been used in a number of successful PIM simulations of MCl_2 systems [19]. The intermediate potential (circles - termed Cl^{3}_{POT}) will be discussed below. It is difficult at the outset to accept that a deficiency in the Cl-Cl potential is the origin of the problem in describing the MCl_3 systems: examination of the magnitude of the Cl-Cl short-range potential at the typical Cl-Cl separation in the liquid ($\sim$ 7au, *e.g.* figure 1.10) shows it to be tiny compared to the coulomb repulsion between the ions.

Actual evaluation of the potential parameters from electronic structure calculations is precluded by the difficulty of performing and interpreting the calculations. An empirical approach to refining the potentials is therefore necessary. The objective of this exercise is to find the best description of the *whole class* of materials within an *ionic* picture. The latter restriction is imposed by requiring that, so far as possible, the interaction potential parameters should be calculated from the properties of the separate ions, in the spirit of the Busing potentials discussed in chapter 1, and by requiring that formal charges are used. Ionic polarizabilities should be consistent with refractive index data. Again in the spirit of the ionic model, the interaction potentials should describe the liquid and crystal phases, and should be transferable to mixtures.

A large part of the work which underlies this thesis was concerned with attempting to find optimum potentials, subject to these constraints. Results with the final potentials are described below. In the sections which follow, we will first survey the quality of the comparison between the experimental and predicted structural information. In the case of the liquid state simulations, the ionic arrangements which are found enable us to explain the distinctive features of the experimental structure factors and their evolution with the cation radius. The more general lessons which can be drawn from this examination are described towards the end of the chapter.

In sections 6.5-6.10 we will present results for seven potentials which differ in substance only through the cation radii, which enter the short-range potentials *via* Busing-like forms (equation 6.1) and through the induction damping parameters (equation 3.25). Their radii are chosen to span (approximately) the range of ion size from La^{3+} to Al^{3+} (the values appropriate to the Tatlipinar potential are listed in table 6.1).

Species	Cl	La	Ce	Tb	Dy	Y	Sc	Fe	Al
Radius (Å)	1.70	1.42	1.40	1.30	1.22	1.20	1.12	0.97	0.90
Polarizability / au	20.0	10.0	10.0	10.0	10.0	4.0	2.1	0.0	0.0

Table 6.1: *Radii and polarizabilities used in the potential model*

Ion Pair	a_{ij} / au	B_{ij} / au	C_6^{ij} / au	C_8^{ij} / au	b / au
Cl-Cl[1]	1.260	36.437	200.0	5000.0	-
Cl-Cl[2]	1.670	128.249	200.0	5000.0	-
Cl-Cl[3]	1.530	100.000	200.0	5000.0	-
La-Cl	2.439	10075.457	102.220	0.0	1.258
Ce-Cl	2.439	9188.352	102.220	0.0	1.267
Tb-Cl	2.439	5795.647	102.220	0.0	1.309
Dy-Cl	2.439	4008.61	0.0	0.0	1.340
Y-Cl	2.439	3655.663	45.815	0.0	1.354
Sc-Cl	2.250	1011.98	26.609	0.0	1.390
Fe-Cl	2.250	534.520	0.0	0.0	1.470
Al-Cl	2.250	396.785	0.0	0.0	1.512

Table 6.2: *Potential parameters for the MCl_3 systems.*

6.2 Potential Details

6.2.1 Improved Cl-Cl Potential

For each system the M-Cl and M-M terms are the same as those that were used in the initial study (chapter 1). The difference is that we will now use the potential obtained in the previous chapter for Cl-Cl [34] (Cl^2_{POT}). A full set of potential parameters is given in table 6.2.

As we shall see in this chapter, the simulated results for the seven systems with the Cl^2_{POT} potential gives structure factors and radial distribution functions which are different from those obtained with the Tatlipinar Cl-Cl potential (Cl^1_{POT}). The new anion-anion potential seems to greatly improve the agreement with experiment for YCl_3 and $DyCl_3$ (sections 6.7 and 6.8). The comparison between predicted and experimental structure factors for the remaining systems ($LaCl_3$, $TbCl_3$, $FeCl_3$ and $AlCl_3$), however, is somewhat worse, with the anion-

anion peak in the rdfs now having moved too far in compared with experiment.

This observation agrees with what was concluded in chapter 5 *i.e.* that altering the Cl-Cl potential has a significant effect on the structure even considering its relatively small energetic contribution. Previously, it had been thought that the anion-cation interactions were by far the most dominant as far as the liquid structure of these systems was concerned. The poorer agreement with experiment for several systems suggests the investigation of a potential (Cl^3_{POT}) intermediate between that of Tatlipinar (Cl^1_{POT}) and that from chapter 5.

This new potential is shown in figure 6.1. This potential (appropriate for all the cations except Y^{3+} and Dy^{3+}) is less repulsive than the Tatlipinar potential, but more so than that now used for Y^{3+} and Dy^{3+}. $DyCl_3$ and YCl_3 are structurally isomorphous. The fact that use of a shorter ranged Cl-Cl potential is indicated for these systems is purely an empirical observation.

6.2.2 Transferability of the new potential

Ideally, we would still like to represent the dependence of the new potential parameters on the ion's radius and hardness by Busing type functions

$$B_{ij} = f(\rho_i + \rho_j)e^{a_{ij}(\sigma_i+\sigma_j)} \tag{6.1}$$

(where $f = 0.014$au). For Cl^3_{POT} the values in table 6.2, coupled with equation 6.1 gives $\rho_{Cl} = 0.092au^{-1}(\equiv 0.173\text{Å}^{-1})$ and $\sigma_{Cl} = 3.04\text{au}(\equiv 1.608\text{Å})$. This compares with a Cl^- radius of 1.70Å and a hardness of 0.210Å^{-1} in the Tatlipinar potential (Cl^1_{POT}) and a radius of 1.527Å^{-1} and a hardness of 0.210Å^{-1} in Cl^2_{POT} if we formulate these in an analogous manner.

For all the cations considered the hardness of the metal ion is now ρ_M=0.111au^{-1} (=0.059Å^{-1}). This compares with ρ_M=0.007Å^{-1} in the earlier study. To regenerate the same B_{MCl} values as were used previously then,

$$\sigma_M^{new} + \sigma_{Cl}^{new} = \sigma_M^{old} + \sigma_{Cl}^{old}, \tag{6.2}$$

These 'new' radii are listed in table 6.3.

Species	Cl	La	Ce	Tb	Dy	Y	Sc	Fe	Al
Radius (Å)	1.527† 1.608‡	1.512	1.492	1.392	1.393	1.374	1.212	1.062	0.992

Table 6.3: *Radii appropriate for use in equation 6.1.* † *Cl^- radius appropriate for $DyCl_3$ and YCl_3.*‡ *Cl^- radius appropriate for all remaining cations*

Clearly, these new values for the ion radii and hardness parameters will give the same values for a_{ij}, B_{ij} as listed in table 6.2 for the anion-anion and anion-cation correlations, but the values for cation-cation interactions will now be quite different. However, in practice, the Coulombic repulsion between cations is so strong, that the short-range repulsion between cations is always negligible.

6.3 Crystal Phase Simulation

The determination of the energy-volume curves for the MCl_3 potentials were carried out as detailed in chapter 2, allowing relaxation of the ionic positions. Where necessary relaxation of the cell shape was allowed. This was only found to be necessary for $TbCl_3$.

6.4 Liquid Phase

The simulations on $LaCl_3$, $CeCl_3$, $TbCl_3$, $DyCl_3$, $ScCl_3$ and YCl_3 each contained 500 ions and were started from the melt obtained from the YCl_3 crystal structure, which was then equilibrated for a run of 36 ps. Full equilibration was considered to have been established when no further change was observed in the liquid structure (from the simulated pdfs). The structural data for calculation of structure factors was then obtained over a subsequent run of 4ps.

The major liquid simulation runs on $AlCl_3$ and $FeCl_3$ involved 960 ions and were obtained by melting the $AlCl_3$ crystal. Each run was performed at, or near the temperature at which diffraction experiments were undertaken and at the deduced experimental density, as quoted in refs. [11–15] (see table 6.4). These densities have not always been directly measured and can be a source of significant uncertainty.

System	Temperature (K)	Density ($g.cm^{-3}$)
$LaCl_3$	1178	3.174
$CeCl_3$	1108	3.234
$TbCl_3$	900	3.580
$DyCl_3$	1100	3.516
YCl_3	1033	2.492
$ScCl_3$	1253	1.643
$FeCl_3$	600	1.78
$AlCl_3$	600	1.277

Table 6.4: *Temperatures and densities used in the simulations of* MCl_3.

6.4.1 Comparison with experimental diffraction data

We begin by comparing the simulation predictions with experiment in reciprocal space, where the experimental results are obtained, in order to assess the quality of the predicted structures.

Neutron Structure Factors

Partial (Ashcroft-Langreth) structure factors $S_{\alpha\beta}(k)$, were calculated both by directly averaging over the correlation functions of the Fourier components of the ion densities, *i.e.*

$$S_{\alpha\beta}(k) = (N_\alpha N_\beta)^{-1/2}\langle\sum_{i\epsilon\alpha}\sum_{j\epsilon\beta}\exp[i\mathbf{k}.\mathbf{r}^{ij}]\rangle, \tag{6.3}$$

and also by Fourier transformation of the partial pair distribution functions (pdf)

$$S_{\alpha\beta}(k) = \delta_{\alpha\beta} + 4\pi n_0\sqrt{c_\alpha c_\beta}\int dr(g_{\alpha\beta}(r) - 1)r\frac{\sin(kr)}{k}, \tag{6.4}$$

where c_α is the concentration of species α. At low k, the former method (when using **k** vectors commensurate with the simulation cell) gives a more reliable structure factor, since it is free of truncation errors. The functions displayed in the figures below were obtained by combining the direct averages, for $k \leq 2\,\text{Å}^{-1}$, with the Fourier transformed pdfs for larger k values.

We can then obtain the total neutron weighted structure factor for comparison with experiment from

$$S_{tot}(k) = b_M^2 c_M[S_{MM}(k) - 1] + 2b_{Cl}b_M\sqrt{c_{Cl}c_M}S_{MCl}(k) + b_{Cl}^2 c_{Cl}[S_{ClCl}(k) - 1], \tag{6.5}$$

where b_α is the coherent neutron scattering length of species α. This is directly comparable to the experimental total neutron weighted structure factor (equation 6.7) which is defined as a combination of *Faber-Ziman* partial structure factors (equation 6.6).

$$S_{\alpha\beta}^{FZ}(k) = 1 + 4\pi n_0\int dr(g_{\alpha\beta}(r) - 1)r\frac{\sin(kr)}{k}, \tag{6.6}$$

$$S_{tot}(k) = b_M^2 c_M^2[S_{MM}^{FZ}(k) - 1] + 2b_{Cl}b_M c_{Cl}c_M[S_{MCl}^{FZ}(k) - 1] + b_{Cl}^2 c_{Cl}^2[S_{ClCl}^{FZ}(k) - 1]. \tag{6.7}$$

Neutron scattering lengths are as given in table 6.5 (ref. [88]). They are such that the experimental total structure factors tend to reflect predominantly the cation-anion and anion-anion partials mainly via the metal concentration term as is shown in table 6.6. The real-space function corresponding to $S_{tot}(r)$ is denoted by $G_{tot}(r)$.

Species	Cl	La	Ce	Tb	Dy	Y	Sc	Fe	Al
b / fm	9.5770	8.24	4.84	7.39	16.9	7.75	12.29	9.50	3.449

Table 6.5: *Neutron scattering lengths used in the calculations of neutron weighted structure factors.*

System	$b_M^2 c_M$ / fm^2	$2 b_{Cl} b_M \sqrt{c_{Cl} c_M}$ / fm^2	$b_{Cl}^2 c_{Cl}$ / fm^2
$LaCl_3$	16.97	68.34	68.79
$CeCl_3$	5.86	40.14	68.79
$TbCl_3$	13.65	61.29	68.79
$DyCl_3$	71.40	140.17	68.79
YCl_3	15.02	64.28	68.79
$ScCl_3$	37.76	101.93	68.79
$FeCl_3$	22.56	78.79	68.79
$AlCl_3$	2.97	28.61	68.79

Table 6.6: *Weighting coefficients of partial Ashcroft-Langreth structure factors as appear in equation 6.5.*

X-Ray Structure factors

Comparison with the X-ray experiment is somewhat more complicated, since the weighting factors now involve the ionic form-factors, which are k-dependent.

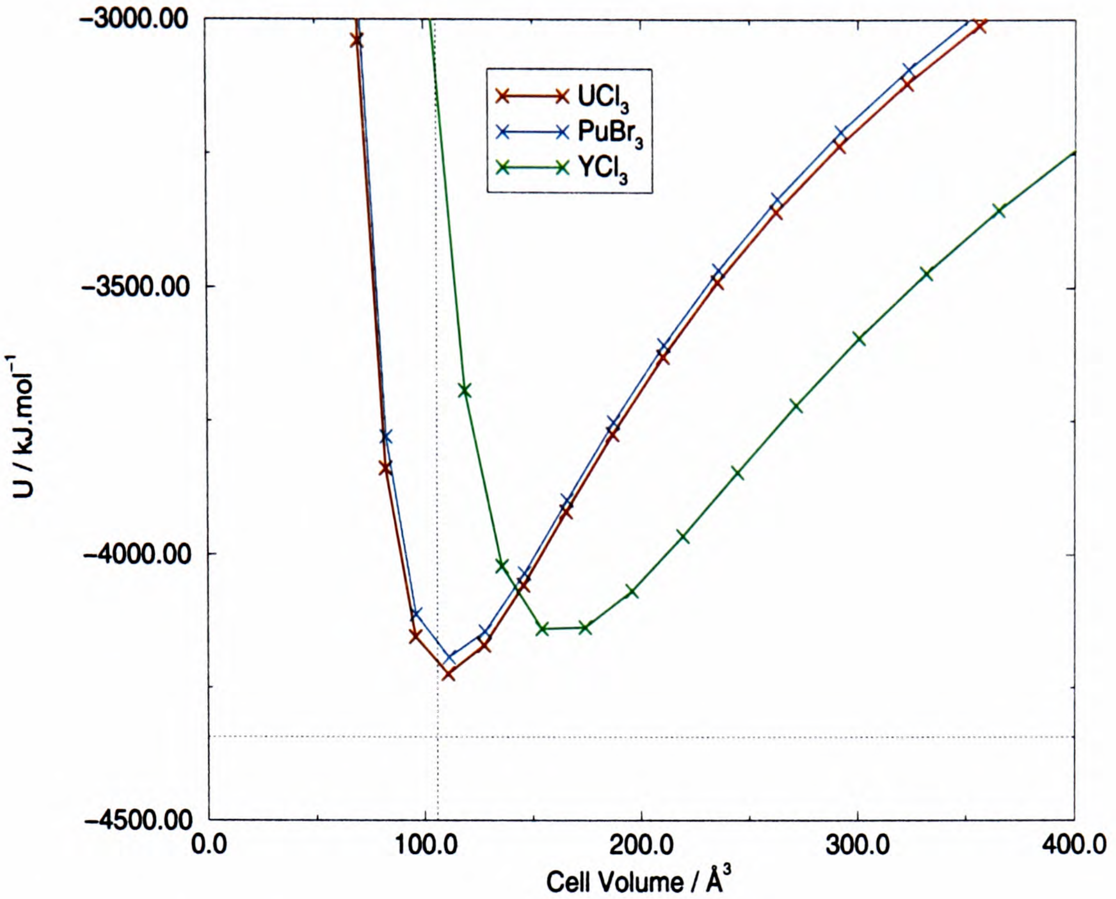

Figure 6.2: *Energy-Volume curves for LaCl$_3$ calculated with Cl^3_{POT}*

The quantity reported is the reduced intensity, $k \cdot i(k)$, given theoretically by:-

$$k \cdot i(k) = k \left[\frac{S_{xr}(k)}{\sum\limits_{\alpha} c_\alpha f_\alpha^2(k)} - 1 \right] \tag{6.8}$$

where S_{xr} is the X-ray weighted structure factor

$$S_{xr}(k) = (f_+(k))^2 c_+ S_{++}(k) + 2f_-(k)f_+(k)\sqrt{c_-c_+}S_{+-}(k) + (f_-(k))^2 c_- S_{--}(k). \tag{6.9}$$

Because of the factor of k, high k structure is more prominent in $k \cdot i(k)$ than in the neutron data. The form-factors were taken from reference [89].

6.5 LaCl$_3$

6.5.1 Crystal Structure

As can be seen in figure 6.2 using the Cl^3_{POT} potential has brought the energy of the UCl$_3$ and PuBr$_3$ structures below that of the YCl$_3$ structure. Compared with the energy-volume curves for $LaCl_3$ in chapter 2 the UCl_3 structure is now predicted to be the most stable with a cell volume and lattice energy in good agreement with experiment (shown by the dotted lines in figure 6.2) (see table 1.1). We saw in chapter 2 that the Tatlipinar potential tended to overstabilize the less tightly bound, low coordination number structures for the larger cation systems. This can now be seen to have been a consequence of the large effective size of the short-range Cl-Cl interaction used in that work, which was inhibiting the more dense packing of the chloride ions in the UCl_3 structure at the experimental density.

6.5.2 Liquid Structure

The experimental and simulated total neutron structure factors are compared in figure 6.3. The agreement of the two seems generally very good. In particular, the amplitude and position of the first-sharp-diffraction peak, or pre-peak, (at $\sim 1.2\ \text{Å}^{-1}$) is excellent – indicating that the simulation is reproducing the intermediate-range order of the liquid.

Intermediate Range Order

A fluid is often said to exhibit a prepeak if there is a peak in the structure factor at a much lower k value than would be expected from 2π divided by the nearest-neighbour separation in the fluid. In a simple melt, the cation-anion separation sets the lengthscale for all interionic correlations in the fluid, whereas in more complex melts other, longer lengthscales can arise due to the formation of complexes or the creation of 'voids' in the liquid structure *inter alia* [48]. Comparison of the total structure factor with the partials indicates that, in this case, the appearance of the prepeak in the total structure factor is due to the interference of the La-Cl and Cl-Cl partials. The amplitude of the predicted principal peak agrees very well with experiment, but it is shifted slightly to low *k*. Its shape is, again, affected by interference between the Cl-Cl and La-Cl partials.

In figure 6.4 we show the comparison of the total neutron weighted pair distribution function (pdf) obtained from the experimental total neutron weighted structure factor by Fourier transformation, $G_{tot}(r)$, with the total neutron-weighted pdf calculated in the simulation. Good agreement is seen in the positions and areas of the peaks in the two functions out to at least 7 Å. In particular, note that the position of the second peak, which the resolution into partials clearly indicates is due to Cl-Cl correlations is excellent. Had the shorter-range Cl-Cl potential (Cl^2_{POT}) been used, this second peak would have been slightly shifted inwards. In real space, the comparison between simulation and experiment would not have been much degraded. However, this small shift would have manifested itself more dramatically in the shape of the total structure factor. The peaks in the simulated pdf are narrower than observed experimentally: the extent to which this is due to deficiencies in the simulation potentials versus the loss of real-space resolution on Fourier transforming the structure factor from a finite range of *k* will be discussed in section 6.6.3.

In the lower part of figure 6.4 we show the partial pdfs, weighted by coherent neutron scattering length and concentration factors (table 6.6) with which they contribute to the total neutron signal. It is clear that there is almost no signature of the metal-metal correlations in the data for $LaCl_3$. Furthermore, the assignment of the first peak to $g_{MCl}(r)$ and of the second to $g_{ClCl}(r)$, assumed in the analysis of the experimental data , seems to be well substantiated. We will discuss the significance of the more distant features in the simulated pdfs below.

Difference Functions Obtained by Isomorphic Substitution

Good approximations to the partial structure factors can be obtained from the experimental data by taking difference functions of the total structure factors for

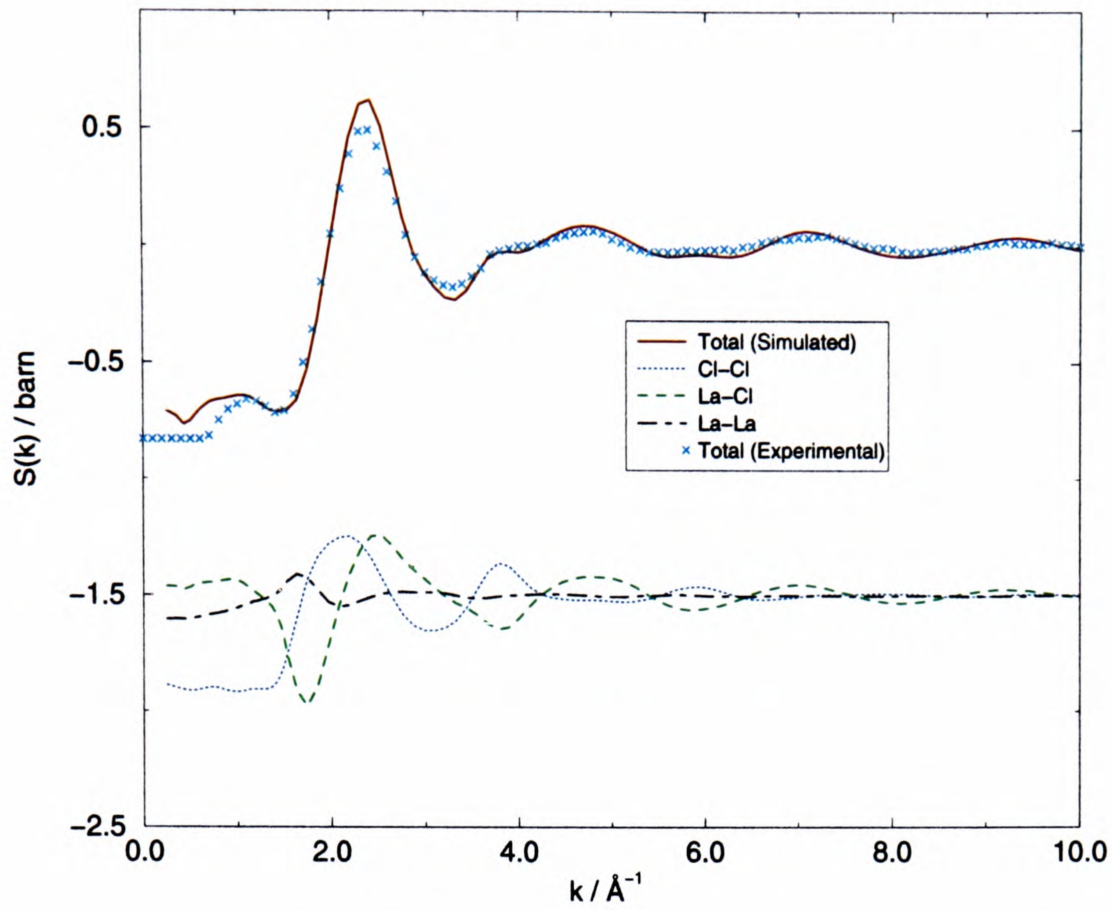

Figure 6.3: *Comparison of experimental and simulated total neutron weighted structure factors for* $LaCl_3$ *simulated with* Cl^{β}_{POT}. *The partial structure factors are shown shifted by a constant of -1.5*

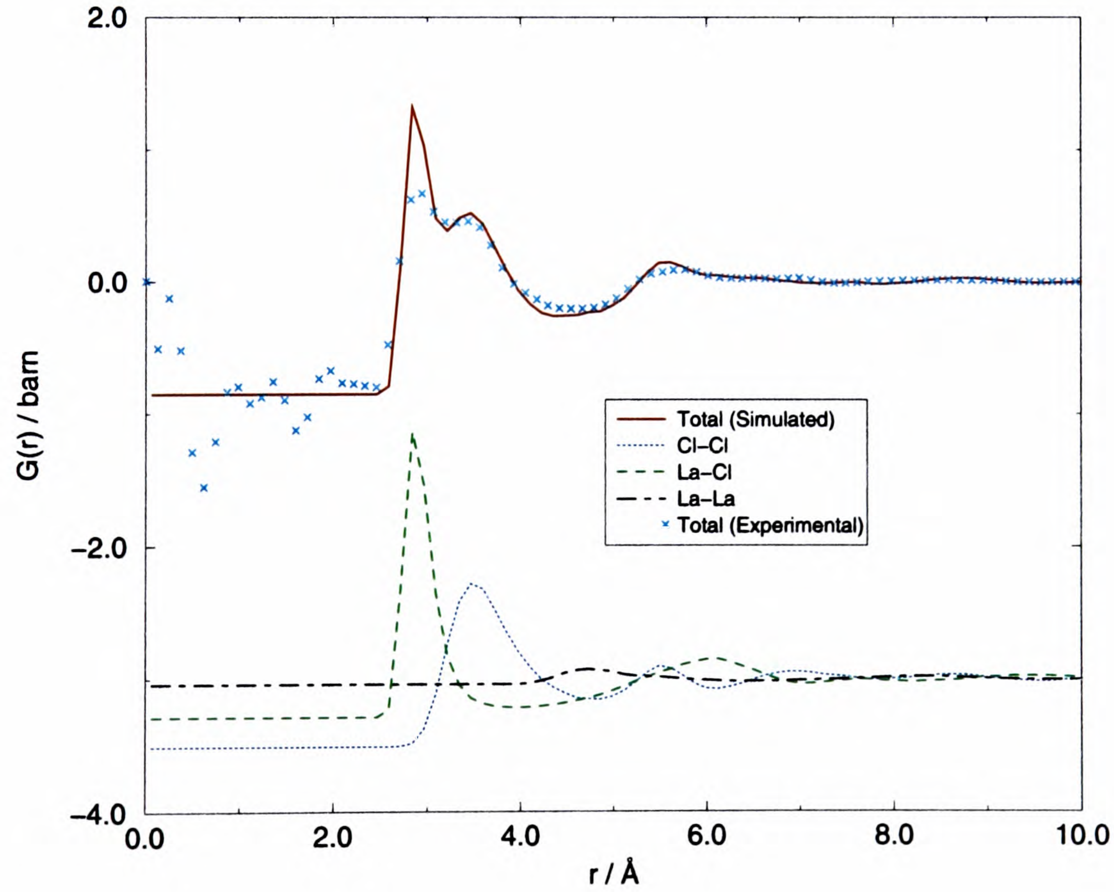

Figure 6.4: *Comparison of simulated and experimental total neutron weighted pdfs for* $LaCl_3$. *The partial pdfs are shown shifted by a constant of -3*

systems with very similar physicochemical properties. Salmon and Wasse [12] have applied this principle to their data for $LaCl_3$ and $CeCl_3$, noting that the ionic radii of La and Ce are very similar. This assumes that $LaCl_3$ and $CeCl_3$ are structurally the same (isomorphic) and differ only in the neutron scattering lengths of the cations.

Assuming $S_{LaLa}(k) = S_{CeCe}(k) = S_{MM}(k)$ and $S_{LaCl}(k) = S_{CeCl}(k) = S_{MCl}(k)$ then the first-order difference function $\Delta_M(k)$ in terms of Ashcroft-Langreth structure factors is given by

$$\begin{aligned} \Delta_M(k) &= S_{LaCl_3}(k) - S_{CeCl_3}(k) \\ &= K_{MM}[S_{MM}(k) - 1] + K_{MCl}S_{MCl}(k), \end{aligned} \tag{6.10}$$

where

$$\begin{aligned} K_{MM} &= c_M(b_{La}^2 - b_{Ce}^2) \\ K_{MCl} &= 2b_{Cl}\sqrt{c_M c_{Cl}}(b_{La} - b_{Ce}). \end{aligned} \tag{6.11}$$

Using tabulated scattering lengths for La^{3+}, Ce^{3+} and Cl^- [88] (table 6.5) gives values for K_{MM} of 111.2 mbarn and K_{MCl} of 282 mbarn *i.e.* the $S_{MCl}(k)$ partial accounts for 72% of $\Delta_M(k)$ and the $S_{ClCl}(k)$ partial structure factor is eliminated.

The cation-anion correlations can be removed by forming the difference function $\Delta F'(k)$ defined as

$$\begin{aligned} \Delta F'(k) &= S_{LaCl_3}(k) - [b_{La}/(b_{La} - b_{Ce})]\Delta_M(k) \\ &= K^*_{ClCl}[S_{ClCl}(k) - 1] - K^*_{MM}[S_{MM}(k) - 1], \end{aligned} \tag{6.12}$$

where

$$\begin{aligned} K^*_{MM} &= b_{La}b_{Ce}c_M, \\ K^*_{ClCl} &= b_{Cl}^2 c_{Cl}. \end{aligned} \tag{6.13}$$

For the case of $LaCl_3$ and $CeCl_3$, K^*_{MM}=99.6 mbarn and K^*_{ClCl}=688 mbarn *i.e.* the anion-anion correlations account for 87% of $\Delta F'(k)$.

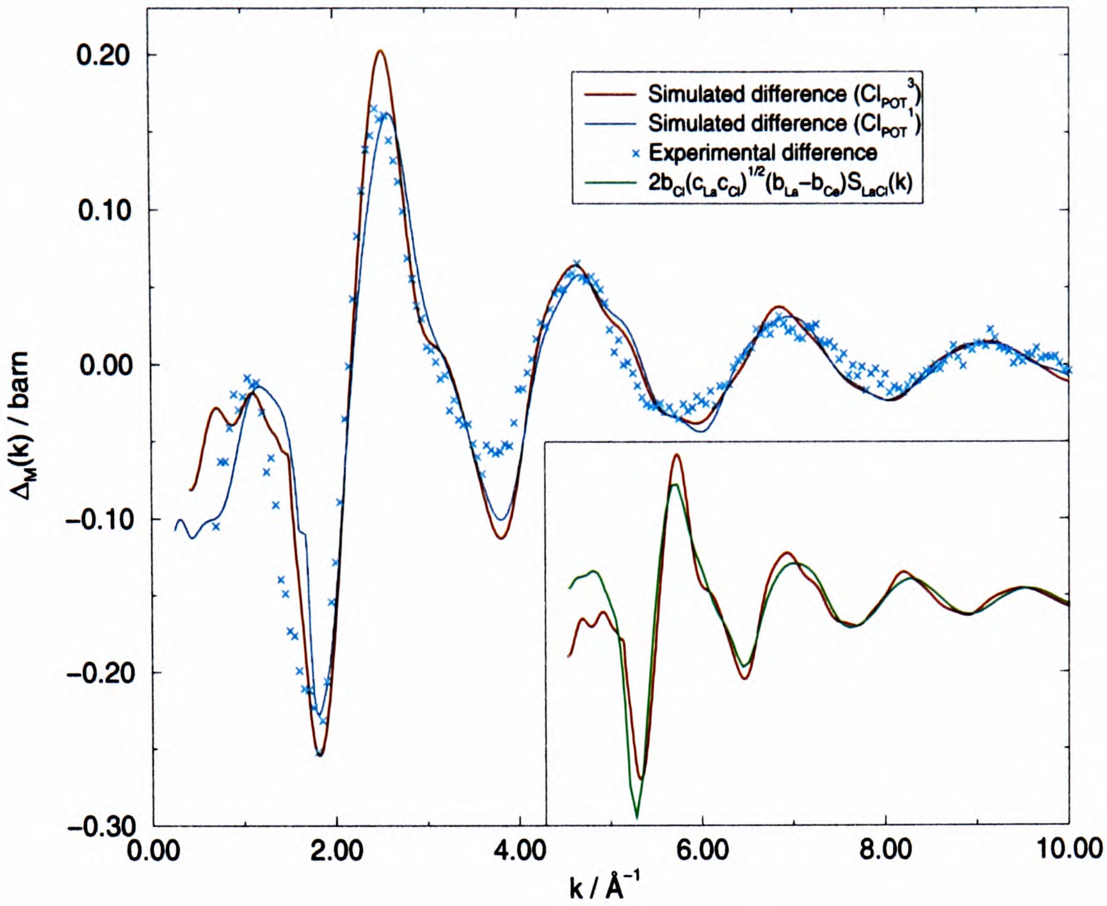

Figure 6.5: *The difference function $\Delta_M(k)$ for $LaCl_3$ and $CeCl_3$ simulated with two different Cl-Cl potentials (Cl_{POT}^1 and Cl_{POT}^3). The inset shows how closely the simulated difference really does correspond to the partial structure factor.*

The differences with the new potential are shown in figures 6.5 and 6.6 and are compared with those obtained with the Tatlipinar Cl-Cl potential (Cl_{POT}^1). The agreement between experiment and calculation is very good for Δ_M(k) for both of the Cl-Cl potentials. However, the agreement for $\Delta F'(k)$ is now much better with the new potential (Cl_{POT}^3). In particular, the amplitude of the first two peaks is much improved and the experimental and calculated data are now in phase at large values of k. Also indicated in figures 6.5 and 6.6 is the degree to which the Δ_M(k) and $\Delta F'(k)$ functions really do correspond to the single S_{MCl}(k) and S_{ClCl}(k) partials, respectively. It can be seen that these experimentally accessible differences give an excellent guide to the shape of the partials in both cases, indicating the value of the isomorphous substitution technique for these closely related materials.

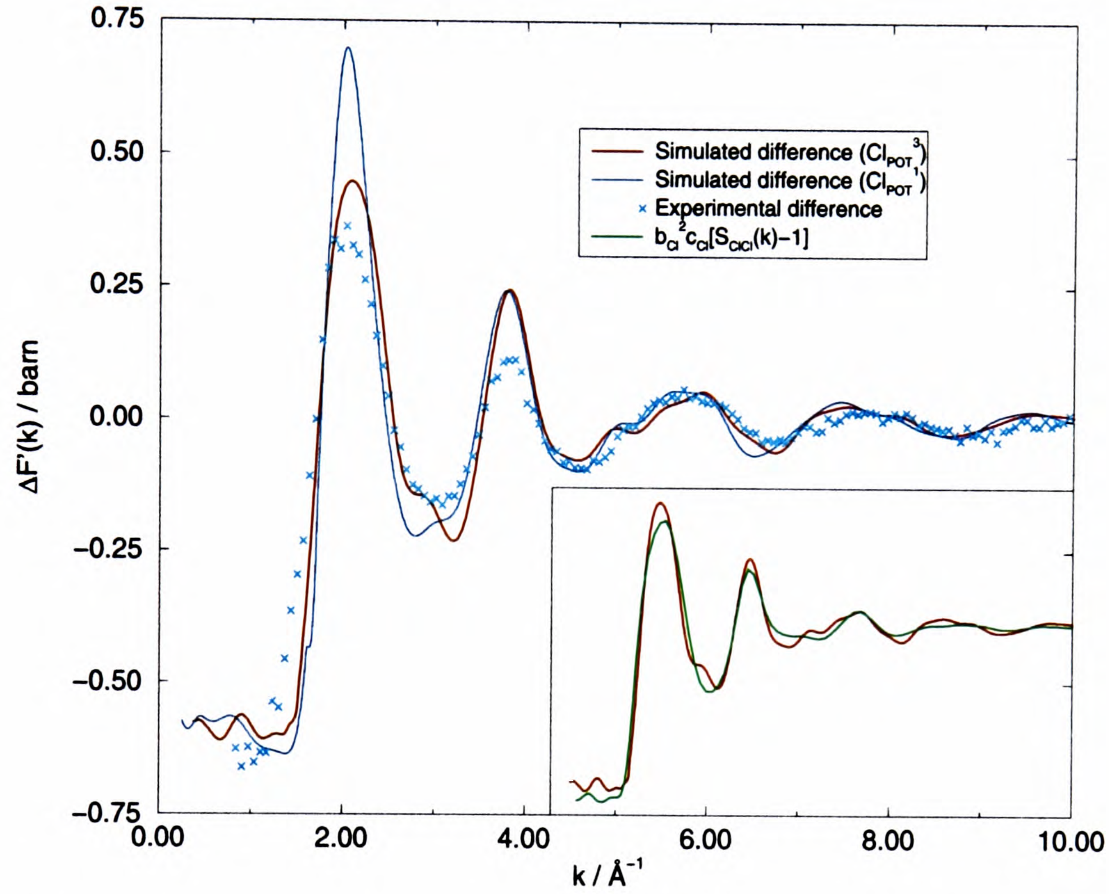

Figure 6.6: *The difference function, $\Delta F'(k)$ for $LaCl_3$ and $CeCl_3$ simulated with two different Cl-Cl potentials (Cl^1_{POT} and Cl^3_{POT}). The inset shows how closely the simulated difference corresponds to the partial structure factor.*

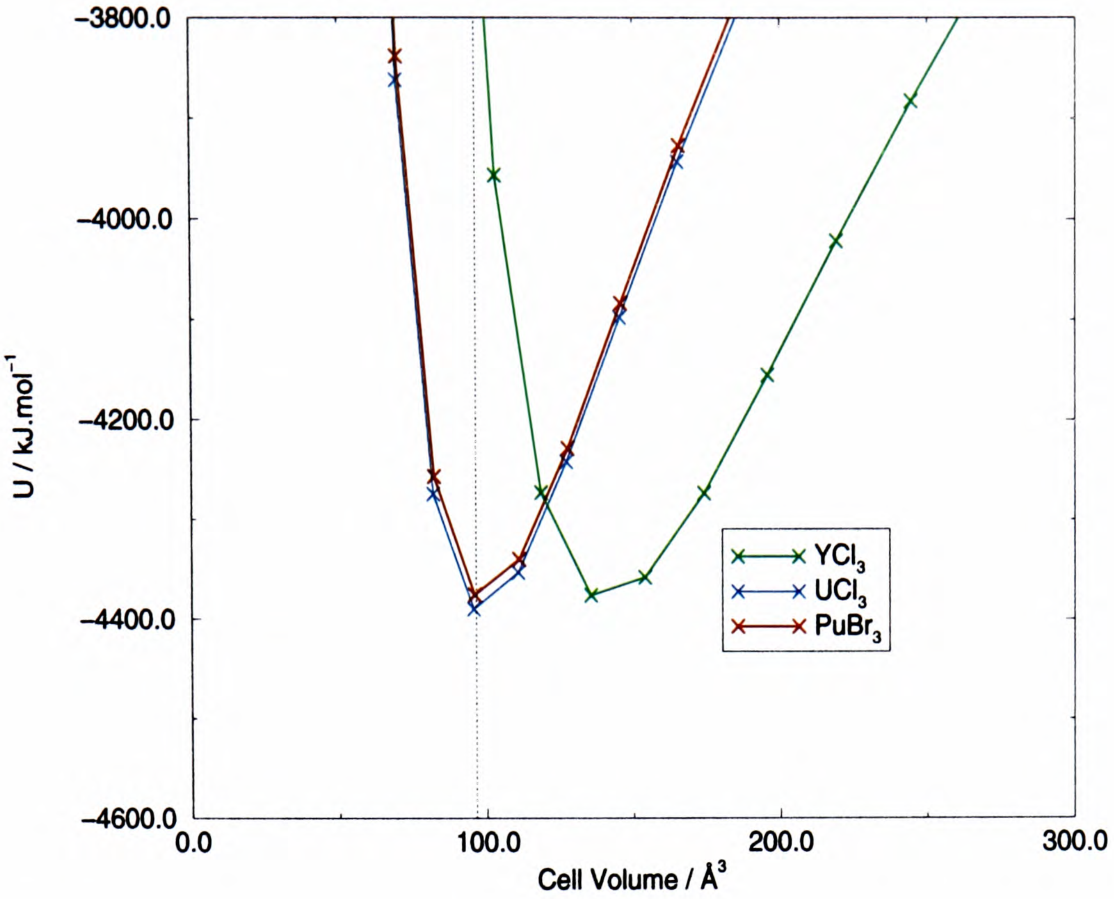

Figure 6.7: *Energy-volume curves for three phases of* $TbCl_3$ *(simulated with* Cl^{3}_{POT}*)*

6.6 $TbCl_3$

6.6.1 Crystal Phase

Whilst there is no lattice energy data available for $TbCl_3$ it is interesting to see how the decrease in cation size has affected the crystal structure predictions. The energy-volume curves are shown in figure 6.7. The simulated cell volume is in good agreement with experiment with the $PuBr_3$ structure being stabilised with respect to the YCl_3 phase. However, the UCl_3 structure is found to be lower in energy then the $PuBr_3$ structure.

As observed by Gunsilius *et al* [90] $TbCl_3$ can be prepared in a metastable UCl_3 crystal structure. On heating to $\sim$ 700K a transition to the stable $PuBr_3$ structure was observed. Given that the UCl_3 and $PuBr_3$ phases are so close in energy we hope to be able to observe such a purely temperature driven transition. To do this we will make use of the Parrinello-Rahman constant stress technique with a fully flexible cell which, in chapter 4, was shown to model phase transitions between alkali halide phases very well.

The simulation was carried out on a 1120 ion system with the PIM $TbCl_3$ potential. The crystal was set up in the almost hexagonal UCl_3 phase with simulation cell lengths of 28.4, 29.5 and 36.9Å and two cell angles of 90° and one of 120° corresponding to an initial volume of 95.6$\AA^3$ per $TbCl_3$ unit. The simulation was run for 2.5ps (at 580K) in an NVT ensemble to allow for suitable equilibration. After this time the cell was allowed to undergo full relaxation with barostat masses, W and W_{g0}, both of 50000au. The applied external pressure was equal to that obtained for the 2.5ps NVT equilibration time. The integrity of the UCl_3 structure was maintained for over 1.25ps of dynamics at 580K in the constant stress ensemble, as monitored through the cell lengths, angles and pdfs. At this point the simulation temperature was raised to 700K corresponding to the experimental transition temperature. Over the next 2ps of dynamics the cell lengths and angles evolved systematically. The final cell had boxlengths of 26, 27 and 41 Å and angles of 88, 90 and 97° corresponding approximately to an orthorhombic cell expected for the $PuBr_3$ structure. This transformed structure had a volume of 100.99 $\AA^3$ per $PuBr_3$ unit. Again, as for the B1→B2 transition in the alkali halides (4.3.1) the final $PuBr_3$ structure must contain defects as the number of ions in the cell, ideal for the UCl_3 startup, is incommensurate with this structure. Slices through the simulation cell at three stages in the transition are shown in figures 6.8(a)-(c). Starting from the UCl_3 structure (6.8(a)) with all Tb-Cl bond lengths equal, on increasing the temperature a layered structure can be seen to form (6.8(c)). Figure 6.8(b) shows an intermediate structure observed just after the rise in temperature to 700K. The breaking of the 'interlayer' metal-anion bonds in this structure is clear. The Tb ions in the resulting structure have the same coordination as in the ideal $PuBr_3$ structure *ie.* 8 anions at approximately equal distance and a further anion in the adjacent layer at a slightly larger distance. However, by comparison with the ideal $PuBr_3$ structure (figure 2.2) it can be seen that the chains are highly distorted.

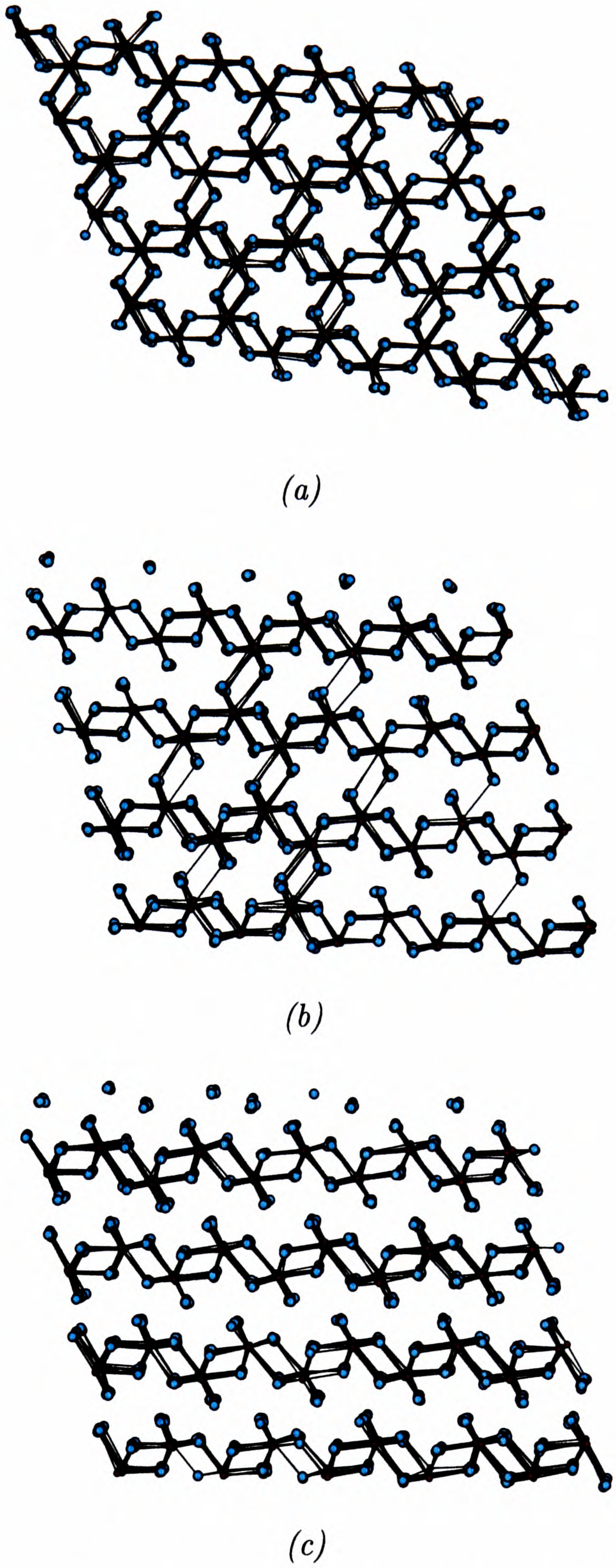

(a)

(b)

(c)

Figure 6.8: *Temperature driven transition from* UCl_3 *phase* → $PuBr_3$ *phase in* $TbCl_3$. *(a) Thermally equilibrated* UCl_3 *startup. (b) Intermediate structure just after the temperature rise to 700K. (c) Final (approximately* $PuBr_3$*) structure.*

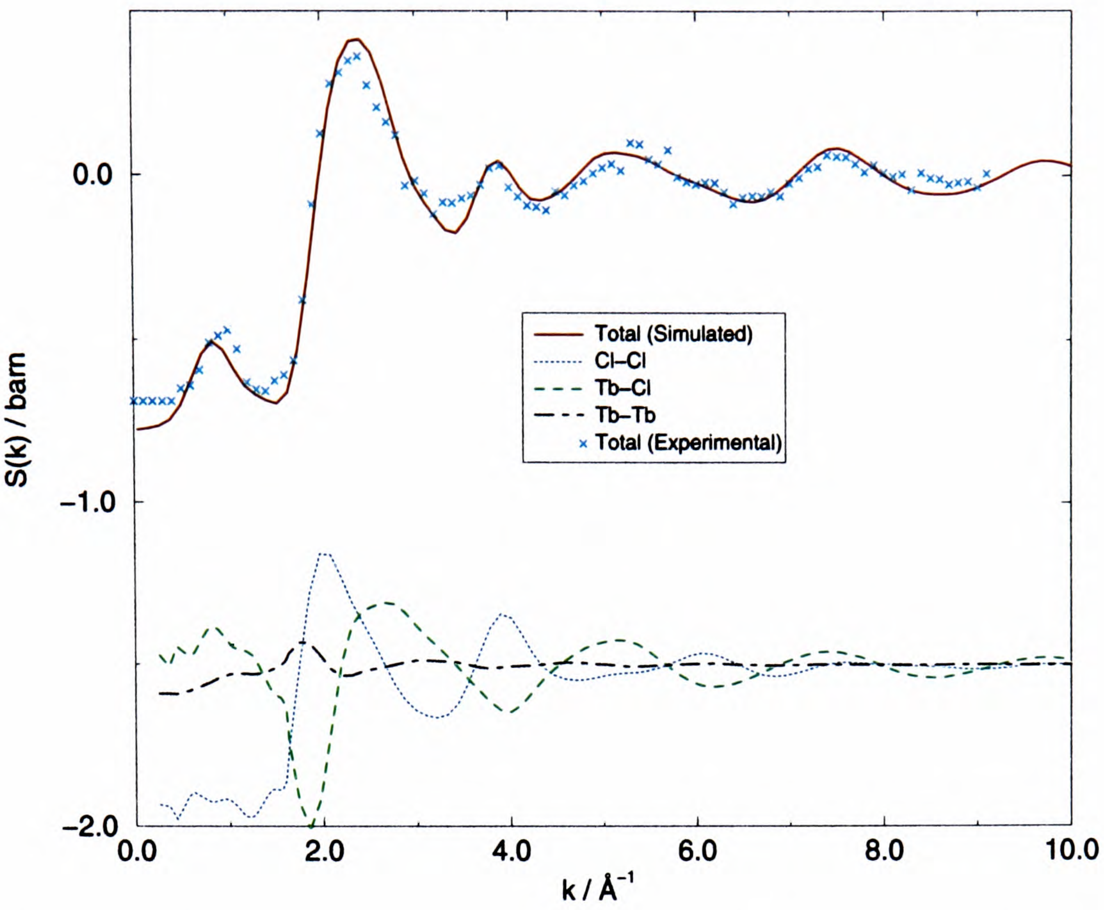

Figure 6.9: *Comparison of simulated and experimental neutron weighted structure factors for* $TbCl_3$ *(simulated with* Cl^3_{POT}*) shown with the neutron weighted partials shifted by a constant of -1.5.*

6.6.2 Liquid Phase

Tb^{3+} is representative of the intermediate-sized rare-earth ions. In figure 6.9 the experimental and simulated total neutron weighted structure factors for the melt are compared along with the simulated neutron weighted partial structure factors. The quality of agreement is excellent, similar to that reported above for $LaCl_3$. The position of the pre-peak is good, notice that it has shifted to lower k compared to $LaCl_3$. At first sight, this is somewhat surprising as a shift to lower k means that the corresponding real space feature has moved to larger r, whereas the size of the cation has become smaller on passing from La to Tb. We will discuss how the reduction of cation size increases the lengthscale of the intermediate range order below.

6.6.3 Problems with truncation of experimental data

The total and partial pdfs for $TbCl_3$ are shown in figure 6.10. An emerging trend in the current simulation results is an excessive 'sharpness' of peaks in the total $G(r)$ compared to those generated from experiment. In order to assess the rôle of the model in this difference, additional analysis is performed which mimics the experimental procedure. In the experiments the diffraction data is gathered over a restricted range of scattering angles. As a result, the consequent Fourier transformation to give the real space distribution functions, is subject to truncation errors, that is, the spurious oscillations arising from the finite cutoff in reciprocal space. In the case of the $TbCl_3$ data, this limitation is likely to be quite severe as the data was gathered only to 10 $Å^{-1}$ (as it had to be corrected for a substantial amount of magnetic scattering). Although such oscillations are most visible for separations less than the distance of closest approach, they may also affect the width and height of the peaks at larger values of r. We concentrate on this system in order to assess the magnitude of the truncation errors.

In order to investigate the effects of this truncation error we have calculated a pdf by back-transforming the *simulated* total structure factor, applying a cut-off in the transform in order to replicate the experimental procedure. We have fixed the value of this cut-off by requiring that the low r oscillations in the simulation transform match those in the experimental data in period and phase, which occurs with a cut-off at 8 $Å^{-1}$. The results for $G_{tot}(r)$ obtained in this way are shown by the magenta line in the upper panel of figure 6.10. It can be seen that these simulation results are much closer to the experimental data in the width and height of the first peak. This suggests that at least part of the discrepancy between the heights and widths of the first peaks, is due to broadening of the experimental real space data through truncation of the back-transform. However, it does not appear to be the whole story. For $TbCl_3$

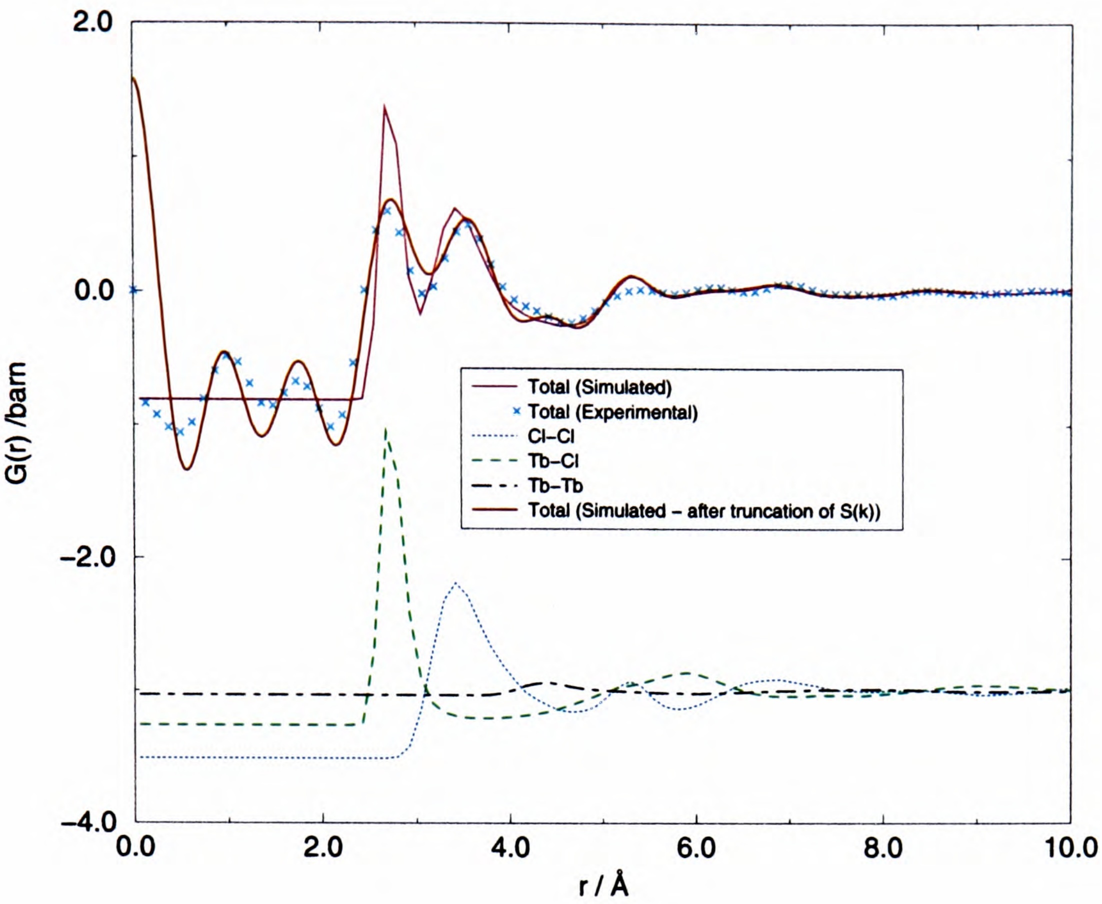

Figure 6.10: *Comparison of simulated and experimental pdfs for* $TbCl_3$ *(simulated with* Cl^3_{POT}*) with the partial pdfs shifted by a constant of -3. Also shown is the simulated total pdf obtained after truncating the structure factor at the experimental cutoff and back transforming*

the cut-off k-value is particularly small: applying the same procedure as above to the other systems data produces a much smaller degree of broadening and leaves the first peak in the simulation $G_{tot}(r)$ still significantly narrower than the experimental function.

6.7 $DyCl_3$

6.7.1 Isotopic Substitution in Neutron Diffraction

Recently, Adya *et al* [10] have reported neutron results for three samples of molten $DyCl_3$ with different isotopic compositions and have used them to separate partial structure factors and radial distribution functions. These partial structure factors enable us to make clear the role of polarization effects in the

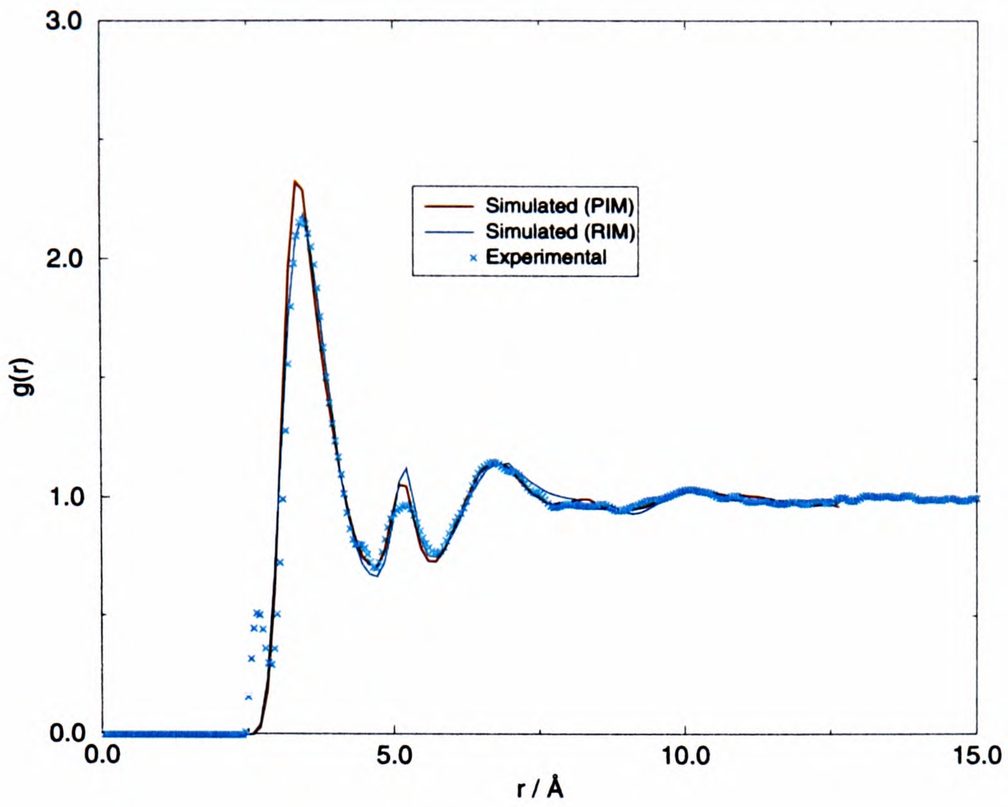

Figure 6.11: *Comparison of the partial Cl-Cl pdf obtained with the PIM and the RIM potentials along with that obtained from Fourier transformation of the experimental neutron partial Cl-Cl structure factor for* $DyCl_3$.

interaction potential in generating good agreement of the simulated and experimental data. Partial pdfs obtained with PIM and RIM potentials are compared in figures 6.11-6.13 with those obtained from fourier transforms of the neutron partial structure factors. The RIM potential has exactly the same short-range terms as the PIM one, it differs only through the omission of the polarization terms.

The $g_{\mathrm{Dy-Cl}}$ and $g_{\mathrm{Cl-Cl}}$ are predicted to have very similar shapes in the RIM and PIM simulations, which indicates that the spatial distribution of the anions is little affected by the polarization effects. In both cases, the predicted pdfs agree well with the experimental ones. The mean coordination number of Cl^- around Dy^{3+} (obtained by integrating $g_{\mathrm{Dy-Cl}}$ up to 3.5Å) is found to be 6.6 (section 6.11.1) and the distribution of Cl-Dy-Cl bond angles is consistent with octahedral coordination. Despite the similarity of $g_{\mathrm{Dy-Cl}}$ and $g_{\mathrm{Cl-Cl}}$ in the RIM and PIM models, the results for $g_{\mathrm{Dy-Dy}}$ in the two simulations are very different. This indicates that, as has been found for MX_2 systems [48], anion polarization

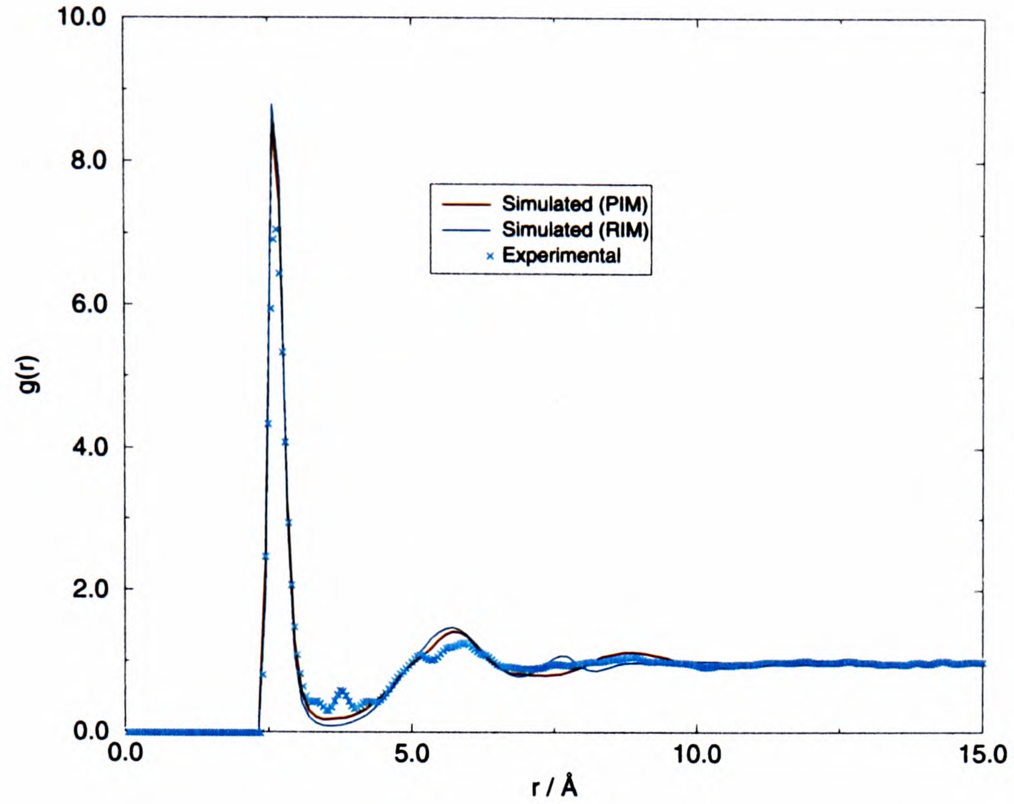

Figure 6.12: *Comparison of the partial Dy-Cl pdfs obtained with the PIM and the RIM potentials along with that obtained from Fourier transformation of the experimental neutron partial Dy-Cl structure factor for* $DyCl_3$.

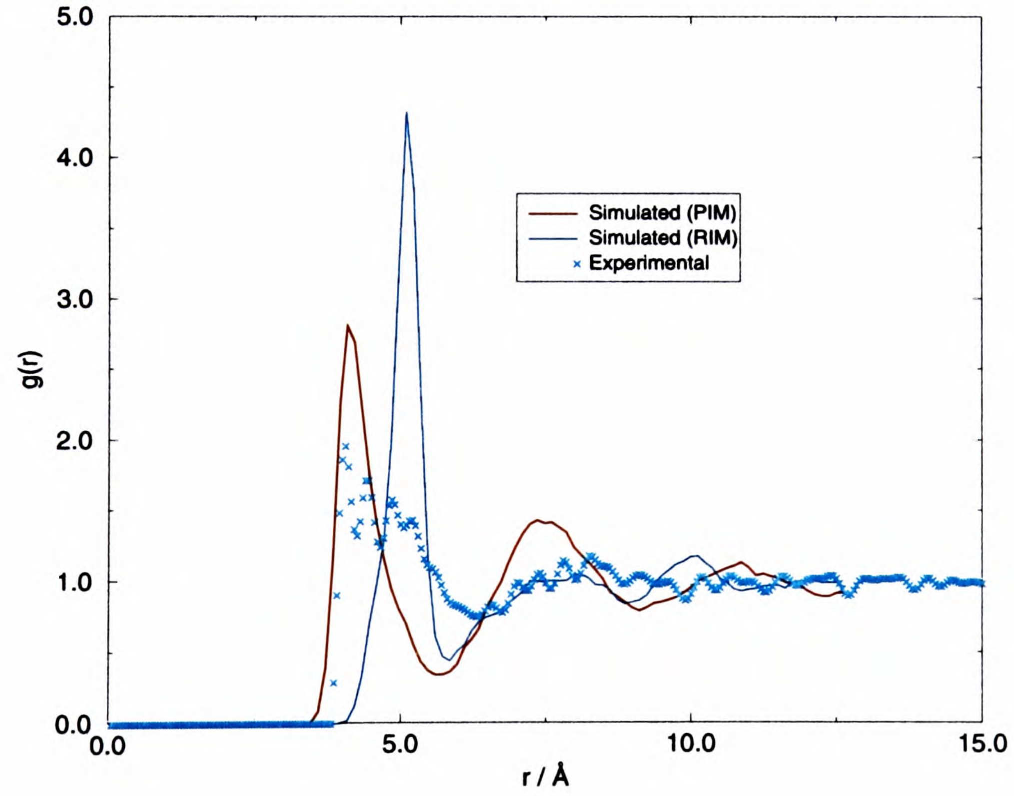

Figure 6.13: *Comparison of the partial Dy-Dy pdfs obtained with the PIM and the RIM potentials along with that obtained from Fourier transformation of the experimental neutron partial Dy-Dy structure factor for* $DyCl_3$.

has a major effect on the way the local coordination polyhedra (octahedra in this case) are connected together, since the connectivity strongly affects the distance of closest approach of the cations. The PIM result for $g_{\mathrm{Dy-Dy}}$ is similar to that obtained experimentally. The first peak is broad and appears to have a shoulder at distances approximately equal to the first peak in the RIM g_{Dy-Dy} (in the experimental data this is more clearly resolved); the first of these at ~4.0Å strongly overlaps the first peak in $g_{\mathrm{Cl-Cl}}$. One would instinctively expect that the strong coulombic repulsion between Dy^{3+} ions would force them to larger separations than for Cl^{-}–Cl^{-}. For the RIM, the first peak in $g_{\mathrm{Dy-Dy}}$, conforms to this expectation since it lies in the first minimum of $g_{\mathrm{Cl-Cl}}$ and it is very sharp, implying that it is determined by strong repulsive interactions. We experimented with many combinations of RIM potential parameters but invariably failed to reproduce the shape of $g_{\mathrm{Dy-Dy}}$ observed experimentally. It is noteworthy that the shoulder on the high separation side of the first peak in the PIM and the second peak in the experimental $g_{\mathrm{Dy-Dy}}$ appears at roughly the same position.

Following our general discussion regarding the role of polarization effects (section 1.2.1) we may anticipate that the first peak in the PIM g_{DyDy} is associated with edge-sharing units, in which pairs of Dy^{3+} cations are held relatively closely by two bridging anions, whilst the shoulder is associated with vertex sharing units and hence corresponds to the first peak observed in the RIM.

It can be seen that the elimination of the polarization effects removes the edge-sharing configurations and moves the peak corresponding to vertex-sharing to larger r – indicating a straightening of the M-Cl-M bond. (See figure 1.5 for an illustration of edge-, vertex- and face- sharing octahedra). Figure 6.14 shows the M-Cl-M bond-angle distribution, which further confirms this picture. In each case two features are prominent, one at angles around 100 degrees and one at larger angles. The feature at larger angles is due to corner sharing octahedra and dominates in the RIM and the feature at low angles is due to edge sharing octahedra and dominates in the PIM.

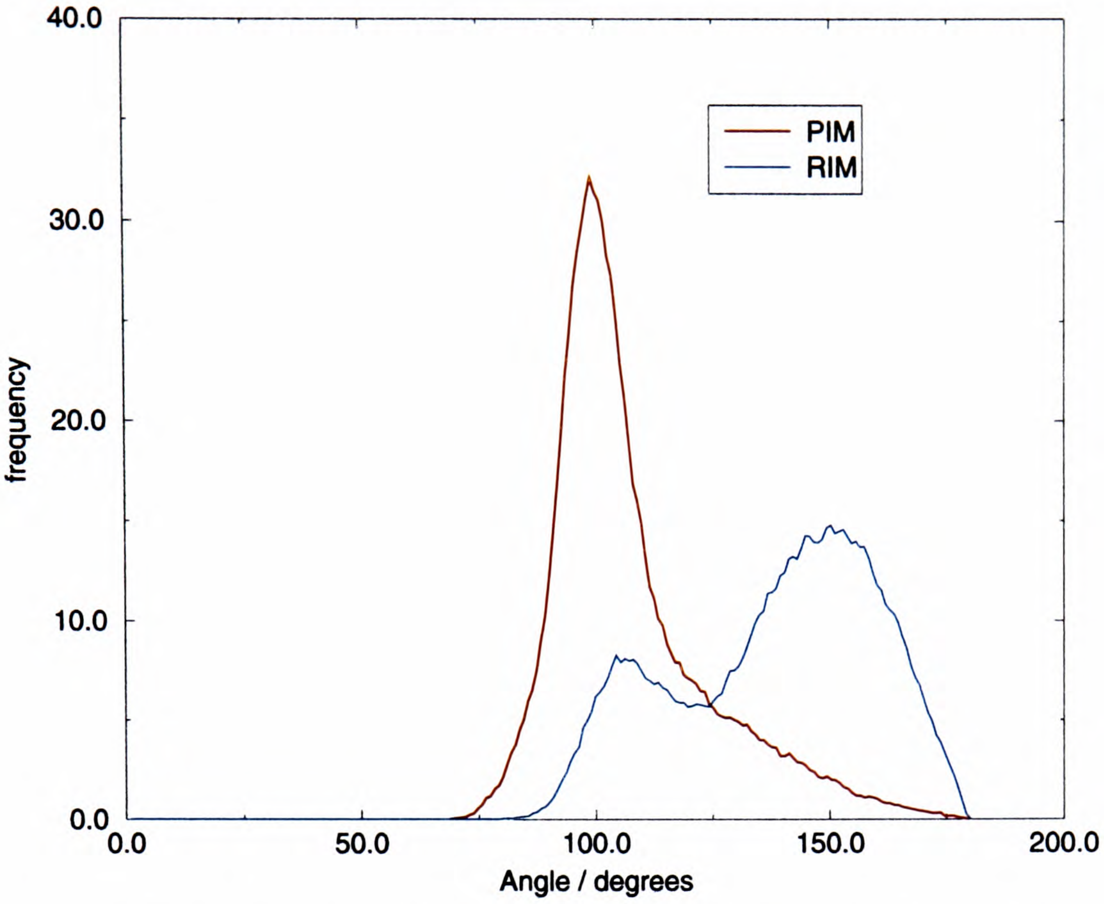

Figure 6.14: *Dy-Cl-Dy Bond angle distibution for $DyCl_3$ calculated with the RIM and PIM.*

6.7.2 The $DyCl_3$ structure factors

In figure 6.15 we show the total neutron structure factor for $DyCl_3$ [10], observed for the natural isotopic abundances, and as calculated using the PIM. A prominent pre-peak is seen in the PIM results. Its position and size are in very good accord with the experimental pre-peak. There is also an apparent pre-peak present in the RIM results (figure 6.16), though it is shifted to slightly larger k-values.

Considering this pre-peak a little further, the feature in the RIM structure factor can, in fact, be attributed to a 'normal' principal peak in g_{DyDy} (figure 6.13) in that it's position, at 1.5Å is $\sim 2\pi$ divided by the nearest-neighbour Dy-Dy separation of ~5Å. The intermediate-ranged ordering of the Dy^{3+} cations in the RIM can be understood simply in terms of the large cation charge compared to the anion. As a result, a major driving force in these systems, modelled with a RIM, is for the highly charged cations to stay well away from each other - the system is strongly charge-ordered giving the near linear M-Cl-M triplets observed in figure 6.14. The effect of polarization, as discussed in the previous section, is to screen the M-M Coulombic interactions and hence reduce the nearest-neighbour M-M separation. As a result, the pre-peak appears to move to smaller scattering angles (lower k) than that predicted by the RIM. Furthermore, the position of the PIM pre-peak is no longer simply related to the nearest-neighbour cation-cation separation. This apparent paradox can be resolved by relating these observations to those for systems of stoichiometry MX_2 [48]. In the RIM, the dominance of the M-M Coulombic repulsions leads to an approximately uniform cation density. The inclusion of the anion polarization effects acts to bring pairs of cations closer together and so creates regions of high and low cation density on an intermediate lengthscale. As a result, as can be seen from figure 6.16, the RIM pre-peak actually splits in the PIM giving a peak at at $\sim 2\text{Å}^{-1}$, which corresponds to the nearest-neighbour Dy-Dy separation, and a 'true' pre-peak at $\sim 1\text{Å}^{-1}$ resulting from the intermediate ranged fluctuations in the cation subdensity.

6.8 YCl_3

Y^{3+} is similar in size to Dy^{3+}, and Ho^{3+} and Er^{3+}. $HoCl_3$ and $ErCl_3$ were studied alongside YCl_3 in Wasse and Salmon's work [13,15] , and shown to exhibit similar structural features. YCl_3 has earlier been studied by Saboungi and co-workers [7]. In figure 6.17 we compare the two experimental total neutron-weighted structure factors with that predicted from the simulation model. Except for a substantial disagreement at low k, affecting the height of the pre-peak, the two experimental structure factors agree very well. Note that this feature is again shifted to low k relative to $LaCl_3$, $TbCl_3$ and $DyCl_3$ and that it has become more prominent as the cation size is reduced. A comparison of the calculated total structure factor with the neutron weighted partials, figure 6.17, shows that

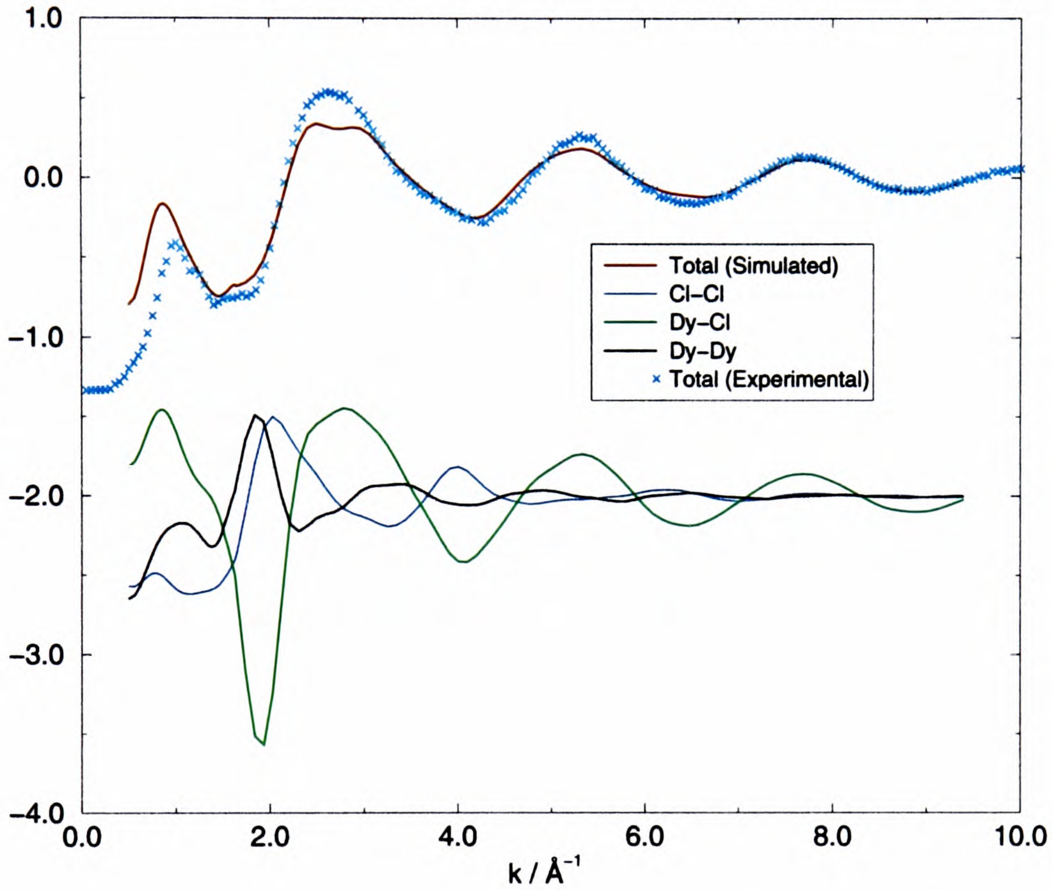

Figure 6.15: *Comparison of total neutron-weighted structure factors for* $DyCl_3$ *obtained from the PIM potential* (Cl^2_{POT}) *and the experiment. The partial structure factors are shown shifted by a constant of -2.*

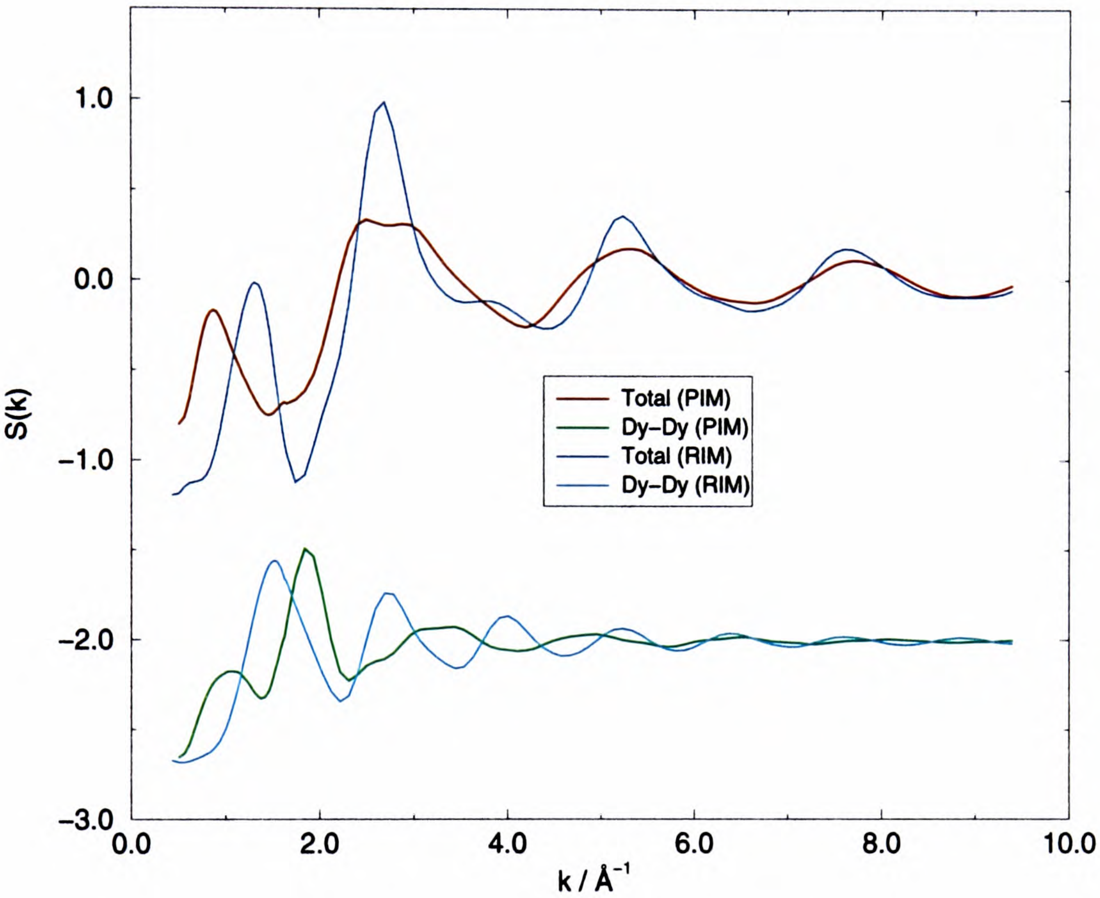

Figure 6.16: *Comparison of total neutron-weighted structure factors and metal-metal partials for* $DyCl_3$ *obtained from the RIM potential* (Cl^2_{POT}) *and the PIM potential* (Cl^2_{POT}).

the pre-peak is caused predominantly by the cation-cation and cation-anion correlations.

It should be recalled that, unlike the remaining systems, for YCl_3 and $DyCl_3$ the same Cl-Cl interaction potential is being used as is appropriate for the FT potential (Cl^2_{POT}). The excellent agreement between the shapes of the very broad principal peaks in the total structure factors owes much to this exception. Were the structure factors for YCl_3 and $DyCl_3$ to have been calculated with the "normal" Cl-Cl potential (Cl^3_{POT}), used for the other systems, the quality of this comparison would have been much poorer (similar to that shown in the calculations done with the Tatlipinar potential, as in figure 1.9). The justification for making an exception of Y and Dy was the very close similarity of the liquid and solid densities for these materials. The very close similarities of the environment of the Cl^- ions is evident from the partial radial distribution functions, shown for YCl_3 in figure 6.18. The sharp first peak in the Y-Cl rdf gives a coordination number of 6.6, which is very similar to that in the crystal. Octahedral coordination was shown explicitly for Dy in the last section from the bond-angle analysis.

6.9 $ScCl_3$

Comparison of simulated and experimental structure factors and pdfs for $ScCl_3$ are shown in figures 6.19 and 6.20. $ScCl_3$ will be discussed extensively in the following chapter and so for now it is sufficient just to point out a couple of striking features in the reciprocal space data. The pre-peak now appears at very low-k and has a very large amplitude – comparable to that of the principal peak. The principal peak is now much broader than in any of the other systems studied. Notice that $ScCl_3$ melts with a large volume change, and is thus different from $DyCl_3$ and YCl_3. To obtain the good agreement with experiment shown, it is necessary to describe $ScCl_3$ with the general Cl-Cl potential (Cl^3_{POT}). Also

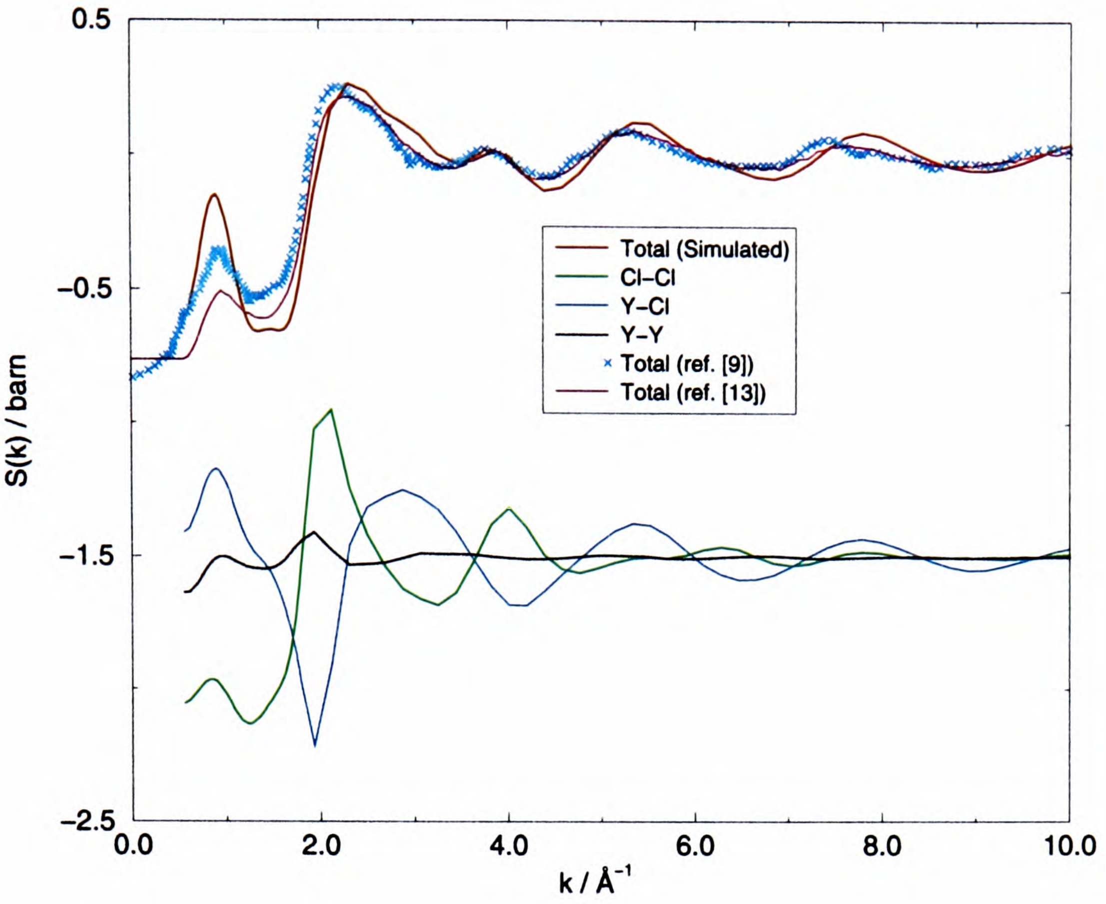

Figure 6.17: *Comparison of simulated and (two sets of) experimental total neutron weighted structure factors for* YCl_3*. The partial structure factors are shown shifted by a constant of -1.5*

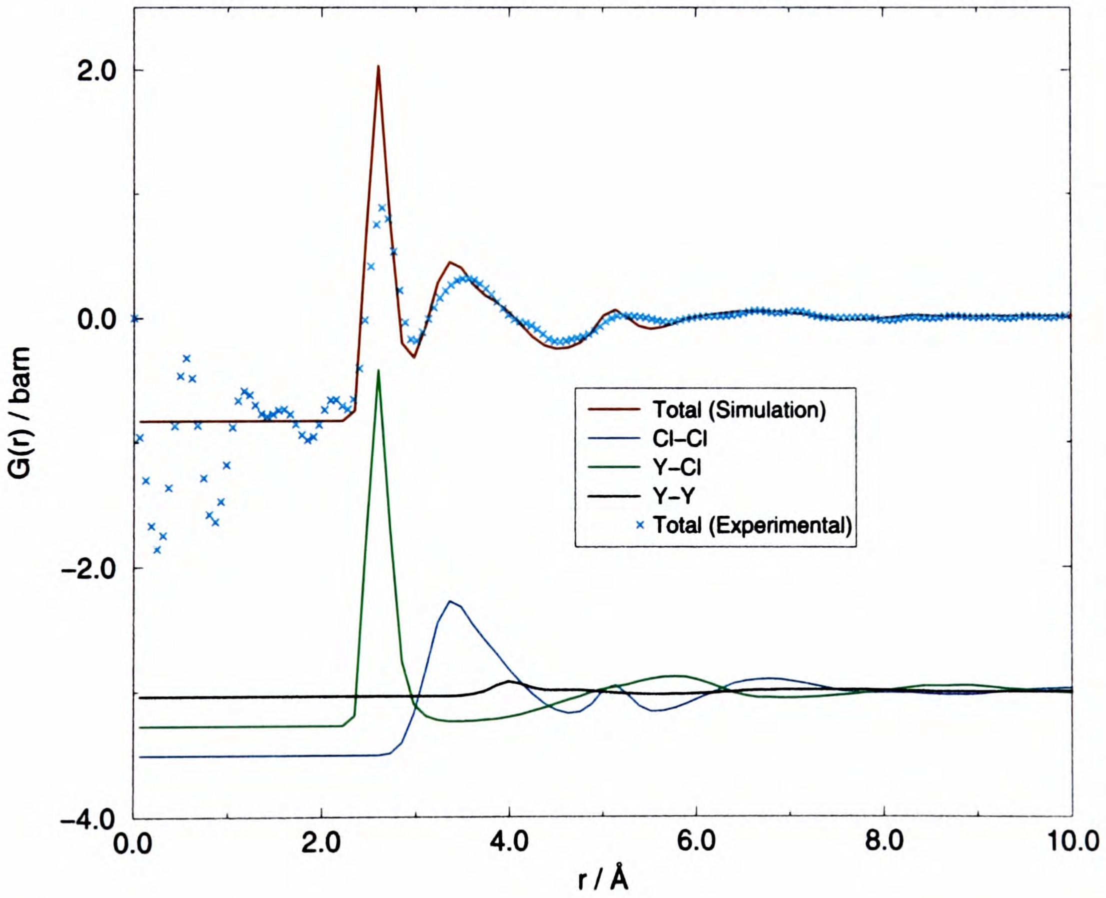

Figure 6.18: *Comparison of simulated and experimental total neutron weighted pdfs for* YCl_3*. The partials are shown shifted by a constant of -3*

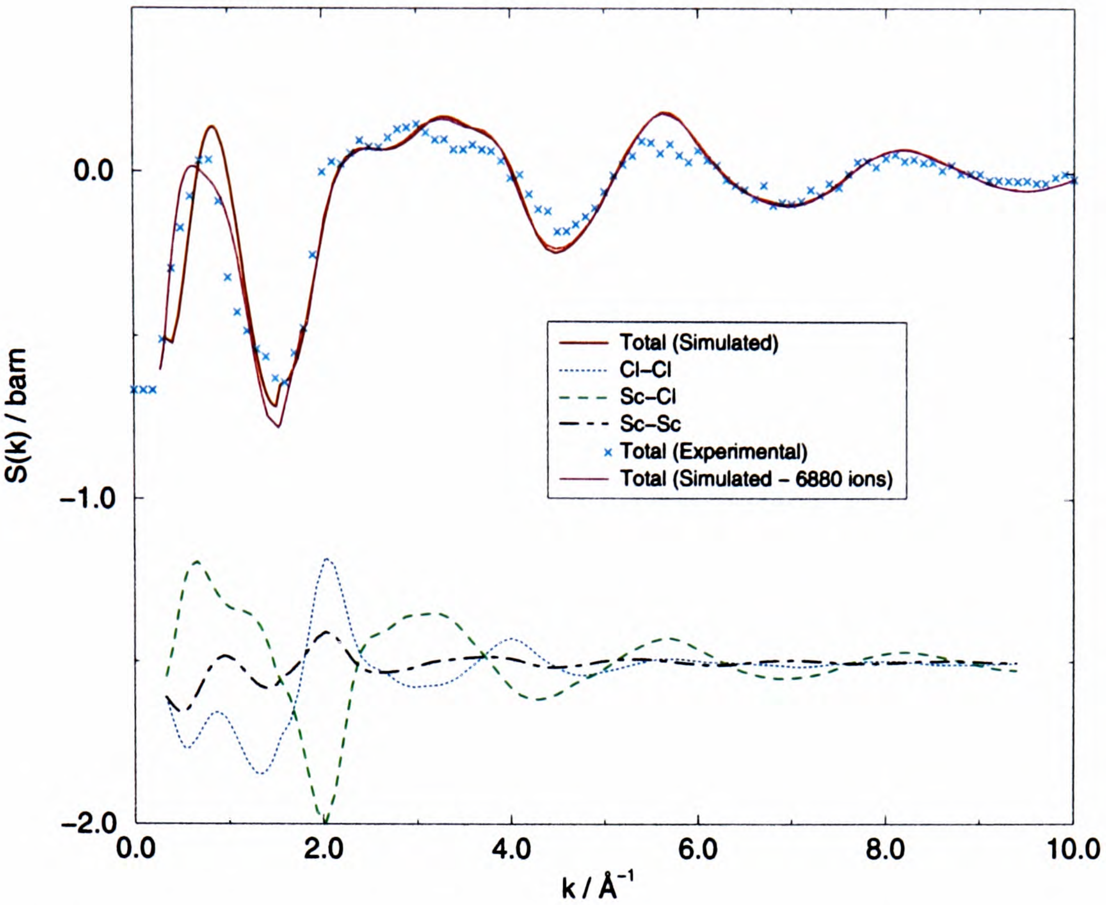

Figure 6.19: *Comparison of simulated and experimental total neutron weighted structure factors for $ScCl_3$. The partial structure factors are shown shifted by a constant of -1.5. Also shown is the total structure factor for a 6880 ion simulation of $ScCl_3$.*

shown in figure 6.19 is the total neutron weighted structure factor obtained for a simulation on 6880 ions. Beyond $\sim 2\text{Å}^{-1}$ the two total structure factors are very similar, the only noticeable difference lies in the position and height of the pre-peak. It will be seen in chapter 7 that $ScCl_3$ consists of chains of edge sharing $ScCl_n$ polyhedra. This improvement seen in the pre-peak in the large system simulation suggests that the length of these chains is of the order of the size of the simulation cell. Thus, in the small system we may be seeing the effects of the periodic boundary conditions [66] which are eradicated in the large system simulation.

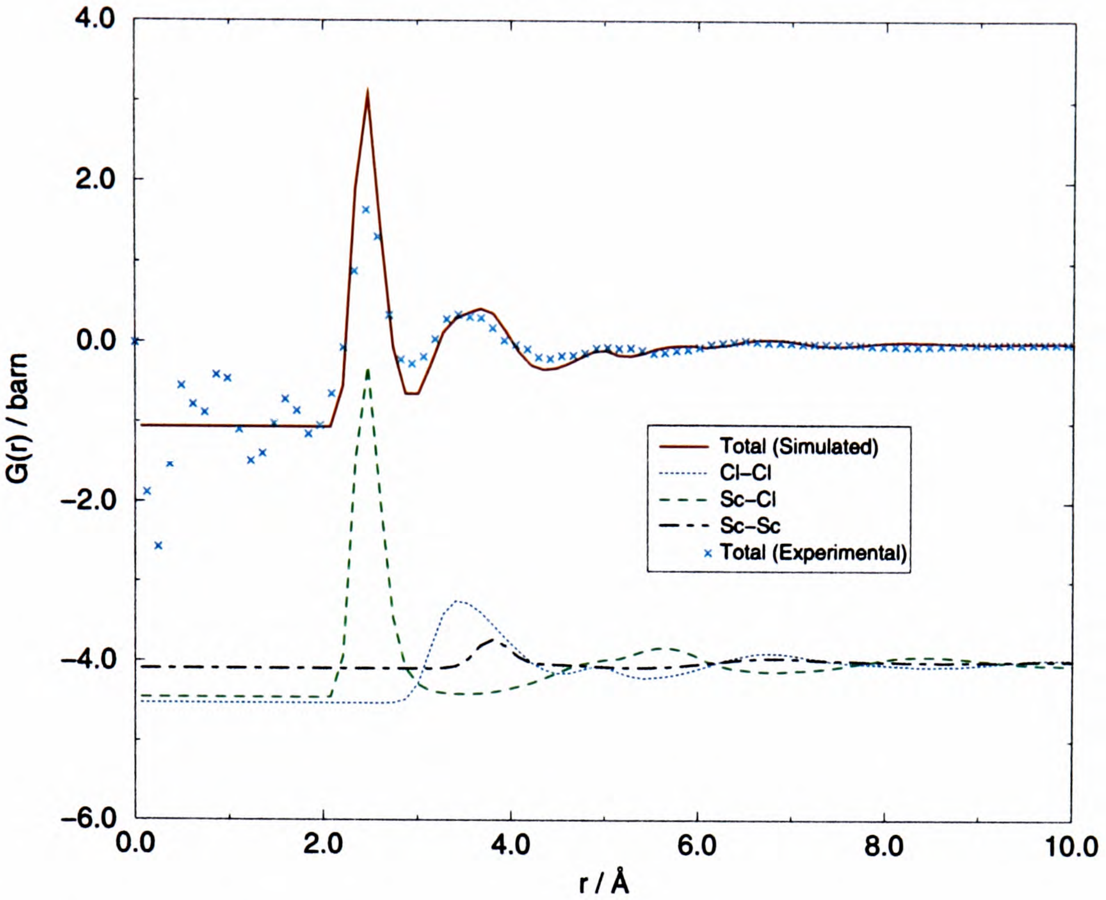

Figure 6.20: *Comparison of simulated and experimental total neutron weighted pdfs for $ScCl_3$. The partial pdfs are shown shifted by a constant of -4.*

6.10 $AlCl_3$ / $FeCl_3$

6.10.1 Crystal Structures

In chapter 2 we saw that the Tatlipinar potential (Cl^1_{POT}) predicted the $AlBr_3$ structure to be more stable with respect to the YCl_3 structure for $AlCl_3$. We now compare the energy-volume curves for the two different structures for $AlCl_3$ with all three Cl-Cl potentials considered (Cl^1_{POT}, Cl^2_{POT} and Cl^3_{POT}) in figure 6.21. As can be seen, use of the Cl^3_{POT} potential still predicts the $AlBr_3$ structure to be the most stable but the differences in energy between the two structures are now very small. Both the predicted volume and energy for YCl_3 are in good agreement with experiment. Following this trend, it would be expected that use of Cl^2_{POT} would reduce this energy difference even further. Indeed, with this potential the YCl_3 structure is now stabilised with respect to the $AlBr_3$.

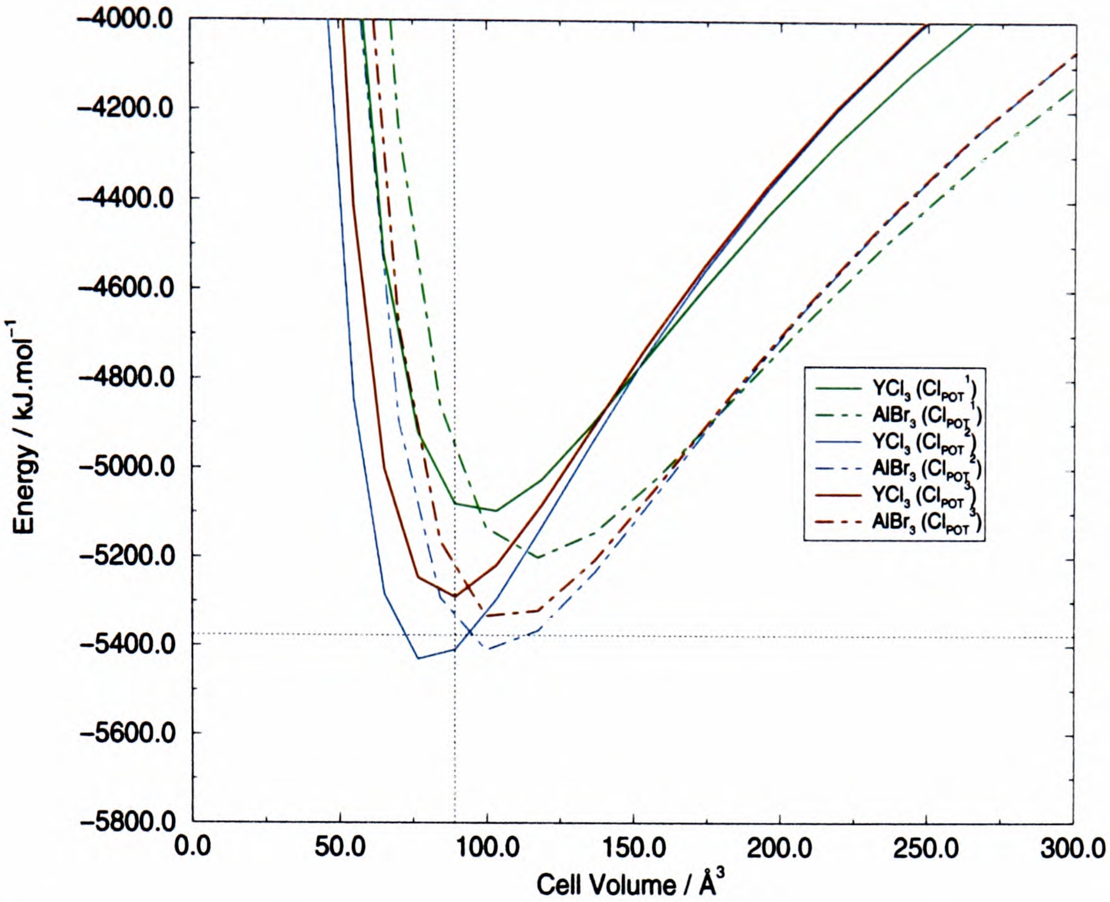

Figure 6.21: *Energy-Volume curves for* $AlCl_3$ *calculated for the* $AlBr_3$ *and* YCl_3 *phases with the three Cl-Cl potentials considered* (Cl^1_{POT}, Cl^2_{POT} *and* Cl^3_{POT}).

6.10.2 Liquid Structure

The $AlCl_3$ total structure factor, figure 6.22, shows an apparent prepeak which is present in all three partials. The prepeak in the calculated partial structure factors, in this case, is due to the existence of two independent lengthscales in the ion-ion correlations. The larger, which determines the low k peak position, is due to intermolecular distances and the shorter is due to the small separation between ions within a single dimer. Note it will be shown that the pre-peak position at $\sim 1\text{Å}^{-1}$ corresponds to the intermolecular (see figure 1.13) interactions. Use of the potential appropriate for YCl_3 and $DyCl_3$ (Cl^2_{POT}) resulted in a polymerization of the dimers.

As can be seen from table 6.6 in section 6.4.1, the total neutron structure factors for $AlCl_3$ and $FeCl_3$ are dominated by $S_{ClCl}(k)$. The overall agreement between the experimental and calculated neutron structure factors, compared in figure 6.22, is seen to be excellent. The only noteworthy discrepancy concerns

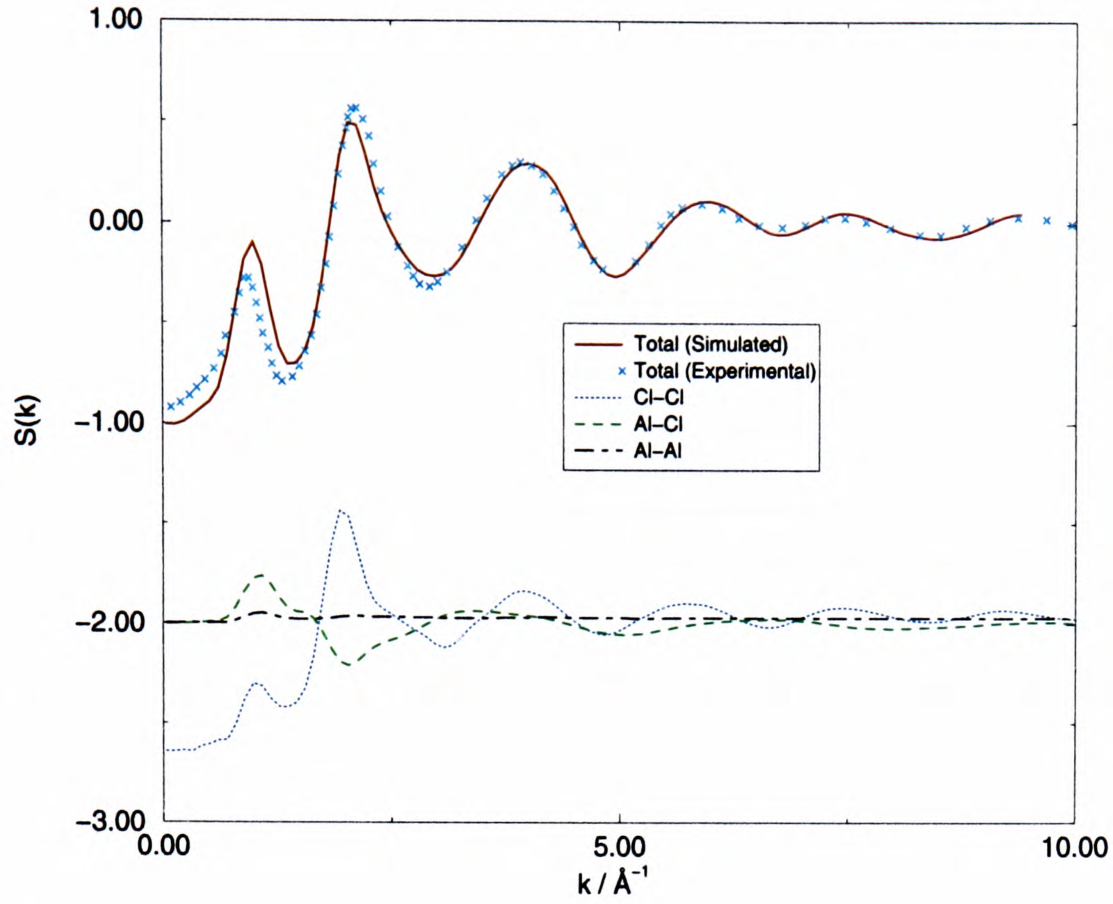

Figure 6.22: *Comparison of simulated and experimental total neutron weighted structure factors for $AlCl_3$. The partial structure factors are shown shifted by a constant of -2.*

the small difference in the position and width of the prepeak, which reflects the interdimer Cl-Cl correlations. This agreement shows that the experimental data *is* compatible with a melt structure which consists largely of dimers, despite the fact that inversion of the $AlCl_3$ data by Reverse Monte Carlo does not appear to force a dimer structure [8]. This could be due to two factors: the $S_{Al,Al}$ makes only a very small contribution to the total structure factor; secondly, the overlapping of the intra- and interdimer distances seen in the simulation Cl-Cl rdf implies that $S_{Cl,Cl}$ will not strongly distinguish between the dimeric liquid and a network of edge-sharing tetrahedra.

The calculated reduced intensity X-ray structure factor is compared with the experimental data for $FeCl_3$ in figure 6.23. The agreement between the two is excellent.

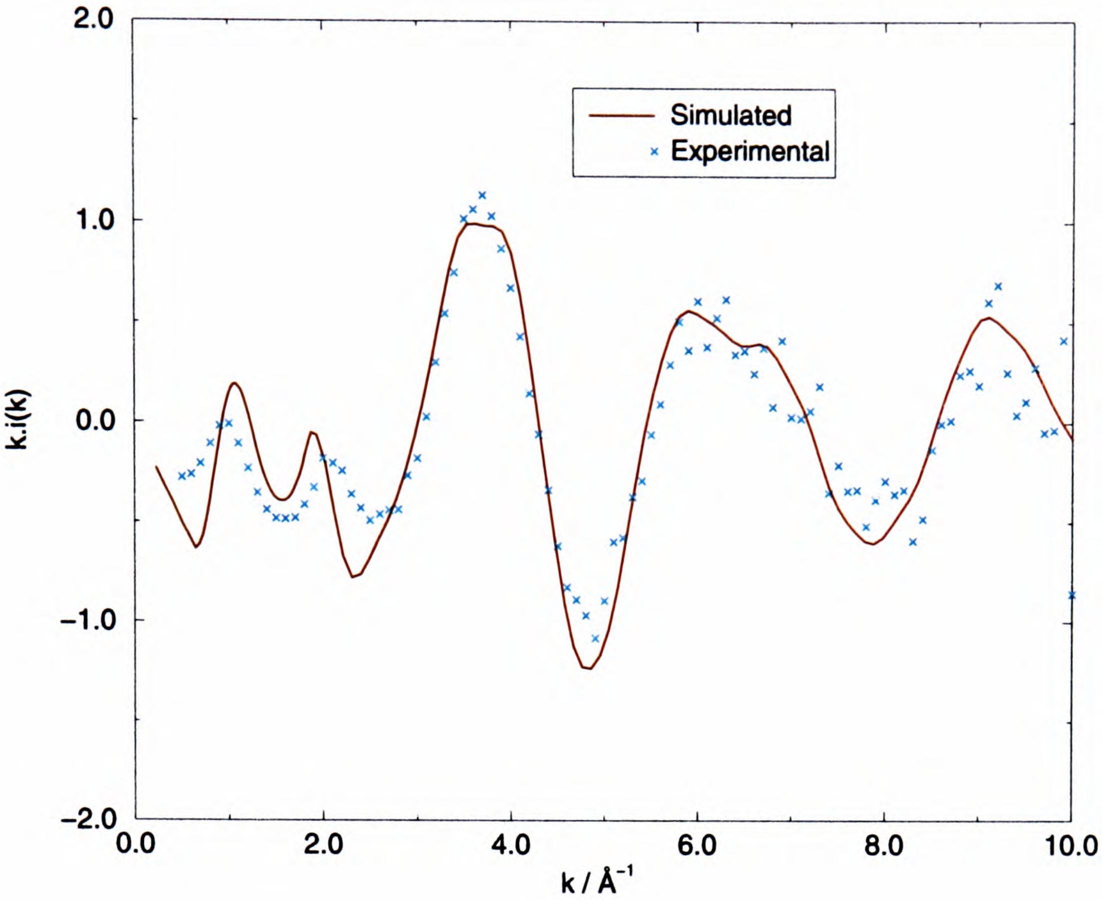

Figure 6.23: *Comparison of simulated and experimental X-Ray structure factors for $FeCl_3$.*

6.11 Influence of ion size on the liquid structure

Figures 6.24 to 6.28 show the pdfs for $LaCl_3$, $TbCl_3$, $DyCl_3$, YCl_3 and $AlCl_3$, respectively. An interesting evolution with cation size is evident which is worth considering in extended detail.

6.11.1 Coordination Number Analysis

A full coordination analysis of each of the melts obtained from the corresponding partial pdfs (using equation 6.14) is shown in table 6.7.

$$\bar{n}_{\alpha}^{\beta} = 4\pi n_0 c_{\beta} \int r^2 g(r) dr \tag{6.14}$$

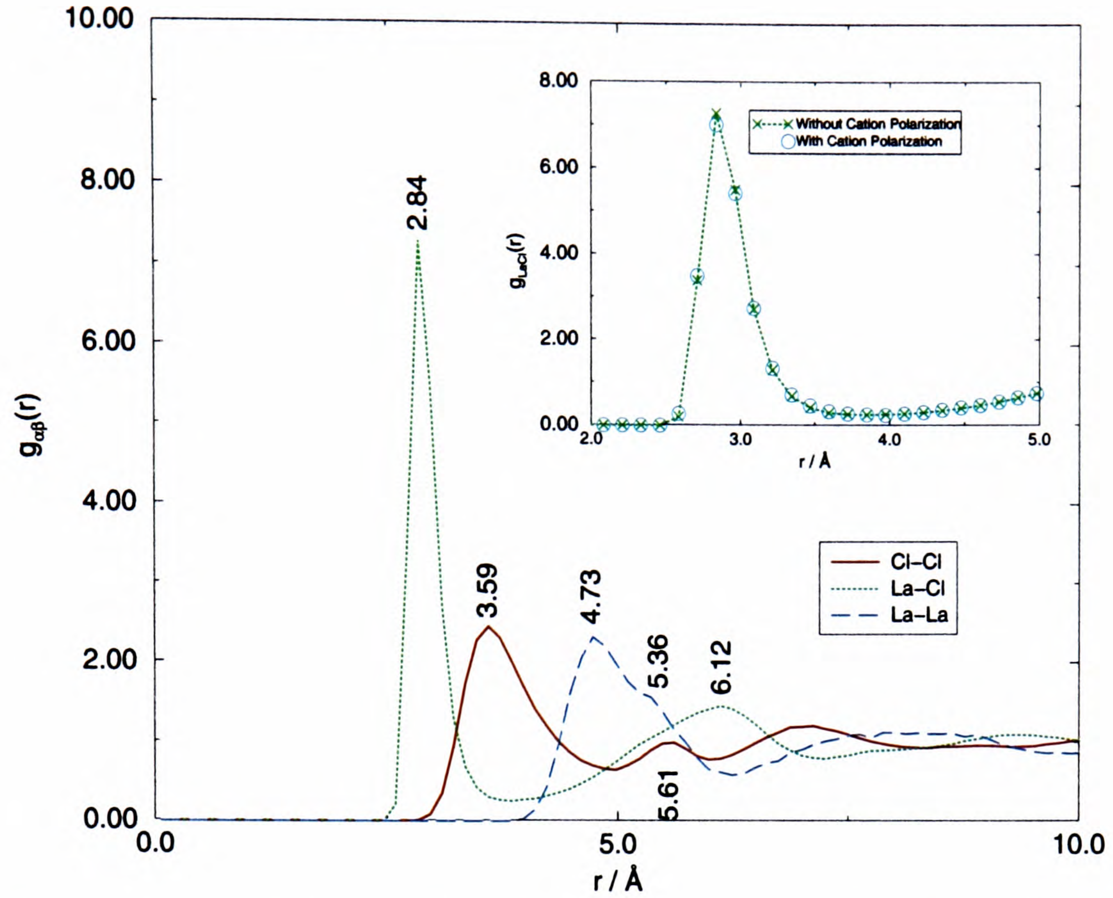

Figure 6.24: *Partial pdfs for* $LaCl_3$*. The inset shows the effect of including cation polarization on* $g_{LaCl}(r)$

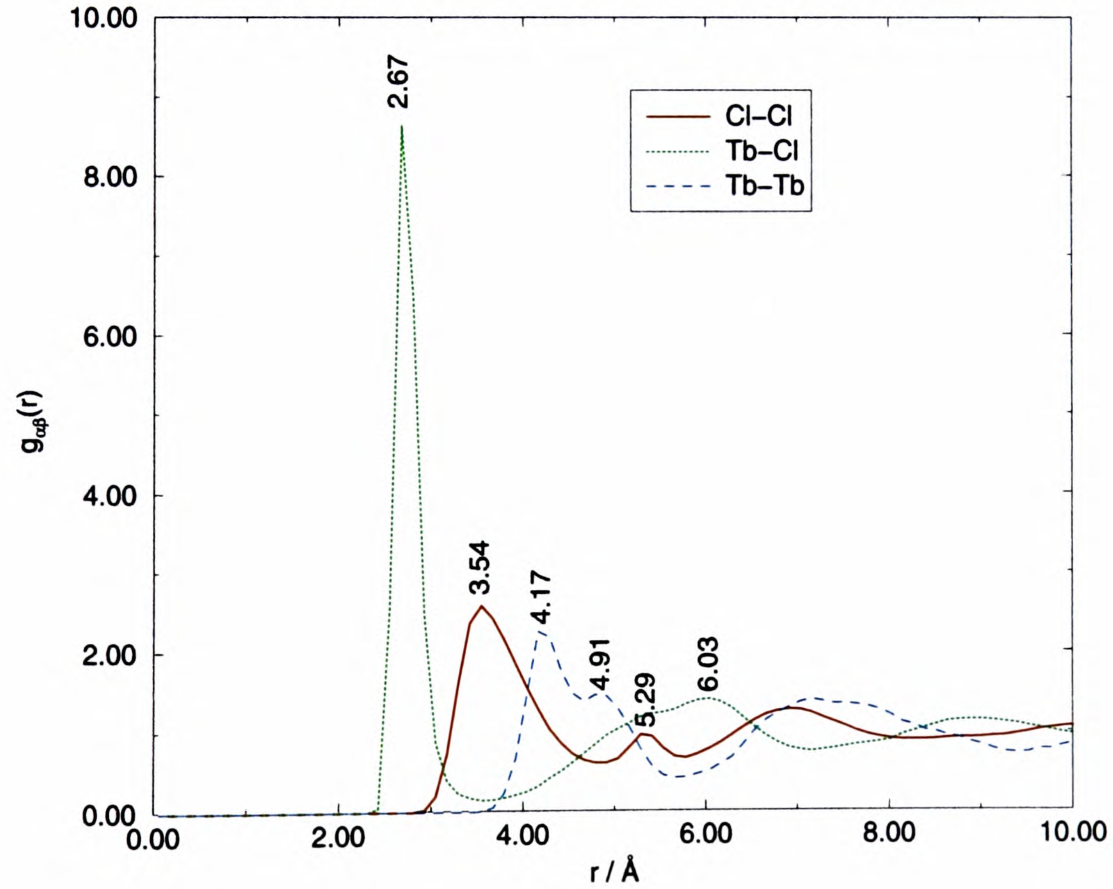

Figure 6.25: *Partial pdfs for* $TbCl_3$

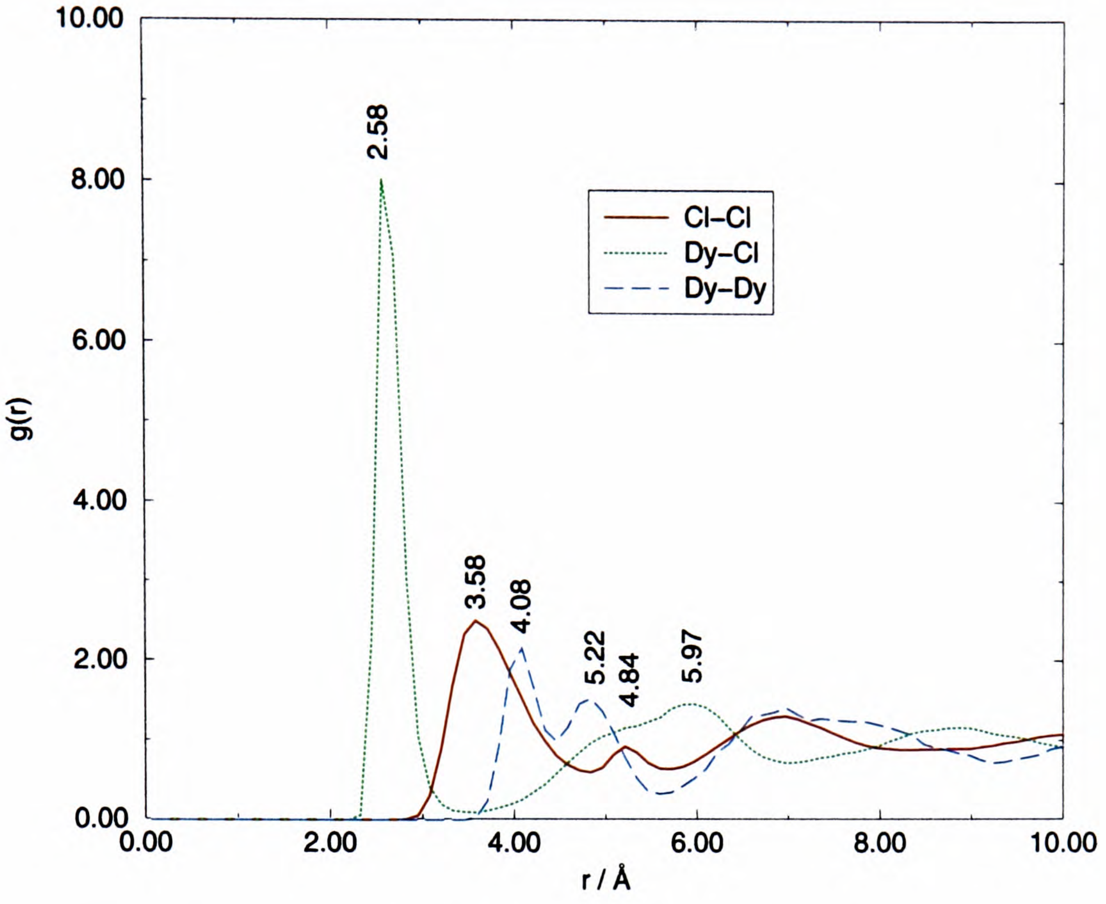

Figure 6.26: *Partial pdfs for* $DyCl_3$

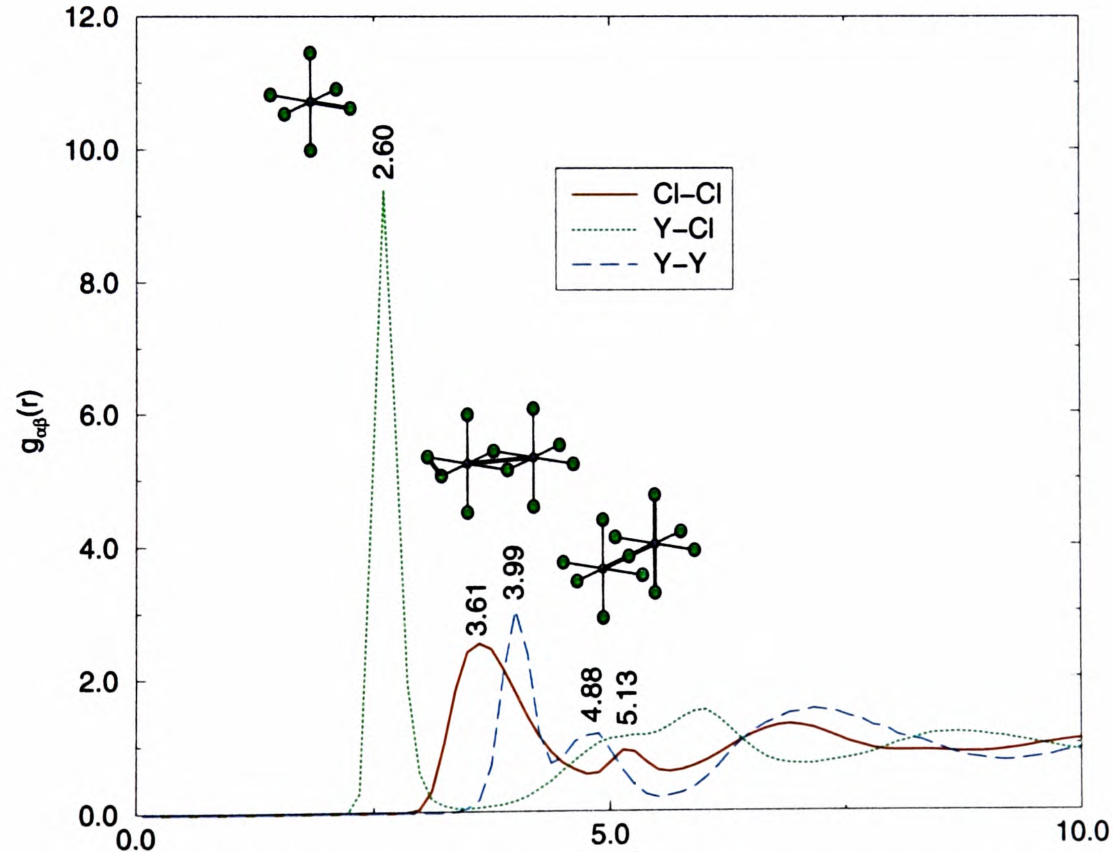

Figure 6.27: *Partial pdfs for* YCl_3*. Molecular models are given showing several of the Y-Cl, Y-Y, and Cl-Cl interion distances corresponding to the various peaks*

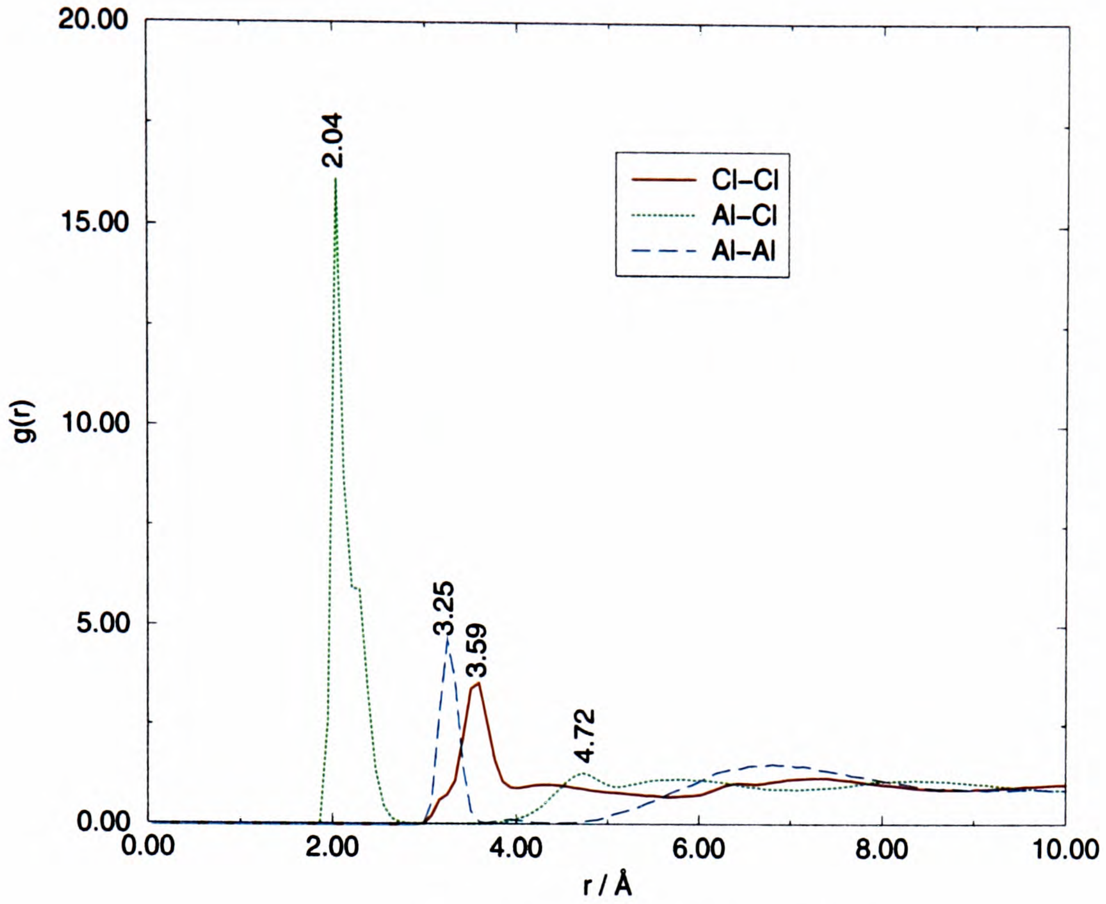

Figure 6.28: *Partial pdfs for* $AlCl_3$

6.11.2 Metal-Anion Correlations

Consider the shape of the cation-anion pdf, $g_{MCl}(r)$. Unsurprisingly, its first peak shifts inwards along the series La→Tb→Dy→Y→Al; more significantly, the depth of the first minimum also increases, indicating that the first coordination shell becomes more tightly bound and less likely to exchange anions. The pair distribution functions (pdf) are very similar for both $AlCl_3$ (figure 6.28) and $FeCl_3$ (and so we omit $FeCl_3$ here). They show a very sharp first peak in the cation–anion function. This is consistent with rigid molecular units. The first coordination sphere about a cation is very well defined and the extremely low, broad minima following the first peak suggests large kinetic barriers to the Cl^- exchange process. Integration over the first peak to this minimum gives coordination numbers of 7.9 for $LaCl_3$, 7.2 for $TbCl_3$, 6.6 for $DyCl_3$, 6.6 for YCl_3 and 4 for $AlCl_3$.

A polyhedral analysis of the structure of fluid configurations (counting the number of Cl^- neighbours within a cutoff radius about each M^{3+} ion), gives

System		R_{+-}Å	Range Å	N_{+-}	R_{--}Å	Range Å	N_{--}
$LaCl_3$	(SIM)	2.84	2.46-3.97	7.9	3.47	2.71-4.86	11.0
	(EXP)	2.93	2.50-3.86	8.2(2)	3.58	3.01-4.79	10.3(2)
$TbCl_3$	(SIM)	2.67	2.30-3.67	7.2	3.42	2.80-4.66	10.6
	(EXP)	2.67	2.27-3.05	7.5(2)	3.55	3.13-4.60	11.9(2)
$DyCl_3$	(SIM)	2.58	2.20-3.46	6.6	3.33	2.58-4.71	10.5
YCl_3	(SIM)	2.60	2.22-3.48	6.6	3.36	2.60-4.62	10.3
	(EXP)	2.64	2.27-2.95	6.2(2)	3.53	2.95-4.54	10.4(2)
$ScCl_3$	(SIM)	2.47	1.94-3.41	5.6	3.41	2.74-5.48	8.3
	(EXP)	2.48	1.96-3.01	5.2	3.42	–	–
$FeCl_3$	(SIM)	2.12	1.95-3.07	4.1	3.69	2.95-5.44	12.56
$AlCl_3$	(SIM)	2.04	1.78-2.99	4.0	3.51	2.82-5.15	9.30

Table 6.7: *Coordination analysis of MCl_3 systems, showing comparison of the peak positions ($R_{\alpha\beta}$) and coordination numbers ($N_{\alpha\beta}$) from experiment [11–15] and simulation. Range indicates the interval of integration for the determination of coordination numbers.*

a more reliable account. The linkages between the polyhedral units were then examined, by finding which pairs of metal ions have common Cl^- ions as neighbours.

These coordination number values are in good agreement with those deduced experimentally by Wasse and Salmon [11–13, 15], from their neutron diffraction data, despite the fact that the simulated first coordination shell appears more highly ordered than the experimental (as judged from the sharpness of the first peak in the total neutron-weighted pdf). Earlier X-ray studies had indicated that $LaCl_3$ was 6-fold coordinated [16] *i.e.* that there was a substantial change in coordination number on melting. Despite the finding of non-ideal coordination numbers for $LaCl_3$ and $TbCl_3$, which would suggest some jostling for positions by the anions within the first shell, the first peak in $g_{MCl}(r)$ is very sharp showing that, in the simulations, these conflicts are somehow resolved.

Cation Polarization

As we have commented above, the narrowness of this MX peak relative to that which is obtained by transforming the experimental diffraction data (with attendant cut-off problems) (figures 6.4, 6.10 and 6.18) is one of the apparent areas of disagreement between the simulation and experiment. As we have noted previously, a polarizable ion is more likely to sit in an asymmetric site than an unpolarizable one and we have therefore examined whether allowing the cation to be polarizable will increase the disorder of the coordination shell. This would have the effect of broadening the first peak in $g_{MCl}(r)$ and reducing it's height. In the inset to figure 6.24 the $g_{MCl}(r)$s with polarizable and unpolarizable cations are seen to be almost identical, from which we conclude that cation polarization has a negligible effect on the structures of the systems studied.

Another notable trend with decreasing cation size is the progressive sharpening and splitting of the second peak in $g_{MCl}(r)$. As we shall see, this is associated with a change in the connectivity of the network formed by joining the local coordination polyhedra around each cation. The cation–anion peak shows a shoulder for $AlCl_3$: this is due to the slight differences in bond length between the aluminium and the chlorides within a dimer depending on whether the chloride is bridging or terminal.

6.11.3 Anion-Anion Correlations

The anion-anion pdf $g_{ClCl}(r)$ has a very similar shape in all liquids, and the position of the first peak, which reflects the separation of adjacent ions within the first coordination shell of a single cation, is constant. The next peak reflects the correlations *across* the first coordination shell (see the key between the peak location and interion separation in figure 6.27). Note that it appears to have a larger area in $LaCl_3$ than in YCl_3, consistent with the higher coordination number of the former. Its position agrees quite accurately with twice the cation-anion separation in each case. The relationship between these lengths gives some insight into the structure of the first shell. For YCl_3 it is consistent with a nearly perfect octahedron, whereas for $LaCl_3$ it indicates a Cl-La-Cl "bond"-angle of less than 90°, consistent with the larger coordination number. The relationship between the positions of the first peaks in $g_{ClCl}(r)$ may be compared to that which would be found for a close-packed lattice of anions, the perspective from which the YCl_3 crystal structure is often discussed [53]. The anion-anion coordination number in the melts (table 6.7) – deduced from the area of the broad first peak in $g_{ClCl}(r)$ – is close to 12, which would be the number of first neighbours in a close-packed lattice. Such a lattice would contain a second next-nearest neighbour shell at $\sqrt{2}R_{--}$, where R_{--} is the anion-anion nearest-neighbour distance. In YCl_3 this relationship is obeyed quite accurately and it would therefore appear that the local order associated with the anion lattice is preserved during melting. This is consistent with the very small associated volume change observed [91].

For $AlCl_3$ the anion–anion peak also shows a shoulder at low r, caused by the Cl–Cl distance depending on whether a given pair consists of two bridging atoms, two terminal ones, or one of each. Notice that this broad, intramolecular first peak overlaps the more uniform intermolecular distribution of Cl-Cl distances. That is, there is substantial interdigitation of the terminal Cl ions on different dimeric units. A coordination number analysis supports this view. Whereas the cation-cation and cation-anion coordination numbers determined by integration over the first peaks are fully consistent with intradimer structure, the integral of the Cl-Cl rdf out to 7.5 bohr gives a value of 4.5, which exceeds the value expected from purely intramolecular correlations (4).

6.11.4 Metal-Metal Correlations

The pdf showing the most dramatic change with cation size is $g_{MM}(r)$. The main peak is a doublet which becomes increasingly well resolved with decreasing cation size. As we have seen in section 6.7, the low r feature corresponds to two cations connected *via* a *pair* of Cl^- ions, which are common to both their coordination shells, *i.e.* edge-sharing between the coordination polyhedra. The large r feature (absent in $AlCl_3$) arises from a pair of cations sharing a single Cl^-, *i.e.* vertex-sharing and it's position is close to (but smaller than) twice the first-neighbour cation-anion separation (figure 6.27); equality would indicate a linear M-Cl-M "bond". The shift of the first feature to substantially smaller separation, shows that the two cations are drawn together by the edge-sharing arrangement. This phenomenon has been discussed previously, in the context of MX_2 stoichiometry, and emphasizes the role of the polarization terms in bending the M-Cl-M bond in vertex-sharing and in promoting edge-sharing [48, 54].

6.11.5 Visualization of instantaneous configurations.

Finally, in figures 6.29-6.35 we show instantaneous configurations (snapshots) of slices through the simulated fluids. In viewing them, it must be recalled that only a thin slice of the simulation cell is shown and that "bonds" to ions not within the slice are omitted. Hence, from a glance at the snapshot one sees more incomplete coordination shells than is, in fact, the case. In each figure the Cl^- anions are represented by the *cyan* circles and the M^{3+} cations by the *red* circles.

Overall, these pictures confirm the trends deduced above from the run-averaged structural measures. As the size of the cation decreases from La^{3+} to Al^{3+} it can be seen that the coordination number of anions around cations reduces from mostly 8 coordinate in $LaCl_3$ to predominantly 7 coordinate in $TbCl_3$ to 4 in $AlCl_3$ and $FeCl_3$. $DyCl_3$ and YCl_3 are largely 6-coordinate and

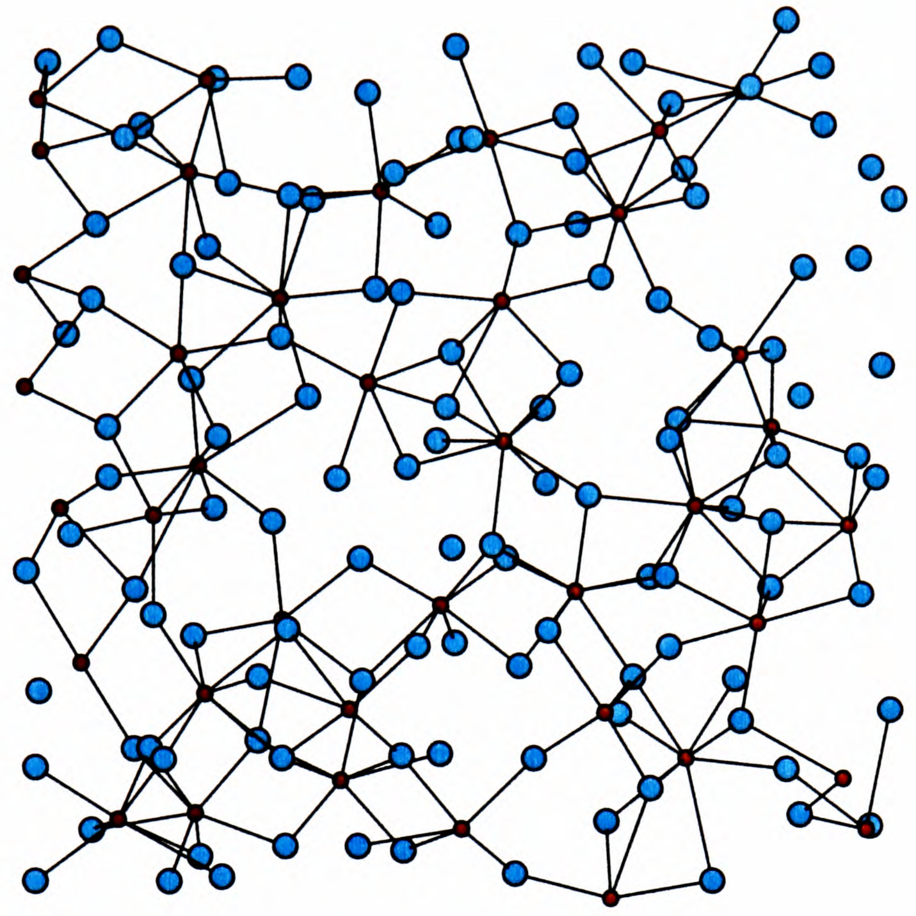

Figure 6.29: *Snapshot of the ion positions in $LaCl_3$*

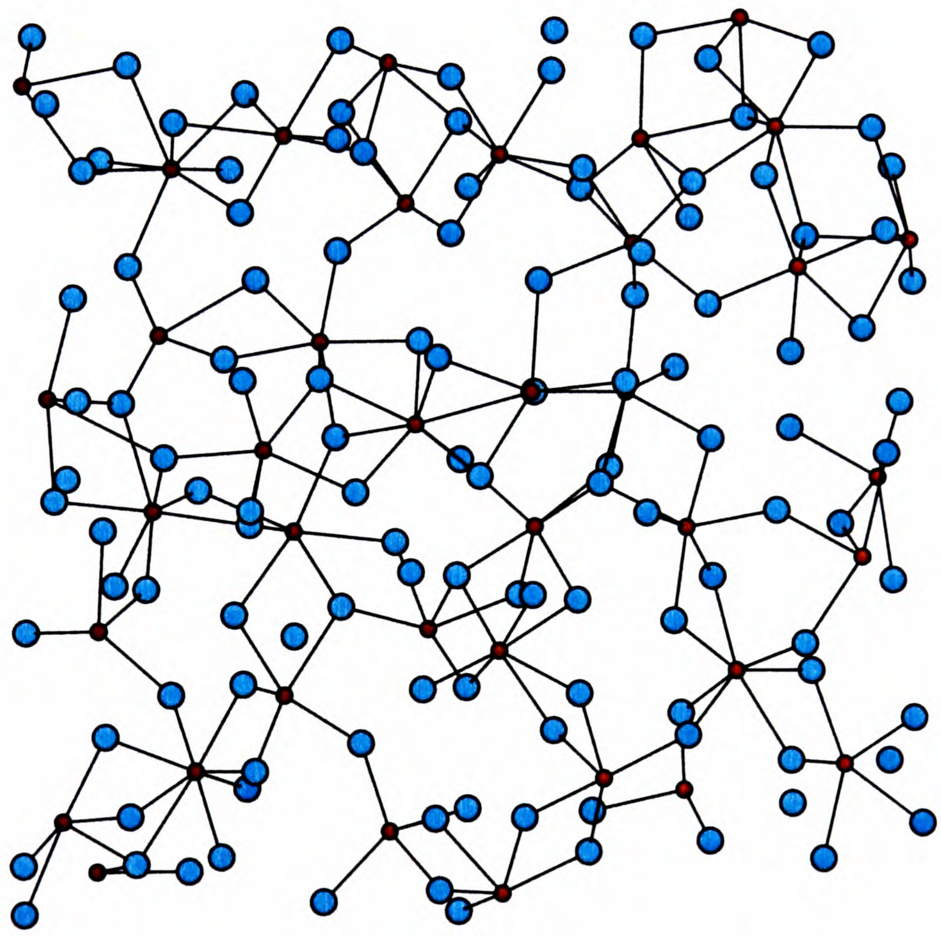

Figure 6.30: *Snapshot of the ion positions in $TbCl_3$*

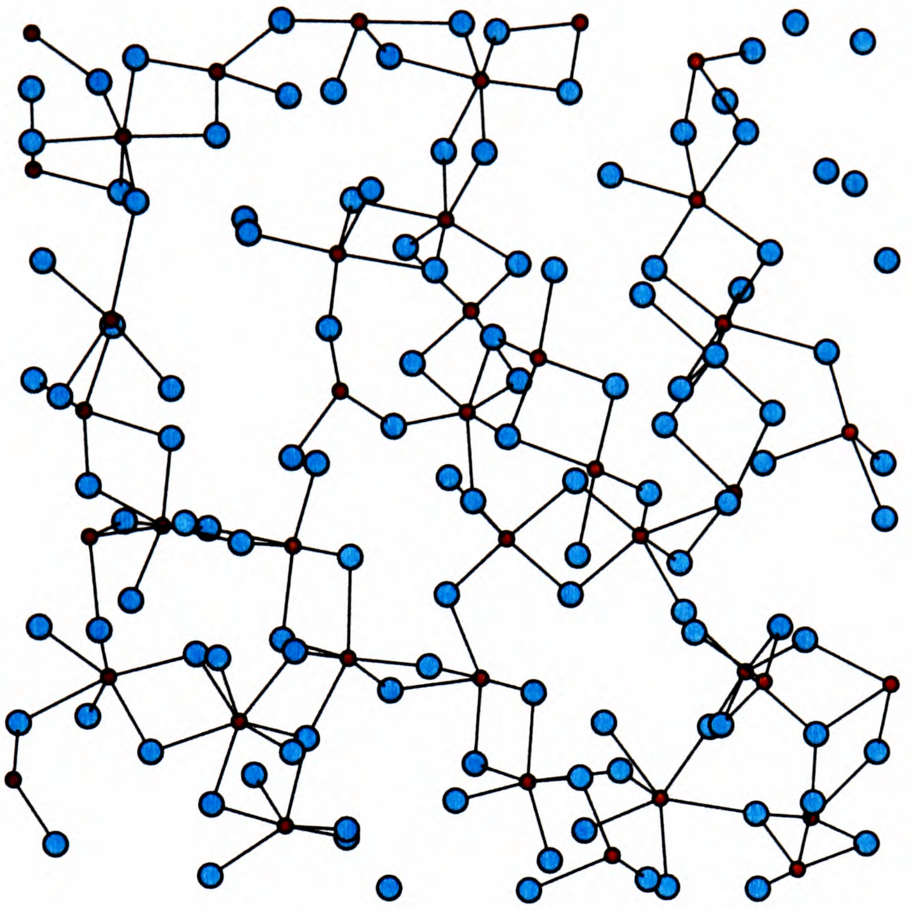

Figure 6.31: *Snapshot of the ion positions in* YCl_3

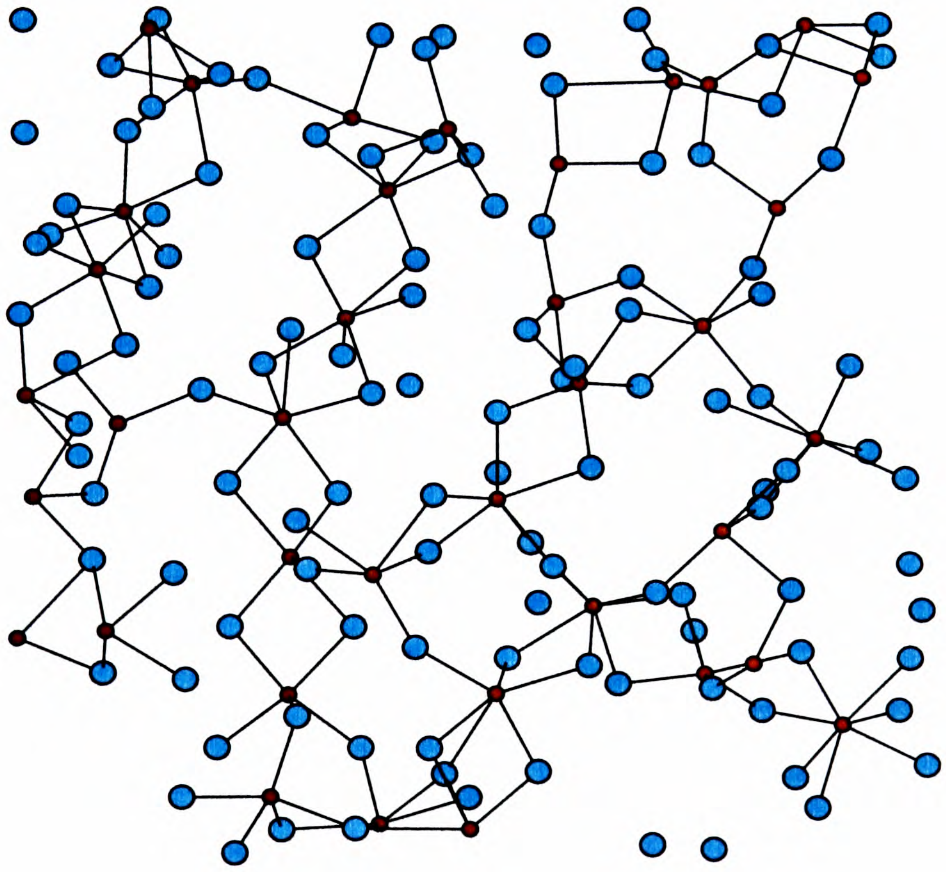

Figure 6.32: *Snapshot of the ion positions in* $DyCl_3$ *simulated with the PIM*

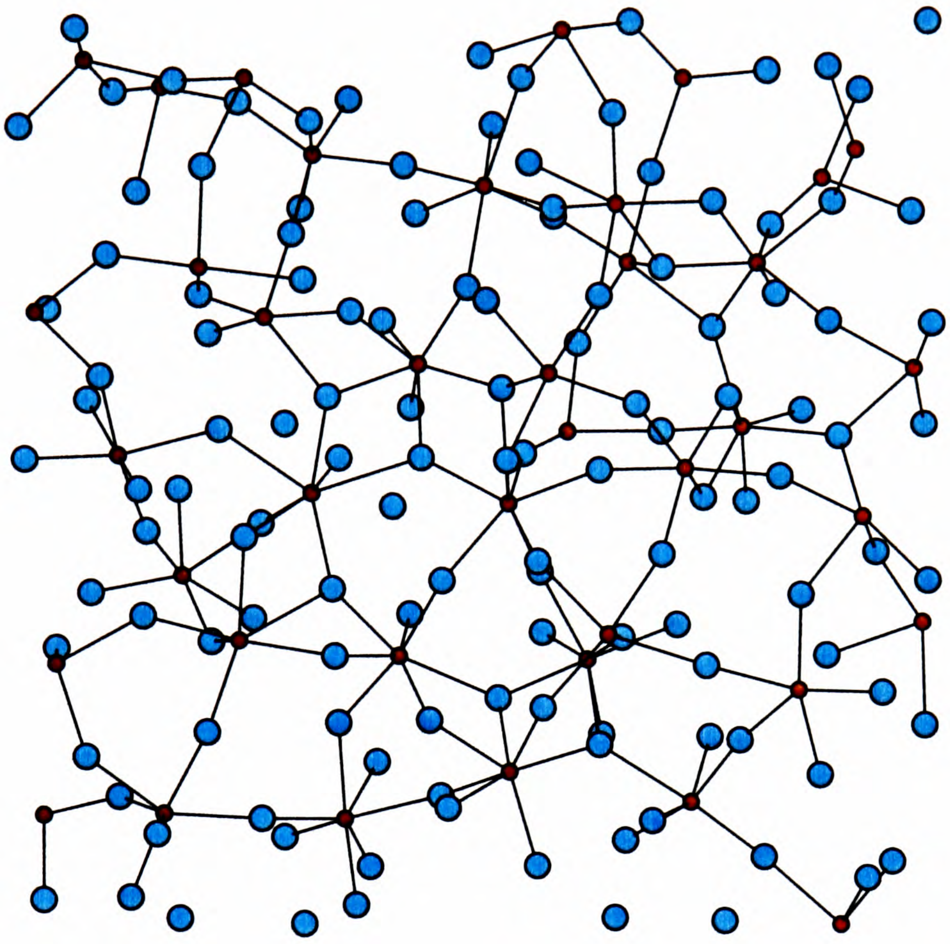

Figure 6.33: *Snapshot of the ion positions in $DyCl_3$ simulated with the RIM*

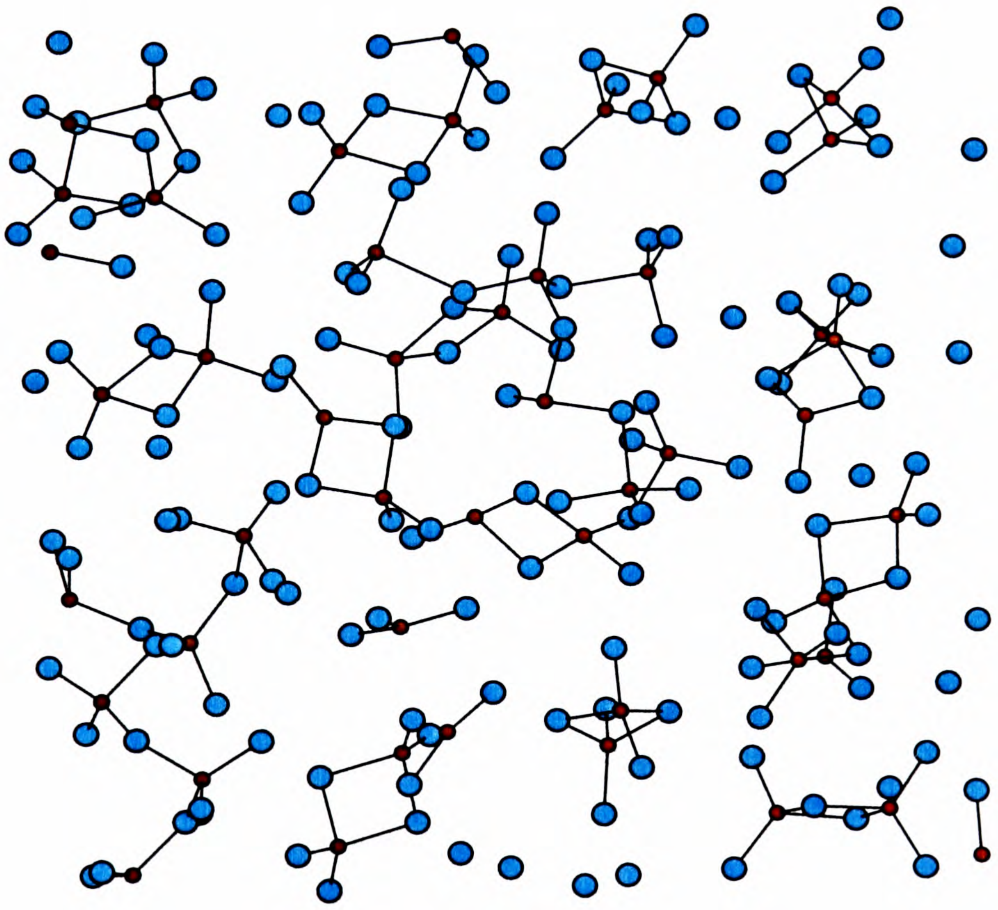

Figure 6.34: *Snapshots of the ion positions in $FeCl_3$*

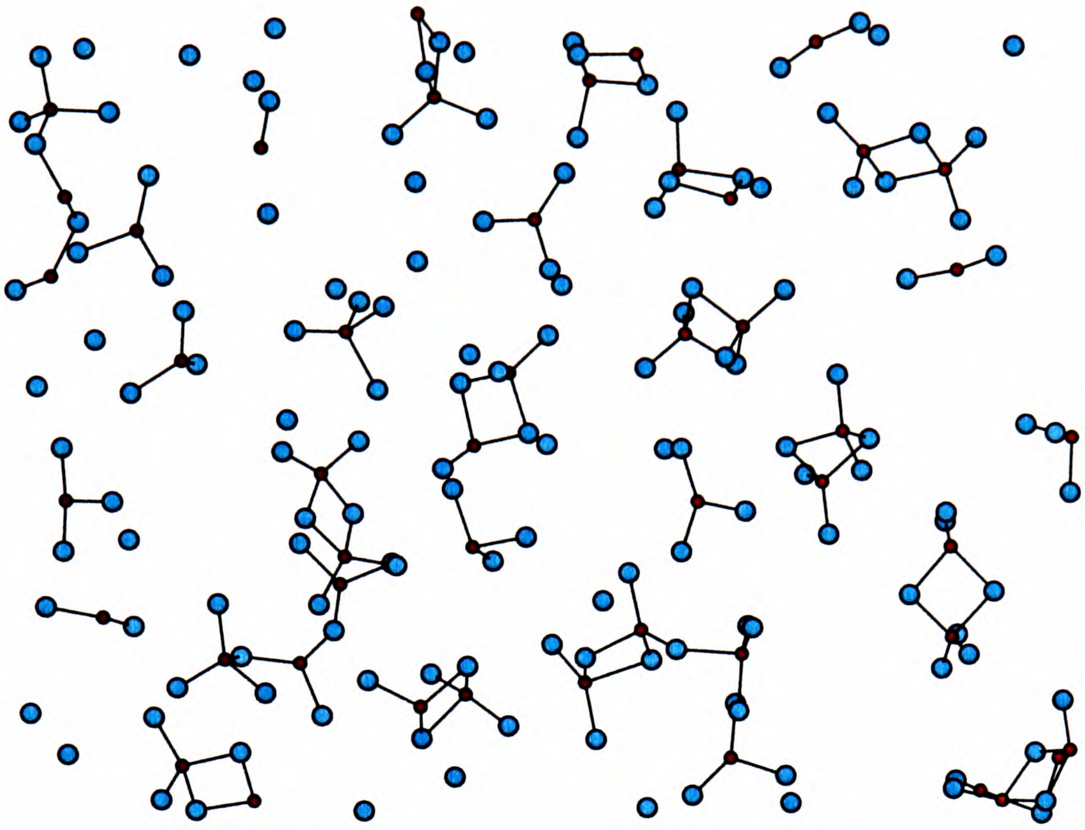

Figure 6.35: *Snapshots of the ion positions in $AlCl_3$*

the distribution of Cl-Y-Cl and Cl-Dy-Cl bond angles is consistent with octahedral coordination. The linking of these polyhedra through edge and vertex sharing can clearly be seen. In YCl_3, 90% of the cation-cation pairs are linked by edge-sharing polyhedra. In $AlCl_3$ the overwhelming majority (81%) of the Al^{3+} ions were four fold coordinate. The remainder are mostly 3-coordinate. Almost all the four coordinate Al^{3+} ions are involved in dimers. The promotion of edge-sharing by the polarization effects is clearly evident from a comparison of figures 6.32 and 6.33 which contain snapshots of the $DyCl_3$ simulations with and without polarization effects respectively. Snapshots of the liquids $AlCl_3$ and $FeCl_3$, figures 6.34 and 6.35, clearly show the presence of the Al_2Cl_6 and Fe_2Cl_6 dimers. The number of complete dimers in these picture is quite low, the reason being that many of the dimers lie across the boundary of the relatively thin slice of the simulation cell illustrated.

6.12 Pressure

The pressure calculated with the polarizable ion potential model was reasonably small in each case (table 6.8). For the systems simulated with Cl^3_{POT} the pressure was positive. The fact that the pressure is positive indicates that the fluid is trying to expand and is consistent with the fact that we have found the crystal structures slightly underbound. For $DyCl_3$ and YCl_3 simulated with Cl^2_{POT} the pressure was negative. The fact that the calculated pressure is negative indicates that these crystal structures are slightly too strongly bound - a feature of the Fumi-Tosi potential. However since the total pressure is the difference between two much larger numbers we regard this result with the generic potential as satisfactory. The major term in the pressure comes from the short range repulsion, this is so large because the induction effects have pulled the ions close enough together so that there is a large overlap. In the polarizable ion model, this effect is countered by the charge-induced dipole interaction.

The inclusion of the dipoles on the anions stabilises the low density fluid structure greatly. Simulations at the experimental density with the same pair potential as we are using but with the polarization effects omitted have large negative pressures – (as is seen for $DyCl_3$ in table 6.8) meaning that the system wants to contract to a higher density fluid.

6.13 Conclusions

Use of the new Cl-Cl potential has led to considerable improvement in the comparison between the simulated and experimental structure factors and pdfs. However, we have seen that a number of issues need to be resolved. In particular the apparent over-structuring of the first coordination shell, as witnessed by the excessive sharpness of the predicted first peak in $g_{MCl}(r)$. While our new potential does a very good job at predicting static structures, there are

System	Pressure (GPa)
$LaCl_3$	0.64
$TbCl_3$	0.58
$DyCl_3$ (PIM)	-0.20
$DyCl_3$ (RIM)	-0.64
YCl_3	-0.50
$ScCl_3$	0.19
$FeCl_3$	0.15
$AlCl_3$	0.10

Table 6.8: *The resulting pressure of simulations on MCl_3 systems.*

still doubts over its effectiveness for describing the dynamical behaviour of these systems.

In the following chapters we will calculate Raman spectra and invesigate the diffusion and conductivity of these systems to validate the potential model on the dynamical behaviour. First we will introduce the construction of potentials for systems in which the concentration of the trihalide salt is changed by the addition of an alkali halide.

Chapter 7

Trivalent metal chlorides: Binary mixtures

7.1 Introduction

A central theme throughout this thesis so far has been the idea of potential model *transferability*. Thus far, this transferability has focussed on the transmutation of potentials based on changes in cation radii. In this chapter an additional aspect of potential transferability will be explored in which a range of trivalent metal chlorides will be modified by alkali halide adducts.

The study of such systems is important if contact is to be made with empirically derived industrial materials which tend to involve several cation types [92–94]. As a result, potential models cannot realistically be generated by the more *ad hoc* procedures often used and so rely on model transferability from simpler systems. Furthermore, the study of metal trihalide/alkali halide mixtures allows connection to be made with a huge range of experimental information. For example, as we shall see in chapter 8, much can be learnt from the systematic evaluation of peaks in Raman spectra as the concentration of metal trihalide changes [46, 95, 96].

In this chapter two examples of such binary mixtures will be considered: $DyCl_3/NaCl$ and $ScCl_3/CsCl$. In both cases we shall study the systematic evolution of the structure centred about the M^{3+} cations.

7.2 $DyCl_3/NaCl$

In mixtures of $DyCl_3/NaCl$ thermodynamic measurements show that a ratio of 3NaCl to $1DyCl_3$ is sufficient to isolate $DyCl_6^{3-}$ complexes [97]. In addition experimental neutron diffraction [10] data is available for this concentration. In the spirit of model transferability we combine the model for $DyCl_3$ derived in chapter 6 with pair potentials which describe the Na-Na and Na-Cl interactions taken from Fumi and Tosi [33] (table 5.1). As for the Dy-Dy cation pair the Dy-Na interaction is assumed to be dominated by simple coulomb repulsion and so the short range terms are set to zero.

The simulations were performed on a 500 ion system (consisting of 300 Cl^- ions, 50 Dy^{3+} ions and 150 Na^+ ions) in a NVT ensemble. As for the pure liquids equilibration was carried out for 36ps (at 1100K) until no further change in the structure was observed. Structural data was then gathered over a run of 4ps. In order to assess the rôle of the polarization effects in these mixtures, already shown to play a critical role in pure $DyCl_3$, we study this system using both a RIM and PIM.

Total structure factors ($S_{total}(k)$) predicted by MD simulations with the PIM and RIM interaction models are depicted in figure 7.1 together with the experimental total structure factor. The simulated total structure factors are calculated in an analogous fashion to those for the pure trihalides (section 6.7) combining the six partial structure factors calculated from simulation, weighted by concentration and neutron scattering length.

$S_{total}(k)$ estimated by the PIM is very similar to the experimental one and is much improved over the RIM prediction. In particular the location of the

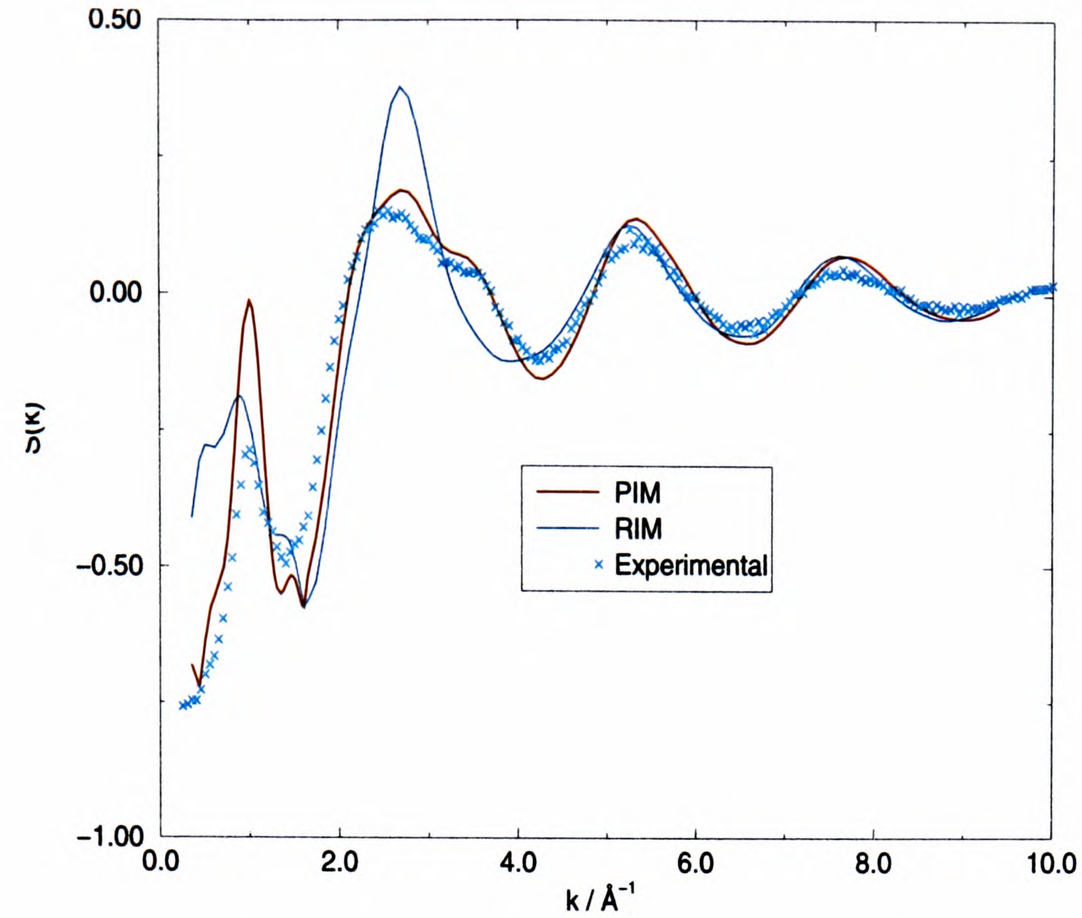

Figure 7.1: *Comparison of experimental and simulated total neutron weighted structure factors for $DyNa_3Cl_6$ calculated with the PIM and RIM.*

first sharp diffraction peak at ~ 1Å^{-1}, estimated with the PIM shows good agreement with the experimental result.

In figure 7.2(a)-(d), partial rdfs of four ionic combinations in the mixture are shown. $g_{\mathrm{Dy-Cl}}$ is similar in the two simulations, with a sharply defined first coordination shell which integrates to six nearest neighbours indicative of octahedral coordination. In contrast to the pure melt (figure 6.12), the first minimum in $g_{\mathrm{Dy-Cl}}$ now goes to zero, indicating a very stable coordination complex from which Cl^- ions exchange only very slowly with the bulk. Significant differences between the RIM and PIM predictions appear in $g_{\mathrm{Dy-Dy}}$. The presence of a peak at around 5.0Å in $g_{\mathrm{Dy-Dy}}$ for the RIM simulation, similar to the position of the first peak in the pure $DyCl_3$ simulations, appears to indicate the presence of dimers or even larger 'polymers' of connected polyhedra. In contrast, the most prominent peak observed in $g_{\mathrm{Dy-Dy}}$ in the PIM simulations is at much larger separations. This is the opposite observation to that in pure $DyCl_3$ where polarization effects act to reduce Dy-Dy separations. The results for the mixtures are suggestive of Dy^{3+} ions, and their nearest neighbour anion coordination shells, becoming disconnected from all such units, that is, discrete $DyCl_6^{3-}$ ions are formed. It would appear therefore, that the polarization effects have promoted the break-up of the network with the subsequent formation of discrete $DyCl_6^{3-}$ molecular ion units.

The stabilization of these discrete units can be understood by considering figure 7.3 in which the stabilization energy obtained by the formation of a dipole on each of the 6 Cl^- ions pointing towards the Dy^{3+} ion acts to stabilize this configuration with respect to the edge sharing $DyCl_6^{3-}$ units seen in the pure melt.

Figures 7.4(a) and (b), show snapshots of the instantaneous configurations of the mixtures for the PIM and RIM systems. In these figures the positions of Dy^{3+} ions (*red* circles), Na^+ (*yellow* circles) and Cl^- ions(*cyan* circles) are shown, along with lines connecting Cl^- ions coordinating to the Dy^{3+} ions . The formation of the discrete $DyCl_6^{3-}$ in the PIM is clear. The RIM results shows significant 'chain' structure in line with the pure $DyCl_3$.

The difference in Na-Dy spatial correlations (figure 7.2(c)) can be understood in terms of simple electrostatics. In the PIM the Na^+ ions tend to lie closer to the Dy^{3+} cations than in the RIM. In the latter case a Na^+ ion is repelled by more than one Dy^{3+} cation as these are in significant chain-like structures. In the PIM the Na^+ ion is coordinated with a single $DyCl_6^{3-}$ molecular anion.

7.3 $ScCl_3/CsCl$

A comprehensive Raman study has been carried out on the binary mixtures of $ScCl_3$ with CsCl by Zissi and Papathedorou [96]. Of particular interest in this study will be a comparison with experiment for $ScCl_3/CsCl$ mixtures with $ScCl_3$ compositions of 15%, 25%, 50%, 75% and the pure $ScCl_3$. In the previous chapter

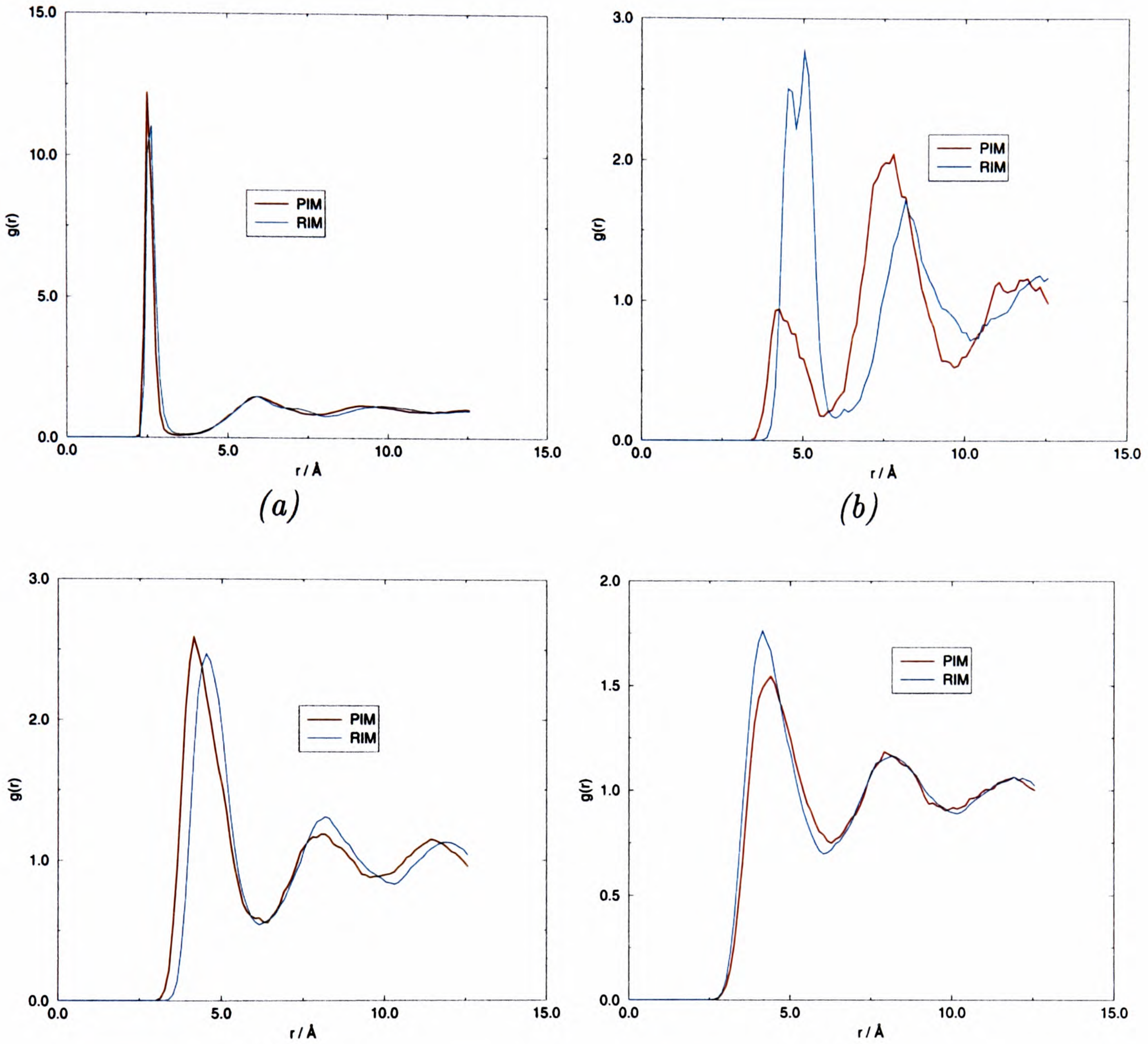

(a) (b) (c) (d)

Figure 7.2: *Partial rdfs for several ionic configurations in molten $DyNa_3Cl_6$. The PIM result is represented by the red lines and the RIM by the blue lines. (a) Dy-Cl correlations (b) Dy-Dy correlations (c) Na-Dy correlations (d) Na-Na correlations.*

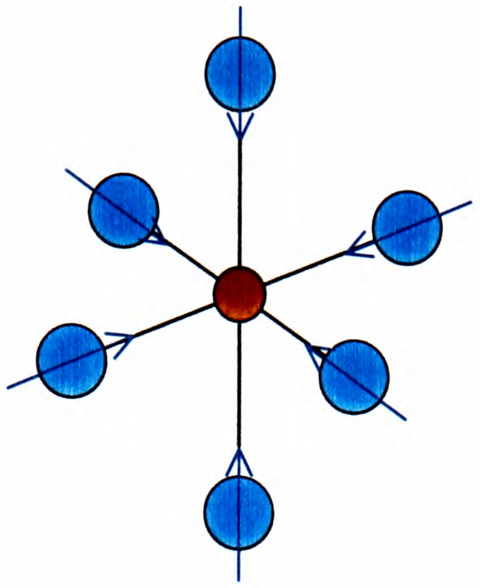

Figure 7.3: *Stabilization of $DyCl_6^{3-}$ molecular units by polarization effects. The arrowhead represents the negative end of the induced dipole.*

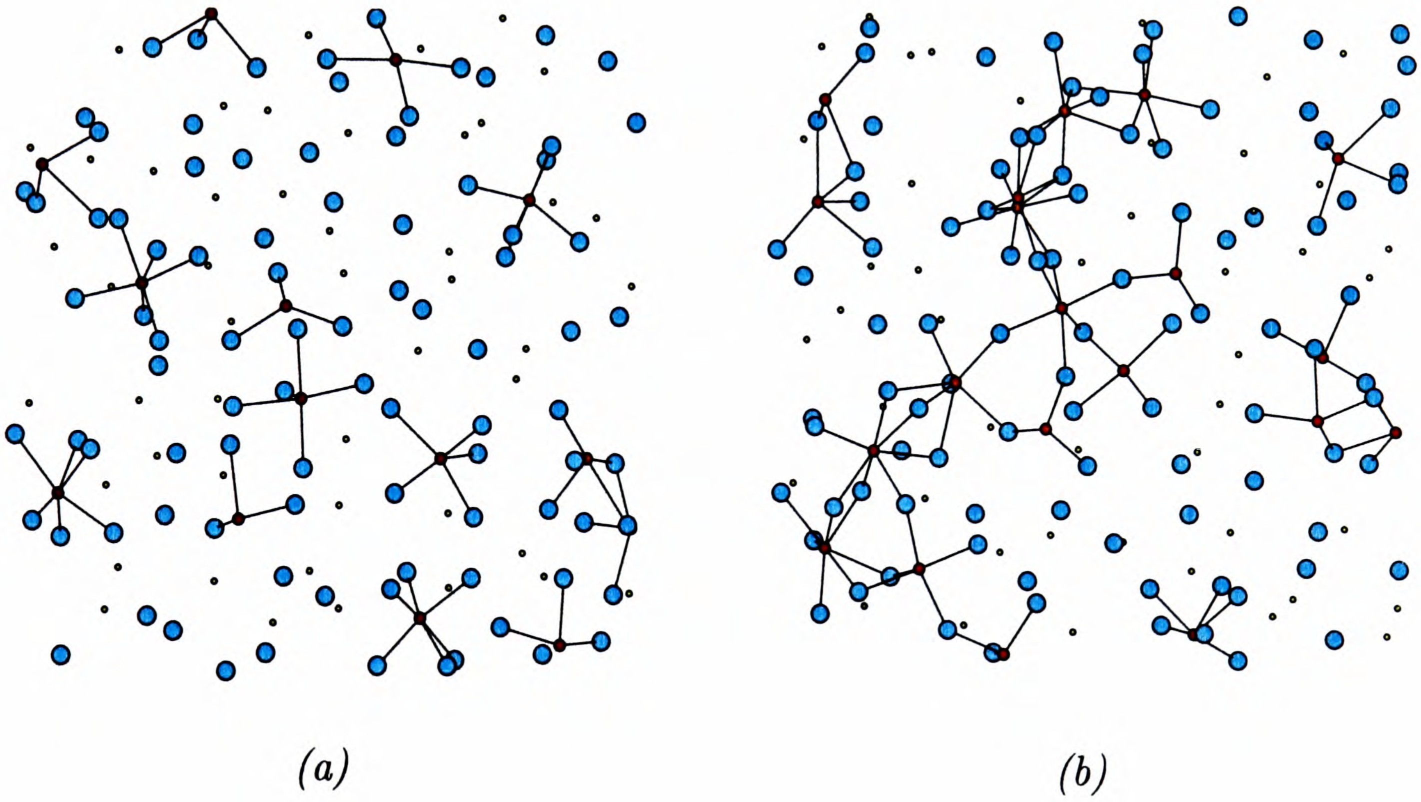
(a)
(b)

Figure 7.4: *Snapshots of $DyNa_3Cl_6$ modelled with the (a) PIM and (b) RIM. The Cl^- ions are represented by cyan circles, the Dy^{3+} by red circles and the Na^+ by yellow circles.*

Amount of $ScCl_3$ (%)	Number of ions		
	Cl^-	Sc^{3+}	Cs^+
100	411	137	0
75	391	117	40
50	365	91	92
25	329	55	164
15	310	36	202

Table 7.1: *Number of ions used in the $ScCl_3/CsCl$ simulations*

we saw how the simulated structure factor and rdf compared with experiment for $ScCl_3$ (figures 6.19 and 6.20).

7.3.1 Simulation details

The potential parameters used for modelling $ScCl_3/CsCl$ are a combination of those used for pure $ScCl_3$ in chapter 6 and the Sangster and Dixon parameters for CsCl listed in table 5.1. Each simulation consisted of a total of 548 ions, the numbers of each type being listed in table 7.1. The simulations were performed at the experimental temperatures and densities at which the Raman studies were performed. These are listed in table 7.2.

7.3.2 Overview of $ScCl_3/CsCl$ Binary Mixtures

Slices through the simulation cell for the various compositions of $ScCl_3/CsCl$ are shown in figure 7.5.

A breakdown of the coordination numbers is given in table 7.3 for all the $ScCl_3$ compositions considered. In all the mixtures it can be seen that the Sc^{3+} ions are mostly 5 and 6 coordinated. Only small amounts of 4 coordinated species are seen in any of the melts.

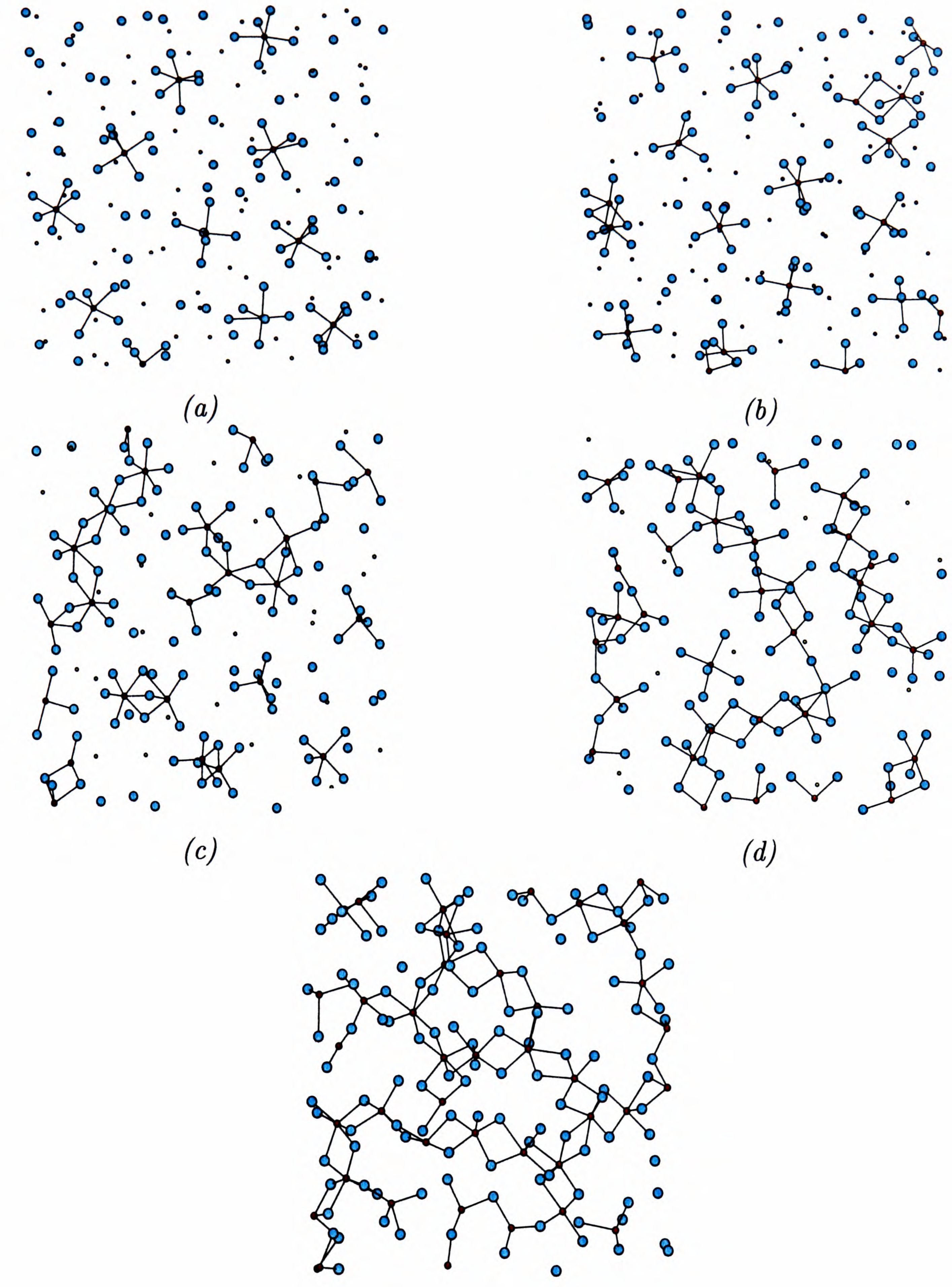

Figure 7.5: *Snapshots of (a) 15%*$ScCl_3$*/85%CsCl (b) 25%*$ScCl_3$*/75%CsCl (c) 50%*$ScCl_3$*/50%CsCl (d) 75%*$ScCl_3$*/25%CsCl mixtures and (e) pure* $ScCl_3$

Amount of $ScCl_3$ (%)	Temperature / K	Density / $g.cm^{-3}$
100	1253	1.6432
75	1128	1.849
50	933	2.098
25	1103	2.289
15	1043	2.548

Table 7.2: *Temperatures and densities at which the $ScCl_3/CsCl$ simulations are performed*

The linkages of these polyhedral units can be investigated by determining the coordination number of each scandium ion by treating anions which are at distances less than the first minimum in the Sc-Cl pdf to be connected to the scandium ion. Scandium ions which are then closer than the distance at which the first minimum appears in the Sc-Sc pdf are then searched over to see if they share any Cl^- anions. If they do not share any Cl^- ions the polyhedra are 'isolated'. If the same pair of Sc^{3+} ions share one chloride ion, the $ScCl_n$ polyhedra are termed 'vertex sharing', 2 - 'edge sharing', 3 - 'face sharing' (section 1.4.2). This connectivity has been tabulated for 5 and 6 coordinated Sc^{3+} ions in tables 7.4 and 7.5. Note that each specifically coordinated unit is judged to be linked to its neighbours regardless of the coordination of the neighbouring cations.

7.3.3 25% $ScCl_3$ and 15% $ScCl_3$

Cs_3ScCl_6(≡25% $ScCl_3$ in CsCl) consists of mostly 6-coordinate species (62%) with a number of 5-coordinated species (38%) (table 7.3). Of these polyhedra the overwhelming majority are isolated (93% for 6-coordination and 85% for 5 coordination). For the 15% $ScCl_3$ simulation 83% of Sc^{3+} ions are 6-coordinated, 17% 5-coordinated. 99% of the 6 coordinated species are isolated and 100% of

Amount of $ScCl_3$ (%)	Coordination number		
	4	5	6
100	3	35	62
75	5	38.5	56.5
50	9	38	53
25	0	38	62
15	0	17	83

Table 7.3: *Comparison of coordination number of Sc^{3+} ions in the various $ScCl_3/CsCl$ mixtures*

Amount of $ScCl_3$ (%)	Connectivity (%)			
	Isolated	Vertex	Edge	Face
100	0	15	78	7
75	0	22	69	9
50	3	13	35	48
25	93	1	2	4
15	99	1	0	0

Table 7.4: *Connectivity of $ScCl_6^{3-}$ species in $ScCl_3/CsCl$ mixtures.*

Amount of $ScCl_3$ (%)	Connectivity (%)			
	Isolated	Vertex	Edge	Face
100	0	24	71	5
75	0	16	53	32
50	0	12	38	50
25	85	13	2	0
15	100	0	0	0

Table 7.5: *Connectivity of $ScCl_5^{2-}$ species in $ScCl_3/CsCl$ mixtures.*

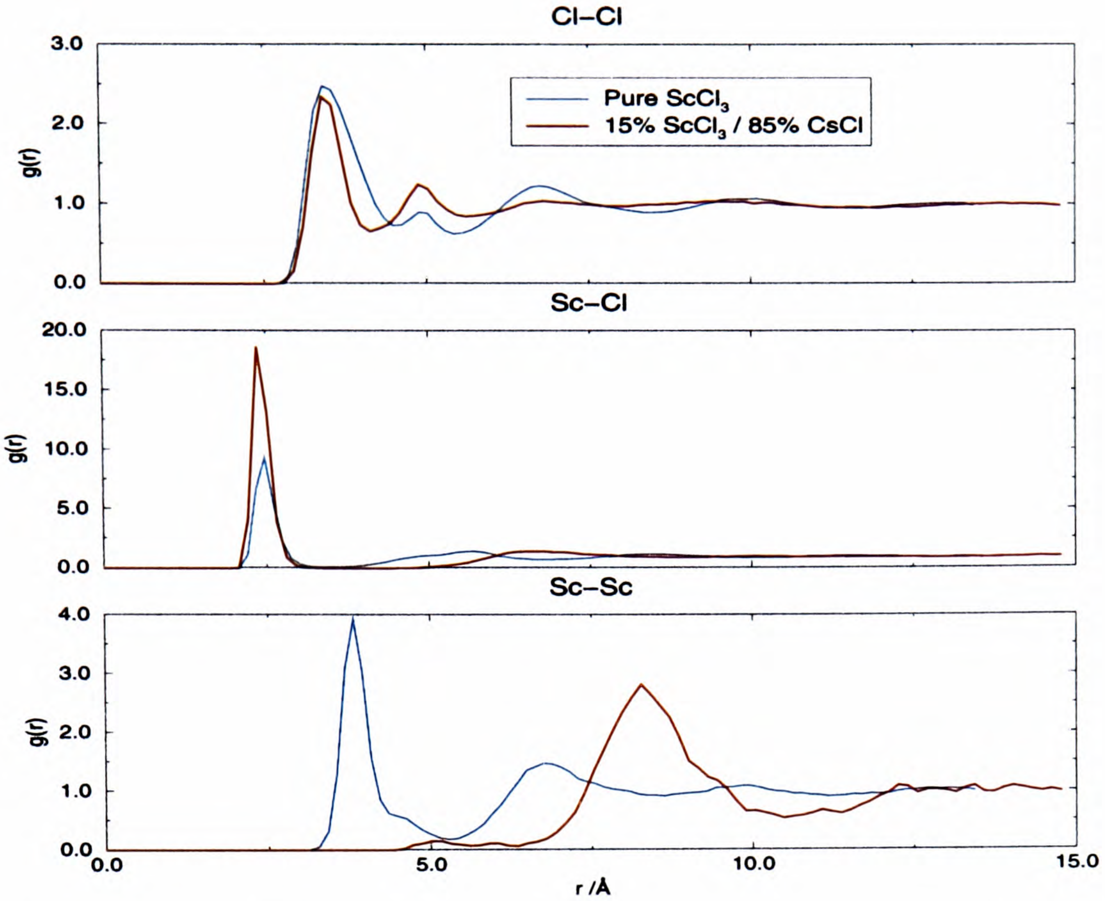

Figure 7.6: *Comparison of partial rdfs in pure* $ScCl_3$ *and* $15\%ScCl_3/85\%CsCl$

5 coordinated species are isolated.

In figure 7.6, partial pdfs of the Cl-Cl, Sc-Cl and Sc-Sc combinations are compared for the 15%$ScCl_3$/85%CsCl mixture with the pure $ScCl_3$. In the 15% $ScCl_3$ mixture g_{ScCl} is seen to have a very broad, flat minimum going to zero indicating a very stable coordination complex from which Cl^- ions exchange very slowly with the bulk. This is similar to that seen in $DyCl_3$/NaCl (figure 7.2(b)). The most prominent peak in g_{ScSc} for the mixture is at much larger separation than that in the pure melt suggesting that the Sc^{3+} ions and their immediate Sc^{3+} neighbours have become disconnected.

From the pdf of the 15% $ScCl_3$ and the analysis of the coordination numbers and connectivity data it is clear that the predominant species present are isolated octahedra as can be seen in figure 7.5(a). At 25% $ScCl_3$ the coordination number analysis shows the mixture to still consist mainly of isolated octahedra.

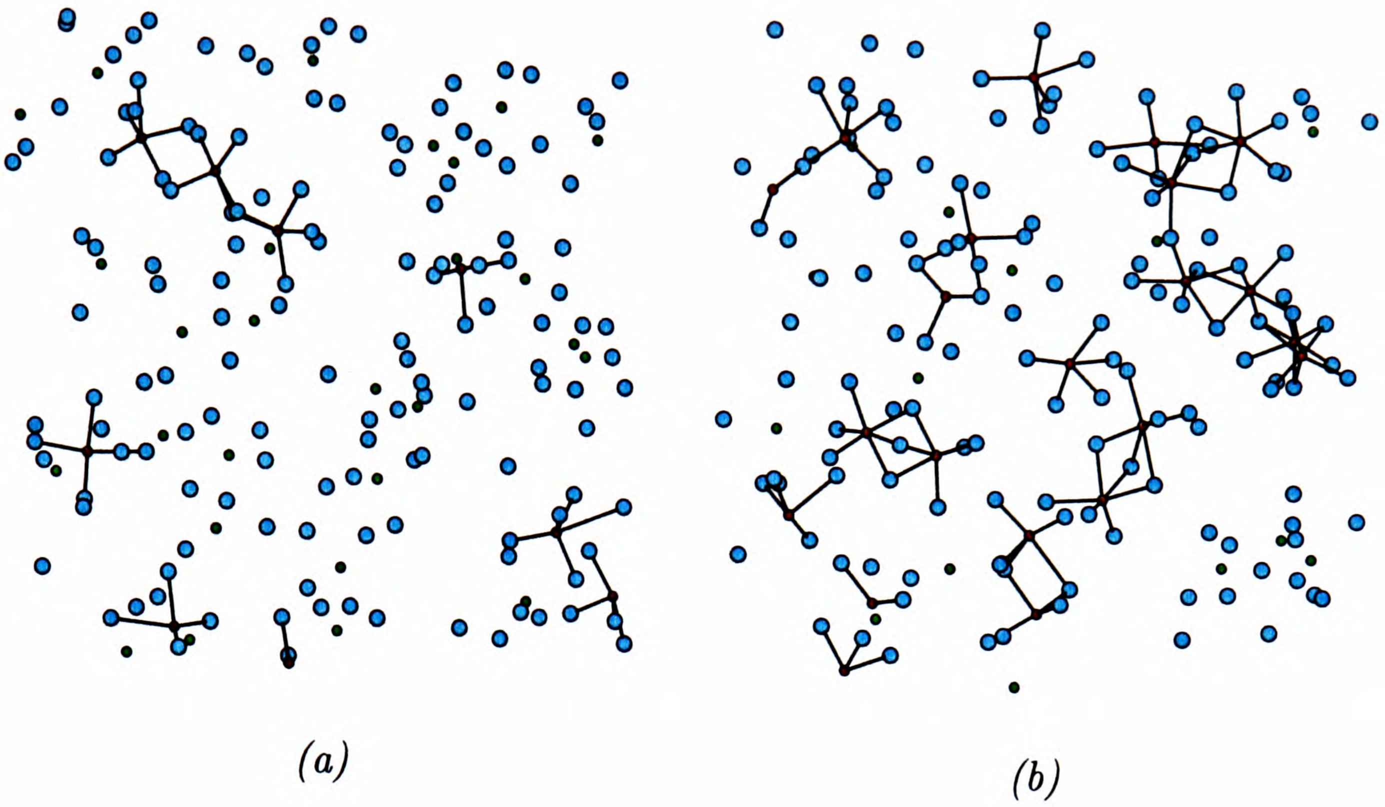

Figure 7.7: *Snapshots showing connectivity of (a) 5 coordinate (b) 6 coordinate* Sc^{3+} *in 50%*$ScCl_3$*/50%CsCl. The face sharing octahedra can clearly be seen in (b)*

7.3.4 50% $ScCl_3$

The change in structure on the addition of further Sc^{3+} to the 25% $ScCl_3$ solution is dramatic.

The ratio of 5 and 6 coordinate polyhedra is very similar (with the evolution of a small percentage of 4 coordinate Sc^{3+}). The dramatic change occurs in the manner in which these polyhedra link together. Tables 7.4 and 7.5 indicate the formation of a large number of face sharing units between both 5 and 6 coordinate sites. In addition, there are a significant number of edge-sharing units but the discrete units, dominant for both 25% and 15% $ScCl_3$ have all but vanished. Such face sharing units are clearly seen in figure 7.5(c). To highlight these units figure 7.7(b) shows a snapshot of the cell highlighting the 6-coordinate Sc^{3+} sites only. Face-sharing dimers are clearly visible.

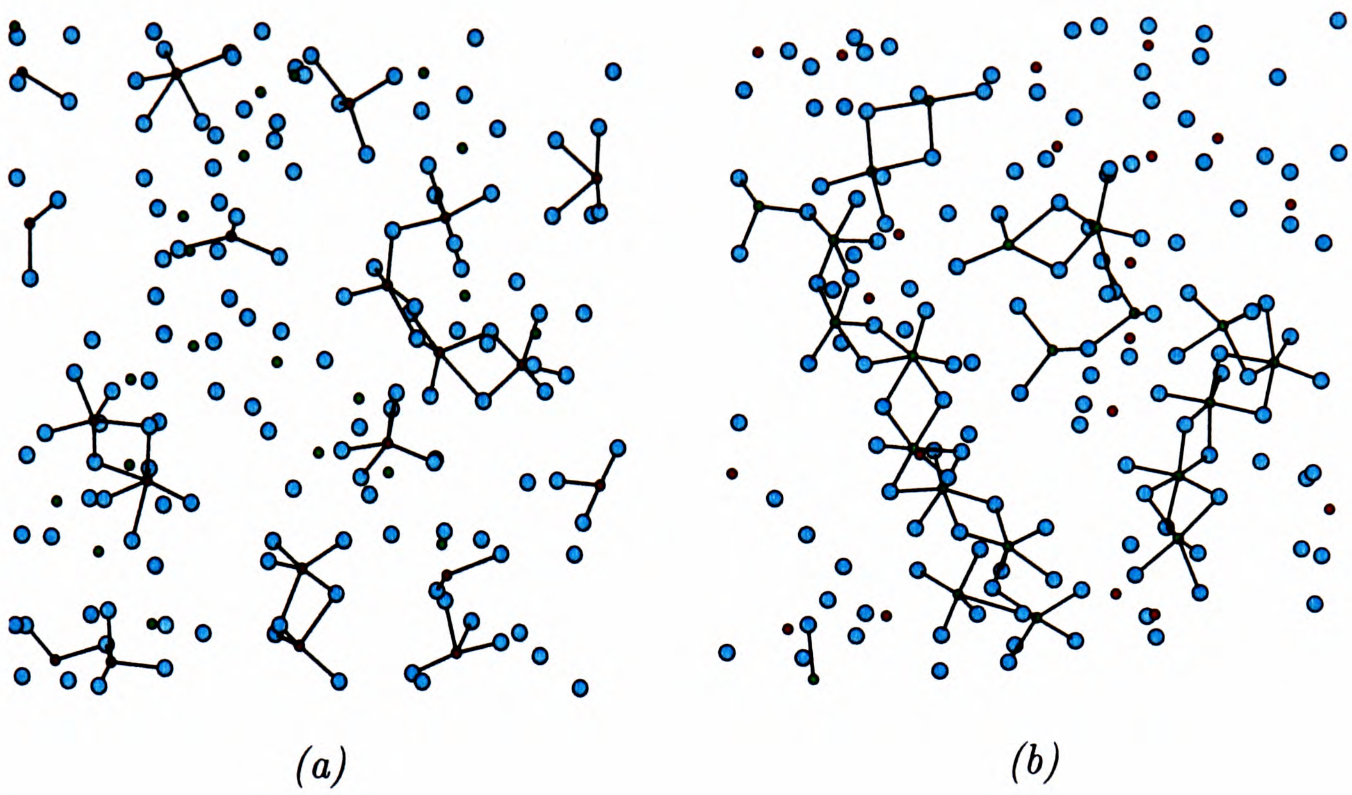
(a) (b)

Figure 7.8: *Snapshots showing connectivity of (a) 5 coordinate (b) 6 coordinate Sc^{3+} in 75% $ScCl_3$/25% CsCl*

7.3.5 75% $ScCl_3$

On reaching a concentration of 75% $ScCl_3$ figure 7.5(d) shows the build up of distinctive chain structures. Figure 7.8 highlights these chains by considering only the 5 and 6 coordinate cations.

7.3.6 $ScCl_3$

Our study of the structure has shown that the average coordination number in $ScCl_3$ is 5.6, with 62% of Sc^{3+} 6-coordinate and 35% 5-coordinate. The connectivity of the polyhedral units is listed in table 7.4 and illustrated in figure 7.5(e).

Tables 7.4 and 7.5 indicate that both the 5 and 6 coordinate Sc^{3+} cations are now dominated by edge-sharing units. It is clear from figure 7.5(e) that these edge-sharing structures percolate to form the chain structures (as in $BeCl_2$ for example [50]). An interesting question regarding the inherent chain structure is, therefore, whether the 5 or 6 coordinate sites in particular are incorporated

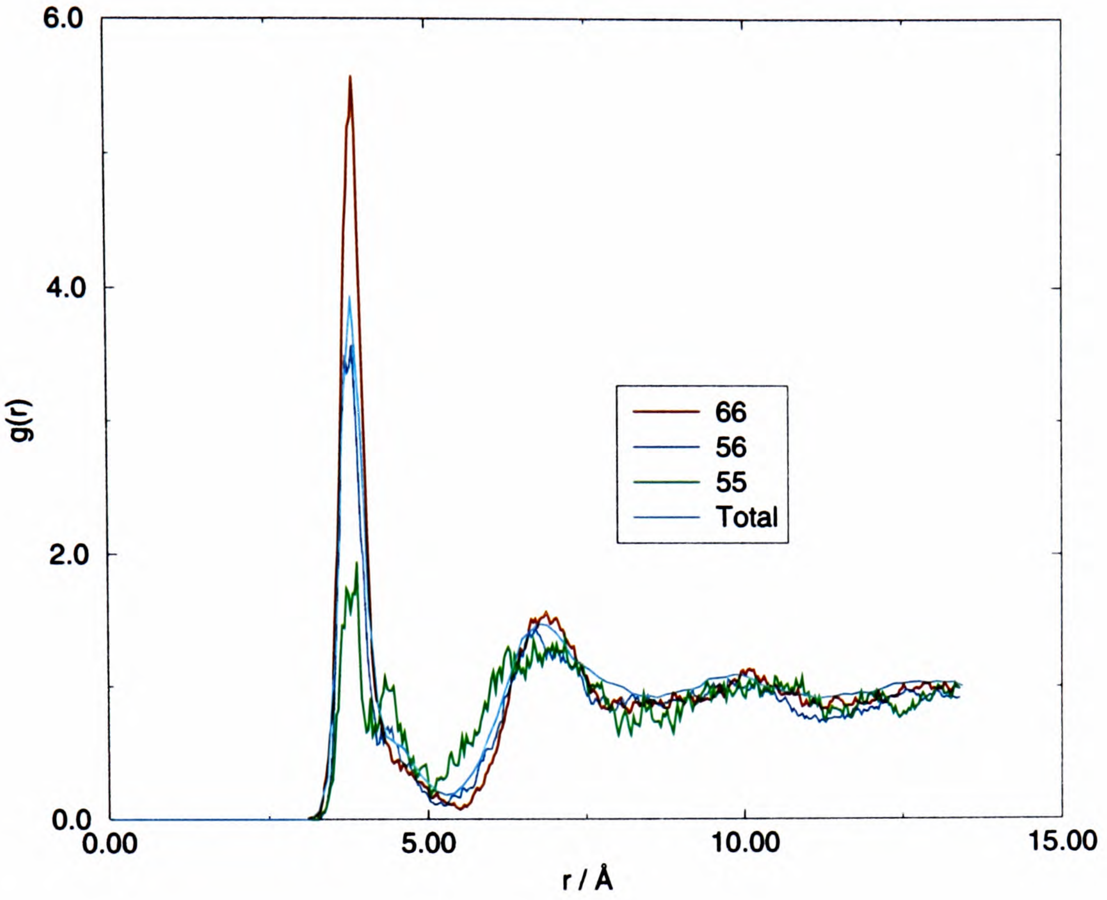

Figure 7.9: *Cation-cation rdfs for 5 and 6 coordinate Sc^{3+}*

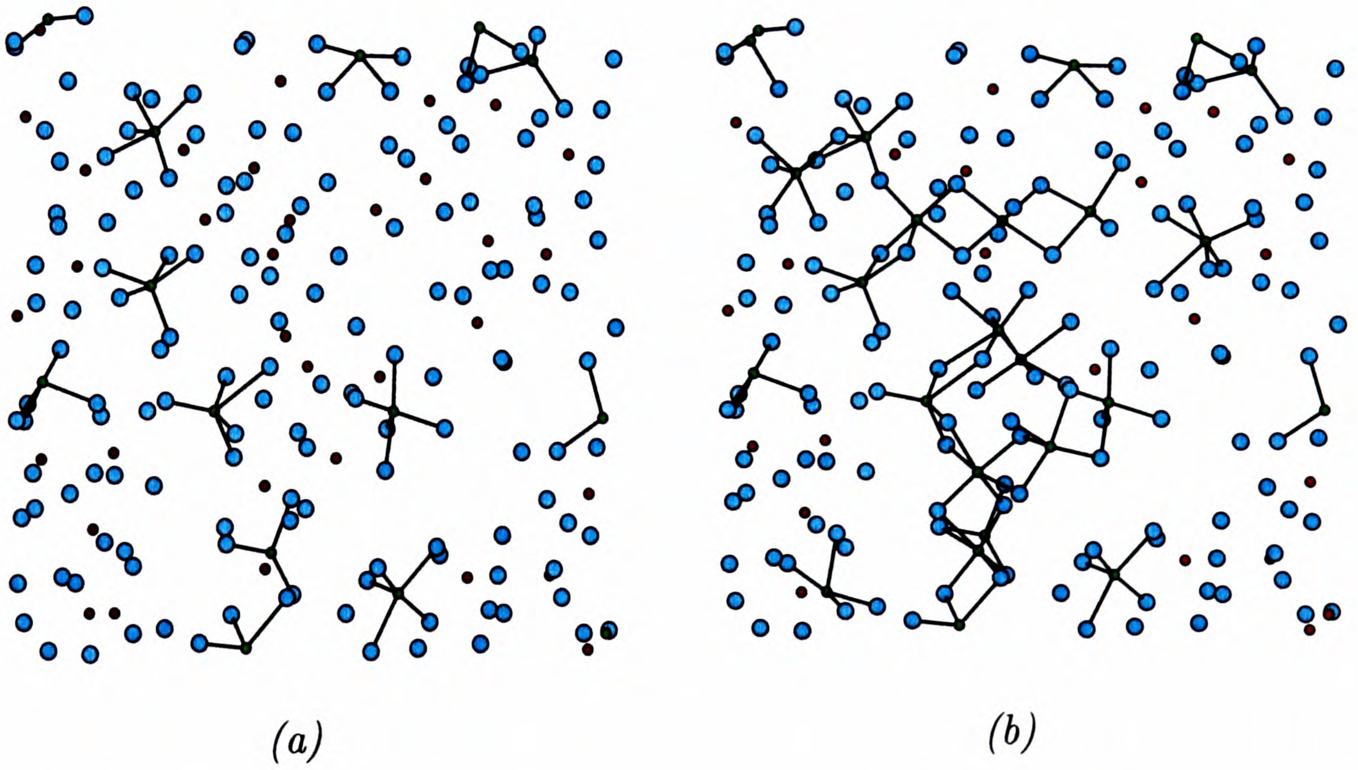

Figure 7.10: *Snapshots showing (a) 5 coordinate (b) 6 coordinate Sc^{3+} in pure $ScCl_3$*

in such percolated units. In $BeCl_2$ for example, 4 coordinate Be^{2+} tetrahedra percolate edge-sharing chains with 3 coordinate Be^{2+} end groups giving overall charge neutral 'polymeric' chains.

Direct analogy with this system might lead us to expect percolating chains of 5-coordinate Sc^{3+} units with 4-coordinate end groups which would give charge neutral chains in the MX_3 stoichiometry. To investigate the inherent chains we define pdfs solely in terms of specific cation coordination numbers (equation 7.1).

$$4\pi r^2 g_{\alpha\beta}(r) = \frac{V}{\sqrt{N_\alpha N_\beta}} \sum_{i=1}^{N_\alpha} \sum_{j=1}^{N_\beta} \delta(|\mathbf{r}_i - \mathbf{r}_j| - r) \qquad (7.1)$$

where α and β label the instantaneous coordination number of the cations. Figure 7.9 shows the cation-cation pdfs for the 6-6, 5-6 and 5-5 coordinate environments along with the total g_{ScSc} for comparison. The 6-6 pdf is the most distinctive displaying a tall sharp peak at around 3.8Å which decays to a very low minimum then a relatively sharp second peak at ~7.0Å. The sharp first and second peaks are indicative of relatively stable (long-lived on the timescale of the simulation) species, in this case the percolating chains.

If the chains were completely straight (linear Sc-Sc-Sc triplets) then the position of the second peak in figure 7.9 would be expected to be at approximately twice that of the first. The fact that the second peak is at a separation considerably less than this value (7.0Å compared to 7.6Å) indicates that, in contrast to $BeCl_2$, these chains are relatively bent on a next-nearest neighbour length-scale. We conclude from figure 7.9, therefore, that the percolating chains are not formed from 5 coordinate Sc^{3+} ion centres, as drawn by analogy from $BeCl_2$, but are formed from mainly 6 coordinate Sc^{3+} ions sites. Figure 7.10 shows two snapshots through the simulation cell highlighting only the 5 and 6 coordinate Sc^{3+} ions respectively. The sections of percolating chains in figure 7.10(b) for the 6 coordinate sites are clear as is the lack of such units in figure 7.10(a).

Chapter 8

Trivalent metal chlorides: Dynamics

8.1 Introduction

In previous chapters the focus of the work has been on obtaining systematic, transferable potential models which reproduce structural properties such as well defined crystal structures and liquid structure from scattering experiments. In addition we saw how these potentials could be used in conjunction with potentials describing the ionic interactions in alkali halides to model binary mixtures. In this chapter we extend the analysis to considering the dynamical properties of these systems. We anticipate that these properties may provide a much sterner test of our models than reproducing the static structure.

There is a wealth of Raman data available for these systems. Indeed, because of the corrosive nature of melts and the high temperatures involved in their study (which make sample containment difficult), until recently almost all the information about the microstructure of melts was inferred from Raman spectroscopy. It is therefore important to show that the properties of the simulated fluids are consistent with the Raman spectra. However, establishing this connection is not straightforward. The peaks in the Raman spectra are usually assigned to vibrations of molecular units, but as we have seen from our simulations and comparison with diffraction data on these systems (with the exception of Al_2Cl_6 and Fe_2Cl_6) the pure melts tend to consist of networks of edge or vertex sharing polyhedra. Fortunately, many Raman studies are not only performed on the pure melt but also on its mixtures with an alkali halide. As we saw in the previous chapter the addition of an alkali halide with a weakly coordinating cation acts to break up the network structure giving rise to such molecular species as MCl_6^{3-}. It is then plausible that the molecular vibrations of these species are responsible for the peaks observed. We thus have a way of making contact with Raman studies of these solutions by calculating the densities of states of the vibrations of such species in our simulations.

However, the extent to which this type of interpretation may be applied in the pure melts, where our direct observations suggest that any molecular units are part of a more extended network remains to be seen. Additional features are found in the Raman spectra of pure $ScCl_3$ which cannot be assigned to isolated molecular units. Furthermore, for $LaCl_3$ the interpretation of the Raman spectrum is at variance with the results of the diffraction studies. The polarized Raman spectrum shows a single strong Raman band, which is taken to imply octahedral coordination around La^{3+} [95]. The diffraction data (and the simulations) suggest a higher coordination number, closer to that of the crystal. In order to make the connection between simulation and experiment more direct (*i.e.* to avoid the *assumption* that molecular units are present) a more complete calculation of Raman spectra is presented which looks at the fluctuating polarizabilities of the melt.

Further information on the dynamics of the melts at long times is contained within ionic mobility data. Whilst the Raman data is concerned with the vibrations of the coordination polyhedra and their network connections, the mobility should reflect the way that these structures break up and allow the ions to travel independently. Initially we will examine the dynamical behaviour of molten MCl_3 salts by looking at the diffusion coefficients of the ions in the melts. Whilst there is no experimental data on the actual diffusion of the ions, we can relate this quantity to available experimental data by calculating conductivities.

8.2 Raman Spectra

Raman spectroscopy gives a different viewpoint on the nature of the local order than the diffraction studies already presented. As we have seen the diffraction studies yield pair distribution functions which have been discussed in terms of local coordination geometry about each ion. The Raman spectra exhibit distinctive bands, which are assigned to the vibrational modes of molecular ion species which are presumed to exist. Thus, in the conventional interpretation of the Raman data, the melt is regarded as a mixture of such species which are in dynamic equilibrium, the positions of the equilibrium being shifted by the addition of other ions (CsCl in the case of $ScCl_3$) or by changes in temperature or pressure. The pair distribution functions show a charge ordering tendency, which persists out to fairly large separations. From the diffraction/simulation viewpoint, therefore, it does not seem reasonable to describe these functions in terms of particular molecular structures.

8.2.1 $ScCl_3$/CsCl - The Experimental data

In pure $ScCl_3$ the study of the diffraction data (section 6.9) suggests a network based on local 5-6 coordination with the nature of the linkages (edge sharing) responsible for the short and intermediate range order not reproduced with simpler potentials. The large pre-peak at low scattering angles is indicative of this. In its mixtures with CsCl the $ScCl_3$ network is broken down giving rise to the type of molecular species suggested by spectroscopy. For example in dilute mixtures (15-25% $ScCl_3$) the 6-coordinate $ScCl_6^{3-}$ ions can clearly be seen

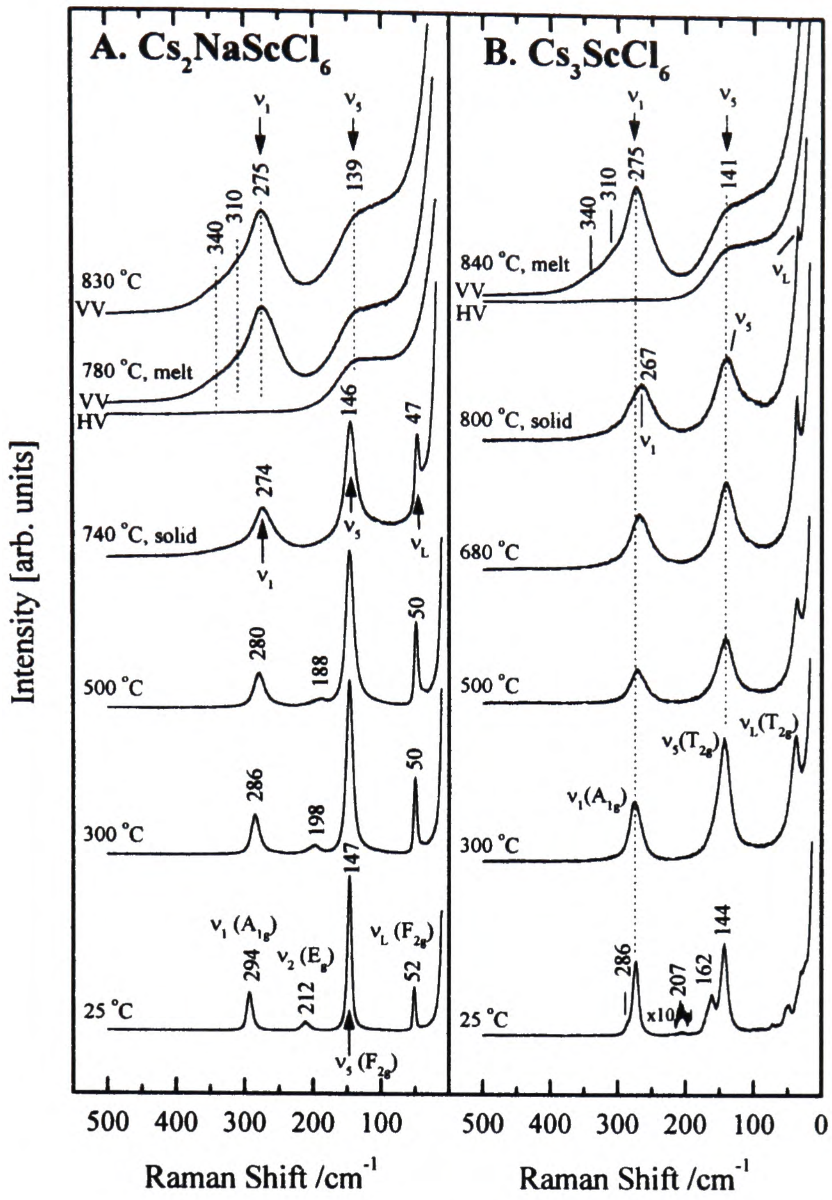

Figure 8.1: *Experimental Raman data for (A) $Cs_2NaScCl_6$ (B) Cs_3ScCl_6*

(section 7.3.3). We saw for $DyCl_3$ that the evolution of the calculated diffraction data in this dilution process is in good accord with that seen experimentally.

The experimental Raman spectra obtained by Zissi and Papatheodorou [96] for various $ScCl_3/CsCl$ compositions are shown in figures 8.1 and 8.2.

While the crystal structure of Cs_3ScCl_6 is not known, by analogy with other systems of the same stoichiometry and ionic size, it is thought to contain discrete $ScCl_6^{3-}$ distorted octahedra [98]. On heating the crystal the bands are broadened. At high temperatures the spectra are the same as those of $Cs_2NaScCl_6$ which is known to contain almost ideal discrete $ScCl_6$ octahedra. At low Sc concentrations, the molten mixtures show bands in the same positions suggesting that the predominant species are $ScCl_6^{3-}$ octahedra.

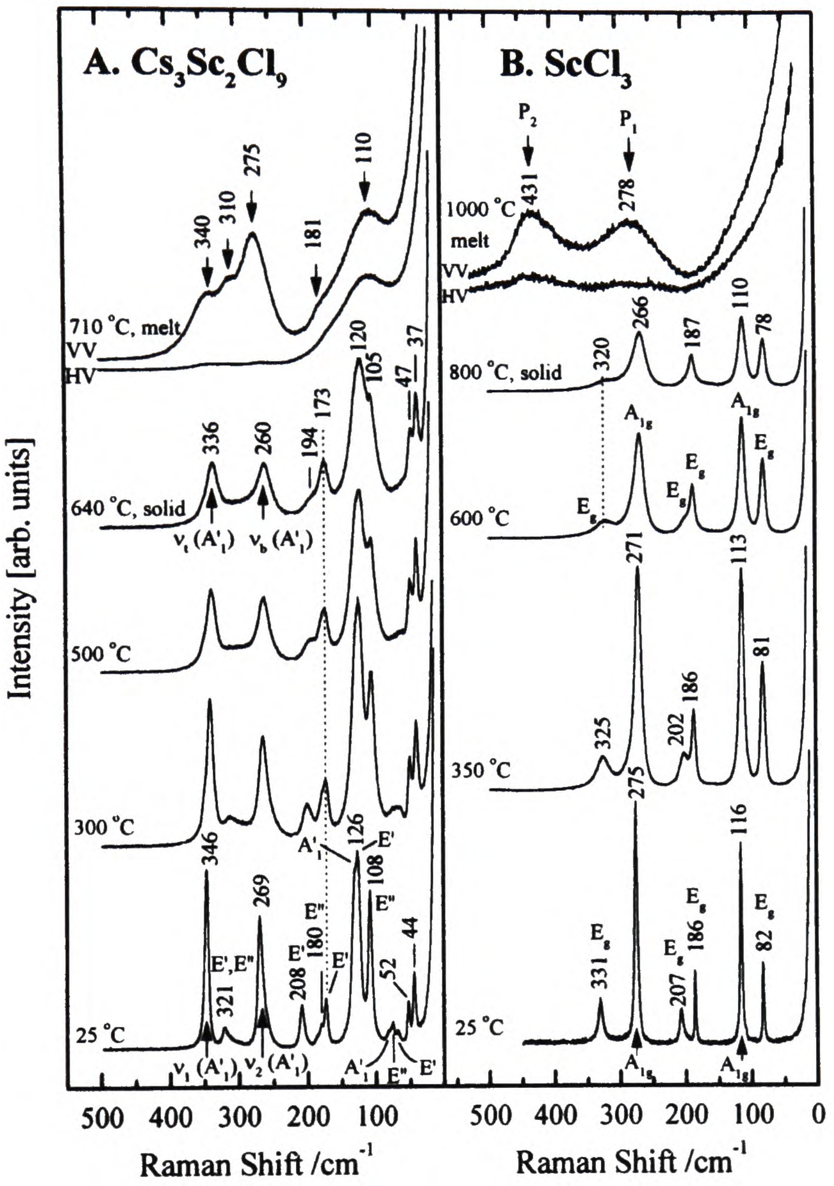

Figure 8.2: *Experimental Raman data for (A) $Cs_3Sc_2Cl_9$ (B) $ScCl_3$*

At higher Sc concentrations, the spectra are discussed with respect to the $Cs_3Sc_2Cl_9$ crystal. The crystal structure of $Cs_3Sc_2Cl_9$ consists of $Sc_2Cl_9^{3-}$ face sharing $ScCl_6^{3-}$ octahedra. In the spectra the position of bands at 336cm^{-1} and 260cm^{-1} are preserved into the melt. These are assigned to terminal and bending A_1 modes of the face sharing dimers. It is concluded that octahedral coordination persists at these higher concentrations with some inter-octahedral linkages forming, as dictated by the stoichiometry.

On increasing the concentration of $ScCl_3$ further an interesting evolution is seen (figure 8.2B). The band at 340cm^{-1} in $Cs_3Sc_2Cl_9$ (351cm^{-1} in 50% $ScCl_3$) moves to higher frequencies (387cm^{-1} in 75% $ScCl_3$) until for the pure melt there are two well separated broad bands, one at 277cm^{-1} and one at 432cm^{-1}. The interpretation of this structure is unclear. It might arise either through a reduction in the Sc^{3+} coordination number (though this tends to be discounted as the pure crystal has the octahedrally coordinated BiI_3 structure), or through vibrations associated with inter-octahedral linkages (or both). This concentration dependence of the Raman spectrum is regarded as unusual by the Raman spectroscopists [96]. In most $MCl_3/M'Cl$ solutions, the structure of the spectrum is relatively unchanged as the MCl_3 concentration is increased [95]. In particular, the origin of the high frequency (432cm^{-1} in pure $ScCl_3$) feature is unclear (though a similar feature is observed in YCl_3 [46]). The band at 278cm^{-1} is presumed to be the A_{1g} mode (present in the solid at 275cm^{-1}).

8.3 Density of States Analysis

One way of making a link with Raman spectra is to examine the vibrational density of states of the ionic melts by looking at the vibrations of molecular ion units. In effect, this involves analysing the spectroscopists' own model for the features that are observed. It is not a calculation of the Raman spectra, *per se* as this requires a study of the fluctuating polarizability due to the interionic interactions (section 8.4).

The DOS is obtained by examining the structure which appears in the spectra of various velocity correlation functions of the ions in the melt *eg.*

$$C_v(\omega) = \Re \int_0^\infty dt e^{i\omega t} \langle \mathbf{v}_i(t) \cdot \mathbf{v}_i(0) \rangle, \tag{8.1}$$

where $\mathbf{v}_i$ is the velocity of a particular ion. This quantity is comparable to the reduced Raman spectra and may be expected to exhibit similar band structure. However, we will obtain different band intensities since the relationship between the polarizability of the melt and the ion coordinates is ignored. For dilute $ScCl_3$ (15-25%) mixtures the interpretation of the Raman spectra might be expected to be relatively straightforward. The $ScCl_6^{3-}$ molecular units are clearly seen and their vibrational modes give rise to clearly resolved features in the DOS (figure 8.3(a) and (b)). The DOS for the range of $ScCl_3$/CsCl compositions are shown in figures 8.3 (a)-(e).

For an isolated octahedron we expect Raman-active vibrational normal modes of symmetry A_{1g}, F_{2g} and E_g [99]. The A_{1g} contributes only to the polarized spectrum whereas the others are depolarized.

By taking appropriate combinations of the relative velocities of ions, the velocities of these symmetry coordinates may be obtained in the course of the simulation, and their oscillation frequencies may be used to identify the structure in the DOS and make contact via the selection rules, with features seen in the Raman spectra [100]. At a given timestep in the simulation, the Cl^- neighbours, $i1 \rightarrow i6$, of a six coordinated Sc^{3+} ion, i are identified. The velocities $\mathbf{v}_{i1}$ and positions $\mathbf{r}_{i1}$ of these neighbours relative to the cation are then calculated, and the velocities parallel and perpendicular to the bond projected out

$$v_{i1}^{\|} = \mathbf{v}_{i1} \cdot \hat{\mathbf{r}}_{i1}, \tag{8.2}$$

where $\hat{\mathbf{r}}_{i1}$ is the unit vector along $\mathbf{r}_{i1}$, and

$$v_{i1}^{\perp} = \mathbf{v}_{i1} - v_{i1}^{\|} \hat{\mathbf{r}}_{i1}. \tag{8.3}$$

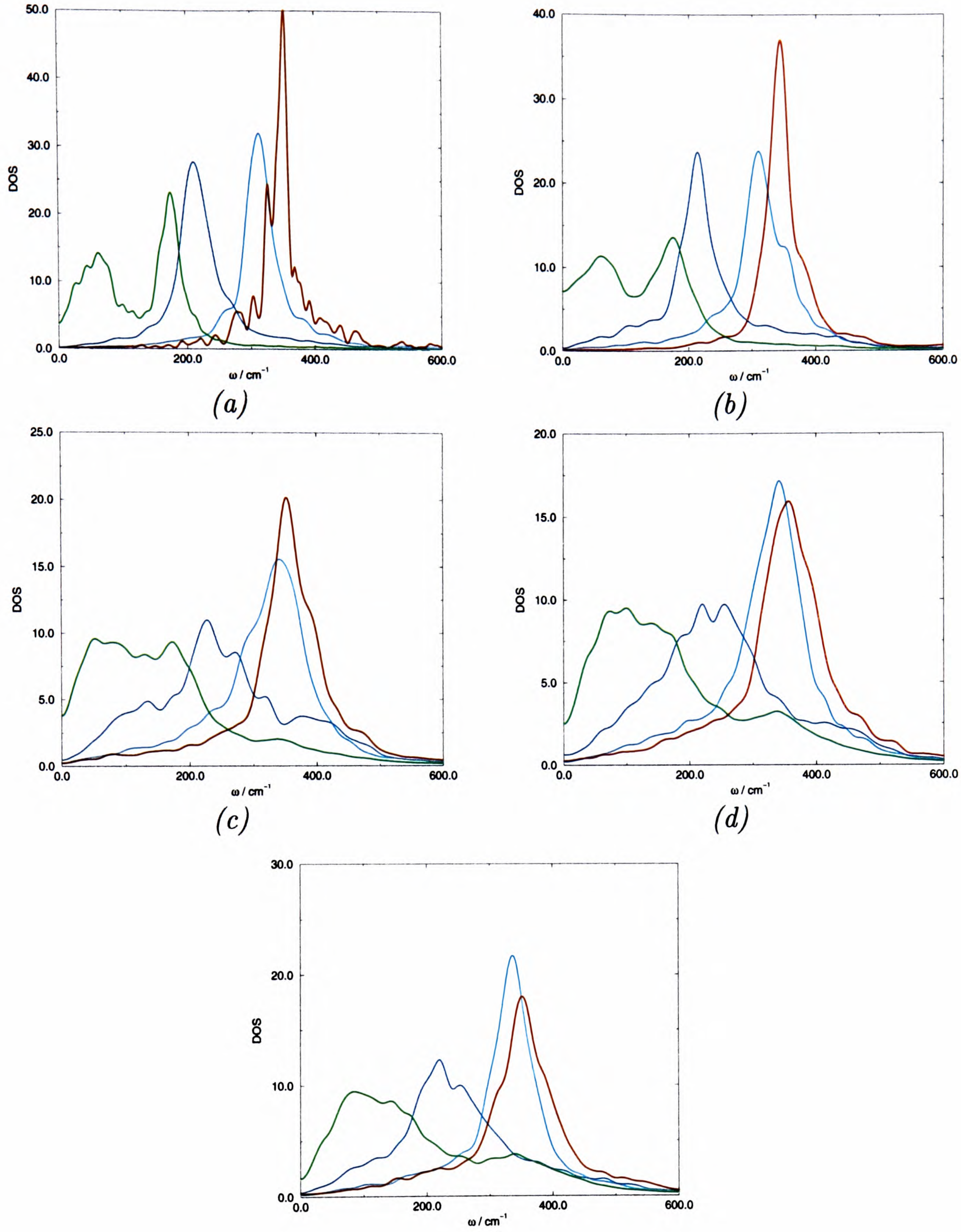

(a) *(b)* *(c)* *(d)* *(e)*

Figure 8.3: *DOS for (a)15%$ScCl_3$/85%CsCl (b)25%$ScCl_3$/75%CsCl (c)50%$ScCl_3$/50%CsCl (d)75%$ScCl_3$/25%CsCl mixtures and (e) Pure $ScCl_3$. The various modes shown are A_{1g}(6-cn)(cyan line), A_{1g}(5-cn)(red line), F_{2g}(green line), E_g(blue line)*

The velocity of the A_{1g} symmetric stretching vibration is then

$$V^i_{A_{1g}} = \sum_{i\alpha=1\to 6} v^{||}_{i\alpha}. \tag{8.4}$$

The symmetry coordinates for the degenerate modes are somewhat more complex. Suppose that we have identified (by consideration of $\hat{\mathbf{r}}_{i\alpha} \cdot \hat{\mathbf{r}}_{i\beta}$) that the pairs $i1 - i2$, $i3 - i4$ and $i5 - i6$ correspond to opposite vertices of the octahedron. One component of the F_{2g} bending vibration is (approximately)

$$V^i_{F_{2g},1} = (\mathbf{v}^{\perp}_{i3} - \mathbf{v}^{\perp}_{i5}) \cdot (\hat{\mathbf{r}}_{i3} - \hat{\mathbf{r}}_{i5}) + (\mathbf{v}^{\perp}_{i4} - \mathbf{v}^{\perp}_{i6}) \cdot (\hat{\mathbf{r}}_{i4} - \hat{\mathbf{r}}_{i6}), \tag{8.5}$$

and the other two components are obtained by permutating labels appropriately. Similarly, one component of the E_g (stretch) is

$$V^i_{E_g,1} = v^{||}_{i1} + v^{||}_{i2} - (v^{||}_{i3} + v^{||}_{i4} + v^{||}_{i5} + v^{||}_{i6})/2^{1/2}, \tag{8.6}$$

and the F_{1u} stretch is

$$V_{F^i_{1u},1} = v^{||}_{i1} - v^{||}_{i2}, \tag{8.7}$$

together with the other permutations. If a Sc^{3+} ion is not six-coordinate at some instant, we enter 0 for the velocity. Were these to correspond exactly to the velocities of the normal modes and were the system to vibrate as a collection of isolated octahedra, the spectra of each of these velocities *eg.*,

$$C_{V_{A_{1g}}}(\omega) = \Re \int_0^{\infty} dt e^{i\omega t} \langle V^i_{A_{1g}}(t) \cdot V^i_{A_{1g}}(0) \rangle, \tag{8.8}$$

would exhibit a peak corresponding to the frequency of the appropriate normal mode of vibration of the octahedral unit.

The densities of states for the dilute 15% $ScCl_3$ mixture (figure 8.3(a)) shows (with the exception of the F_{2g} velocity) that each of the spectra exhibit a single peak and that our approximate symmetry coordinates are representing the normal modes adequately. The Raman active vibrations of the $ScCl_6^{3-}$ octahedra give rise to a single peak for the symmetric stretching mode located at

	Frequency of mode / cm^{-1}			
Amount of $ScCl_3$ (%)	A_{1g} (6)	A_{1g} (5)	E_g	F_{2g}
100	336	352	219	185
75	342	357	220	100
50	341	352	227	52
25	310	344	214	62,175
15	312	352	211	62,175

Table 8.1: *Peak positions in DOS for $ScCl_3/CsCl$ mixtures*

$v(A_{1g})$ ~312cm^{-1} and for asymmetric stretching mode $v_2(E_g)$=211cm^{-1}. The bending mode spectrum exhibits a double peak structure with maxima at 62 and 175cm^{-1}. The peak positions are tabulated in table 8.1.

In the experimental spectra for 15% $ScCl_3$ the peaks are observed at $v(A_{1g})$=275cm^{-1}. This compares well with the positions of the corresponding simulation although the simulated frequencies are a little on the high side (312 compared with 275cm^{-1} experimentally). In the crystal spectra of 25% $ScCl_3$ there are two F_{2g} bands at 52 and 147cm^{-1} (62 and 175cm^{-1} from densities of states). The higher of these is due to the internal vibrations of the octahedron and the low frequency vibration is due to a translational (lattice) mode. The appearance of the lattice mode in experimental studies of solutions has been noticed previously [100]. Overall, then, it would appear that the calculated vibrational frequencies of the isolated octahedral units found in the simulations at very low $ScCl_3$ concentrations correspond quite well with the positions of observed Raman bands.

We have also shown DOS for the symmetric strectch of the five coordinate units in figures 8.3 and table 8.1. These bands are at around 350cm^{-1} in all the melts and so, as expected, do not result in any contribution to the high frequency band in the pure $ScCl_3$.

On increasing the $ScCl_3$ concentration we have seen that the Sc^{3+} ions remain predominantly six coordinate in the melt (with a number of 5 coordinate Sc^{3+}) but that the polyhedral units now link together to form a network. It can be seen that on increasing the $ScCl_3$ concentration all the peaks are broadened and the F_{2g} feature that was split into a doublet in 15% $ScCl_3$ now only consists of a single broad peak. For the pure $ScCl_3$ the peaks are at $v_1(A_{1g})$=336cm^{-1}, $v_2(E_g)$=219cm^{-1} and $v_5(F_{2g})$=185cm^{-1} These frequencies are similar to those of the isolated octahedral units calculated for the 15% $ScCl_3$ mixture. The bands become broader as the only substantial consequence of the inter-octahedral coupling. No new bands have appeared to account for the increasingly complex Raman spectrum actually observed. In particular, in none of the simulated DOS have we seen any feature at the high frequencies (432cm^{-1}) observed in the experimental spectrum of the pure melt.

8.4 Light Scattering

In this section a more direct calculation of the Raman spectrum is attempted. Raman light scattering is caused by the fluctuation in the polarization density of the melt induced by the interionic interactions. While these phenomena have been extensively investigated in van der Waals materials *e.g.* liquid argon the mechanisms responsible for the interaction induced polarizability are not well understood for ionic materials. Madden and co-workers [28, 102–104] have attempted to understand the interaction-induced polarizability in ionic materials using electronic structure calculations on distorted crystals. The influence of the environment on the ionic polarizability is decomposed into an asymptotic and a short-range contribution. The asymptotic contribution contains the changes in the ionic polarizability brought about by the field and field gradient at the centre of the ion due to the charges on the other ion, this response is calculated via hyperpolarizabilities appropriate to the condensed phase environment. The short-range term describes the additional effect of the confining potential discussed in the Introduction. The Raman spectra are obtained by calculating the dependence of the melt polarizability on the ionic coordinates. This is discussed for alkali halides in refs [104] and [105]. These calculations were shown to *predict* the experimentally observed Raman spectrum for LiF by Dracopoulos and Papatheodorou [106].

8.4.1 Interaction induced polarizability model

The instantaneous polarizability in a sample of N molecules or ions induced by an external, optical frequency field E^0 is given by [104]

$$P(\mathbf{r}) = \sum_i \mathbf{p}_i \delta(\mathbf{r} - \mathbf{r}_i), \tag{8.9}$$

and

$$\mathbf{p}_i = \alpha_i(\mathbf{R}_N)\{E^0(\mathbf{r}_i) + \sum_{ji}{}' \mathbf{T}(\mathbf{r}_{ij})\mathbf{p}_j\}. \tag{8.10}$$

This polarization fluctuates because of the molecular motion, which is responsible for the light scattering spectrum. In equations 8.9 and 8.10 $\mathbf{p}_i$ is the instantaneous induced dipole on molecule i and $\mathbf{T}$ is the dipole-dipole interaction tensor $(\nabla\nabla\mathbf{r}_{-1})$. $\alpha_i(\mathbf{R}_N)$ is the instantaneous polarizability of ion i, its dependence on the relative position of the ions in the sample is indicated explicitly.

If the sample is a static crystal then the position of every ion in the sample is known and the $\langle\alpha(\mathbf{R_N})\rangle$ is given by the polarizability of the ion appropriate to that single configuration - this is known as the in-crystal polarizability. The relationship of the in-crystal polarizability to that of the free ion has been investigated in electronic structure calculations. It was found that the in-crystal polarizability for cations is the same as the value for an isolated ion (*ie.* as we have seen the environmental effects on cation polarizabilities are negligible) but that anionic polarizabilities are extremely sensitive to environmental effects.

The light scattering spectrum is determined by the time-dependent correlation function of the fluctuating part of P, *ie.*,

$$I_{ab}(\omega) \propto \Re \int_0^\infty dte^{i\omega t} \langle \Delta P_a(\mathbf{k}, t) \Delta P_a(\mathbf{k}, 0) \rangle, \tag{8.11}$$

where $I_{ab}(\omega)$ is the spectrum of light scattered with scattering vector **k**, frequency shift ω, and polarized along the direction a when the incident field is polarized along b. To determine the light scattering spectrum, the polarization, and hence the ionic polarizabilities, must be known at all the ionic configurations visited in the melt and appropriate averages taken. Fowler and Madden [28] suggested that anion polarizabilities for melt configurations could be determined from electronic structure calculations on distorted crystals. In general terms, one would expect two effects to contribute to the response of the polarizability to a change in the crystalline environment, arising from the electronic distortions induced by the ionic field at the site of the ion and from short-range overlap interactions with neighbouring ions. In the model described below these effects are contained within two separately computed terms - so that their distinctive influence on the spectra may be traced

$$\alpha(\mathbf{R}_N) = \mathbf{I}\alpha^{cryst} + \alpha^{as}(\mathbf{R}_N) + \alpha^{sr}(\mathbf{R}_N), \tag{8.12}$$

where **I** is the unit tensor, α^{cryst} is the in-crystal polarizability and α^{as} and α^{sr} are the asymptotic and short-range contributions to the polarizability that arise from the departure of the instantaneous ionic environment in the melt from that in the crystal. α^{as} describes the influence of the ionic field and field gradient (which are both zero in the cubic crystalline environment). It is given by

$$\begin{aligned} \alpha^{as,i}_{\alpha\beta}(\mathbf{R}_N) &= (1/2)\gamma_{\alpha\beta\gamma\delta}\left\{{\sum_{ji}}' Q_j \nabla_\gamma (\mathbf{r}_{ij})^{-1}\right\} \\ &\times \left\{{\sum_{ki}}' Q_k \nabla_\delta (\mathbf{r}_{ik})^{-1}\right\} \\ &+ (1/3)B_{\alpha\beta,\gamma\delta}{\sum_{ji}}' Q_j \nabla_\gamma \nabla_\delta (\mathbf{r}_{ij})^{-1}, \end{aligned} \tag{8.13}$$

where Q_j is the charge on ion j and γ and B are hyperpolarizabilities which describe contributions to the change in the polarizability of the ion which are quadratic in the field at the ion and proportional to the field gradient, respectively. In equation 8.13 the Greek subscripts refer to Cartesian components of the tensors (repeated indices are summed over); when the ionic environment is spherically symmetrical, these tensor components are specified by a single number:

$$\gamma_{\alpha\beta\gamma\delta} = (1/3)\bar{\gamma}\{\delta_{\alpha\beta}\delta_{\gamma\delta} + \delta_{\alpha\gamma}\delta_{\beta\gamma} + \delta_{\alpha\delta}\delta_{\beta\gamma}\}, \tag{8.14}$$

and

$$B_{\alpha\beta,\gamma\delta} = \bar{B}\{(3/4)[\delta_{\alpha\gamma}\delta_{\beta\gamma} + \delta_{\alpha\delta}\delta_{\beta\gamma}] - (1/2)\delta_{\alpha\beta}\delta_{\gamma\delta}\} \tag{8.15}$$

values for $\bar{\gamma}$ and $\bar{B}$ are taken from the mean, in-crystal hyperpolarizabilities obtained in electronic structure calculations. The significance of the values of α^{sr} for distorted crystal configurations was then considered, α^{sr} being defined as the difference between the total polarizability for the anion in the distorted crystal and the sum of α^{cryst} and α^{as}.

It was shown that only the nearest neighbour cations made an appreciable contribution to α^{sr} and that it could be viewed as the consequence of the changes in the degree of confinement of the anion charge density in the potential well caused by the electrostatic and overlap interactions as the neighbours departed from the perfect crystalline arrangement. In order to incorporate the influence of this short-range, confining potential on the anionic polarizability in a computationally convenient form, Madden and Board suggested that the distorted crystal results for α^{sr} could be used to parameterize a Drude model [107] for the ionic polarizability. In the simple Drude model the polarization of an atom by an electric field is represented through the effects of the field on a pair of charges, $+Q$ located on the nucleus and $-Q$ harmonically bound to it with a spring of force constant K. The polarizability of the atom is then

$$\alpha = Q/K. \tag{8.16}$$

In the melt the ionic polarizability is not a simple scalar and depends on the configuration of the other ions, so the above equation is generalized to

$$\alpha^{i}(\mathbf{R}_N) = \alpha^{as,i}(\mathbf{R}_N) + Q[\mathbf{K}_i(\mathbf{R}_N)]^{-1}. \tag{8.17}$$

The force constant for ion i, $\mathbf{K}_i$ depends upon the position of near neighbouring ions in a way which reflects the influence of their confining potential on the ion's polarizability. For computational convenience it is desirable to express $\mathbf{K}_i$ as a function of pair separations; since $\mathbf{K}_i$ is a second rank, symmetric tensor the most general expression of this form is

$$\mathbf{K}_i(\mathbf{R}_N) = \left[K_0 + \sum_{ji}{}' G(r_{ij})\right]\mathbf{I} + \sum_{ji}{}' H \times (r_{ij})(3\mathbf{r}_{ij}\mathbf{r}_{ij} - \mathbf{I}), \tag{8.18}$$

here G and H are short-range, scalar functions of the interionic distance. In the Born-Mayer form for the interionic potential 1.7, the short-range interactions are exponential in form; it seems desirable to use the same form for G and H, *i.e.*:

$$G(r_{ij}) = a_{ij} exp[-(r_{ij} - \sigma_{ij})/c_{ij}], \tag{8.19}$$

and

$$H(r_{ij}) = b_{ij} exp[-(r_{ij} - \sigma_{ij})/d_{ij}]. \tag{8.20}$$

8.4.2 The Light Scattering Spectrum

The full expression for the polarization induced by the external field (equations 8.9 and 8.10) must be solved iteratively in order to treat the dipole-induced dipole terms in a self consistent manner. Here we make use of a simpler form obtained by iterating only once and replacing the instantaneous value of $\alpha(\mathbf{R}_N)$ in equation 8.10 by $\mathbf{I}\alpha^{cryst}$ so that the dipole induced dipole term is calculated as if the ions responded with their in-crystal polarizability. If we further neglect the spatial dependence of $\mathbf{E}^0$ over the range of interparticle distances which contribute to the dipole-induced dipole term (*i.e.* take a long wavelength limit as is normal in the treatment of van der Waals materials) we obtain

$$\lim_{k\to 0} P_\alpha(\mathbf{k}) = \sum_i \left\{ \alpha^i_{\alpha\beta}(\mathbf{R}_N) + {\sum_{ji}}' (\alpha_{cryst})^2 T_{\alpha\beta}(\mathbf{r}_{ij}) \right\} E^0_\beta. \qquad (8.21)$$

This first-order dipole-induced dipole (DID) model will be adequate provided that the DID terms do not make the largest contribution to the fluctuating part of the polarization, otherwise higher order DID effects are likely to be important. In this limit the response of the sample can be expressed in terms of an effective polarizability, Π,

$$\lim_{k\to 0} P_\alpha(\mathbf{k}) = \Pi_{\alpha\beta} E^0_\beta. \qquad (8.22)$$

When the explicit form for the terms appearing in the polarization are used in the general expression for the spectrum we obtain

$$I_{ab}(\omega) \propto |E^0_b|^2 \Re \int_0^\infty dt e^{i\omega t} \langle \Delta\Pi_{ab}(t) \Delta\Pi_{ab}(0) \rangle, \qquad (8.23)$$

where $\Delta\Pi_{\alpha\beta}$ is a component of the fluctuating part of the polarizability of the sample. This may be written as a sum of contributions from the different mechanisms discussed above.

$$\Delta\Pi_{\alpha\beta}(t) = \Delta\Pi^{sr}_{\alpha\beta}(t) + \Delta\Pi^{DID}_{\alpha\beta}(t) + \Delta\Pi^{B}_{\alpha\beta} + \Delta\Pi^{\gamma}_{\alpha\beta}(t), \qquad (8.24)$$

and

$$\Pi^{sr}(t) = \sum_i q\{\mathbf{K}^i[\mathbf{R}_N(t)]\}^{-1}, \tag{8.25}$$

$$\Pi^{DID}(t) = \sum_i \sum_{ji}{}' (\alpha^{cryst})^2 \mathbf{T}(\mathbf{r}_{ij}) \tag{8.26}$$

and where the two contributions to the asymptotic term, quadratic in the field and linear in the field gradient, have been represented separately,

$$\Pi^{B}_{\alpha\beta}(t) = \sum_i B_{\alpha\beta,\gamma\delta} \sum_{ji}{}' \nabla_\gamma \nabla_\delta (\mathbf{r}_{ij})^{-1}, \tag{8.27}$$

and

$$\Pi^{\gamma}_{\alpha\beta\gamma\delta}(t) = \sum_i \gamma_{\alpha\beta\gamma\delta} \left[\sum_{ji}{}' \nabla_\gamma (\mathbf{r}_{ij})^{-1}\right] \times \left[\sum_{ki}{}' \nabla_\delta (\mathbf{r}_{ij})^{-1}\right]. \tag{8.28}$$

In the liquid phase the spectrum found for any combination of incident and scattered polarizations may be expressed in terms of the isotropic and anisotropic spectra. [$I_{ISO}(\omega)$ and $I_{ANI}(\omega)$, respectively]. In particular,

$$I_{ZZ}(\omega) = I_{ISO}(\omega) + (4/3) I_{ANI}(\omega), \tag{8.29}$$

and

$$I_{xz}(\omega) = I_{ANI}(\omega), \tag{8.30}$$

are the polarized and depolarized spectra. I_{ISO} involves fluctuations in the trace of the polarizability of the sample,

$$\Pi_{ISO} = (1/3)(\Pi_{xx} + \Pi_{yy} + \Pi_{zz}), \tag{8.31}$$

at the level of the interaction-induced polarizability of individual ions it reflects spherically symmetric distortions of the ion. The experimental spectra presented for $ScCl_3$, $ScCl_3/CsCl$ and $LaCl_3$ are the polarized spectra and so it is this that we will attempt to calculate. The DID polarizability and the B part of the asymptotic terms make no contribution to the isotropic spectrum since the T tensor and B are traceless tensors and so in the results presented these terms will be ignored. I_{ANI} is determined by the fluctuating part of the traceless component of the polarizability tensor Π_{ANI}. This consists of five independent elements, given in terms of the space fixed Cartesian components by

$$\Pi_{ANI,1} = 2\Pi_{zz} - \Pi_{xx} - \Pi_{yy}, \tag{8.32}$$

$$\Pi_{ANI,2} = \sqrt{3}(\Pi_{xx} - \Pi_{yy}), \tag{8.33}$$

$$\Pi_{ANI,3} = \sqrt{12}\Pi_{xy}, \tag{8.34}$$

$$\Pi_{ANI,4} = \sqrt{12}\Pi_{xz}, \tag{8.35}$$

$$\Pi_{ANI,5} = \sqrt{12}\Pi_{yz}, \tag{8.36}$$

In practice, we calculate the spectra of all 5 and average. Π_{ANI} reflects anisotropic fluctuations in the anionic environment with the symmetry of *d* orbitals. All 4 contributions to the total polarizability of the sample may contribute to this spectrum.

8.5 Light Scattering Simulations

8.5.1 Simulation Details

The polarizability correlation functions were calculated from ionic coordinates generated for pure $ScCl_3$, 25% $ScCl_3$ /75% CsCl and pure $LaCl_3$. The initial temperatures and densities are as listed in table 7.2 for $ScCl_3$ and $ScCl_3$/CsCl and in table 6.4 for $LaCl_3$. The simulations were equilibrated for over 50ps and averages computed over a further 72ps (≡200000 MD steps).

The γ, B and DID polarizabilities involve the Coulomb field, field gradient and the dipole-induced dipole interaction tensor. These are all slowly decaying functions of the interionic separation. At the temperatures of experiment the results did show the effect of the underlying cubic symmetry of the simulation cell. This was seen in the five independent elements of the anisotropic polarizability not behaving identically, on average. Rather they grouped into a set of two (of E_g symmetry) and a set of three (of T_{2g} symmetry). To overcome this problem elevated temperatures of 1750K for $ScCl_3$ and 2000K for $LaCl_3$ were used. No such problem was encountered in the 25%$ScCl_3$/75% CsCl as here the simulation cell consists mostly of CsCl which will have melted well below the simulation temperature of 1103K.

The hyperpolarizabilities were the same in all the simulations and took values of $B_{\alpha\beta,\gamma\delta} = -342.0$au and $\gamma_{\alpha\beta,\gamma\delta}$=2270.0au. The undistorted polarizability of the chloride ion was taken to be 27.9 au and the radii and polarizabilities remain the same as for the structural studies (tables 6.1 and 6.3). The short range parameters appropriate for use in equations 8.19 and 8.20 are listed in table 8.2. Note that this does not mean that the La^{3+}, Sc^{3+} and Cs^{+} are being treated as identical as far as the short-range polarizability is concerned, the cation radius enters the expression for the polarizability (equation 8.19). These parameters are very similar to those uncovered in the electronic structure calculations on alkali halides and can be expected to give a short-range interaction induced polarizability of the correct range. Although there is clearly a good deal of arbitrariness in these short-range parameters, they produce a good value for the average polarizability in crystalline environments.

	a	b	c	d
−−	0.0011	0.0011	1.8200	1.8200
+−	0.0031	0.00275	1.323	1.196
++	0.00	0.00	0.00	0.00

Table 8.2: *Short-range potential parameters for use in equations 8.19 and 8.20*

8.5.2 Simulated Isotropic Raman spectrum - 25% $ScCl_3$ solution

As discussed above, the analysis of the Raman bands in dilute solution in terms of the bands in the vibrational DOS of the isolated octahedral units seemed reasonably consistent. It therefore makes sense to discuss this spectrum first, despite the fact that it is technically more difficult to calculate than for the pure melts.

The contributing mechanisms to the isotropic spectra are the short-range and γ terms. Figure 8.4 shows these contributions to the spectra along with the total spectra obtained by taking in to account the short-range gamma cross correlation. The short range contribution is seen to have a pronounced peak close to the frequency of the A_{1g} mode that emerged from the DOS calculations, *i.e.* this contribution to the polarizability seems to behave in accord with the standard spectroscopic interpretation. It also has a shoulder at 180cm^{-1} which is probably the F_{2g} band which appears at 175cm^{-1} in the densities of states and 147cm^{-1} in experiment. The gamma contribution shows a quite different spectrum; it exhibits a main band at slightly higher frequencies than the A_{1g}. This is not simply due to a difference of resolution, the respective oscillations in the polarizability correlation functions of the sr and gamma polarizabilities have different periods. This main band itself has a shoulder at 415cm^{-1}. These frequencies do not appear to correspond to frequencies of normal modes of the octahedral units.

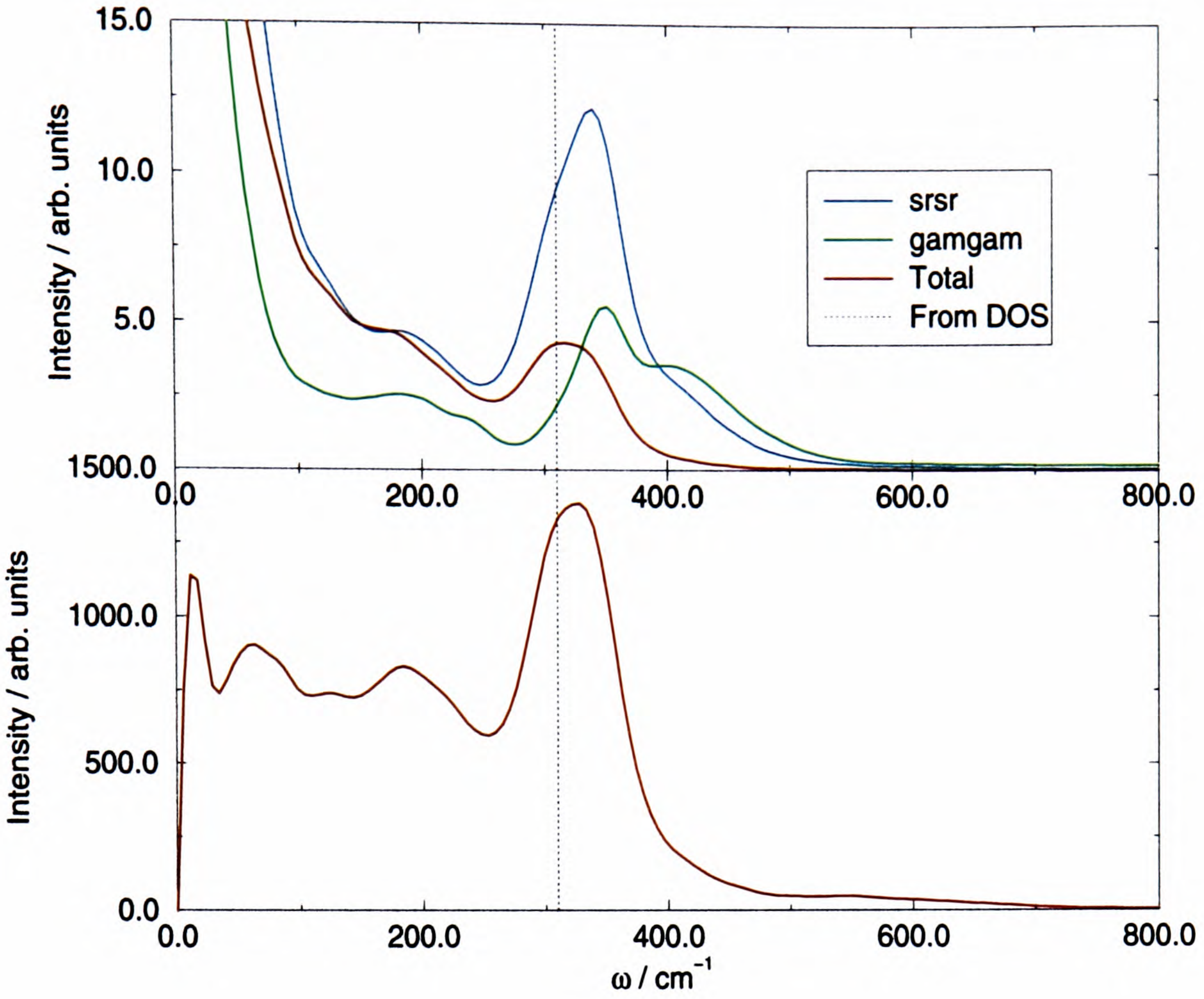

Figure 8.4: *Light scattering spectra for 25%ScCl$_3$/75 %CsCl mixture. The lower panel shows the total spectrum multipled by frequency.*

The total spectrum obtained by combining the sr and gamma spectra *and* the spectrum arising from the cross-correlation of these polarizabilities is shown in the figure. In this case, the cross term seems to cancel the distinctive features of the gamma spectrum. The total spectrum has a structure very similar to that seen in the experimental spectrum of the dilute solution with a single main peak at 315cm^{-1}, slightly higher than the peak observed experimentally, and close to the frequency of the A$_{1g}$ mode of the octahedral units. Thus, despite the presence of significant contributions to the total polarizability from both the sr and gamma terms, the total spectrum is in good accord with experiment.

8.5.3 Simulated Isotropic Raman Spectrum - Pure ScCl$_3$.

The isotropic spectra calculated for the pure ScCl$_3$ melt at a temperature of 1750K are shown in figure 8.5. As in the solution spectra, the position (336cm^{-1})

of the A_{1g} (6-coordinate) stretch from the density of states is in very good agreement with the strong peak in the spectra from the short-range autocorrelation function from the light scattering (figure 8.5).

The spectrum of the gamma polarizability is quite different, and it has changed markedly from the dilute solution. It has a *minimum* close to the A_{1g} band and a broad peak centered at a frequency of $\sim$500cm^{-1}. This may well be the feature that results in the broad high frequency band observed in the Raman spectra, albeit appearing at too high a frequency in the simulation.

The total spectrum (including the short-range - gamma cross term) is also shown in the figure. In the lower panel of the figure 8.5, the spectra multiplied by a factor of ω is shown: this helps to suppress the strong central line of the Raman spectrum and to accentuate the bands of interest. Since both the gamma and sr spectra are of similar intensity, and because the cross-correlation between them is quite considerable, the total spectrum resembles neither the *sr* or *gamma* spectra strongly. Note that there is a shift in the position of the main peak of the sr spectrum to a frequency very close to that observed experimentally. This suggests that the association of the main band with the A_{1g} octahedral vibration may not always be reliable - it could be affected by the scattering mechanism. It further suggests an explanation for the shifting of the bands observed in the $ScCl_3$/CsCl mixtures as the concentration is varied. This consequence of the interference between the sr and gamma polarizabilities has previously been noted in $ZnCl_2$ [108].

The high frequency feature of the gamma spectrum is diminished in the total spectrum but still appears with a significant intensity. (At least) two high frequency bands are therefore seen in the pure $ScCl_3$ – one in the region where the octahedral stretch would normally be expected, and one at considerably higher frequency. The calculations therefore reproduce, at least qualitatively, this difference between the appearance of the spectra of pure $ScCl_3$ and its dilute solution (where the high frequency band is not observed). This is the

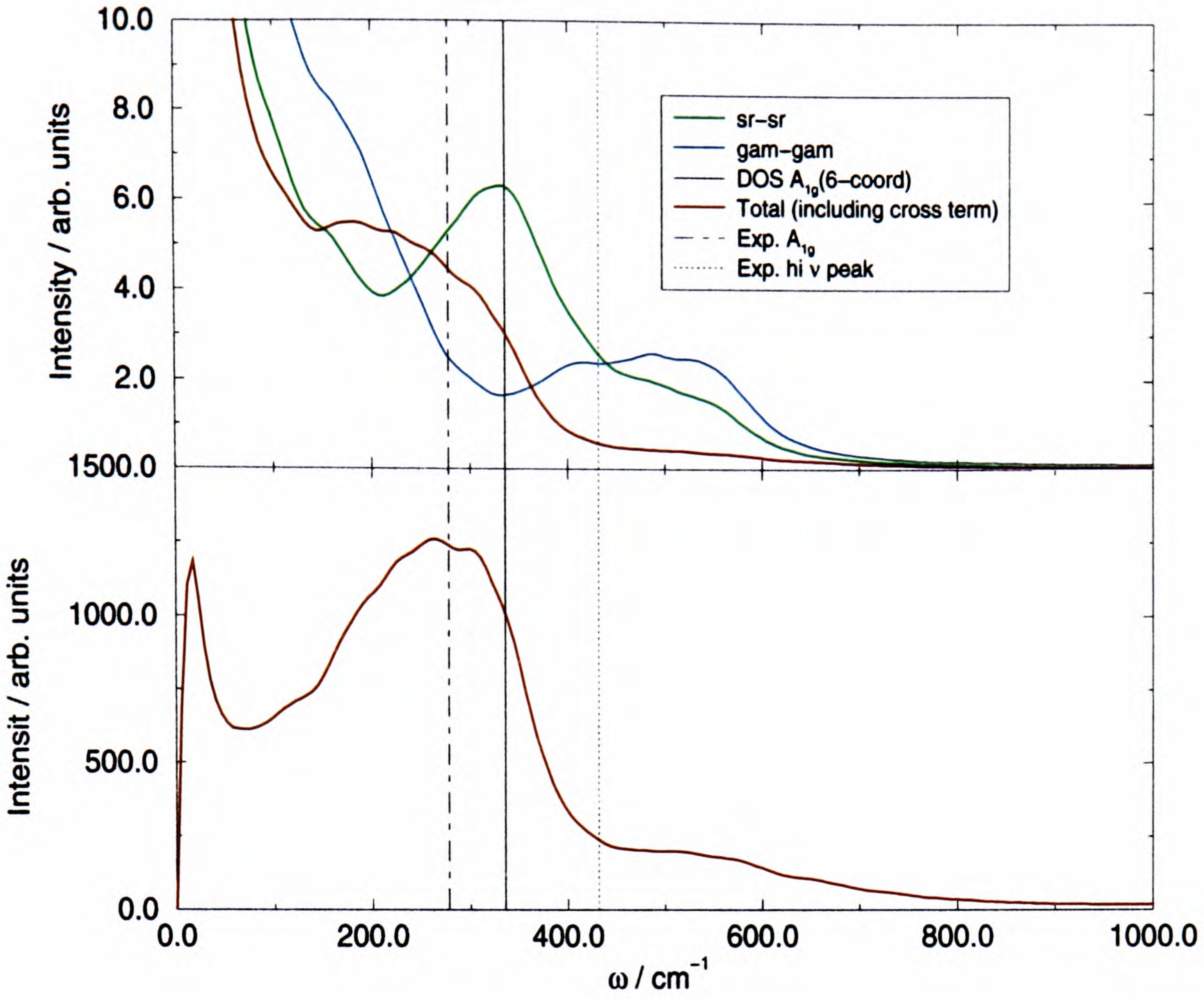

Figure 8.5: *Light scattering spectra for pure $ScCl_3$. The lower panel shows the total spectrum multiplied by frequency. Also shown by the vertical lines are the positions of the experimental bands and the DOS result.*

distinctive property of the $ScCl_3$ spectra relative to the trivalent chlorides of the lanthanides.

In the calculation of these spectra we have assumed that the short-range and gamma mechanisms contribute equally, with the slightly arbitrarily chosen parameter values described above. However, we cannot be certain of relative size of these contributions and so in figure 8.6 we show spectra with differing contributions from the short-range and gamma mechanisms. Although changing the relative weights of the two terms does change the appearance of the total spectra, it does not appear to be possible to improve the overall agreement of simulated spectrum with experiment by these means alone.

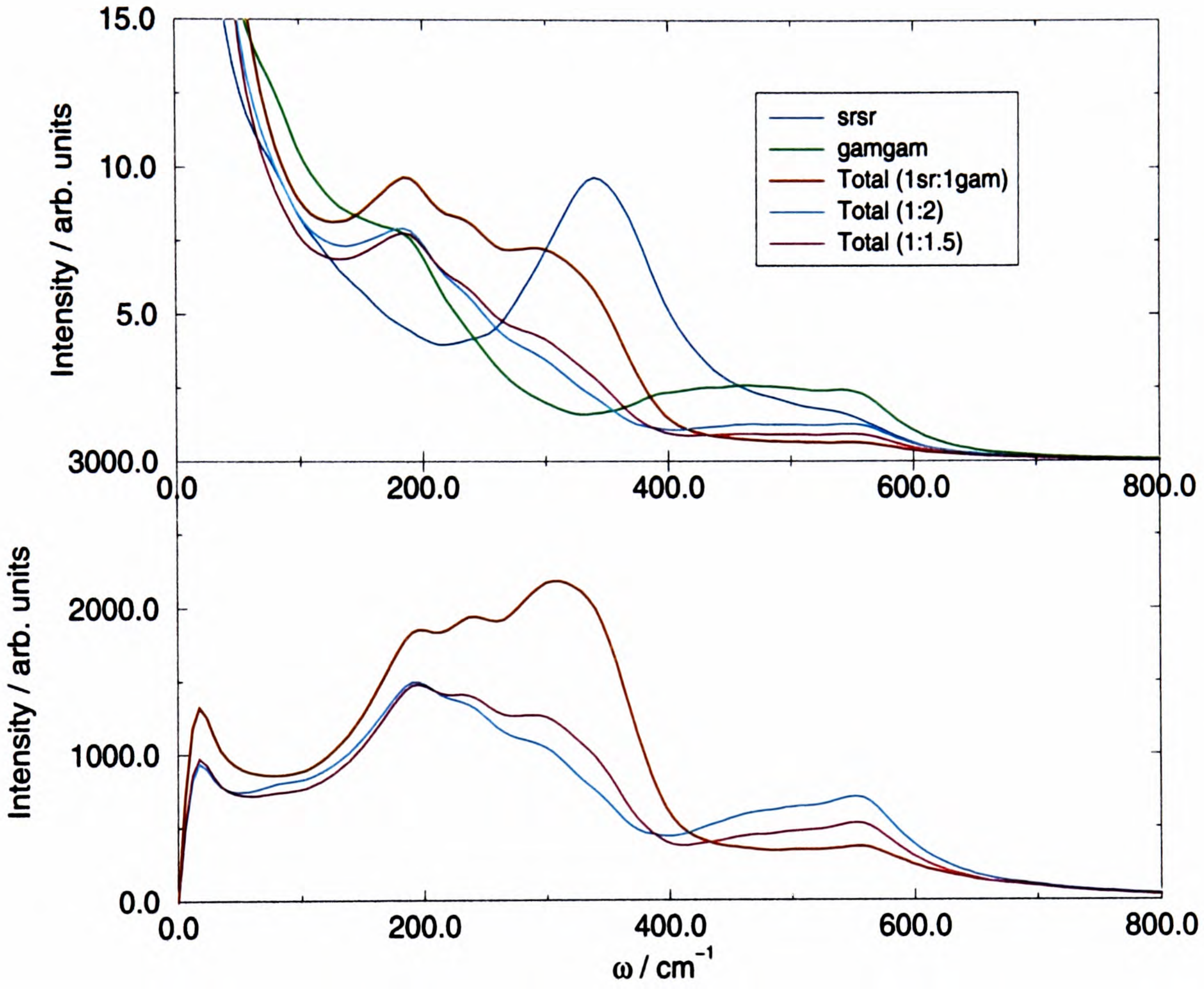

Figure 8.6: *Light scattering spectra for pure* $ScCl_3$ *higlighting the effect of differing contributions from the two different mechanisms (short-range:gamma).*

8.5.4 Simulated Isotropic Raman Spectrum – $LaCl_3$

From Raman studies $LaCl_3$ has been supposed to consist of $LaCl_6^{3-}$ octahedra [95]. The isotropic Raman spectrum consists of a single peak at around 250cm^{-1}, and the depolarised spectrum is also consistent with the number of Raman active modes expected for an octahedron. In our studies (which are consistent with experimental neutron data) the La^{3+} ions are mostly 8-coordinate and are present as edge and vertex sharing polymeric units - but we have seen that the anions do tend to orient themselves around La^{3+} ions in a symmetrical fashion. The crystal structure of $LaCl_3$ is nine-coordinate (UCl_3), and many workers from other fields have questioned the reliability of the Raman assignment.

The simulated light scattering results for pure $LaCl_3$ are shown in figure 8.7. Again the separate sr and gamma spectra are shown together with the total spectrum which includes the effect of the cross correlation. The light scattering calculation for this structure shows a peak in the sr-sr term at ~260cm^{-1}, which is close to where the band is seen experimentally (see the discussion in ref. [100]), and no significant structure elsewhere. A striking difference with the $ScCl_3$ case discussed above is that no structure is seen in the gamma spectrum. Thus, when the total spectrum is calculated, only a single strong feature is seen at the frequency of the sr band. Thus despite the fact that the local coordination of the La^{3+} ions is *not* octahedral, the appearance of the calculated isotropic spectrum is fully consistent with that expected from a collection of isolated octahedral units.

8.6 Conclusions - Raman Scattering

Overall, the calculated isotropic Raman spectra agree semi-quantitatively with those observed experimentally. It seems fair to conclude that the simulated structures and their vibrational dynamics are consistent with the Raman observations. The qualitative difference between the spectra of $ScCl_3$ and of the

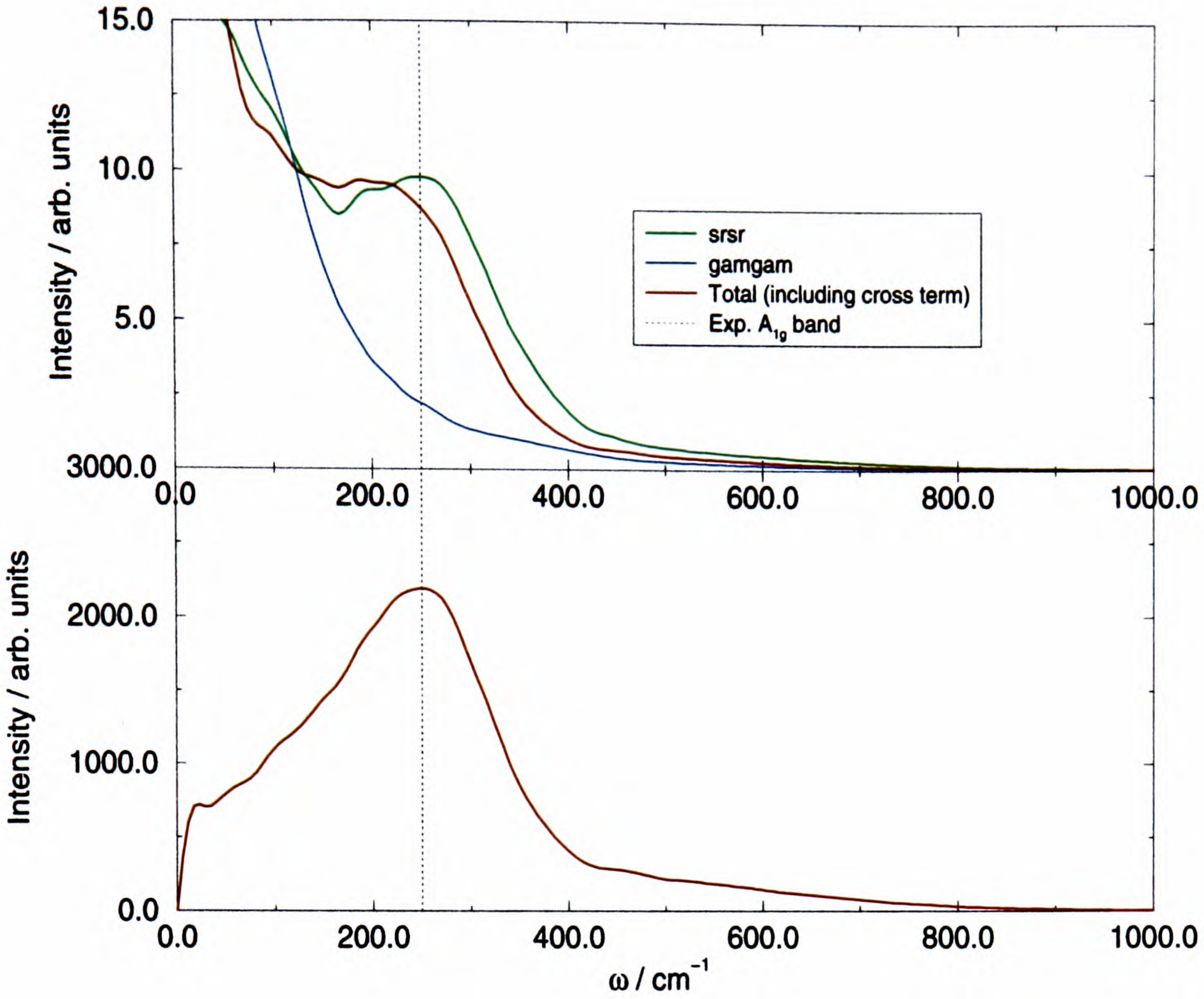

Figure 8.7: *Light scattering spectra for pure $LaCl_3$*

lanthanide halides was reproduced. Furthermore, the calculated Raman spectrum for $LaCl_3$ is in excellent agreement with experiment, despite the fact that the simulated liquid is known to be ~8-coordinate. The reasons for these differences have not yet been analysed. The association of the Raman bands with vibrational modes of polyhedral molecular units within the liquid seems to be well justified in dilute solutions and also in the $LaCl_3$ pure melt. In the case of pure $ScCl_3$ features associated with the inter-polyhedral connections seem to become spectrally active through the gamma polarizability mechanism.

8.7 Ion Mobility and Conductivity

The Raman bands give information about the oscillations of the ions on a timescale on which the network structure is unchanging. On a much longer timescale the bonds of the network can break and re-form. The diffusion coefficient and conductivity of the system are observable properties which are affected by these processes.

The diffusion coefficient is related to the mean squared displacement by the Einstein relation,

$$D_\alpha = \lim_{t\to\infty} \frac{1}{6t} < |\mathbf{r}_i(t) - \mathbf{r}_i(0)|^2 >, \tag{8.37}$$

where ion i belongs to species α. This implies that by calculating the mean-square displacements (msd) out to sufficiently long times that the plot of the msd versus time is linear, we can extract the diffusion coefficient from the slope. In the computer simulation, care must be taken *not* to apply periodic boundary conditions when evaluating this expression. Alternatively, the diffusion coefficient can be calculated from the time integral of the velocity correlation function

$$D_\alpha = \frac{1}{3}\int_0^\infty < \mathbf{v}_i(t) \cdot \mathbf{v}_i(0) > dt. \tag{8.38}$$

For practical calculations, the former route is to be preferred, as it is difficult to judge when the velocity correlations have died away to zero, whereas the linearity of the msd plot is more readily appreciated.

The ionic conductivity is normally expressed as a similar integral over the charge current correlation function [72]

$$\lambda^K = \frac{\beta e^2}{V}\int_0^\infty J(t)dt, \tag{8.39}$$

where $\beta = 1/kT$, e is the electronic charge and J is

$$\begin{aligned} J(t) &= \sum_{i=1}^{N}\sum_{j=1}^{N} Q_i Q_j < \mathbf{v}_i(t) \cdot \mathbf{v}_j(t) > && (8.40)\\ &= \sum_{i=1}^{N} Q_i^2 < \mathbf{v}_i(t) \cdot \mathbf{v}_i(0) > && (8.41)\\ &+ \sum_{j=1}^{N}\sum_{i\neq j}^{N} Q_i Q_j < \mathbf{v}_i(t) \cdot \mathbf{v}_j(0) > . && (8.42) \end{aligned}$$

The conductivity therefore involves the relative motion of the cations and anions. It is much more difficult to calculate than the diffusion coefficient as it is a collective quantity. A frequently used approximation is to neglect all the correlations in the velocities of different ions, which leads to the so-called Nernst-Einstein relationship for the conductivity

$$\lambda^{NE} = \beta e^2(\rho_+ Q_+^2 D_+ + \rho_- Q_-^2 D_-), \tag{8.43}$$

where ρ_α is the number density of species α.

It is convenient to re-express the conductivity in the form of a mean-square displacement to make clear the problems of converging the integral in equation 8.39. This expression is

$$\lambda^K = \frac{\beta e^2}{V} \lim_{t\to\infty} (6t)^{-1} \left\langle \left| \sum_i Q_i \left(\mathbf{r}_i(t) - \mathbf{r}_i(0)\right) \right|^2 \right\rangle \tag{8.44}$$

as can be shown by substituting

$$\mathbf{r}_i(t) - \mathbf{r}_i(0) = \int_0^t d\tau\ \mathbf{v}_i(\tau) \tag{8.45}$$

to obtain

$$\lambda^K = \frac{\beta e^2}{V} \lim_{t\to\infty} (6t)^{-1} \int_0^t d\tau \int_0^t d\tau' \sum_i \sum_j Q_i Q_j \left\langle \mathbf{v}_i(\tau) \cdot \mathbf{v}_j(\tau') \right\rangle . \tag{8.46}$$

Now, using the stationarity of the correlation function and changing variables to $\tau \to \tau - \tau'$ (ref. [72] pg 201) we obtain

$$\lambda^K = \frac{\beta e^2}{3V} \int_0^\infty d\tau \sum_i \sum_j Q_i Q_j \left\langle \mathbf{v}_i(\tau) \cdot \mathbf{v}_j(0) \right\rangle , \tag{8.47}$$

which is equation 8.39.

Equation 8.44 can be written in the form:

$$\lambda^K = \frac{\beta e^2}{V} \lim_{t\to\infty} (6t)^{-1} \left\langle |Q_+ \Delta_+(t) + Q_- \Delta_-(t)|^2 \right\rangle , \tag{8.48}$$

where $\Delta_\alpha(t)$ is the *net* displacement of all the ions of species α in time t. This equation makes it clear that (bearing in mind the opposite signs of the cation and anion charges) that the conductivity involves the displacement of the set of cations relative to the set of anions. Equation 8.48 may be re-written as

$$\lambda^K = \frac{\beta e^2}{V} \lim_{t\to\infty}(6t)^{-1}\left[Q_+^2\left\langle|\Delta_+(t)|^2\right\rangle + Q_-^2\left\langle|\Delta_-(t)|^2\right\rangle + 2Q_+Q_-\left\langle\Delta_+(t)\cdot\Delta_-(t)\right\rangle\right]. \tag{8.49}$$

The Nernst-Einstein approximation can be written in an equivalent form:

$$\lambda^{NE} = \beta e^2 \lim_{t\to\infty}(6t)^{-1}\left[Q_+^2\rho_+\left\langle|\Delta_+(t)|^2\right\rangle + Q_-^2\rho_-\left\langle|\Delta_-(t)|^2\right\rangle\right]. \tag{8.50}$$

where $\Delta_\alpha(t)$ is the displacement of a *single* ion of species α.

The difference between the last two expressions is illustrated in figures 8.8, 8.9 and 8.10 for $LaCl_3$, YCl_3 and $ScCl_3$ (all at temperatures just above the melting point) respectively. The figures contain the msd for ions of each species, from which the individual ionic diffusion coefficents can be estimated. The figures also show the three factors appearing in the square-brackets of equation 8.49, which give the collective msd of anions, cations and their cross-correlation, and their sum (labelled $\sum c_i Q_i^2.msdcorr(i)$), whose long-time slope gives the conductivity λ^K. The fact that the cross-correlation is negative shows that the overall motion of anions and cations is closely linked. This cross correlation is so strong in $ScCl_3$ that, although the ions are diffusing, there is almost no net conduction. If the ions were diffusing independently this sum would coincide with the square-bracketed term in the corresponding Nernst-Einstein expression (equation 8.50) (labelled $\sum c_i Q_i^2.msd(i)$) in the upper panel. It can be seen that in all cases the real conductivity is much lower than the Nernst-Einstein value, and in the $ScCl_3$ case vanishingly so.

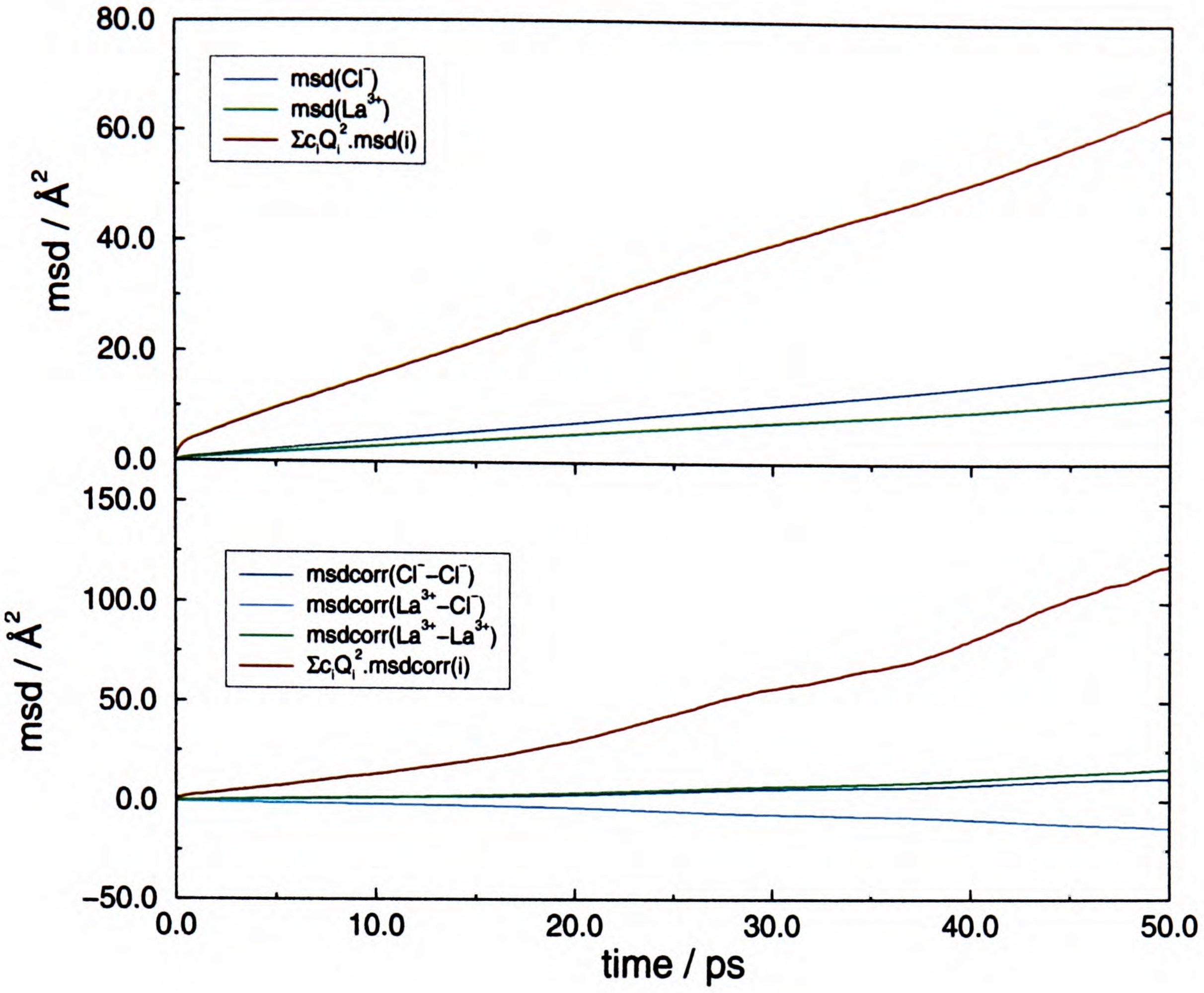

Figure 8.8: *Mean square displacements of the ions in* $LaCl_3$. *The upper panel shows the total msd (equation 8.50) and the lower panel shows the net msd (msdcorr) (equation 8.49).*

Values for the diffusion coefficients are shown in table 8.3. Unless otherwise indicated the results presented in table 8.3 are for calculations on 500 ion systems at the experimental temperatures and densities just above the melting point, as in the structural studies. Except for the $ScCl_3$ run on the large system, the calculations were done over 50ps. As can be seen from the figures, a typical anion has an msd of $\sim$20Å^2 in this period which is normally regarded as sufficient for an ion to have escaped from the initial local structure and diffusion to have set in. The diffusion coefficients have not been measured for these systems. Note that the lowest diffusivities occur for those systems which melt with small volume changes (like Tb, Dy and Y) where, as we have seen in the structural studies, the local coordination around the cation is closest to octahedral. This is in accord with the *trend* of mobilities, as judged from the conductivity.

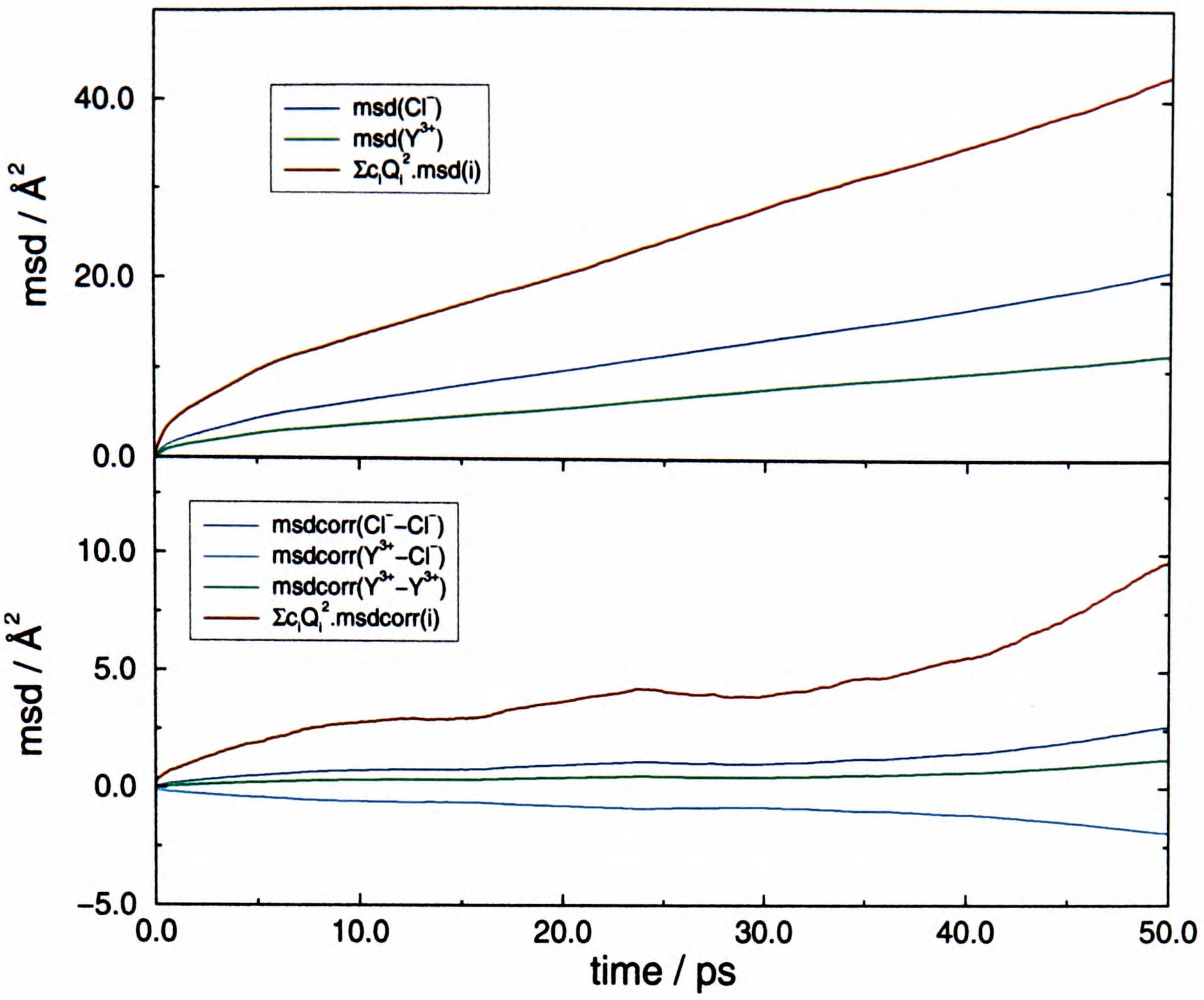

Figure 8.9: *Mean square displacements of the ions in YCl_3.*

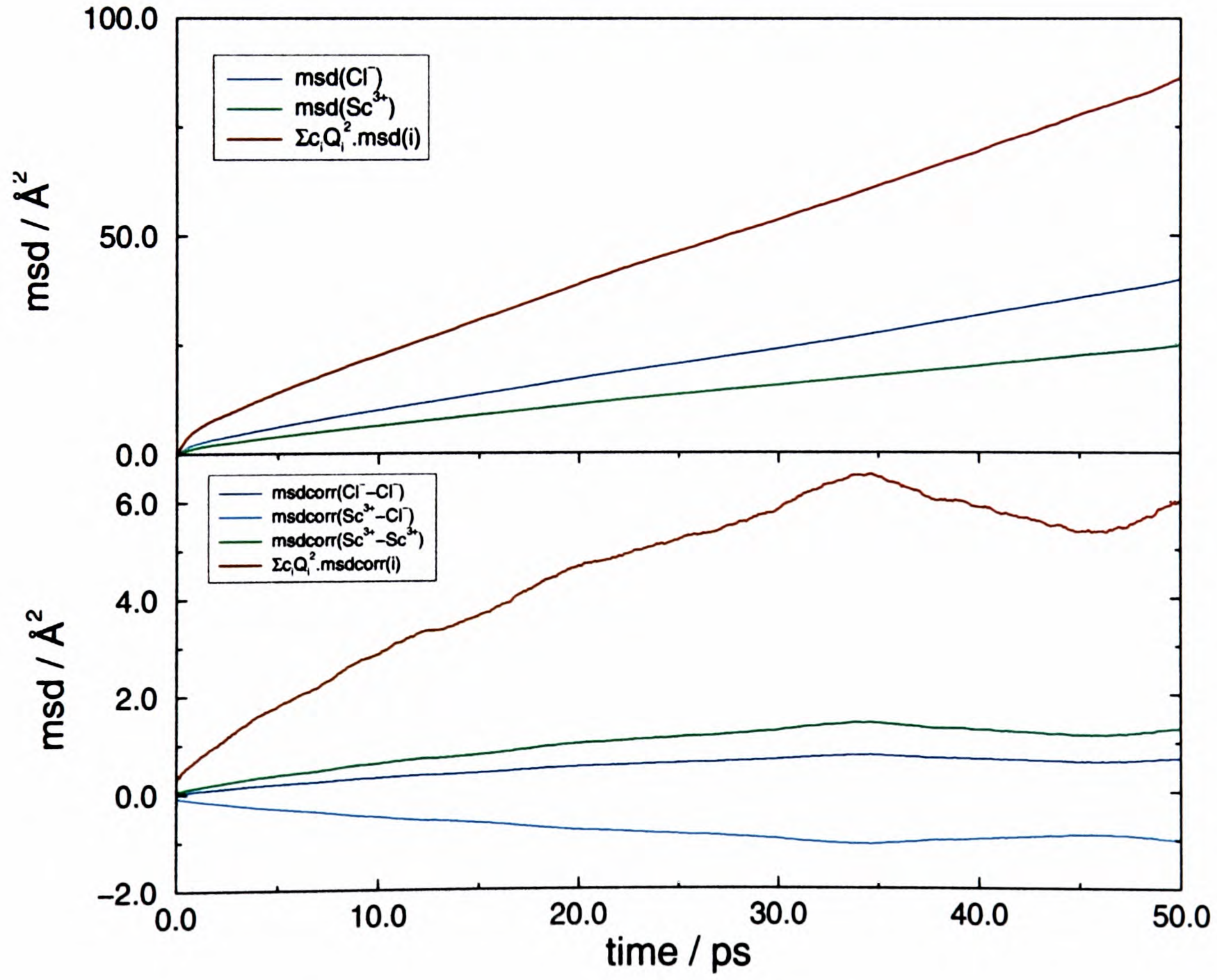

Figure 8.10: *Mean square displacements of the ions in $ScCl_3$.*

Experimental conductivities and conductivities estimated from the Nernst-Einstein equation are also shown in the table, together with experimental values for the conductivities where these are available [109]). The table shows that the Nernst-Einstein equation always overestimates the conductivity, due to its neglect of the correlations between the displacements of different ions. The discrepancy becomes less pronounced as the system becomes more mobile, as judged from the value of the diffusion coefficients. $AlCl_3$ is an insulator, yet the Nernst-Einstein equation (equation 8.43) predicts a finite conductivity for $AlCl_3$. The non-conductivity does not arise due to the ions not moving - the ionic diffusion coefficients are quite large. Rather the motion of the Al^{3+} and Cl^- ions is so strongly correlated (within the Al_2Cl_6 dimers) that it does not conduct.

In all cases, the conductivity calculated from the simulation is smaller than the experimental value. This suggests that the simulated melts are slightly less fluid than in reality. At present, the reasons for this apparent shortcoming of the simulation model are not understood. It is possible that the size of the simulation cell may be to blame. The large system $ScCl_3$ run (6880 ions) appears to have a much larger diffusion coefficient that the same system in a 500 ion cell. Such a diffusion coefficient would be consistent with that required to give the observed conductivity. This suggests that, because of the extended network structure in these fluids, the periodic boundary conditions are inhibiting the ionic diffusion. However, the diffusion coefficients in the large system were only determined in a 4ps run (though sufficient for an msd of 20Å^2) and further work is required before this explanation of the low mobilities can be firmly presented.

System	Temp. (K)	Self Diffusion Coefficient ($\times$ 10^{-5}cm^2.s^{-1})		Conductivity (S.cm^{-1})		
		Anion	Cation	λ^{NE}	λ^{K}	Experimenta
$LaCl_3$	1200	0.45	0.23	0.413	0.306	1.3
YCl_3	1100	0.33	0.17	0.323	0.279	0.3
	1200	0.63	0.35	0.595	0.128	
$ScCl_3$	1300	1.25	0.79	1.007	0.033	0.5
6880 ions	1253	2.4	1.9	2.6	–	
$AlCl_3$	550	3.04	2.93	6.916	1.6×10^{-4}	$5\times10^{-}$
	600	3.45	3.29	7.137	8.3×10^{-3}	

Table 8.3: *Diffusion coefficients and conductivities of MCl_3 systems.*

Chapter 9

Transferability of potential model to trivalent metal bromides

9.1 Introduction

We have seen that use of the Polarizable Ion Model predicts both the structure and dynamics of a wide range of trivalent metal chloride systems very well. The transferability with a change in cation radius has been well established. In addition, the transferability to binary mixtures with alkali halides has been demonstrated both in static and dynamical studies.

In this chapter we will look at the transferability of the interaction potential with respect to the *anion* radius by comparing calculated and experimental diffraction data for bromides. The work described in this thesis so far has concentrated exclusively on metal chlorides owing to the range of experimental data available. However, since more information is currently becoming available for the heavier halide ion systems [12,15] it seems appropriate to investigate model scaling arguments to the full by attempting to simulate some of these systems.

This intention to scale anion parameters in a physically transparent manner has been shown from *ab-initio* studies to be appropriate between chlorides and bromides [67]. For the anion-anion potential parameters we will follow the same procedure that was adopted for the chloride interactions.

Recent neutron scattering work has begun to focus on metal tribromides [12, 15]. In order to make contact with this work the same four systems will be studied here: $LaBr_3$, $CeBr_3$, YBr_3 and $DyBr_3$. Following the chloride work the choice of the La/Ce and Y/Dy pairs allows for the derivation of approximate partial structure factors via the difference functions (section 6.5).

9.2 Simulation model and details

Following the findings on the alkali chlorides (chapter 5) we treat the bromide ion as non compressible and so model the ion-ion short range interactions via the usual pair potential (equation 1.7).

The a_{ij} and B_{ij} parameters scaled with the anion radius from the parameters appropriate for the chlorides, are given in table 9.1. The increase in radius on going from Cl→Br is accompanied by an increase in polarizability (table 9.2). A value of 30au is chosen, consistent with those obtained from *ab initio* studies [26] and refractive indices [84].

Ab-initio studies on alkali halides have shown that the short range damping parameter, b (section 3.2) can be scaled successfully with a change in anion radius on moving from the chloride to the bromide ion [67].

Simulations were performed on 500 ions at the experimental temperatures and densities (table 9.3). The runs were once again started from the melt obtained from the YCl_3 crystal structure and were then equilibrated for the usual 36ps followed by a data accumulation run of 4ps. Comparison is once again made with recent neutron scattering work with the predicted structure factors calculated as outlined in section 6.4.1. The scattering lengths are as in table 6.5

Ion Pair	a_{ij} / au	B_{ij} / au	C_6^{ij} / au	C_8^{ij} / au	b / au
Br-Br[1]	1.556	140.351	333.084	5000.0	-
Br-Br[2]	1.500	165.000	333.084	5000.0	-
La-Br	4.009	6.4×10^7	142.788	0.0	1.200
Ce-Br	2.439	16726.845	142.788	0.0	1.216
Dy-Br	2.439	7297.427	142.788	0.0	1.287
Y-Br	2.439	6654.917	65.064	0.0	1.296

Table 9.1: *Potential parameters for the MBr_3 systems.*

Species	Br
Radius (Å)	1.83
Polarizability / au	30.0

Table 9.2: *Radii and polarizabilities used in the potential model for MBr_3*

with the additional value of 6.795fm used for Br^-.

9.3 Simulation Results

Two pairs of bromides were considered in the recent neutron scattering studies [12]. $LaBr_3$ and $CeBr_3$ represent two large cation systems whilst $DyBr_3$ and YBr_3 are typical intermediate sized cation systems. We shall now consider each pair in turn.

9.3.1 $LaBr_3$ / $CeBr_3$

The experimental and simulated total neutron structure factors are compared in figure 9.1 for $LaBr_3$ and figure 9.2 for $CeBr_3$ Again, the agreement between predicted and experimental structure factors is very good, with the position and height of the pre-peak (at $\sim 1Å^{-1}$) being well reproduced. The pre-peak

System	Temperature (K)	Density (g.cm^{-3})
$LaBr_3$	1083	4.481
$CeBr_3$	1053	4.496
$DyBr_3$	1190	4.15
YBr_3	1213	3.45

Table 9.3: *Temperatures and densities used in the MBr_3 simulations.*

can again be associated with both the anion-cation and cation-cation spatial correlations.

The simulated total pdfs and those from the transformation of the experimental diffraction data are compared in figures 9.3 and 9.4 . Good agreement is seen with the familiar problem of the peaks being too sharp in the simulated data – associated with the greater amplitude of the oscillations in the total structure factors in figures 9.1 and 9.2 compared with experiment.

The strength of these oscillations, particularly in the case of $LaBr_3$ but also clear for $CeBr_3$, perhaps points to a partial breakdown in the scaling arguments. As can be seen in figures 9.1 and 9.2 the strength of these oscillations is almost entirely attributable to those in the M-Br partial structure factor. In transferring from the M-Cl to M-Br potentials we have assumed a constant steepness of the repulsive wall of the anion's electron density. Our chemical intuition may lead us to expect a less steep wall for the M-Br short range interactions with respect to the M-Cl as the Br^- is a larger anion with a more slowly decaying electron density on moving radially outwards from the nucleus. Indeed, one would expect such a reduction in wall hardness to reduce the sharpness of the first peaks in the M-X pdf. However, bearing in mind this approximation, the agreement in figures 9.1 and 9.2 is excellent.

Small differences in the general shape of the bromide total structure factors, with respect to the chloride analogues, can be traced to the greater weighting of

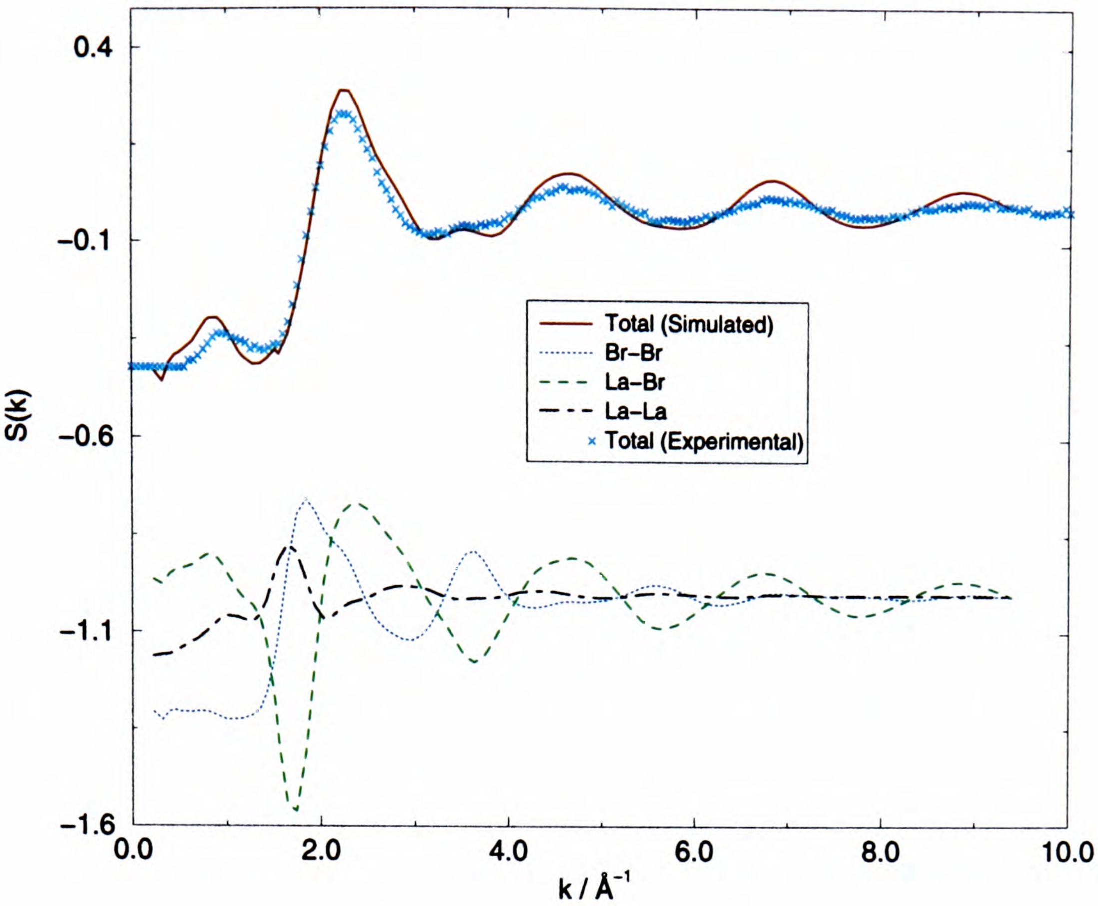

Figure 9.1: *Comparison of simulated and experimental total neutron weighted structure factors for LaBr$_3$. The partial structure factors are shown shifted by a constant of -1.0*

the metal-anion and metal-metal terms as the scattering length of the Cl$^-$ ion is greater than that of Br$^-$. For example, the pre-peak in figure 6.3 is significantly stronger than that in figure 9.1.

As was the case for LaCl$_3$ and CeCl$_3$ (section 6.5) these systems are isomorphous and so we can form the differences (Δ_M and ΔF'(k)) approximating the M-Br and Br-Br partial structure factors. Very good agreement is found between simulation and experiment (figures 9.5 and 9.6).

Figures 9.7 and 9.8 show two snapshots through the simulation cells for LaBr$_3$ and CeBr$_3$. The structures appear to consist of typical ionic liquids of connected polyhedra as was observed for LaCl$_3$ and CeCl$_3$ (section 6.5).

9.3.2 DyBr$_3$ / YBr$_3$

The predicted and experimental total structure factors and rdfs are shown in figures 9.9 - 9.12. Once again these systems are isomorphous and so the differences

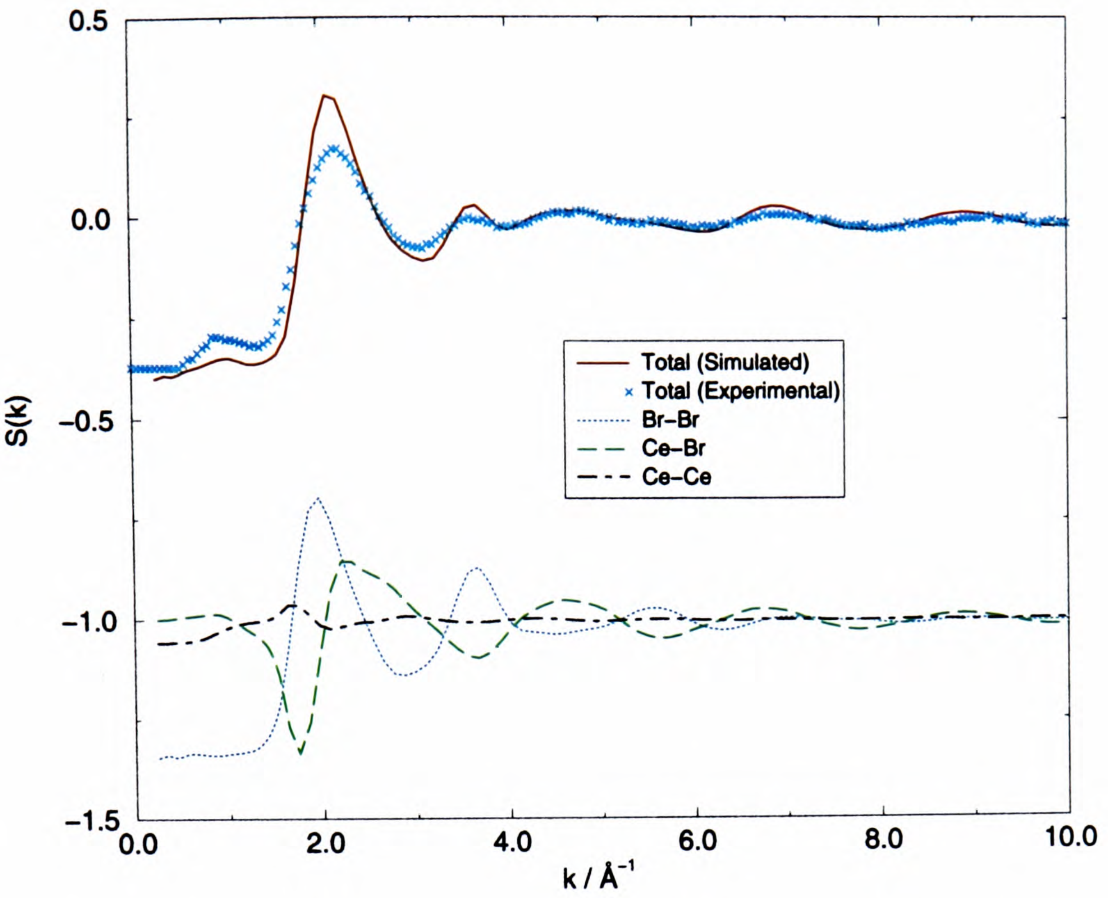

Figure 9.2: *Comparison of simulated and experimental total neutron weighted structure factors for* $CeBr_3$. *The partial structure factors are shown shifted by a constant of -1.*

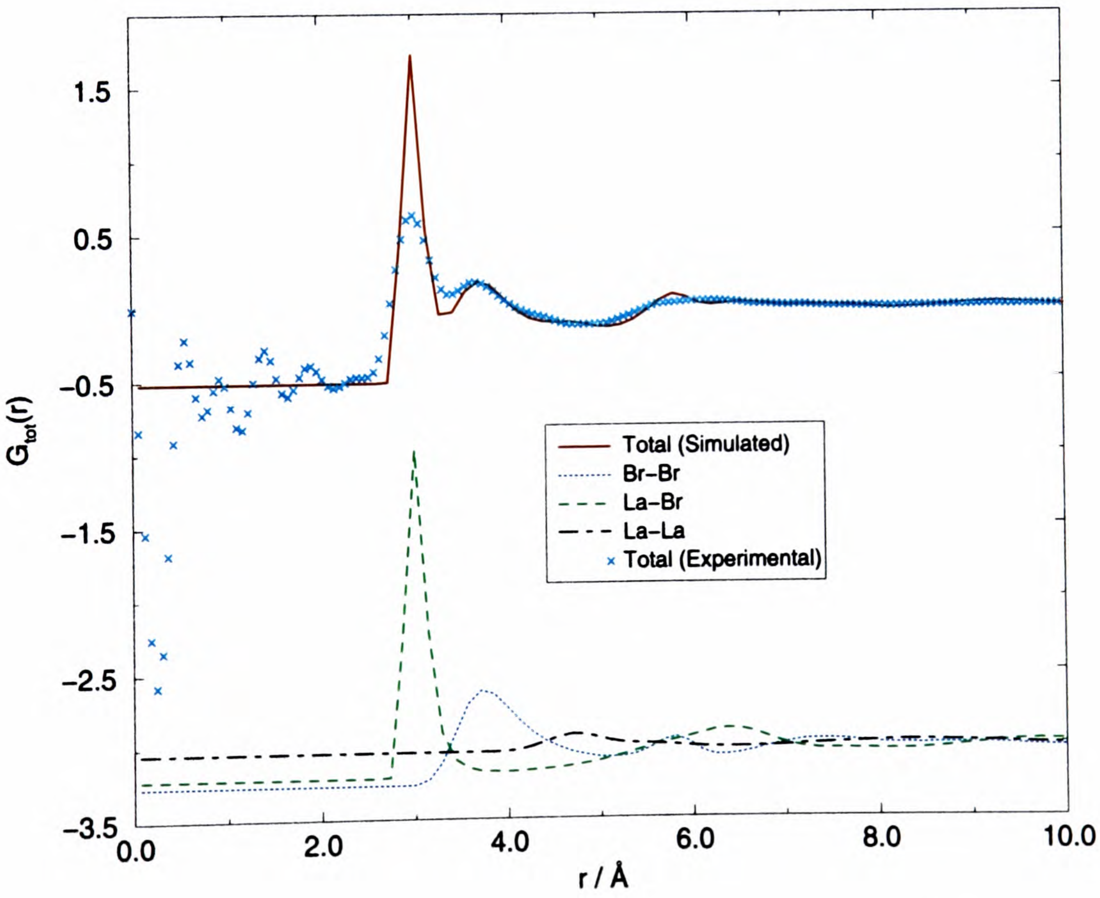

Figure 9.3: *Comparison of simulated and experimental total neutron weighted pdfs for* $LaBr_3$. *The partial pdfs are shown shifted by a constant of -3.*

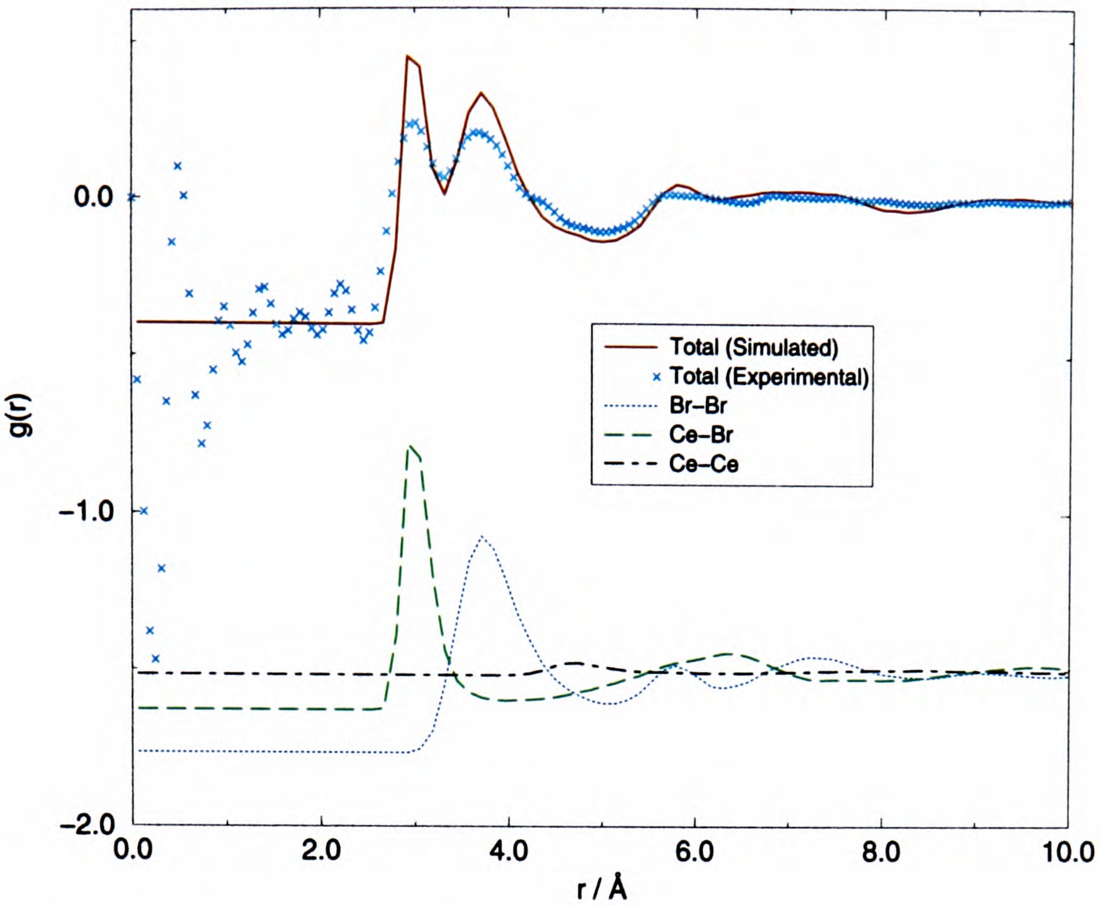

Figure 9.4: *Comparison of simulated and experimental total neutron weighted pdfs for* $CeBr_3$*. The partial pdfs are shown shifted by a constant of -1.5.*

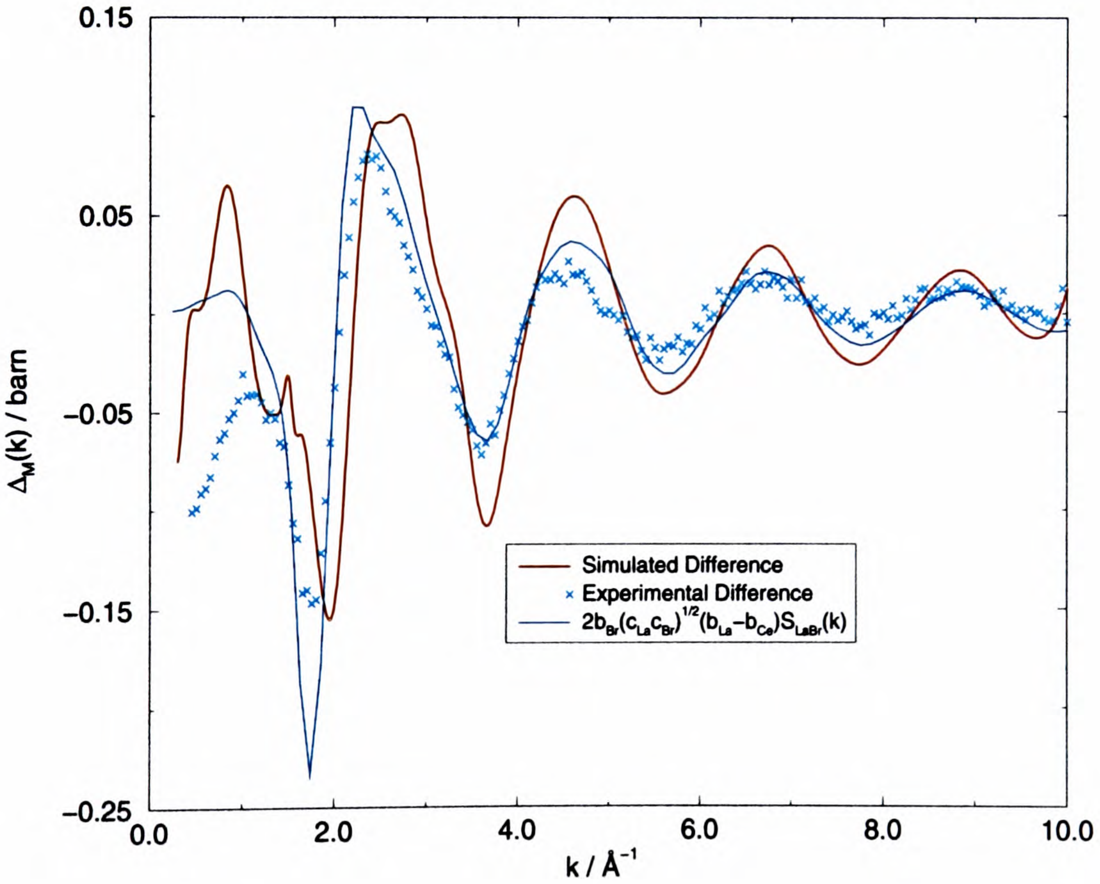

Figure 9.5: *The difference function,* $\Delta_M(k)$ *, obtained by using the isomorphous assumptions from the data for* $LaBr_3$ *and* $CeBr_3$

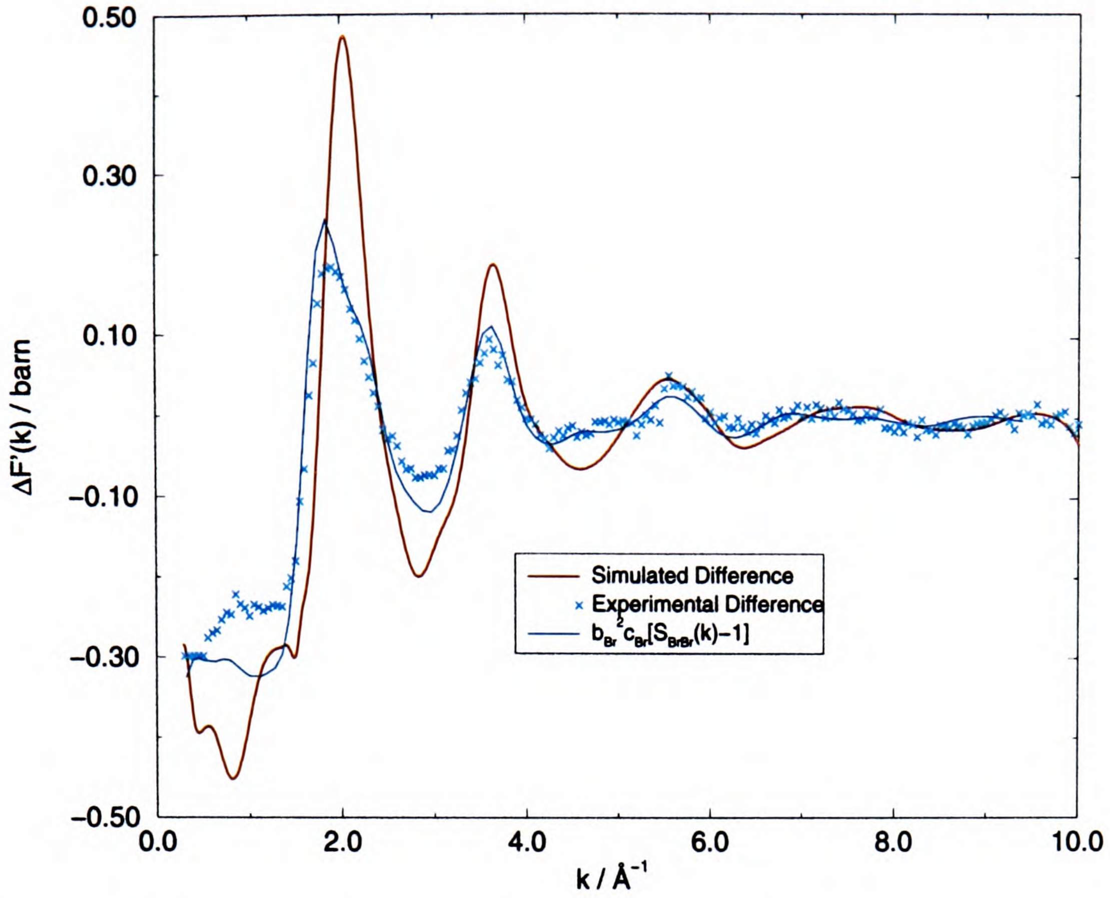

Figure 9.6: *The difference function* $\Delta F'(k)$ *, obtained by using the isomorphous assumptions from the data for* $LaBr_3$ *and* $CeBr_3$

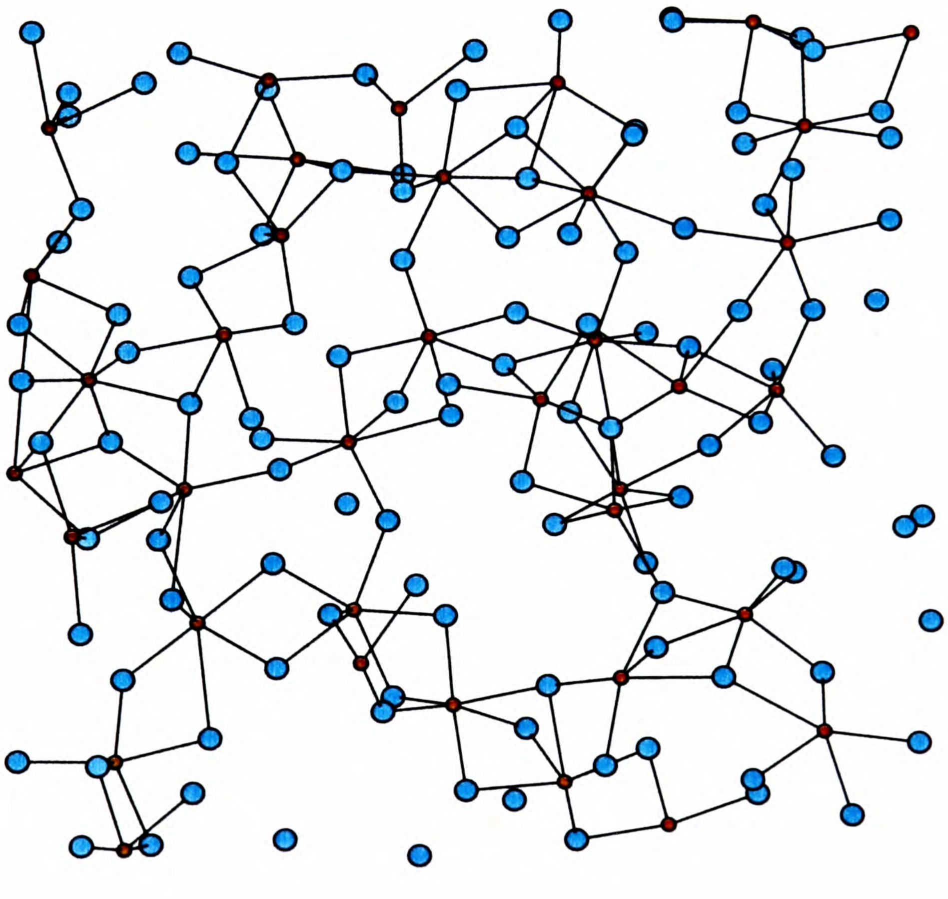

Figure 9.7: *Snapshot of the ion positions in* $LaBr_3$.

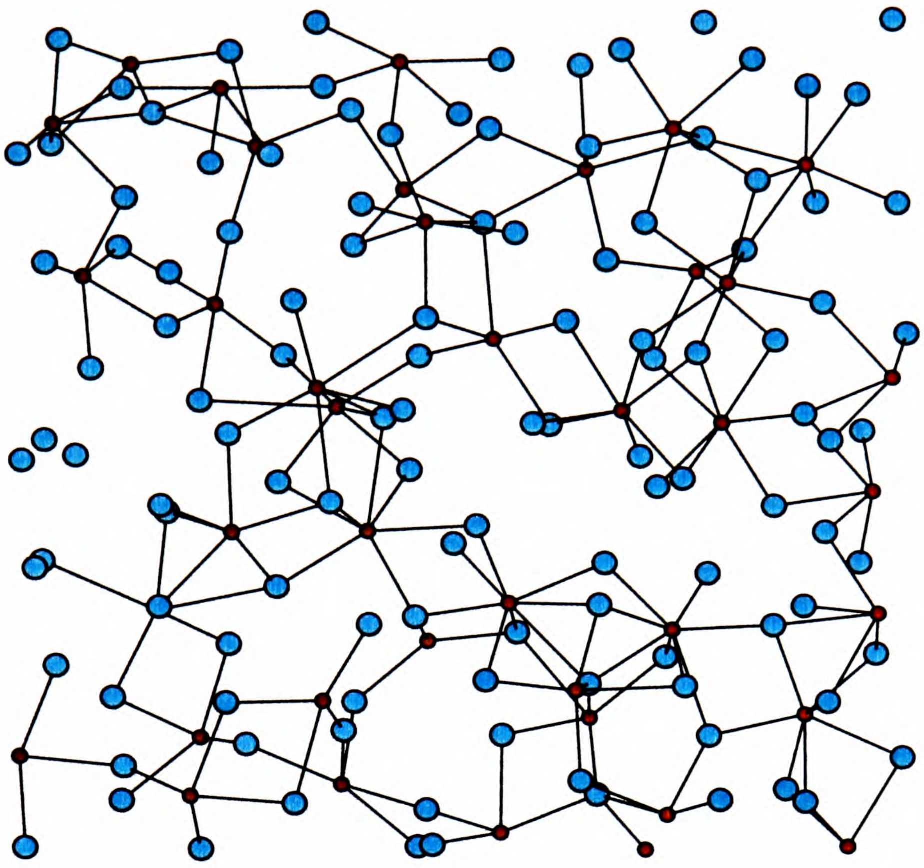

Figure 9.8: *Snapshot of the ion positions in $CeBr_3$.*

are formed as in figures 9.13 and 9.14.

Figures 9.15 and 9.16 show two snapshots through these simulation cells. As was the case for $ScCl_3$, chain like structures are evident in both cells.

9.3.3 Coordination number analysis

The coordination numbers obtained from simulation are compared with those from experiment in table 9.4.

The connectivity of the polyhedral units has been analysed as outlined in section 7.3.2 and is tabulated for 6 coordinate units in table 9.6.

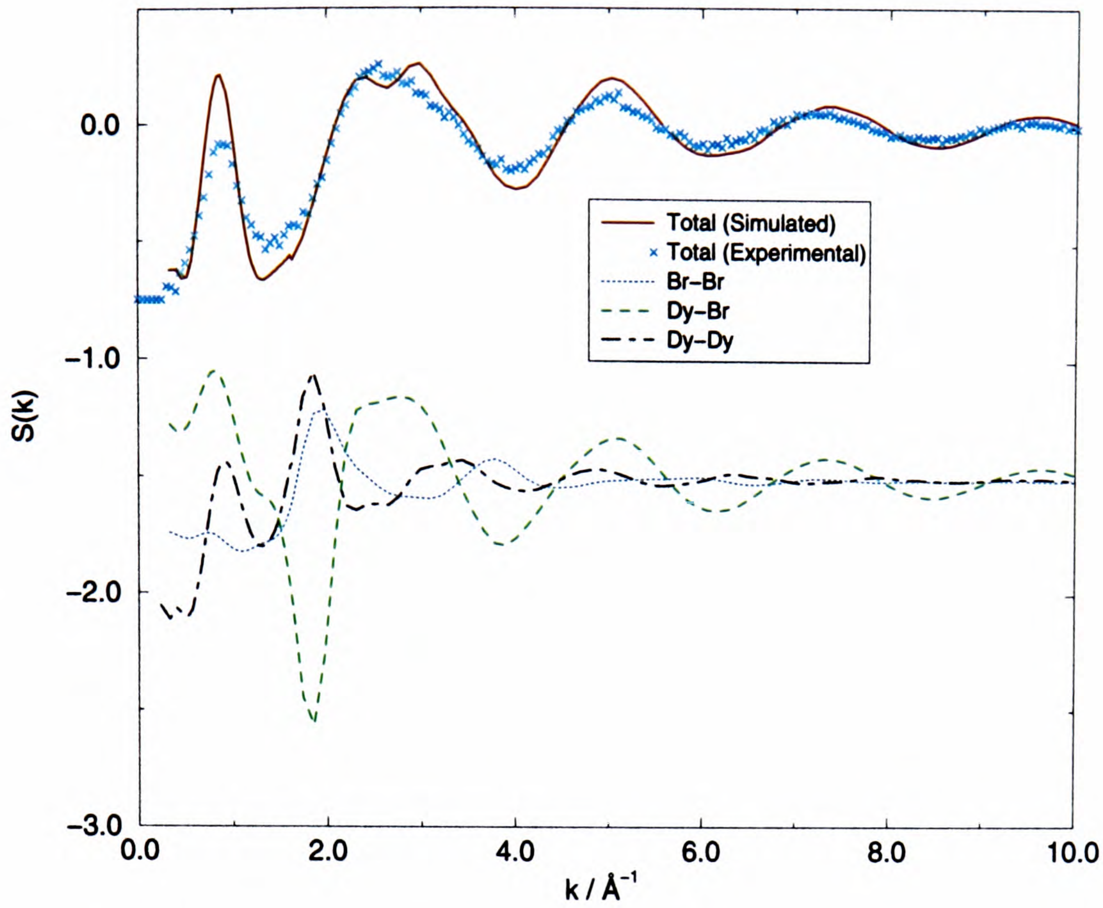

Figure 9.9: *Simulated total neutron weighted structure factor for $DyBr_3$ compared with the experimental total structure factor and, below, the neutron-weighted partials shifted by a constant of -1.5*

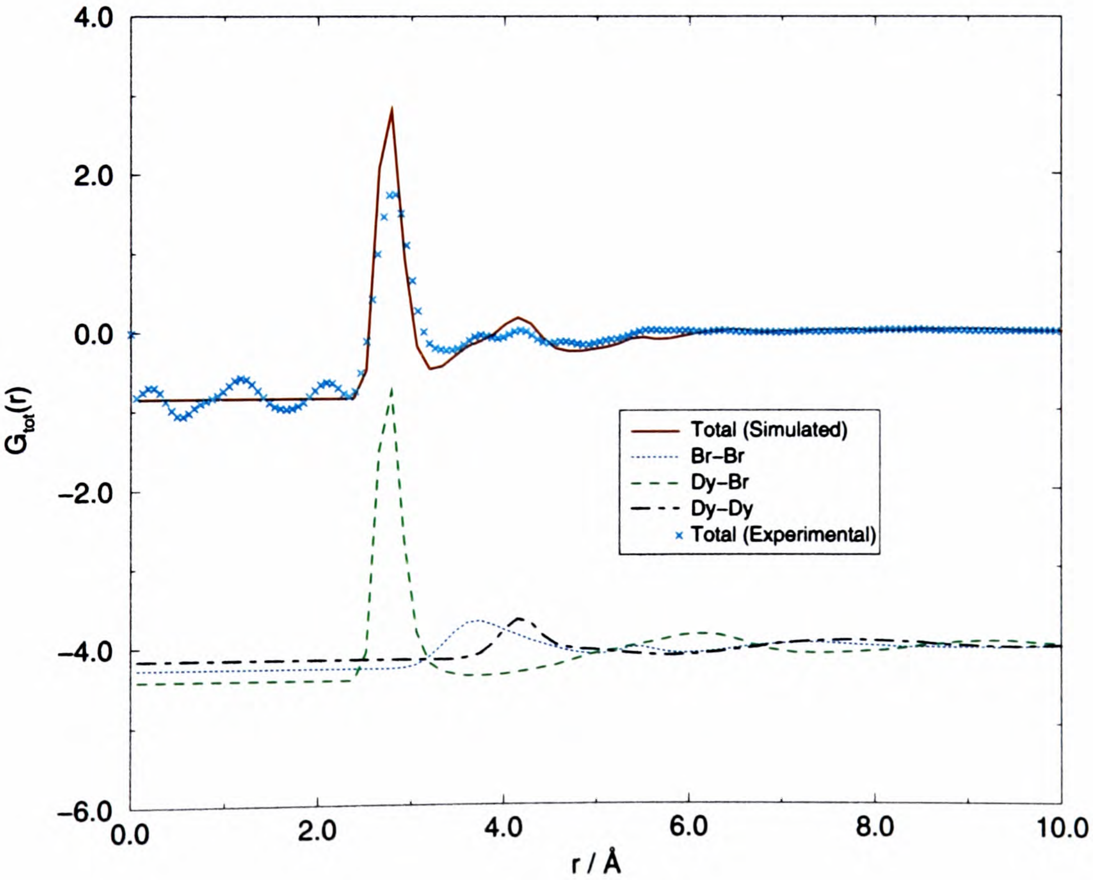

Figure 9.10: *Comparison of simulated and experimental pdfs for $DyBr_3$*

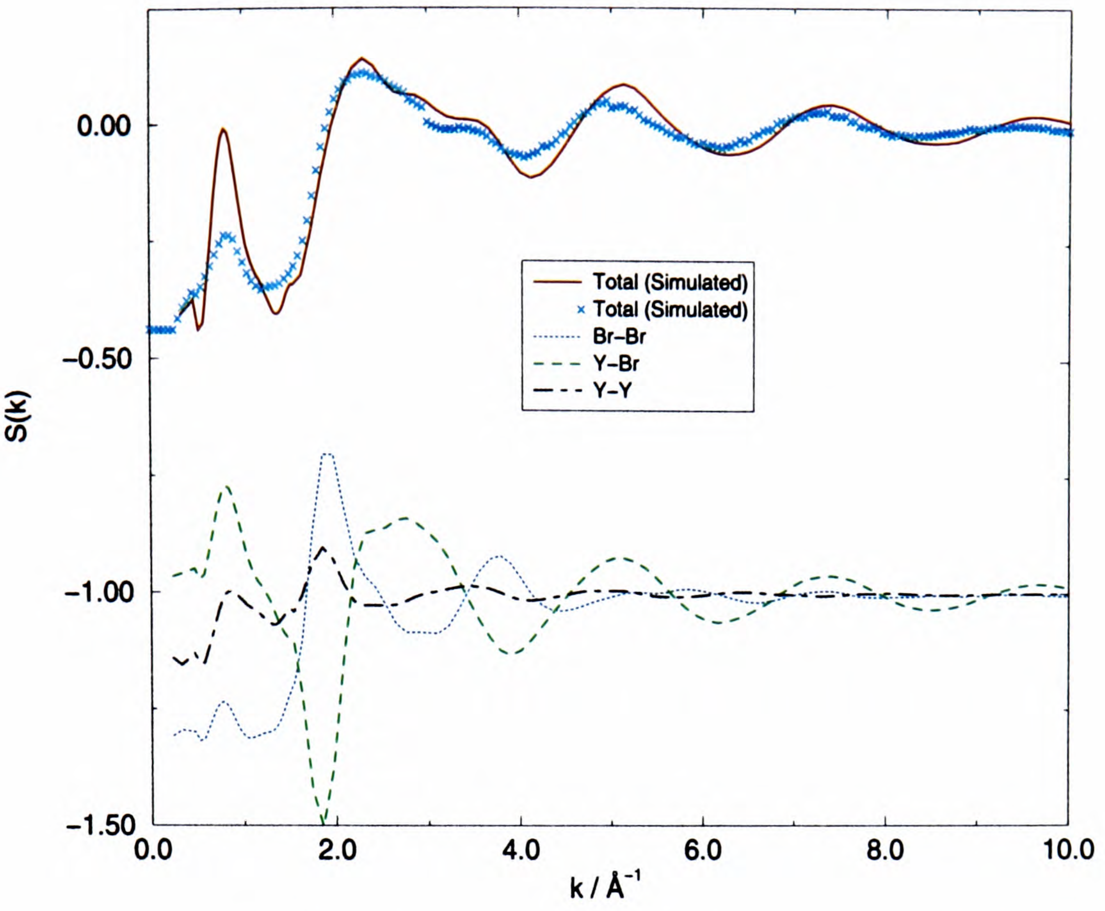

Figure 9.11: *Simulated total neutron weighted structure factor for YBr_3 compared with the experimental total structure factor and, below, the neutron-weighted partials shifted by a constant of -1.0*

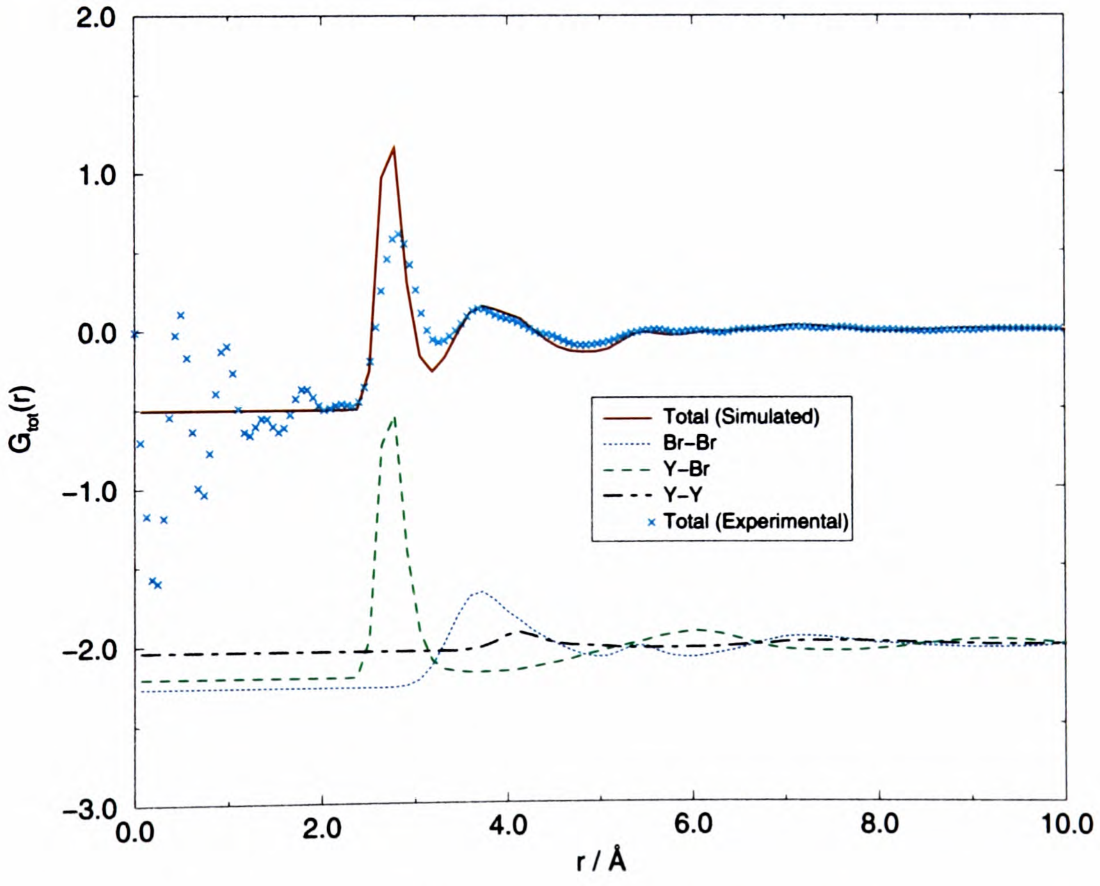

Figure 9.12: *Comparison of simulated and experimental total neutron weighted pdfs for YBr_3. The partial pdfs are shown shifted by a constant of -2.*

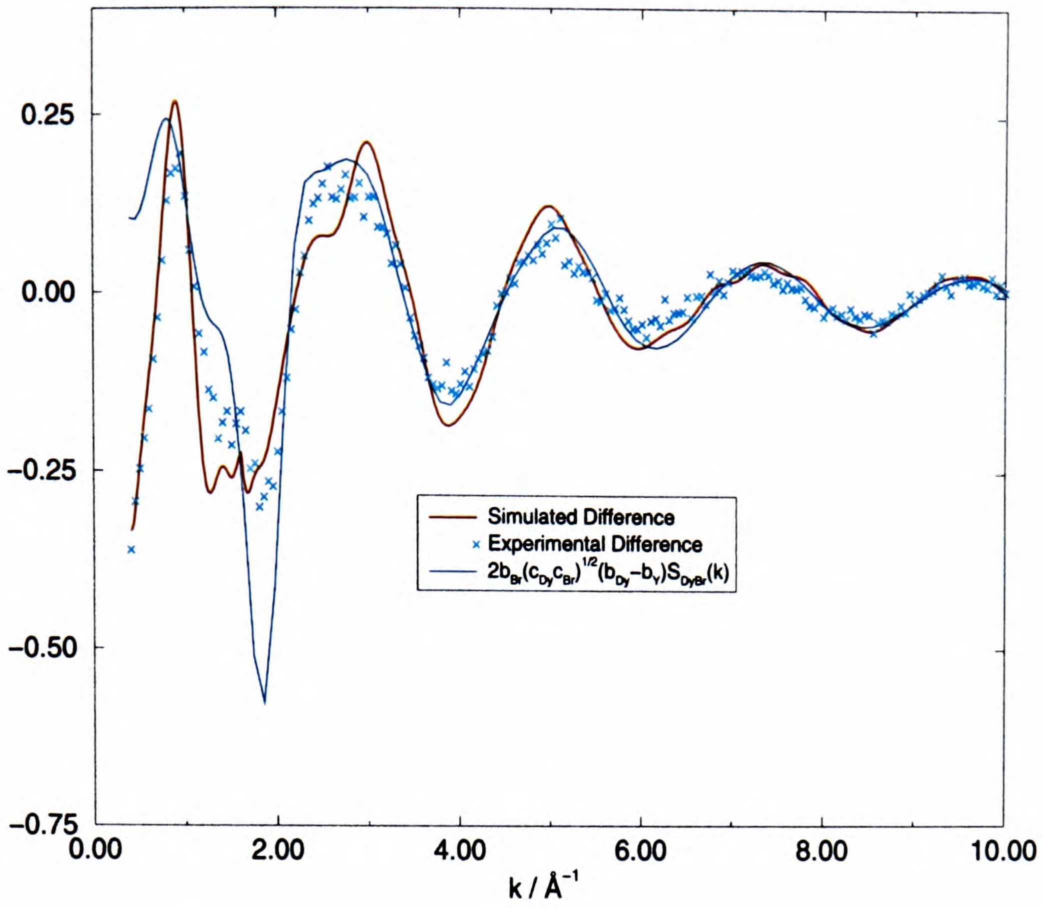

Figure 9.13: *The difference function, $\Delta_M(k)$, obtained by using the isomorphous assumptions from the data for $DyBr_3$ and YBr_3*

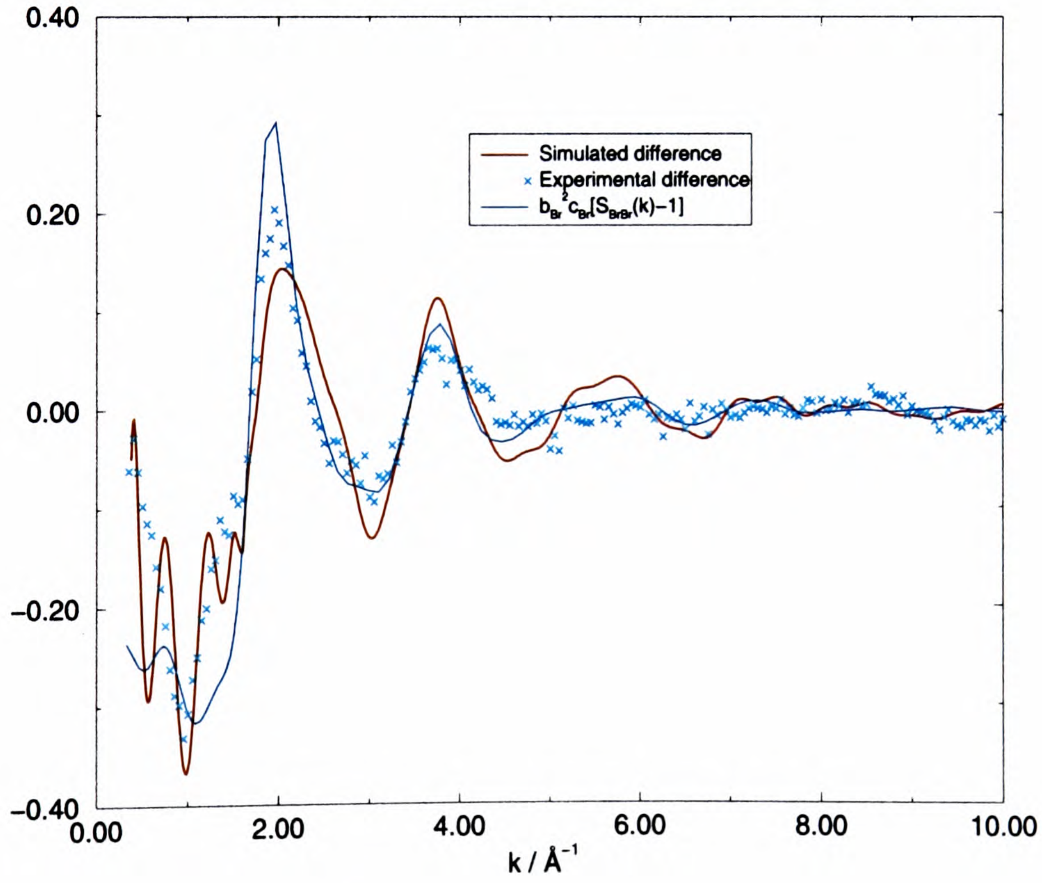

Figure 9.14: *The difference function, $\Delta F'(k)$, obtained by using the isomorphous assumptions from the data for $DyBr_3$ and YBr_3*

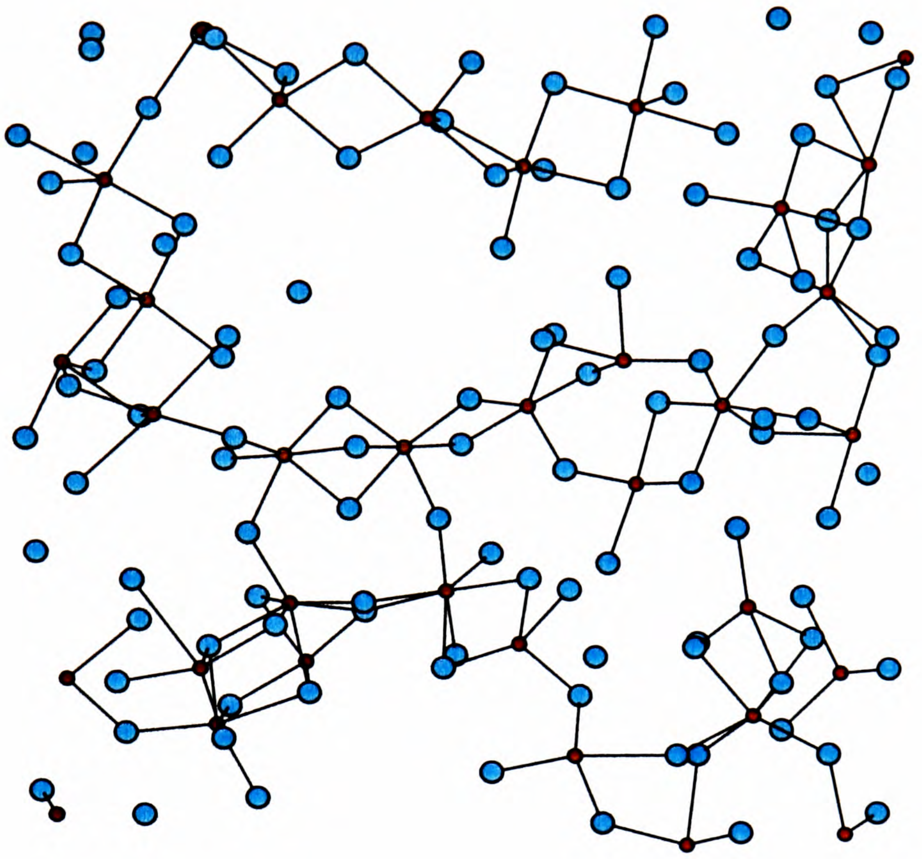

Figure 9.15: *Snapshot of the ion positions in $DyBr_3$.*

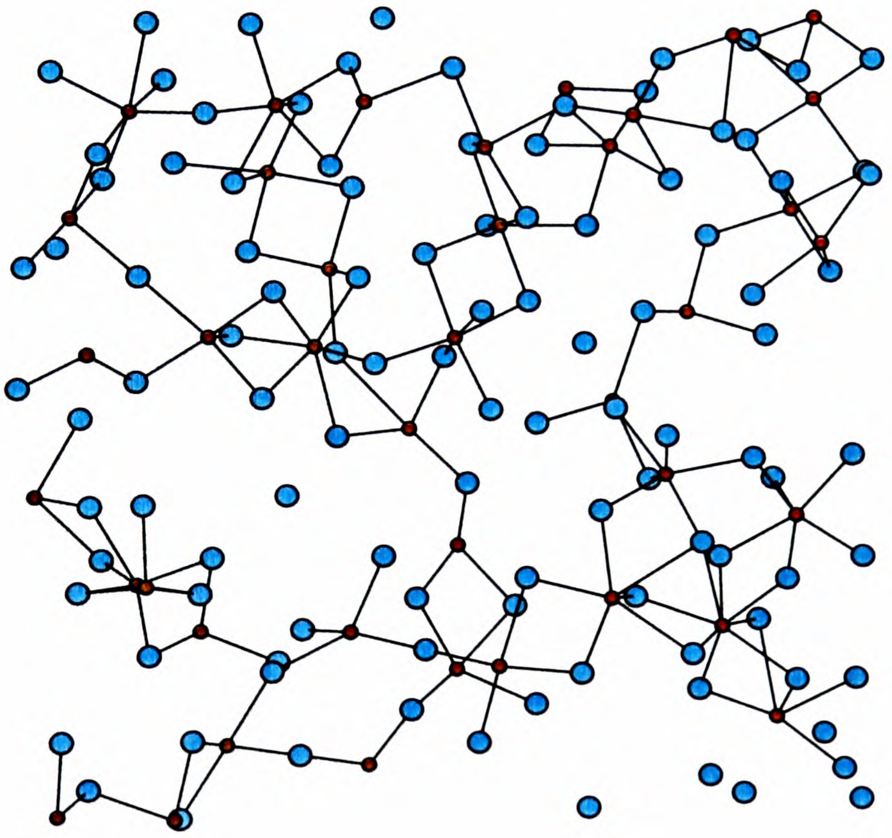

Figure 9.16: *Snapshot of the ion positions in YBr_3.*

System		R_{+-} Å	Range Å	N_{+-}	R_{--} Å	Range Å	N_{--}
$LaBr_3$	(SIM)	3.01	2.59-3.98	7.14	3.70	2.87-5.10	10.56
	(EXP)	3.01	–	7.40	3.76	–	9.30
$CeBr_3$	(SIM)	2.92	2.53-3.96	6.62	3.70	2.92-5.13	10.60
	(EXP)	3.01	–	7.40	3.76	–	–
$DyBr_3$	(SIM)	2.79	2.38-3.60	5.98	3.74	2.79-4.96	9.70
	(EXP)	2.79	2.33-3.33	6.10	3.76	–	–
YBr_3	(SIM)	2.78	2.24-3.59	6.11	3.73	2.78-4.95	9.93
	(EXP)	2.81	2.33-3.25	6.00	3.70	–	–

Table 9.4: *Coordination analysis of MBr_3 systems, showing comparison of the peak positions ($R_{\alpha\beta}$) and coordination numbers ($N_{\alpha\beta}$) from experiment [12, 15] and simulation. Range indicates the interval of integration for the determination of coordination numbers.*

9.4 Structural Trends in Bromides and Chlorides

The general structural trends in the metal tribromides are analogous to those observed for the chlorides. The structures observed for both the Ce/La and Dy/Y pairs of cations in the bromides are typical of those seen for chlorides with smaller cations. This trend can be understood in terms of the radius-ratios listed in table 9.7. Both YBr_3 and $DyBr_3$, which display chain structures characteristic of $ScCl_3$, have similar radius ratios to this chloride whilst both $CeBr_3$ and $LaBr_3$ have much smaller radius ratios than their chloride counterparts. As a result, it would appear that the anion polarization effects are very similar in the same radius ratio ranges, that is the increase in anion size with the resulting reduction in the electric fields, (present on the anion sites) is counterbalanced by the increase in anion polarizability coupled with the change in damping parameter.

System	Coordination number (%)				
	5	6	7	8	9
$LaBr_3$	0	17.5	58.4	23.4	0.7
$CeBr_3$	0	8.9	47.2	37.6	6.4
$DyBr_3$	4.0	74.4	20.0	1.6	0
YBr_3	5.6	74.4	17.6	2.4	0

Table 9.5: *Comparison of coordination number of M^{3+} ions in the various systems.*

System	Connectivity			
	Isolated	Vertex	Edge	Face
$LaBr_3$	12.5	62.5	25.0	0
$CeBr_3$	66.7	0.0	33.3	0.0
$DyBr_3$	0	32.0	60.8	7.2
YBr_3	0	18.3	75.7	6.1

Table 9.6: *Connectivity of MBr_6^{3-} species*

$\sigma(M^{3+})/\sigma(X^-)$	Sc	Y	Dy	Tb	Ce	La
Cl	0.659	0.706	0.718	0.765	0.824	0.835
Br	0.612	0.656	0.667	0.710	0.765	0.776

Table 9.7: *Comparison of radius-ratios in MCl_3 and MBr_3.*

9.5 Conclusions

In this chapter the transferability of the potential models developed for the metal trichlorides in the previous chapters has been investigated. All of the parameters in these models have been taken either from *ab initio* sources or by using ion radii in physically transparent scaling procedures. In general, this procedure appears to generate acceptable models for the bromides as evidenced by the excellent agreement of the calculated total structure factors with those from experiment for the four systems considered. The persistence of oscillations in the total structure factors, attributed almost entirely to oscillations in the M-Br partial structure factor, perhaps indicate that a less steep repulsive wall for the bromide's electron density may be required. Overall, however, the agreement is excellent.

The general structural trends in these bromides follows the same pattern as the chlorides. Although the same structural trends for the bromides appear for different cations compared with the chlorides, the same features emerge in the same ranges of cation/anion radius-ratios. This indicates that the MCl_3 and MBr_3 structural trends may be the same in terms of a 'reduced' model in which the increase in anion polarization on going from Cl^- to Br^- is counterbalanced by changes in anion size and damping parameters.

Chapter 10

Conclusions

Starting from a potential with parameters obtained by fitting Raman data on MCl_3 melts, and supplemented by anion polarization we have shown that we can predict reasonably well the liquid structure of MCl_3. However, this potential fails on the crystal structures tending to predict low coordination number, more loosely bound structures to be more stable than those observed experimentally. A thorough re-evaluation of the potential has been undertaken. In the course of evaluating the potential a number of interesting observations were made.

Since there is no *ab initio* data available on these MX_3 systems it was necessary to make contact with the alkali halides, for which *ab initio* data is available.

It was noted that there are no known physically realistic pair potentials in the literature which stabilise the B2 structure over the B1 for CsCl. By evaluating the energy-volume curves for the CsCl Rigid Ion potential it was concluded that applying a positive pressure to the crystal should result in a transition to the B1 phase. This was observed with the transition being of the Martensitic type. Similarly for LiCl the Rigid Ion potential predicted the most stable crystal to be the B3 blende structure rather than the experimentally observed B1 structure. Again applying a positive pressure resulted in the transition to the B1 phase, but in this case an interesting observation of the role of polarization effects was made. If polarization effects were omitted then the transition occurred via a concerted mechanism involving two deformations which resulted in the B1 phase exhibiting a number of grain boundaries. The inclusion of polarization effects lowered the energy of transition and the transformation progressed by a melting of the crystal (pressure driven amorphisation) and then a renucleation to give a perfect B1 structure.

The different crystal structures considered in each case for CsCl and LiCl were very close in energy. To predict the correct ground state crystal for these systems it was found to be necessary to include CIM effects. In contrast it was shown that the RIM for NaCl correctly predicted the ground state B1 structure and use of this potential plus polarization effects predicted the phonon dispersion curves very well. Paradoxically, inclusion of compressible ion effects resulted in a worse agreement between predicted and experimental phonons.

Once it had been shown that the Parrinello-Rahman constant stress ensemble was working well for the relatively simple alkali haides it was applied to $TbCl_3$. In this system it was shown that the energy difference between two crystal phases was so small that we were able to observe a temperature driven transition (while maintaining a constant stress).

It was shown that for alkali halides compressible ion effects were only important for different structures which were very close in energy. These effects were thus proposed to be negligible for the MCl_3 systems considered and so with an improved potential for MCl_3 we went on to model a wide range of trivalent chlorides which differed only in the cation radius. The improved potential was shown to reproduce the liquid and crystal structures very well. It was found, contrary to conclusions from earlier experimental studies, that instead of $LaCl_3$, $TbCl_3$, $DyCl_3$ and YCl_3 all consisting of MCl_6 octahedra in the melt, that in fact $LaCl_3$ was 8 coordinate, $TbCl_3$ was 7 coordinate and $DyCl_3$ and YCl_3 were almost ideally octahedral. Approximations to partial structure factors, which are much more informative than totals, were obtained for $LaCl_3$. These agreed very well with experiment. The structure of $DyCl_3$ - the only MCl_3 system to date for which partial structure factors are available was predicted very well. In particular the cation-cation partial structure factor illustrated how important the polarization effects are in these systems. The rigid ion model predicted the structure to consist mostly of vertex sharing octahedral units. The inclusion of polarization illustrated the bending of the M-X-M bonds to form an edge sharing octahedral network. This observation was well substantiated by the experimental data.

Using the same potential for $AlCl_3$ and $FeCl_3$, showed that the model predicted the existence of the M_2Cl_6 dimers which are supposed to exist from experimental studies. This really is a remarkable observation: that the same potential can be transferred unchanged to model an ionic liquid like $LaCl_3$ and liquids which are commonly termed 'covalent' like $AlCl_3$ and $FeCl_3$. The 'transferable' potential used has been shown to model the structure of trivalent metal halides extremely well.

The potential was then used to see how it transferred to modelling the dynamical behaviour of these systems.

It was shown that the ionic conductivity decreased with a decrease in ion radius on going from $LaCl_3$ - an ionic conductor to $AlCl_3$ - an insulator. This decrease was not due solely to a decrease in diffusion of the ions, but was shown, in addition, to be connected with the correlation between the ions in the melt.

Dilute mixtures (15%-25%) of $ScCl_3$ in CsCl were predicted to consist of octahedral $ScCl_6^{3-}$ units and connection was made with the Raman spectra by calculating Densities of States and light scattering spectra (due to a fluctuating polarizability model). The predicted frequencies were close to the expeimental values but tended to be a little ($\sim$ 15%) on the high side. A feature absent from the DOS calculations appeared in the isotropoic gamma contribution to the light scattering spectra for pure $ScCl_3$. This was proposed to be due to vibrations of edge sharing octahedra in chains and responsible for the high-frequency peak seen by experiment for which no real assignation exists.

The experimental Raman spectra of $LaCl_3$ had previously been assigned to octahedral vibrations as above, but in our simulations we found that the La^{3+} ions tended to have higher coordination numbers (typically 8). Calculation of the light scattering spectra has shown that this coordination is compatible with the experimentally observed spectra.

Finally we have shown how the potential used can be transferred to successfully model the structure of trivalent metal bromides.

Now that potentials for metal trihalides have been developed and rigorously tested, the stage is set for further simulation study on the dynamics of technologically important systems of which these salts are a component.

Bibliography

[1] P. A. Madden and M. Wilson, *Chem. Soc. Rev.*, **25**, 339 (1996)

[2] M. Wilson, P. A. Madden, N. C. Pyper and J. H. Harding, *J. Chem. Phys.*, **104**, 8068 (1996)

[3] A. J. Rowley, P. J̈emmer, M. Wilson and P. A. Madden, *J. Chem. Phys.* **108**, 10209 (1998).

[4] M. Wilson, P. A. Madden, M. Hemmati and C. A. Angell, 1996, *Phys. Rev. Lett.* **77**, 4023.

[5] Y. Okamoto, H. Hayashi and T. Ogawa, *J. Non-crystalline Solids* **139** 205-207 (1996)

[6] T. Ogawa *et al Proc. Int. Conf. on Emerging Nuclear Fuel Cycle Systems*, Global '95, 207 (1995)

[7] M.-L. Saboungi, D.L. Price, C. Scamehorn and M.P. Tosi, Europhys. Lett., **15**, 283 (1991)

[8] Y. S. Badyal, D. A. Allen and R. A. Howe, *J. Phys. Condens. Matter* , **6**, 10193 (1994)

[9] Y. S. Badyal, M.-L. Saboungi, D. L. Price, D. R. Haeffner and S. D. Shastri, *Europhys. Lett.* , **39**(1), 19 (1997)

[10] A.K. Adya, R. Takagi, Y. Sato, M. Gaune-Escard, A.C. Barnes and H. E. Fischer – to be published.

[11] J. C. Wasse and P. S. Salmon *Physica B*, **241-243**, 967 (1998).

[12] J. C. Wasse and P. S. Salmon *J. Phys.: Condens. Matter*, **11** 1381 (1999)

[13] J. C. Wasse and P. S. Salmon *J. Phys.: Condens. Matter*, **11** 2171 (1999).

[14] J. C. Wasse and P. S. Salmon *J. Phys.: Condens. Matter*, **11** 9293 (1999).

[15] J. C. Wasse, PhD Thesis, University of East Anglia (1998).

[16] J. Mochinaga, Y. Iwadate and K. Fukushima, Mater. Sci. Forum, **73-75** 147 (1991)

[17] R. L. Harris, R. E. Wood and H. L. Ritter, *J. Am. Chem. Soc.*, **73**, 3151 (1951).

[18] H. Tatlipinar, Z. Akdeniz, G. Pastore and M.P. Tosi, *J. Phys.: Condens. Matter*, **4**, 8933 (1992)

[19] M. Wilson, and P. A. Madden, *J. Phys: Condens. Matter*, **6**, 159, 1994.

[20] M. Wilson and P. A. Madden, *J. Phys. Condens. Matter* **11**, A237 (1999)

[21] M. C. C. Ribeiro, M. Wilson and P. A. Madden, *J. Chem. Phys.*, **109** 22, 9859 (1998)

[22] N. C. Pyper, *Chem. Phys. Lett.* **220**, 70 (1994)

[23] M. Parrinello and A. Rahman *Phys. Rev. Lett.* **45**, 1196 (1980).

[24] N. C. Pyper, *Philos. Trans. A*, **320**, 107 (1986).

[25] G.D. Mahan *Sol. State Ionics* **1**, 29 (1980).

[26] N. C. Pyper, *Adv. Sol. Stat. Chem.*, **2**, 223, (1991)

[27] G. D. Mahan and K. R. Subbaswamy, *Local Density Theory of Polarizability*, Plenum, London (1990)

[28] P. W. Fowler and P. A. Madden, 1984, *Phys. Rev. B*, **29** , 1035.

[29] M. Sprik, *Computer Simulation in Chemical Physics*, eds. M. P. Allen and D. J. Tildesley (Kluwer, Berlin, 1993).

[30] A. D. Buckingham, *Adv. Chem. Phys.*, **12**, 107 (1967)

[31] P. W. Fowler and P. A. Madden *Phys. Rev. B*, **31** 5443 (1985)

[32] M. L. Huggins and J. E. Mayer, *J. Chem. Phys.* **1**, 643 (1933)

[33] M.J.L. Sangster and M. Dixon, *Adv. Phys.*, **23**, 247 (1976)

[34] M. P. Tosi and F. G. Fumi, *J. Phys. Chem. Solids* **25**, 31 (1964)

[35] R. W. Busing, *Trans. Am. Cryst. Assoc.* **6**, 57 (1970)

[36] J. C. Slater and J. G. Kirkwood *Phys. Rev.* **37**, 382 (1931).

[37] G. Starkschall and R. G. Gordon, *J. Chem. Phys.*, **56**, 2801 (1972)

[38] K. T. Tang and J. P. Toennies, *J. Chem. Phys.*, **80**, 3726 (1984)

[39] G. Pastore, Z. Akdeniz and M. P. Tosi, *J. Phys. Condens. Matter* **3**, 8297 (1991)

[40] M. C. Abramo and C. Caccamo, *J. Phys. Condens. Matter*, **6**, 4405 (1994)

[41] M. Rovere, and M. P. Tosi, 1986, *Rep. Prog. Phys*, **49**, 1001.

[42] Tosi, M.P., Price, D.L. and Saboungi, M-L., *Ann. Rev. Phys. Chem.* **44**, 173 (1993).

[43] Enderby, J.E., and Barnes, A.C., *Repts. Prog. Phys.*, **53**, 85, (1990).

[44] M. Wilson, P.A. Madden and B.J. Costa-Cabral, *J. Phys. Chem.*, **100**, 1227 (1996)

[45] A. D. Alvarenga, M. L. Saboungi, U. A. Curtiss and M. Grimsditch, 1994, *Molec. Phys.*, **81**, 409.

[46] G. N. Papatheodorou, 1977 *J. Chem. Phys.*, **66**, 2893

[47] F. Hutchinson, A. J. Rowley, M. K. Walters, M. Wilson, P. A. Madden, J. C. Wasse and P. S. Salmon *J. Chem. Phys.* **111**, 1 (1999).

[48] M. Wilson and P. A. Madden, *Phys. Rev. Lett.* **80**, 532 (1998).

[49] M. Wilson, P. A. Madden, N. N. Medvedev, A. Geiger and A. Appelhagen, *J.C.S. Faraday Trans.*, **94**, 1221 (1998).

[50] M. Wilson and P. A. Madden, *Molec. Phys.*, **92**, 197 (1997)

[51] F. Hutchinson, M. K. Walters, A. J. Rowley and P. A. Madden, *J. Chem. Phys.* **110**, 5821 (1999).

[52] A. F. Wells, 1984, *Structural Inorganic Chemistry, 5^{th} ed.* (Clarendon, Oxford).

[53] Müller, U., 1993, *Inorganic Structural Chemistry* (Wiley, Chichester).

[54] M. Wilson, and P. A. Madden, 1993, *J. Phys.: Condens. Matter*, **5**, 2687; M. F. Foley, M. Wilson and P. A. Madden, 1995, *Phil. Mag. B*, **71**, 557.

[55] B. Morosin, *J. Chem. Phys.*, **49**, 7, 3007 (1968)

[56] *CRC Handbook of Chemistry and Physics*, edited by D. R. Lide (CRC Press, Boca Raton, 1993)

[57] D. H. Templeton and G. F. Carter, *J. Phys. Chem*, **58**, 940 (1954)

[58] J. H. Harding and N. C. Pyper, 1995, *Phil. Mag. Lett.*, **71**, 113.

[59] M. Wilson, D.Phil. Thesis, University of Oxford (1994)

[60] A. J. Rowley, *D.Phil. Thesis*, Oxford University, (1998)

[61] R. Car and M. Parrinello, *Phys. Rev. Lett.*, **55**, 2471 (1985).

[62] M. Sprik and M. L. Klein, *J. Chem. Phys.*, **89**, 7556 (1998)

[63] S. Nosé, *J. Chem. Phys.*, **81**, 511 (1984)

[64] W. G. Hoover, *Phys. Rev. A* **31**, 1695 (1985)

[65] G. J. Martyna, M. L. Klein and M. E. Tuckerman, *J. Chem. Phys.* **97**, 2635 (1992)

[66] M. P. Allen and D. J. Tildesley, 1987, *Computer Simulation of Liquids* (Clarendon, Oxford).

[67] P. J̈emmer, M. Wilson, P. A. Madden and P. W. Fowler *J. Chem. Phys.* **111**, 2038 (1999).

[68] P. Ewald, *Ann. Phys.* **64**, 253 (1921)

[69] S. Nosé and M. L. Klein, *Mol. Phys.* **50**, 1055 (1983)

[70] H. C. Andersen, *J. Chem. Phys.*, **72**, 4, 2384 (1980)

[71] G. J. Martyna, D. J. Tobias and M. L. Klein, *J. Chem. Phys.* **101**, 5 (1994)

[72] J. P. Hansen and I. R. McDonald, 1986, *Theory of Simple Liquids, 2^{nd} Edn.*, (Academic, NY).

[73] J. N. Wilson and R. M. Curtis, *J. Phys. Chem.* **74**, 187 (1970)

[74] P. D'Arco, L-H. Jolly and B. Silvi, *Phy. of the Earth and Planetary Interiors* **72**, 286 (1992)

[75] M. D. Knudson, Y. M. Gupta and A. B. Kunz,*Phys. Rev. B*, **59** 11704 (1999)

[76] D. A. Porter and K. E. Easterling, *Phase Transformations in Metals and Alloys* Chapman and Hall (1992)

[77] R. Takagi, F. Hutchinson, P. A. Madden, A. K. Adya and M. Gaune-Escard , *J. Phys.: Condensed Matter*, **11**, 645 (1999).

[78] A. May, *Phys. Rev.* **52** (1937) 339 ; A. May, *Phys. Rev.* **54** (1938) 629

[79] J. E. Mayer, *J. Chem. Phys.*, **1** 270 (1933)

[80] E. Fois, P. A. Madden and M. Wilson *unpublished work.*

[81] M. J. Castiglione, M. Wilson and P. A. Madden, *J. Phys. Condens. Matter* **11** 9009 (1999)

[82] J. Emsley, *The Elements* (Clarendon Press, Oxford 1991)

[83] P. C. Pistorius *Prog. Solid State Chem.* **11**, 1 (1976)

[84] P. W. Fowler and N. C. Pyper, *Proc. R. Soc. Lond. A*, **398**, 377 (1985)

[85] F. Birch, *J. Geophys. Res.* **83** 1257 (1978)

[86] G. Raunio, L. Almqvist and R. Stedman, *Phys. Rev.* **178**, 1496 (1969)

[87] Ashcroft and Mermin *Phys. Rev.* **178**, 1496 (1969)

[88] V.F. Sears, *Neutron News*, **3**, 26 (1992).

[89] D. T. Cromer, and J. T. Waber, 1974, *International Tables for X-Ray Crystallography,* edited by J. A. Ibers and W. C. Hamilton, (Kynoch Press, Birmingham), p.71.

[90] H. Gunsilius, H. Borrmann, A. Simon and W. Urland, *Z. Naturforsch B.* **43**, 1023 (1988)

[91] A. R. Ubbelohde, 1978 *The Molten State of Matter* (John Wiley & Sons).

[92] Y. Iwadate, K. Fukushima, R. Takagi and M. Gaune-Escard, *Electrochemistry* **67** 553 (1999)

[93] K. Shirao, T. Iida, K. Fukushima and Y. Iwadate, *J. Alloys and Compounds* **281** 163 (1998)

[94] K. Fukushima, M. Hayakawa, Y. Iwadate, *J. Alloys and Compounds* **245** 66 (1996)

[95] G. N. Papatheodorou, *Inorg. Nucl. Chem. Letters* **11** 483 (1975)

[96] G. D. Zissi and G. N. Papatheodorou *Chem. Phys. Lett.* **308** 51 (1999)

[97] R. Takagi, L. Rycerz and M. Gaune-Escard, *Denki Kagaku* **62** 240 (1994)

[98] M. Prie, H. J. Seifert, *J. Therm. Anal.*, **45** 349 (1995)

[99] L. R. Morss, M. Siegal, L. Stenger, N. Edelstein, *Inorg. Chem.* **9** 1771 (1970)

[100] E. A. Pavlatou, P. A. Madden and M. Wilson, *J. Chem. Phys.* **107** (24), 10446 (1997)

[101] M. C. C. Ribeiro, M. Wilson and P. A. Madden, *J. Chem. Phys.* **109**, 9859 (1998)

[102] K. F. O'Sullivan and P. A. Madden, *J. Chem. Phys*, **95**, 1980 (1991)

[103] K. F. O'Sullivan, DPhil. Thesis, University of Oxford (1990)

[104] P. A. Madden and J. A. Board, *J. Chem. Soc., Faraday Trans. 2* **83**, 1891 (1987)

[105] P. A. Madden, K. O'Sullivan, J. A. Board and P. W. Fowler, *J. Chem. Phys.* **94** 918 (1991)

[106] G. N. Papatheodorou and V. Dracopoulos, *Chem. Phys. Lett.*, **241** 345 (1995)

[107] J. O. Hirschfelder, C. F. Curtiss and R. B. Bird, *Molecular Theory of Gases and Liquids* Wiley, New York (1954)

[108] M. C. C. Ribeiro, M. Wilson and P. A. Madden, *J. Chem. Phys.* **110** 4803 (1999)

[109] G. J. Janz, 1968, *NBS 15*(National Bureau of Standards).

Appendix A

Forces and Energies via Ewald Summation

The Ewald sum can be described by the zeroth order T tensor T^{ij}. This consists of a real and reciprocal space part.

$$T^{ij} = \frac{\mathrm{erfc}(\eta' r_{ij})}{r_{ij}} + \frac{1 - \mathrm{erfc}(\eta' r_{ij})}{r_{ij}} \tag{A.1}$$

First, consider the real part

$$T^{ij}_{real} = T^{ij}\mathrm{erfc}(\eta' r_{ij}) \tag{A.2}$$

Differentiating once gives

$$\begin{aligned} \frac{\partial T^{ij}_{real}}{\partial r^i_\alpha} &= T^{ij}_{\alpha,real} \\ &= T^{ij}_\alpha \left[\mathrm{erfc}(\eta' r_{ij}) + \frac{2\eta' r^{ij}}{\pi^{1/2}} e^{-\eta'^2 r^2_{ij}} \right], \end{aligned} \tag{A.3}$$

and a second time gives

$$\frac{\partial^2 T^{ij}_{real}}{\partial r^i_\alpha \partial r^i_\beta} = T^{ij}_{\alpha\beta(real)} = T^{ij}_{\alpha\beta}\left[\mathrm{erfc}(\eta' r^{ij}) + \frac{2\eta' r^{ij}}{\pi^{1/2}} e^{-\eta'^2 r^2_{ij}}\right] - \frac{4\eta' r^{ij}}{\pi^{1/2}} T^{ij}_\alpha r^{ij}_\beta e^{-\eta'^2 r^2_{ij}}. \tag{A.4}$$

The reciprocal space part is given by

$$T^{ij}_{recip} = \frac{1}{2\pi V}\sum_{k\neq 0}\frac{1}{k^2} e^{-\pi^2 k^2/\eta'^2}\cos(\mathbf{k}\cdot\mathbf{r}_{ij}) \tag{A.5}$$

$$\frac{\partial T^{ij}_{recip}}{\partial r^i_\alpha} = T^{ij}_{\alpha,recip} = \frac{1}{2\pi V}\sum_{k\neq 0} -\frac{k_\alpha}{k^2} e^{-\pi^2 k^2/\eta'^2}\sin(\mathbf{k}\cdot\mathbf{r}_{ij}) \tag{A.6}$$

and for the 2nd derivative

$$\frac{\partial^2 T^{ij}_{recip}}{\partial r^i_\alpha \partial r^i_\beta} = T^{ij}_{\alpha\beta,recip} = \frac{1}{2\pi V}\sum_{k\neq 0} -\frac{k_\alpha k_\beta}{k^2} e^{-\pi^2 k^2/\eta'^2}\cos(\mathbf{k}\cdot\mathbf{r}_{ij}) \tag{A.7}$$

The expressions allow terms such as the charge-charge, charge-dipole and dipole-dipole forces and energies to be treated via an Ewald summation. For example, the $q - \mu$ interaction energy can be written as

$$U_{q-\mu} = \sum_i \sum_{j<i} (-q^i T^{ij}_\alpha \mu^j_\alpha + \mu^i_\alpha T^{ij}_\alpha q^j) \tag{A.8}$$

ignoring the short-range term. Therefore, the energy is found within the model by substituting the equations for the real and reciprocal space summations of T^{ij}_α from equations A.3 and A.6 and evaluating the resulting terms. Similarly the contribution to the electric field gradient on ion i from the changes on the surrounding ions can be expressed as

$$E^i_{\alpha\beta} = \sum_{j\neq i} T^{ij}_{\alpha\beta} q^j \tag{A.9}$$

Hence, substitution for $T^{ij}_{\alpha\beta} q^j$ from equations A.4 and A.7 generates the Ewald sum for this term.

A.1 Self and k=0 terms

The self-interaction term that arises in the calculation of the charge-charge energy is calculated by considering the limiting value of $T^{ij}(1-\mathrm{erfc}(\eta' r_{ij}))$ for $i = j$ (equation A.11). This self term corresponds to the limiting value of the sum as $r_{ij} \to 0$,

$$\begin{aligned} -\frac{1}{2}\left(\frac{1-\mathrm{erfc}(\eta' r_{ij})}{r_{ij}}\right)\Bigg|_{i=j,l=0} &= -\frac{1}{2}\lim_{r\to 0}\frac{1-\mathrm{erfc}(\eta' r)}{r} \\ &= -\frac{1}{2}\lim_{r\to 0}\frac{\frac{2\eta'}{\sqrt{\pi}}e^{-\eta'^2 r^2}}{1} \qquad \text{(A.10)} \\ &= -\frac{\eta'}{\sqrt{\pi}} \qquad \text{(A.11)} \end{aligned}$$

where the half is due to the double sum and the limit has been derived via L'Hopital's rule. We have also used the result that

$$\frac{\partial}{\partial r}[\mathrm{erfc}(\alpha r)] = \frac{-2\alpha}{\pi^{1/2}}e^{-\alpha^2 r^2}$$

Similarly we must consider the limiting values of $T^{ij}_{\alpha}(1-\mathrm{erfc}(\eta' r_{ij}))$ and $T^{ij}_{\alpha\beta}(1-\mathrm{erfc}(\eta' r_{ij}))$ since these will arise in the course of a direct calculation of the Ewald sums for these interaction tensors. The differentiation of the T^{ij} sums has already given us the rest of the terms. Firstly, for T^{ij}_{α}

$$\begin{aligned} -\left(\frac{r^{ij}_{\alpha}(1-\mathrm{erfc}(\eta' r_{ij}))}{r^{ij^3}}\right)\Bigg|_{i=j,1=0} &= -\lim_{r\to 0}\frac{1-\mathrm{erfc}(\eta' r)}{r^2} \\ &= -\lim_{r\to 0}\frac{\frac{2\eta'}{\sqrt{\pi}}e^{-\eta'^2 r^2}}{2r} \\ &= -\lim_{r\to 0}\frac{\frac{-4r\eta'^3}{\sqrt{\pi}}e^{-\eta'^2 r^2}}{2} \\ &= 0 \qquad \text{(A.12)} \end{aligned}$$

ie. there are no additional terms in the charge-dipole energies. For $T^{ij}_{\alpha\beta}$ we obtain

$$\begin{aligned}
\left.\left(\frac{(3r^{ij}_{\alpha}r^{ij}_{\beta} - r^{ij^2}\delta_{\alpha\beta})(1-\mathrm{erfc}(\eta' r^{ij}))}{r^{ij^5}}\right)\right|_{i=j,\mathbf{l}=0} &= -\lim_{r\to 0}\frac{2(1-\mathrm{erfc}(\eta' r))}{r^3} \\
&= -\lim_{r\to 0}\frac{\frac{4\eta'}{\sqrt{\pi}}e^{-\eta'^2 r^2}}{3r^2} \\
&= -\lim_{r\to 0}\frac{\frac{-8r\eta'^3}{\sqrt{\pi}}e^{-\eta'^2 r^2}}{6r} \\
&= \lim_{r\to 0}\left(\frac{\frac{-8r\eta'^3}{\sqrt{\pi}}e^{-\eta'^2 r^2}}{6} + \frac{\frac{16r\eta'^5}{\sqrt{\pi}}e^{-\eta'^2 r^2}}{6}\right) \\
&= \frac{-4\eta'^3}{3\sqrt{\pi}} \qquad \text{(A.13)}
\end{aligned}$$

ie. therefore an additional term arises in the dipole-dipole energy, $-\mu^i_\alpha T^{ij}_{\alpha\beta}\mu^j_\beta$

$$U^{\mu-\mu}_{const} = -\sum_i \frac{2\eta'^3 \mu^{i2}}{3\sqrt{\pi}} \qquad \text{(A.14)}$$

Appendix B

Equations of Motion for the Parrinello-Rahman Scheme

From Martyna *et al* [71] the equations of motion are integrated using

$$\mathbf{s}_i(t+\delta t) = e^{-\epsilon(t+\delta t)}\mathbf{h}_0^{-1}(t+\delta t)\mathbf{r}_i(t+\delta t) \tag{B.1}$$

differentiating this with respect to t gives

$$\dot{\mathbf{s}}_i(t+\delta t) = e^{-\epsilon(t+\delta t)}\mathbf{h}_0^{-1}(t+\delta t)\mathbf{v}_i(t+\delta t) \tag{B.2}$$

differentiating once again with respect to t

$$\begin{aligned}\ddot{\mathbf{s}}_i(t+\delta t) &= e^{-\epsilon(t+\delta t)}\mathbf{h}_0^{-1}(t+\delta t)\left\{\frac{\mathbf{f}_i(t+\delta t)}{m_i} - 2\mathbf{v}_{g0}(t+\delta t)\mathbf{v}_i(t+\delta t)\right. \\ &- \left(2+\frac{d}{N_f}\right)v_\epsilon(t+\delta t)\mathbf{v}_i(t+\delta t) \\ &- \left. v_\xi(t+\delta t)\mathbf{v}_i(t+\delta t)\right\}\end{aligned} \tag{B.3}$$

The Velocity-Verlet algorithm (section 3.2) is then used on $\dot{\mathbf{s}}_i$ and $\ddot{\mathbf{s}}_i$ and the expressions obtained are converted into the desired quantities $\mathbf{r}_i(t+\delta t)$, $\mathbf{v}_i(t+\delta t)$, $\mathbf{v}_{g0}(t+\delta t)$. Using the Velocity-Verlet scheme

$$\mathbf{s}_i(t+\delta t) = \mathbf{s}_i(t) + \dot{\mathbf{s}}(t)_i\delta t + \ddot{\mathbf{s}}_i(t+\delta t)\frac{\delta t^2}{2} \tag{B.4}$$

substituting for $\mathbf{s}_i$, $\dot{\mathbf{s}}_i$ and $\ddot{\mathbf{s}}_i$ results in

$$\begin{aligned}
\mathbf{r}_i(t+\delta t) &= e^{[\epsilon(t+\delta t)-\epsilon(t)]}\mathbf{h}_0(t+\delta t)\mathbf{h}_0^{-1}(t)\Bigg\{\mathbf{r}_i(t) + \mathbf{v}_i(t)\delta t \\
&+ \Bigg[\frac{\mathbf{f}_i(t)}{m_i} - \mathbf{v}_i(t)v_\xi(t) - 2\mathbf{v}_{g0}(t)\mathbf{v}_i(t) \\
&- \left(2 + \frac{d}{N_f}\right)\mathbf{v}_i(t)v_\epsilon(t)\Bigg]\frac{\delta t^2}{2}\Bigg\}
\end{aligned} \tag{B.5}$$

Using Velocity-Verlet on equation 3.53

$$\xi(t+\delta t) = \xi(t) + \dot{\xi}(t)\delta t + \ddot{\xi}(t)\frac{\delta t^2}{2} \tag{B.6}$$

$$\xi(t+\delta t) = \xi(t) + v_\xi(t)\delta t + G_\xi(t)\frac{\delta t^2}{2} \tag{B.7}$$

where

$$G_\xi(t) = \frac{1}{Q}\Bigg[\sum_{i=1}^{N} m_i\mathbf{v}_i(t)^2 + Wv_\epsilon(t)^2 + W_{g0}Tr[\mathbf{v}_{g0}(t)\mathbf{v}_{g0}^t(t)] \tag{B.8}$$

$$- \, (N_f + d^2)kT\Bigg] \tag{B.9}$$

For the isotropic barostat position

$$\epsilon(t+\delta t) = \epsilon(t) + \dot{\epsilon}(t)\delta t + \ddot{\epsilon}(t)\frac{\delta t^2}{2} \tag{B.10}$$

$$\epsilon(t+\delta t) = \epsilon(t) + v_\epsilon(t)\delta t + \left[\frac{F_\epsilon(t)}{W} - v_\epsilon(t)v_\xi(t)\right]\frac{\delta t^2}{2} \tag{B.11}$$

where

$$F_\epsilon(t) = dV(t)[P_{int}(t) - P_{ext}] + \frac{d}{N_f}\sum_{i=1}^{N} m_i \mathbf{v}_i(t)^2 \tag{B.12}$$

From equation 3.51

$$\mathbf{h}_0(t+\delta t) = \mathbf{h}_0(t) + \dot{\mathbf{h}}_0(t)\delta t + \ddot{\mathbf{h}}_0(t)\frac{\delta t^2}{2} \tag{B.13}$$

$$\mathbf{h}_0(t+\delta t) = \left\{\mathbf{I} + \mathbf{v}_{g0}(t)\delta t + \left[\frac{1}{W_{g0}}\mathbf{F}_{g0}(t) + \mathbf{v}_{g0}(t)^2 - v_\xi(t)\mathbf{v}_{g0}(t)\right]\frac{\delta t^2}{2}\right\}\mathbf{h}_0(t) \tag{B.14}$$

The evolution of the cell volume with time comes from

$$V(t+\delta t) = V(t) + \dot{V}(t)\delta t + \ddot{V}(t)\frac{\delta t^2}{2} \tag{B.15}$$

$$V(t+\delta t) = V(t) + 3V(t)v_\epsilon(t)\delta t + \left\{\frac{3F_\epsilon(t)}{W} - v_\xi(t)v_\epsilon(t) + d^2 v_\epsilon(t)^2\right\}V(t)\frac{\delta t^2}{2} \tag{B.16}$$

The following quantities must all be iterated to self consistency. From the Velocity-Verlet expression

$$\dot{\mathbf{s}}_i(t+\delta t) = \dot{\mathbf{s}}_i(t) + [\ddot{\mathbf{s}}_i(t) + \ddot{\mathbf{s}}_i(t+\delta t)]\frac{\delta t}{2} \tag{B.17}$$

$$\begin{aligned}
\mathbf{v}_i(t+\delta t) &= e^{[\epsilon(t+\delta t)-\epsilon(t)]}\mathbf{h}_0(t+\delta t)\mathbf{h}_0^{-1}(t)\left\{\mathbf{v}_i(t) + \left[\frac{\mathbf{f}_i(t)}{m_i} - \mathbf{v}_i(t)v_\xi(t)\right.\right. \\
&- \left.2\mathbf{v}_{g0}(t)\mathbf{v}_i(t) - \left(2 + \frac{d}{N_f}\right)\mathbf{v}_i(t)v_\epsilon(t)\right]\frac{\delta t}{2} \\
&+ \left[\frac{\mathbf{f}_i(t+\delta t)}{m_i} - \mathbf{v}_i(t+\delta t)v_\xi(t+\delta t)\right. \\
&- \left.\left.2\mathbf{v}_{g0}(t+\delta t)\mathbf{v}_i(t+\delta t) - \left(2 + \frac{d}{N_f}\right)\mathbf{v}_i(t+\delta t)v_\epsilon(t+\delta t)\right]\frac{\delta t}{2}\right\}
\end{aligned}$$

$$v_\xi(t+\delta t) = v_\xi(t) + [G_\xi(t) + G_\xi(t+\delta t)]\frac{\delta t}{2} \tag{B.18}$$

$$v_\epsilon(t+\delta t) = v_\epsilon(t) + \left[\frac{F_\epsilon(t)}{W} - v_\epsilon(t)v_\xi(t)\right]\frac{\delta t}{2} + \left[\frac{F_\epsilon(t+\delta t)}{W} - v_\epsilon(t+\delta t)v_\xi(t+\delta t)\right]\frac{\delta t}{2} \tag{B.19}$$

$$\begin{aligned} \mathbf{v}_{g0}(t+\delta t) &= \left\{\mathbf{v}_{g0}(t) + \left[\frac{\mathbf{F}_{g0}(t)}{W_{g0}} + \mathbf{v}_{g0}(t)^2 - \mathbf{v}_{g0}(t)v_\xi(t)\right]\frac{\delta t}{2}\right\} \cdot \mathbf{h}_0(t)\mathbf{h}_0^{-1}(t+\delta t) \\ &+ \left[\frac{1}{W_{g0}}\mathbf{F}_{g0}(t+\delta t) + \mathbf{v}_{g0}(t+\delta t)^2 - \mathbf{v}_{g0}(t+\delta t)v_\xi(t+\delta t)\right] \cdot \frac{\delta t}{2} \end{aligned} \tag{B.20}$$

where

$$F_{g0}(t) = V(t)[\mathbf{P}_{int}(t+\delta t) - \mathbf{I}P_{ext}] - \frac{V(t+\delta t)}{d}Tr[\mathbf{P}_{int}(t+\delta t) - \mathbf{I}P_{ext}]\mathbf{I} \tag{B.21}$$

The velocities are determined iteratively from

$$\mathbf{v}_i^k(t+\delta t) = \frac{1}{[1 + (\delta t/2)v_\xi^{k-1}(t+\delta t)]} \times \left\{\mathbf{v}_i(t) + \left[\frac{\mathbf{f}_i(t)}{m_i} - \mathbf{v}_i(t)v_\xi(t) + \frac{\mathbf{f}_i(t+\delta t)}{m_i}\right]\frac{\delta t}{2}\right\} \tag{B.22}$$

with an initial guess of

$$v_\xi^0(t+\delta t) = v_\xi(t-\delta t) + 2G_\xi(t)\delta t \tag{B.23}$$

The constraint that $det[\mathbf{h}_0] = 1$ is enforced with a Shake/Rattle routine.

Appendix C

Stress Tensor

C.1 Derivation of Stress Tensor

In this Appendix we will derive the contributions to the stress tensor arising from the interactions amongst charges and dipoles. The contributions involving the dipoles does not appear to have been derived previously.

The stress tensor, Π, is obtained from [69]

$$-\frac{\partial U}{\partial h_{\alpha\beta}} = \sum_{\gamma} \Pi_{\alpha\gamma} V h^{-1}_{\beta\gamma} \tag{C.1}$$

and for each of the terms of interest ($q - q$, $q - \mu$, and $\mu - \mu$) the Ewald representation gives

$$U = U_{real} + U_{recip} + U_{const}. \tag{C.2}$$

We will consider each of these contributions to the total coulomb energy in turn. During the derivation we will make use of the following relations:

$$\frac{\partial V}{\partial h_{\alpha\beta}} = V h^{-1}_{\beta\alpha}, \tag{C.3}$$

$$\mathbf{k}_n = \hat{\mathbf{h}}^{-1^t}\mathbf{n}, \tag{C.4}$$

$$\frac{\partial h^{-1}_{\mu\nu}}{\partial h_{\alpha\beta}} = -h^{-1}_{\mu\alpha}h^{-1}_{\beta\nu}, \tag{C.5}$$

the latter is obtained from the differentiation of $\mathbf{hh}^{-1} = \mathbf{I}$.

C.1.1 Reciprocal part of coulomb energy

Following Nosé and Klein [69] the reciprocal space part of the interaction energy of a system of molecules containing charged sites is given by

$$U_{recip} = \frac{1}{2\pi V}\sum_{n}{}' S(\mathbf{k}_n)S(-\mathbf{k}_n)Q(\mathbf{k}_n) \tag{C.6}$$

where

$$S(\mathbf{k}_n) = \sum q_j e^{2\pi i\cdot\mathbf{k}_n(\mathbf{hs}_j+\mathbf{p}^k_j)} \tag{C.7}$$

and

$$Q(\mathbf{k}_n) = \frac{e^{-\pi^2|\mathbf{k}_n|^2/\eta'^2}}{|\mathbf{k}_n|^2} \tag{C.8}$$

where $\mathbf{r}^k_i$ are the coordinates of site k of molecule i in the cell frame, $\mathbf{s}_i$ locates the centre of mass of molecule i in the Cartesian frame and $\mathbf{p}^k_i$ is a vector drawn from the centre of mass of molecule i to a site of dipole charge in the Cartesian frame. Note, the cell matrix, $\mathbf{h}$, only acts on the ion centres of mass.

In order to generate stress tensor expressions including dipoles we have made the associations illustrated in figure C.1. Each ion is treated as a 3-site molecule and the dipole is treated as a charge of $+\delta$ at a displacement $\mathbf{p}^1_i$ from the centre of molecule i and a charge of $-\delta$ at a displacement $-\mathbf{p}^1_i$, giving a dipole of

$$\mu = 2\delta\mathbf{p}. \tag{C.9}$$

From C.6

$$U_{recip} = U_{recip}[V, S(\mathbf{k}_n), S(-\mathbf{k}_n), Q(\mathbf{k}_n)] \tag{C.10}$$

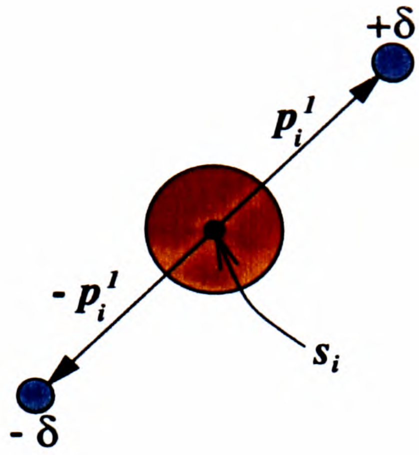

Figure C.1: *Illustration of 3-site molecule used in derivation of Stress Tensor components*

$$\frac{\partial U_{recip}}{\partial h_{\alpha\beta}} = \frac{\partial U_{recip}}{\partial V}\cdot\frac{\partial V}{\partial h_{\alpha\beta}} + \frac{\partial U_{recip}}{\partial S(\mathbf{k}_n)}\cdot\frac{\partial S(\mathbf{k}_n)}{\partial h_{\alpha\beta}} + \frac{\partial U_{recip}}{\partial S(-\mathbf{k}_n)}\cdot\frac{\partial S(-\mathbf{k}_n)}{\partial h_{\alpha\beta}} + \frac{\partial U_{recip}}{\partial Q(\mathbf{k}_n)}\cdot\frac{\partial Q(\mathbf{k}_n)}{\partial h_{\alpha\beta}} \tag{C.11}$$

From C.11 it follows that

$$\frac{\partial U_{recip}}{\partial h_{\alpha\beta}} = -\frac{1}{2\pi V^2}\frac{\partial V}{\partial h_{\alpha\beta}}\sum_{\mathbf{n}}{}' S(\mathbf{k}_n)S(-\mathbf{k}_n)Q(\mathbf{k}_n) \tag{C.12}$$

$$+ \frac{1}{2\pi V}\sum_{\mathbf{n}'}\frac{\partial S(\mathbf{k}_n)}{\partial h_{\alpha\beta}}S(-\mathbf{k}_n)Q(\mathbf{k}_n) \tag{C.13}$$

$$+ \frac{1}{2\pi V}\sum_{\mathbf{n}'}S(\mathbf{k}_n)\frac{\partial S(-\mathbf{k}_n)}{\partial h_{\alpha\beta}}Q(\mathbf{k}_n) \tag{C.14}$$

$$+ \frac{1}{2\pi V}\sum_{\mathbf{n}'}S(\mathbf{k}_n)S(-\mathbf{k}_n)\frac{\partial Q(\mathbf{k}_n)}{\partial h_{\alpha\beta}} \tag{C.15}$$

Using identity C.3, the term C.12 becomes

$$-\frac{1}{2\pi V}h^{-1}_{\beta\alpha}\sum_{\mathbf{n}}{}' S(\mathbf{k}_n)S(-\mathbf{k}_n)Q(\mathbf{k}_n) \tag{C.16}$$

Differentiating the 2nd term (C.13) gives

$$\begin{aligned}
\frac{\partial S(\mathbf{k}_n)}{\partial h_{\alpha\beta}} &= \sum_j q_j \cdot 2\pi i \frac{\partial}{\partial h_{\alpha\beta}} \left\{ (\mathbf{k}_n \cdot \hat{\mathbf{h}}\mathbf{s}_j + \mathbf{p}_j^k) \right\} e^{2\pi i \mathbf{k_n} \cdot (\hat{\mathbf{h}}\mathbf{s_j} + \mathbf{p_j^k})} \\
&= \sum_j q_j \cdot 2\pi i \frac{\partial}{\partial h_{\alpha\beta}} \left\{ \underbrace{(h^{-1})^t_{\mu\nu}}_{=\mathbf{h}^{-1}_{\nu\mu}} n_\nu h_{\mu\psi} s_{j\psi} + \underbrace{(h^{-1})^t_{\mu\nu}}_{=\mathbf{h}^{-1}_{\nu\mu}} n_\nu p_{j\psi} \right\} e^{2\pi i \mathbf{k_n} \cdot (\hat{\mathbf{h}}\mathbf{s_j} + \mathbf{p_j^k})} \\
&= \sum_j q_j \cdot 2\pi i \{ \, (-h^{-1}_{\nu\alpha} h^{-1}_{\beta\mu} n_\nu h_{\mu\psi} s_{j\psi} + h^{-1}_{\nu\mu} n_\nu \delta_{\alpha\beta,\mu\psi} s_{j\psi}) \qquad \text{(C.17)} \\
&- \; h^{-1}_{\nu\alpha} h^{-1}_{\beta\mu} n_\nu p_{j\psi} \, \} \, e^{2\pi i \mathbf{k_n} \cdot (\hat{\mathbf{h}}\mathbf{s_j} + \mathbf{p_j^k})} \\
&= \sum_j q_j \cdot 2\pi i \left\{ (-h^{-1}_{\nu\alpha} \delta_{\beta\psi} s_{j\psi} n_\nu + h^{-1}_{\nu\mu} n_\nu \delta_{\alpha\beta,\mu\psi} s_{j\psi}) \right. \qquad \text{(C.18)} \\
&- \; h^{-1}_{\beta\mu} k_{n,\alpha} p_{j\beta} \, \} \, e^{2\pi i \mathbf{k_n} \cdot (\hat{\mathbf{h}}\mathbf{s_j} + \mathbf{p_j^k})} \\
&= \sum_j q_j \cdot 2\pi i \left\{ (-h^{-1}_{\nu\alpha} s_{j\beta} n_\nu + h^{-1}_{\nu\alpha} n_\nu s_{j\beta}) - h^{-1}_{\beta\mu} k_{n,\alpha} p_{j\beta} \right\} e^{2\pi i \mathbf{k_n} \cdot (\hat{\mathbf{h}}\mathbf{s_j} + \mathbf{p_j^k})} \\
&= -\sum_j q_j \cdot 2\pi i k_{n,\alpha} p^k_{j,\beta} h^{-1}_{\beta\mu} e^{2\pi i \mathbf{k}_n \cdot \mathbf{r}_i^k}
\end{aligned}$$

Here we have used the relation C.5. Equation C.13 now becomes

$$-\frac{1}{2\pi V} S(-\mathbf{k}_n) Q(\mathbf{k}_n) \sum_j q_j \cdot 2\pi i k_{n,\alpha} p^k_{j,\beta} h^{-1}_{\beta\mu} e^{2\pi i \mathbf{k}_n \cdot \mathbf{r}_i^k}. \tag{C.19}$$

Similarly the 3rd term (C.14) becomes

$$-\frac{1}{2\pi V} S(\mathbf{k}_n) Q(\mathbf{k}_n) \sum_j q_j \cdot 2\pi i k_{n,\alpha} p^k_{j,\beta} h^{-1}_{\beta\mu} e^{-2\pi i \mathbf{k}_n \cdot \mathbf{r}_i^k}. \tag{C.20}$$

For the 4th term (C.15)

$$\frac{\partial Q(\mathbf{k}_n)}{\partial h_{\alpha\beta}} = \frac{\partial |\mathbf{k}_n|^2}{\partial h_{\alpha\beta}} \left\{ \frac{-\pi^2 \eta'^2}{|\mathbf{k}_n|^2} - \frac{1}{|\mathbf{k}_n|^4} \right\} e^{-\pi^2 |\mathbf{k}_n^2| \eta'^2} \tag{C.21}$$

with

$$\frac{\partial(|\mathbf{k}_n|^2)}{\partial h_{\alpha\beta}} = \frac{\partial}{\partial h_{\alpha\beta}} \left\{ \underbrace{(h^{-1})^t_{\mu\nu}}_{\mathbf{h}^{-1}_{\nu\mu}} n_\nu n_\psi (h^{-1})_{\psi\mu} \right\}. \tag{C.22}$$

If we now again make use of C.5 then

$$\begin{aligned}\frac{\partial(|\mathbf{k}_n|^2)}{\partial h_{\alpha\beta}} &= -h^{-1}_{\nu\alpha}h^{-1}_{\beta\mu}n_\nu n_\psi h^{-1}_{\psi\mu} - h^{-1}_{\nu\mu}n_\nu n_\psi h^{-1}_{\psi\alpha}h^{-1}_{\beta\mu} \\ &= -(k_{n,\alpha}k_{n,\mu} + k_{n,\mu}k_{n,\alpha})h^{-1}_{\beta\mu} \\ &= -2k_{n,\alpha}k_{n,\mu}h^{-1}_{\beta,\mu}\end{aligned}$$

and so

$$\frac{\partial Q(\mathbf{k_n})}{\partial h_{\alpha\beta}} = \left(\frac{-\pi^2\eta'^2}{|\mathbf{k}_n|^2} - \frac{1}{|\mathbf{k}_n|^4}\right) e^{-\pi^2\eta'^2|\mathbf{k}_n|^2}\left\{-2k_{n,\alpha}k_{n,\mu}h^{-1}_{\beta\mu}\right\}. \tag{C.23}$$

Inserting this expression in C.15 we see that it becomes

$$\frac{1}{2\pi V}\sum_{\mathbf{n}'} S(\mathbf{k}_n)S(-\mathbf{k}_n)\left(\frac{-\pi^2\eta'^2}{|\mathbf{k}_n|^2} - \frac{1}{|\mathbf{k}_n|^4}\right) e^{-\pi^2\eta^2|\mathbf{k}_n|^2}\left\{-2k_{n,\alpha}k_{n,\mu}h^{-1}_{\beta\mu}\right\}. \tag{C.24}$$

Collecting up from equations C.16, C.19, C.20 and C.24 we obtain

$$\begin{aligned}\frac{\partial U_{recip}}{\partial h_{\alpha\beta}} &= -\frac{1}{2\pi V}h^{-1}_{\beta\alpha}{\sum_n}' S(\mathbf{k_n})S(-\mathbf{k_n})Q(\mathbf{k_n}) \\ &+ \frac{1}{2\pi V}{\sum_n}' S(\mathbf{k_n})S(-\mathbf{k_n})\left\{-2k_{n,\alpha}k_{n,\mu}h^{-1}_{\beta\mu}\right\}\overbrace{\frac{e^{-\pi^2\eta'^2|\mathbf{k_n}|^2}}{|\mathbf{k}_n|}}^{Q(k_n)}\left(-\pi^2\eta - \frac{1}{|\mathbf{k_n}|^2}\right) \\ &- \frac{h^{-1}_{\beta\mu}}{2\pi V}\sum_i Q(\mathbf{k}_n)2\pi i(k_{n,\alpha}p^k_{i,\beta})\left\{S(\mathbf{k}_n)e^{-2\pi i\mathbf{k}_n\cdot\mathbf{r}_i}\right. \\ &- \left.S(-\mathbf{k_n})e^{2\pi i\mathbf{k_n}\cdot\mathbf{r_i}}\right\}\end{aligned} \tag{C.25}$$

Therefore from C.1

$$\begin{aligned}\sum_\gamma \Pi_{\alpha\gamma}Vh^{-1}_{\beta\gamma} &= \left\{\frac{-1}{2\pi V}{\sum_n}' S(\mathbf{k_n})S(-\mathbf{k_n})Q(\mathbf{k_n})h_{\beta\mu^{-1}}\right\} \\ &\times \left\{-\delta_{\alpha\mu} + 2k_{n,\alpha}k_{n,\mu}\left(\pi^2\eta + \frac{1}{|\mathbf{k_n}|^2}\right)\right\} \\ &- h^{-1}_{\beta\mu}Q(\mathbf{k}_n)\sum_i 2\pi i(k_{n,\alpha}p^k_{i,\beta})\left\{S(\mathbf{k}_n)e^{-2\pi i\mathbf{k}_n\cdot\mathbf{r}_i}\right. \\ &- \left.S(-\mathbf{k_n})e^{2\pi i\mathbf{k_n}\cdot\mathbf{r_i}}\right\}\end{aligned} \tag{C.26}$$

and so

$$
\begin{aligned}
\Pi^{recip}_{\alpha\mu} &= \frac{1}{2\pi V^2}\sum_n{}' Q(\mathbf{k_n})\left[S(\mathbf{k_n})S(-\mathbf{k_n})\left\{\delta_{\alpha\mu} - 2k_{n,\alpha}k_{n,\mu}\left(\pi^2\eta + \frac{1}{|\mathbf{k_n}|^2}\right)\right\}\right. \\
&- \sum_{i,k} 2\pi i k_{n,\alpha} p^k_{i,\beta}\left\{S(\mathbf{k}_n)e^{-2\pi i\mathbf{k}_n\cdot\mathbf{r}_i^k}\right. \\
&- \left.\left. S(-\mathbf{k_n})e^{2\pi i\mathbf{k_n}\cdot\mathbf{r_i^k}}\right\}\right] \qquad (C.27)
\end{aligned}
$$

which agrees with Nosé's result [69].

We can now separate expressions for the (reciprocal space) charge-charge, charge-dipole and dipole-dipole contributions to the stress tensor from the general expression for a three site molecule. The dipole moment is $2\delta\mathbf{p}_i^1$ from fig. C.1 and eqn. C.9 and so for the 3-site molecule

$$
\begin{aligned}
S(\mathbf{k_n}) &= \sum_i q_i e^{2\pi i\mathbf{k_n}(\hat{\mathbf{h}}\mathbf{s_i}+\mathbf{p_i^k})} \\
&= \sum_i \left(q_i e^{\mathbf{s_i}} + \delta e^{(\mathbf{s_i}+2\pi i\mathbf{k_n}\cdot\mathbf{p_i^1})} - \delta e^{(\mathbf{s_i}-2\pi i\mathbf{k_n}\cdot\mathbf{p_i^1})}\right) \qquad (C.28)
\end{aligned}
$$

where, in the interests of brevity, the substitution $2\pi i\mathbf{k_n}(\hat{\mathbf{h}}\mathbf{s_i}) \equiv \mathbf{s_i}$ has been used.

Nosé's expression for the reciprocal part of the stress tensor (C.27) becomes:-

$$
\begin{align*}
\Pi_{\alpha\beta} &= \frac{1}{2\pi V^2}\sum_n{}' Q(\mathbf{k_n})\Bigg\{\Bigg[\Bigg(\sum_i (\ q_i e^{\mathbf{s_i}} + \delta e^{(\mathbf{s_i}+2\pi i\mathbf{k_n}\cdot\mathbf{p_i^1})} \\
&- \delta e^{(\mathbf{s_i}-2\pi i\mathbf{k_n}\cdot\mathbf{p_i^1})}\Bigg)\Bigg(\sum_j (\ q_j e^{-\mathbf{s_j}} + \delta e^{-(\mathbf{s_j}+2\pi i\mathbf{k_n}\cdot\mathbf{p_j^1})} \\
&- \delta e^{(\mathbf{s_j}-2\pi i\mathbf{k_n}\cdot\mathbf{p_j^1})}\Bigg)\Bigg] \\
&\times \left\{\delta_{\alpha\beta} - 2\frac{(1+\pi^2\eta^2|\mathbf{k_n}|^2)}{|\mathbf{k_n}|}k_{n,\alpha}k_{n,\beta}\right\} \\
&- \sum_i 2\pi i k_{n,\alpha}\delta p^k_{i,\beta}\Bigg\{\Bigg[\left\{e^{-(\mathbf{s_i}+2\pi i\mathbf{k_n}\cdot\mathbf{p_i^1})} + e^{(\mathbf{s_i}-2\pi i\mathbf{k_n}\cdot\mathbf{p_i^1})}\right\} \\
&\times \sum (\ q_j e^{\mathbf{s_j}} + \delta e^{(\mathbf{s_j}+2\pi i\mathbf{k_n}\cdot\mathbf{p_j^1})} - \delta e^{(\mathbf{s_j}-2\pi i\mathbf{k_n}\cdot\mathbf{p_j^1})}\ )\Bigg] \\
&- \Bigg[\left\{e^{(\mathbf{s_i}+2\pi i\mathbf{k_n}\cdot\mathbf{p_i^1})} + e^{(\mathbf{s_i}-2\pi i\mathbf{k_n}\cdot\mathbf{p_i^1})}\right\} \tag{C.29} \\
&\times \sum_j \left(q_j e^{-\mathbf{s_j}} + \delta e^{-(\mathbf{s_j}+2\pi i\mathbf{k_n}\cdot\mathbf{p_j^1})} - \delta e^{-\mathbf{s}_j-2\pi i\mathbf{k}_n\cdot\mathbf{p}_j^1}\right)\Bigg]\Bigg\} \tag{C.30}
\end{align*}
$$

Expanding $e^{-(\mathbf{s_i}+2\pi i\mathbf{k_n}p_i^1)} = e^{-\mathbf{s_i}}(1-2\pi i\mathbf{k_n}\mathbf{p_i^1})+O(p^2)$ and substituting into equation C.30 gives

$$
\begin{align*}
\Pi_{\alpha\beta} &= \frac{1}{2\pi V^2}\sum_n{}' Q(\mathbf{k_n})\Bigg\{\Bigg(\Bigg[\sum_i (q_i e^{\mathbf{s_i}}) \\
&+ \Bigg(\sum_j e^{-\mathbf{s_j}}2\delta(-2\pi i\mathbf{k_n}\cdot\mathbf{p_j^1})\Bigg)\Bigg] \\
&\times \Bigg[\sum_i 2\delta(2\pi i\mathbf{k_n}\cdot\mathbf{p_i^1})e^{\mathbf{s_i}} + \sum_j e^{-\mathbf{s_j}}q_j\Bigg] + O(p^2)\Bigg) \\
&\times \left\{\delta_{\alpha\beta} - 2\frac{(1+\pi^2\eta^2|\mathbf{k_n}|^2)}{|\mathbf{k_n}|^2}\mathbf{k_{n,\alpha}}\mathbf{k_{n,\beta}}\right\} \\
&- \sum_i 2\pi i\mathbf{k_{n,\alpha}}2\delta\mathbf{p^1_{i,\beta}}\left[e^{-\mathbf{s_i}}\sum_j q_j e^{\mathbf{s_j}} - e^{\mathbf{s_i}}\sum_j q_j e^{-\mathbf{s_j}}\right]\Bigg\} \tag{C.31}
\end{align*}
$$

If we now replace

$$2\delta p^1_{i,\alpha} = \mu_{i,\alpha} \tag{C.32}$$

then C.31 becomes

$$\begin{aligned}
\Pi_{\alpha\beta} &= \frac{1}{2\pi V^2}\sum_n{}' Q(\mathbf{k}_n)\left\{\left[\sum q_i e^{\mathbf{s}_i}(-2\pi i\mathbf{k}_n)\mu\right]\left[\sum q_j e^{-\mathbf{s}_j} + \sum e^{\mathbf{s}_j}(2\pi i\mathbf{k}_n)\mu\right]\right. \\
&\times \left\{\delta_{\alpha\beta} - 2\frac{(1+\pi^2\eta'^2|\mathbf{k}_n^2|)}{|\mathbf{k}_n|^2}k_{n,\alpha}k_{n,\beta}\right\} \\
&- \left.\sum_i 2\pi i k_{n,\alpha}\mu\left[e^{-\mathbf{s}_\mathbf{i}}\sum_j q_j e^{\mathbf{s}_\mathbf{j}} - e^{\mathbf{s}_\mathbf{i}}\sum_j q_j e^{-\mathbf{s}_\mathbf{j}}\right]\right\} \qquad \text{(C.33)}
\end{aligned}$$

From this expression we can extract the charge-charge, charge-dipole and dipole-dipole contributions to the stress tensor as the terms which contain no factors of the dipole moment, one factor, and two factors respectively.

Charge-charge

$$\begin{aligned}
\Pi_{\alpha\beta} &= \frac{1}{2\pi V^2}\sum_n{}' Q(\mathbf{k}_n)\left\{\sum q_i e^{\mathbf{s}_i}\sum_j q_j e^{-\mathbf{s}_j}\right\} \\
&\times \left\{\delta_{\alpha\beta} - 2\frac{(1+\pi^2\eta'^2|\mathbf{k}_n^2|)}{|\mathbf{k}_n|^2}k_{n,\alpha}k_{n,\beta}\right\} \qquad \text{(C.34)}
\end{aligned}$$

Charge-dipole

$$\begin{aligned}
\Pi_{\alpha\beta} &= \frac{1}{2\pi V^2}\sum_n{}' Q(\mathbf{k_n})2\pi i\left(\left\{\sum_{ij}(-)q_i e^{\mathbf{s}_\mathbf{i}}e^{-\mathbf{s}_\mathbf{j}}\mathbf{k}_{\mathbf{n},\gamma}\mu_{j,\gamma} + q_j\mathbf{k}_{\mathbf{n},\gamma}\mu_{i,\gamma}e^{-\mathbf{s}_\mathbf{i}}e^{\mathbf{s}_\mathbf{j}}\right\}\right. \\
&\times \left\{\delta_{\alpha\beta} - 2\frac{(1+\pi^2\eta^2|\mathbf{k_n}|^2)}{|\mathbf{k_n}|^2}\mathbf{k}_{\mathbf{n},\alpha}\mathbf{k}_{\mathbf{n},\beta}\right\} \\
&- \left.\sum_{ij}\mathbf{k}_{\mathbf{n},\alpha}\mu_{i,\beta}q_j(e^{-\mathbf{s}_\mathbf{i}}e^{\mathbf{s}_\mathbf{j}} - e^{\mathbf{s}_\mathbf{i}}e^{-\mathbf{s}_\mathbf{j}})\right) \qquad \text{(C.35)}
\end{aligned}$$

Dipole-dipole term

$$\begin{aligned}
\Pi_{\alpha\beta} &= \frac{1}{2\pi V^2}\sum_n{}' Q(k_n)\left\{\left(\sum_i 2\pi i k_{n,\gamma}\mu_{i,\gamma}e^{\mathbf{s}_i}\right)\left(\sum_j(-)2\pi i k_{n,\mu}\mu_{j,\nu}e^{-\mathbf{s}_j}\right)\right. \\
&\times \left\{\delta_{\alpha\beta} - 2\left(1+\frac{\pi^2\eta^2|k_n|^2}{|k_n|^2}\right)k_{n,\alpha}k_{n,\beta}\right\} \\
&- \sum_i 2\pi i k_{n,\alpha}\mu_{i,\beta}\left[e^{-\mathbf{s}_i}\sum_j e^{\mathbf{s}_j}2\pi i k_{n,\gamma}\mu_{j,\gamma}\right. \\
&- \left.\left.e^{\mathbf{s}_i}\sum e^{-\mathbf{s}_j}(-2\pi i)k_{n,\gamma}\mu_{j,\gamma}\right]\right\} \qquad \text{(C.36)}
\end{aligned}$$

The traces of these expressions should reduce to the respective contributions to the pressure, which Rowley [60], has shown correspond to one, three and five times the respective energies. These relationships can be used to test the validity of the above expressions and are found to be satisfied.

C.1.2 Real space part

The real space part of the interaction energy between a set of charges is

$$U_{real} = \frac{1}{2}\sum_{i}\sum_{j\neq i} q_i q_j \frac{\mathrm{erfc}(\eta' r_{ij})}{|\mathbf{r_{ij}}|}. \tag{C.37}$$

Since this is simply a pairwise additive form, its contribution to the stress tensor is of the usual virial form (*c.f.* equation 3.57).

From A.3

$$\frac{\partial U_{real}}{\partial r_{i,\alpha}} = \frac{1}{2}\sum_{i}\sum_{j\neq i} q_i q_j \cdot \left\{ \frac{\mathrm{erfc}(\eta' r^{ij}) + \frac{2\eta' r_{ij}}{\pi^{1/2}} e^{-|r_{ij}|^2 \eta^2}}{|r_{ij}|} \right\} \tag{C.38}$$

$$\begin{aligned} \Pi_{\alpha\beta} &= \frac{1}{2V}\sum_{i} q_i q_j \sum_{i\neq j} \frac{(\mathbf{r}_{ij})_\alpha (\mathbf{h}(\mathbf{s}_i - \mathbf{s}_j))_\beta}{|\mathbf{r}_{ij}|^3} \\ &\times \left\{ \mathrm{erfc}(\eta' r_{ij}) + \frac{2 r_{ij} \eta'}{\pi^{1/2}} e^{-r_{ij}^2 \eta'^2} \right\} \end{aligned} \tag{C.39}$$

C.1.3 Constant Term

$$U_{const} = -\sum_{i} \frac{q_i^2 \eta'}{\pi^{1/2}} \tag{C.40}$$

This term depends only on η, so we can ignore this term in the calculation of the stress tensor.